Mechanics of living cells: nonlinear viscoelasticity of single fibroblasts and shape instabilities in axons

Von der Universität Bayreuth
zur Erlangung des Grades eines
Doktors der Naturwissenschaften (Dr. rer. nat.)
genehmigte Abhandlung

vorgelegt von

Pablo A. Fernández

geboren in Buenos Aires,
Argentinien

1. Gutachter: Prof. Dr. A. Ott
2. Gutachter: Prof. Dr. K. Kruse

Tag der Einreichung: 24. 07. 2006
Tag des Kolloquiums: 15. 11. 2006

Zusammenfassung

Die Biomechanik ist ein Gebiet großer biologischer Relevanz. Trotz der Komplexität der biologischen Materie weist die Mechanik von Zellen und weichen Geweben generische Eigenschaften auf allen Längeskalen auf. Unter denen befinden sich Frequenzabhängigkeiten, die Potenzgesetzen gehorchen und an Gläser erinnern, und exponentielle Verformungs-Spannungsbeziehungen. Hauptziel der Biomechanik ist das Verständnis des Zusammenhangs zwischen solchem allgemeinen Verhalten und dem Zytoskelett, ein allgegenwärtiges Netzwerk semiflexibler Filamente, das für die mechanische Integrität, Architektur und Kontraktilität von Zellen verantwortlich ist.

Der erste Teil der vorliegenden Arbeit widmet sich mechanischen Experimenten an einzelnen Fibroblasten unter einachsiger Spannung. Fibroblasten findet man im Bindegewebe. Sie sind nahe Verwandte der Muskeln und deswegen besonders geeignet für rheologische Experimente. Das mechanische Verhalten kräftiger Zellen, die hohen Zugspannungen standhalten und die ohne weiteres um große Strecken gedehnt werden können, erweist sich als sehr gut reproduzierbar. Alle wichtigen Aspekte der Biomechanik können dann beobachtet werden: aktive Kontraktion, Zugversteifung und Plastizität.

Werden die Fibroblasten zwischen mit Fibronectin beschichtete Mikroplatten gebracht, nehmen sie eine regelmäßige, symmetrische Form an und erzeugen Kräfte. Dies bestätigt die Eignung dieser experimentellen Geometrie für mechanische Messungen. Wird eine konstante Zelllänge ℓ vorgegeben, nimmt die Kraft F mit der Zeit zu. Dieses aktive Verhalten wird genauer untersucht indem der konstanten Zelllänge Oszillationen mit Frequenzen im Bereich 0.1–1 Hz überlagert werden. Um im Bereich der linearen Antwort zu bleiben, sind die Dehnungsamplituden stets kleiner als 5%. Die Antwort auf die überlagerten Oszillationen wird dann durch den viskoelastischen Modul $|\Theta|$ und den Verlustwinkel δ charakterisiert. Es stellt sich heraus, dass diese Antwortparameter eine bestimmte Funktion der von der Zelle erzeugten mittleren Kraft $\langle F \rangle$ sind. Die folgende *Versteifungsbeziehung* gilt bei allen untersuchten Fibroblasten: Bei niedriger Kraft ist der Modul unabhängig von $\langle F \rangle$, gleich Θ_0; oberhalb einer Kraft F_C gehorcht die Beziehung zwischen dem viskoelastischen Modul und $\langle F \rangle$ einem Potenzgesetz mit Exponenten im Bereich 1-1.8. Der Verlustwinkel δ hingegen ändert sich nur schwach mit der Kraft. Die Parameter F_C, Θ_0 sind stark korreliert, so dass F_C/Θ_0 im Wesentlichen unabhängig von der Zelle ist.

Erstaunlicherweise sind die Moduln zwar eine Funktion der mittleren Kraft, aber unabhängig von der Zelllänge. Deshalb ist dieses mechanische Verhalten kein „strain stiffening“, sondern es ist eher ein Beispiel aktiven, intrinsischen „*stress* stiffenings“. Es spielt außerdem keine Rolle, auf welche Art und Weise die Kraft geändert wird. Dies kann „aktiv“ durch die Zelle geschehen,

was dem oben beschriebenen Experiment bei konstanter Länge entspricht; Oder aber „passiv“ indem der Experimentator die Zelle dehnt. Die Versteifungsbeziehung bleibt in beiden Fällen gleich. Eine Unterscheidung zwischen aktiver und passiver Spannung ist deswegen bedeutungslos. Die Versteifungsbeziehung ist allgemeingültig, unabhängig von der Art des rheologischen Experiments. Sie gilt einzig und allein dann nicht mehr, wenn die Dehnungsrate $\sim$200 nm/s überschreitet.

Die Versteifungsbeziehung gilt auch, wenn man die Mikroplatten unspezifisch mit Silane-Glutaraldehyd beschichtet, was ein Anhaltspunkt dafür ist, dass dieses Verhalten auf grundlegende mechanische Eigenschaften der belasteten Komponenten der Zelle zurückzuführen ist. Tatsächlich spielt das Aktin-Myosin System für diese Experimente eine wesentliche Rolle, wie gezielte Schädigung des Zytoskeletts mit geeigneten Drogen beweist. Sowohl die Depolymerisation des Aktins als auch die Blockierung des Myosins wirkt negativ auf Steifigkeit, Kraft Erzeugung und Adhäsion.

Darüber hinaus ähnelt die Versteifungsbeziehung sehr Ergebnissen von rheologischen Messungen an Aktingelen. Sowohl die Exponenten als auch das Verhältnis F_C/Θ_0 sind vergleichbar. Solche quantitative Übereinstimmung zwischen lebender und toter Materie wurde bisher nicht beobachtet. Unter physiologischen Bedingungen betragen Filamentlängen und Vernetzungsabstände $\sim$100 nm, wobei die Persistenzlänge von Aktin gleich 10 μm ist. Die mechanischen Eigenschaften von Aktingelen haben ihren Ursprung sicherlich in dem semiflexiblen Verhalten der Filamente. Der Mechanismus ist jedoch bis jetzt noch nicht ganz verstanden. In dieser Arbeit wird eine einfache Erklärung vorgestellt. Es wird gezeigt, dass „stress stiffening“ in Fibroblasten eine große Ähnlichkeit zu dem nichtlinearen mechanischen Verhalten von Euler-Bernoulli Balken besitzt. Bei Biegeverformungen unter 30% zeigen Euler-Bernoulli Balken einen linearen Bereich auf; oberhalb tritt Potenzgesetzversteifung mit einem Exponent 1.75 auf.

Unsere Ergebnisse können auch mit anderen Experimenten an lebenden Materialien verglichen werden. Sowohl in Versuchen an ganzen Geweben als auch in mikrorheologischen Untersuchungen wird Potenzgesetzversteifung mit Exponenten in der Nähe von 1 festgestellt. Im Gegensatz zu unseren Experimenten wird jedoch kein linearer Bereich bei niedrigen Kräften und deshalb auch keine quantitative Übereinstimmung zu Aktingelen beobachtet. Unsere Experimente an einzelnen Zellen, die eine sehr viel höhere Auflösung haben und wesentlich besser kontrollierbar sind, schlagen erstmals eine Brücke zwischen der ganzen Biomechanik und *in vitro* Experimenten an toten Aktingelen.

Wird ein oszillationsloses Experiment durchgeführt, in dem die Zelle mit konstanter Geschwindigkeit gedehnt wird, ergibt sich für Verformungen oberhalb 10% eine näherungsweise lineare Beziehung zwischen der Kraft F und der Zelllänge ℓ, die bis zu Verformungsamplituden von mindestens 100% gültig bleibt. Dies steht in erstaunlichem Gegensatz zu der oben beschriebenen, in oszillatorischen Experimenten gefundenen Versteifung. Versteifung kann also nur auf differentielle Weise beobachtet werden, indem man Oszillationen *kleiner* Amplitude überlagert und den Zusammenhang zwischen den viskoelastischen Parametern $|\Theta|$, δ und der mittleren Kraft $\langle F \rangle$ betrachtet. Im Zuge unserer Auffassung der Versteifungsbeziehung als *elastischer* Antwort, muss angenommen werden, dass Fibroblasten bei Verformungen oberhalb $\sim$10% *plastisch* fließen. Tatsächlich erinnert das mechanische Verhalten von Fibroblasten an das

von elastisch-plastischen Metallen, und zwar an kinematische Plastizität, ein Merkmal von Materialien, die aus einer plastisch fließenden Matrix mit eingebetteten elastischen Komponenten bestehen. Obwohl eine gründliche Charakterisierung noch durchgeführt werden muss, steht jetzt ein geeigneter phänomenologischer Rahmen zur Verfügung.

Angesichts der Reproduzierbarkeit und der für biologische Verhältnisse ungewöhnlichen Einfachheit des beobachteten mechanischen Verhaltens ist es erstrebenswert, das Experiment zu erweitern, um gleichzeitig viele Zellen untersuchen zu können. Derart wäre es z.B. möglich unterschiedlich gentechnisch veränderte Zellen schnell zu charakterisieren. Dazu wurde eine Verfahren entwickelt, durch die das rheologische Verhalten einer Monoschicht aus $\sim 10^5$ Fibroblasten mit einem kommerziellen Rheometer gemessen werden kann. Die Fibroblasten haften zwischen zwei, am Rheometer befestigten, optisch flachen Glasplatten. Das von uns entwickelte Verfahren ermöglicht eine genaue Justierung der Glasplatten, ohne die eine Messung ausgeschlossen ist. Derart wurden vielversprechende Ergebnisse gewonnen.

Von Interesse ist außerdem die mikroskopische Visualisation der Struktur des Zytoskeletts unter den Bedingungen des Experiments. Leider nehmen die Zellen dann eine zylindrische, 3-dimensionale Geometrie an, bei der die Auflösung feiner Details unmöglich wird. Als Alternative wurde ein lithographisches Muster entwickelt, das aus parallelen, $10\,\mu$m breiten, $30\,\mu$m tiefen Schlitzen besteht. Wenn das Muster mit Fibronektin beschichtet ist, kriechen die Fibroblasten in die Schlitze und nehmen Formen ähnlich wie im Experiment an. Hier gibt es aber die Möglichkeit die Zellen zu fixieren, um sie mit konfokaler oder Röntgen– Mikroskopie zu beobachten.

Der zweite Teil der vorliegenden Arbeit betrifft Experimente an Neuriten. Zu denen gehören unter anderen Axonen – aus denen Nerven bestehen– und PC12 Neuriten, ein Modelsystem für Axonen. Bei ihnen handelt es sich um lange, zylinderförmige Röhren voller parallel verteilter Mikrotubuli. Neuriten werden hier durch Änderungen des osmotischen Drucks aus dem Gleichgewicht gebracht. Mit Hilfe der Bildanalyse wird der Zeitverlauf des Volumens und der Fläche des Neurites nach einem hypo- bzw. hyperosmotischen Schock gemessen.

Nach einem hypoosmotischen Schock verändern sich Neuriten in zweierlei Hinsicht. Zum einen schwellen sie, da Wasser hineinfließt. Zum anderen tritt eine peristaltische Modulation der Form auf. Wir interpretieren diese Formveränderung als Pearling Instabilität – eine Art von Rayleigh-Plateau Instabilität, die von der schnellen Zunahme der Membranspannung hervorgerufenen wird. Die Instabilität wird durch das zeitabhängige Fourier-Spektrum der Neuritenform charakterisiert. Um die Rolle des Zytoskeletts zu erforschen werden hypoosmotische Schocks nach Zugabe unterschiedlicher spezifischer Drogen durchgeführt. Der Beitrag der Mikrotubuli zur Stabilität der Neurite erweist sich als der von größter Bedeutung. Depolymerisation der Mikrotubuli durch Nocodazol hat zweierlei Effekte: die Amplitude der Modulation nimmt stark zu, und die Wellenzahl der am schnellsten wachsenden Fouriermode wird um etwa 10% größer.

Die genaue Analyse des Zeitverhaltens des Neuritvolumens und der Instabilität nach einem hypoosmotischen Schock zeigt, dass das Volumen zurück zu seinem ursprünglichen Wert relaxiert, und die zylindrische Form wiedergewonnen wird, indem die peristaltische Modulation zerfällt. Bemerkenswerterweise relaxiert die Instabilität eindeutig schneller als das Volumen, was auf eine Entkopplung zwischen Membranspannung und Neuritform während der Relaxation

hindeutet. Wir schlagen vor, dass dies auf Fusion von inneren Vesikeln an die Membran zurückzuführen ist.

Das Zeitverhalten des Neuritvolumens nach hypoosmotischen Schocks kann näherungsweise durch eine anfängliche Schwellrate, ein maximales Volumen, und eine Relaxationszeit beschrieben werden. Diese Parameter wurden bei unterschiedlichen Temperaturen und Anfangsschockstärken $\Delta\Pi_0$ untersucht. Die Schwellrate hängt nichtlinear von der Anfangsschockstärke ab: Sie sättigt oberhalb von $\Delta\Pi_0 = 0.3\,\mathrm{RT}\,300\,\mathrm{mM}$. Das maximale Volumen V_M skaliert linear mit dem Anfangsvolumen V_0. Die Betrachtung von V_M/V_0 als Funktion von $\Delta\Pi_0$ offenbart, dass Neuriten bei schwachen Schocks $\Delta\Pi_0 \leq 0.3\,\mathrm{RT}\,300\,\mathrm{mM}$ genauso wie perfekte Osmometer schwellen, bevor die Relaxationsphase auftritt. Bei starken Schocks, $\Delta\Pi_0 = 0.5\,\mathrm{RT}\,300\,\mathrm{mM}$, schwellen Neuriten eindeutig weniger als perfekte Osmometer. Deswegen muss sich bei starken Schocks die innere Osmolarität schon während der Schwellphase verändert haben, oder aber hydrostatischer Druck muss entstanden sein. Die Abhängigkeit zwischen Relaxationszeit und Temperatur gehorcht einem Arrheniusgesetz, was darauf hinweist, dass die Relaxationsrate von der Bewegung von Ionen durch Kanäle bestimmt ist.

Gleiche Versuche wurden auch nach Schädigung des Aktins, Myosins, und der Mikrotubuli mit Drogen durchgeführt. Keine dieser Behandlungen hat die Relaxationsphase beeinflußt. Das liefert einen Anhaltspunkt dafür, dass sie ausschließlich durch Veränderungen des osmotischen Drucks, ohne Beitrag vom hydrostatischen Druck, stattfindet. Hingegen führt die Schädigung des Zytoskeletts, insbesondere die Depolymerisation der Mikrotubuli, zu deutlich schnellerem und stärkerem Schwellen. Der Einfluss der Drogen zum einen auf das Zeitverhalten des Neuritvolumens und zum anderen auf die „Pearling“-Instabilität lassen vermuten, dass in der anfänglichen Schwellphase hydrostatischer Druck in den Zellen entsteht und die Schwellrate bestimmt.

Zusammenfassend wurden reproduzierbare Experimente auf der Skala der ganzen Zelle entwickelt, die quantitative Aussagen über biologisch relevante Phänomene ermöglichen. Sowohl die Experimente an Fibroblasten als auch diejenigen an Axonen betreffen beide hoch symmetrische Systeme, deren einfache Geometrie das physikalische Verständnis erleichtert. Erste Interpretationen der Phänomene wurden gefunden, die auf allgemeinen mechanischen Konzepten basieren.

Contents

List of Figures

Chapter 1

Introduction

die Physik **muss** *stimmen*

– a würzburger biophysicist, on biophysics

This thesis is divided in two main sections: nonlinear viscoelasticity of fibroblasts, and shape instabilities in axons. Both studies focus on mechanical behaviour. The observed phenomena are quantitatively analysed, with the aim of their physical modelling. Both address single cells with axially symmetric shapes. In the first case, the geometry is achieved as fibroblasts adapt to the symmetrical boundary conditions of the experiment. In the second case, axons already have a cylindrical geometry. This geometry is purposely chosen as to ease understanding of the underlying physics. In both studies the living nature of the system is integrated in the phenomenology: fibroblast viscoelasticity is probed in presence of active contractile behaviour, and axons recover from the induced shape instabilities by means of homeostatic mechanisms. The phenomena under study – nonlinear elasticity, plasticity, hydrodynamic instability – are of physical nature. They are studied with the hope of shedding quantitative light onto biological processes – cell shape, mechanical integrity, cytoskeletal self-organisation. Thus, this work can be classified as belonging to biophysics (1, 2).

On biophysics

The meaning of this term is difficult to precise. Indeed, biophysicists are most often people who have studied either medicine, biology, biochemistry, chemistry, mathematics, or physics– not biophysics. The more so as physics pretends to be a discipline which explains everything, or at least is in principle able to do so. Such claims of universality may make biologists feel it is not worthwhile investigating the physics of living matter, since anyway they won't be different from those of dead matter. Vitalism has lost ground and it is no longer a major goal to show that no new physics underlie biology. Thus, today biologists sometimes view the study of the physics of living matter as biologically irrelevant; if it is the same physics found everywhere else, how can it be important to explain life?

A kind of biophysics which is unanimously appreciated by the scientific community is the development of new physical techniques to study biological problems. This is indeed a field of utmost importance. Suffice it to think of the contributions of X-ray crystallography or NMR to

biology and biochemistry. However, the physics here is limited to the measurement device; the interpretation of the results is done in essentially biological terms, so this is more of a biological application of physics. Classified as belonging to biophysics one also finds biochemistry, since it is ruled by physics and underlies biology (2). To me, this also misses the point. Biochemistry is indeed subject to the rules of organic and physical chemistry but it deals with chemical entities which are absolutely unique to life. Moreover, biochemical structures are of striking universality among all living beings. This uniqueness and inner simplicity make it a well-defined field on its own. Outstanding examples of biochemical problems are protein folding, or the action of isomerases on DNA – problems deeply different from those in non-biological chemistry.

So in our quest for biophysics we turn to biology. Biology arose as the systematic description of the natural world, as a discipline involved with extensive collection of data and its classification. Taxonomy then provided the essential grounds for the discovery of evolution. Once endowed with evolution, biology makes sense, becomes amenable to human understanding– it no longer is the dream of remote gods. Biology is released, allowed to change; it redefines itself through the interactions among its actors. Biological features are realised to have functions which justify their existence in an ecological context. Out of this breakthrough arise quantitative disciplines such as physiology and population genetics. With the development of modern molecular genetics, however, biology has lost this vitality. Present-day biologists think in terms of genomics, proteomics, ionomics, bioinformatics. The main conclusions are that a certain gene is essential for a given response; questions of how and why are not addressed. The situation resembles somewhat the taxonomic beginning of biology– a static data landscape where life is missing. Presumably, in the future bioinformatics will also liven up, once genome dynamics are understood.

From my humble position, I regard biophysics as a force opposing the taxonomic approach in biology. Biophysics is for me the search for simplicity which characterises physics, in that most complex of all scenarios–life. The best example of this approach is probably given by Schrödinger's "naïve musings" (3), but one may also regard D'Arcy Thompson, Mayer, or Mendel (the Planck of biology?) as biophysicists (4). I apologise if this classification is offensive to the reader; it is not intended as historical revision, but only as illustration of our (much less ambitious!) goals and approach.

On biomechanics

Evolution makes biology alive. Its actors move, eat each other, shape the landscape. As biology is extended by the exploration of the microscopical world, new landscapes of sheer complexity are found in each milimeter of tissue. The building blocks of biology can also crawl, eat bacteria, shape their environments (5). This dynamic interaction with the surroundings requires mechanical forces. Enter biomechanics, along with bioenergetics maybe the most biophysical field in biophysics. Mechanics lies at the very roots of physics. It deals with stress fields, invisible entities which decide whether something moves, deforms, or breaks (6, 7). The biological relevance of mechanics is huge, bearing directly on the fate of the individuum. From the antilope running away from the tiger, to the cancerous cell crawling into the blood stream, to the bacteria swimming for food, mechanics rules biology as the master of motion and integrity. Within the

biologically relevant length scales, from a few nanometres to meters, mechanics is essentially scale free: the same concepts used to describe the bending of a bone can be applied to the bending of an actin filament (8, 9). This economy of concepts is a consequence of the continuum approach, of focusing on geometrical, generic features. In a way, biomechanics is unavoidable. When a force bends a bone or a filament it does not care about the genes coding for them; only the bending modulus is relevant.

In the last years, the role of biomechanics as information carrier has been revealed at the single-cell level (10–12). The mechanical properties of the extracellular medium are now known to be cues to cells. That mechanics can transfer information is observed at familiar length scales; one may think of trees following gravity, or bones growing according to tension.

The cytoskeleton

The cytoskeleton is a term as vast as biophysics itself. It refers to a collection of filaments and crosslinkers which endow the cell with internal structure, mechanical integrity and the ability to generate forces. Excellent introductions can be found in Bray (5) or in Howard (9). Along with the cell membrane, the cytoskeleton confers the cell with long-term stability: it provides an internal scaffold which hinders diffusion, allowing for compartimentalisation, directional transport and architecture. Most striking is the dynamic nature of this scaffold, which can disassemble and change structure within seconds in response to biochemical cues. In a very real sense, the cytoskeleton is the frontier between biochemistry and biophysics.

Of all the cytoskeletal subcomponents, the most relevant for us is actin (5, 9, 13). Monomeric actin is a globular protein which binds to itself forming actin filaments with a diameter of 7 nm. In the process of polymerisation the monomers consume energy via ATP hydrolysis, which confers this filamentous system with astonishing versatility. By capping filament ends with specialised proteins, the growth of actin filaments can be exquisitely controlled by the cell. Moreover, filament growth can generate significant forces (14). This process plays a fundamental role in cell locomotion (5, 15). Forces can also be generated by myosins, molecular motors acting on actin filaments which can contract actin networks. When activated, myosin molecules bind together forming bipolar filaments able to slide actin filaments past each other. Coarse-grained models for such active gels inspired in the physics of liquid crystals have been proposed (16–18) and shown to reproduce many features of cell dynamics.

The status of the cytoskeleton as the frontier between biochemistry and biophysics is nicely illustrated by the fact that cytoskeletal strain is biochemically recognised (12). As discussed in the next chapter, the formation of contacts between the extracellular matrix and the cytoskeleton requires mechanical tension. It has also been directly shown that straining actin filaments changes their affinity for intracellular proteins (19). This also works in the other direction; the architecture of the cytoskeleton is under biochemical regulation. An outstanding example is given by intracellular calcium, a universal effector in cell signalling. Changes in intracellular Ca^{2+} concentration trigger a multitude of responses, among them activation of myosin as well as severing of actin filaments via gelsolin (discussed in chapter 2). The combination of contraction and changes in filament length can have dramatic effects on the mechanical properties of the cytoskeletal network. An attractive idea along these lines is the solation-contraction coupling hy-

pothesis of Taylor and coworkers (20, 21). Its basic tenet is that a highly crosslinked gel of actin filaments cannot contract, as the forces generated by myosins are opposed by internal strain of the gel. Contraction requires its partial solation, either through filament severing by gelsolin, or by dissociation of crosslinking proteins. Both processes are triggered by an increase in calcium concentration. Cytoplasmic pattern-formation and shape oscillations have been modelled based on these concepts (22).

May the preceding examples illustrate the situation in the field. On one hand we have the complex, highly dynamic phenomena inside the cell, leading to force generation, spreading, directional crawling. On the other hand, a plethora of minimal theories have been developed, showing that a few idealised components can qualitatively reproduce the observed behaviour. With the current understanding of the cytoskeleton, often several microscopical mechanisms can be proposed for a given macroscopic process; actually *proving* an explanation to be correct is a daunting task, which requires several complementary experiments on the same system.

With the aim of minimising this uncertainty, *in vitro* experiments have become very fashionable in the last years. By isolating and purifying a few components, the self-organising, self-assembling capabilities of cytoskeletal components can be subject to intensive study (23, 24). Particularly relevant for us are rheological measurements on actin gels (25–29), which have revealed quite generic stress stiffening responses (30, 31). Chapter 2 discusses these results in more detail.

Single-cell mechanics

Biomechanics, being a quantitative discipline, is deeply affected by the intrinsic variability of biological materials. To complicate matters, biological tissues show highly nonlinear responses and often are naturally in a stressed state. Therefore, simple experiments where only an elastic modulus is measured can give widely different results. This makes biomechanics somewhat paradoxical. A good measurement in biomechanics should include a detailed study of the zero force state; but the probe may have never been at zero stress, may even be fragile and difficult to handle under such conditions (8).

At the single cell level, the situation is much worse. When going over the literature on single cell mechanics, one finds values for the Young's modulus of a cell covering up to 3 orders of magnitude (32–39). To some extent, these discrepancies reflect the different methodologies used, as well as the slightly different length scales studied. A more subtle problem is the responsiveness of cells to the measurement. In particular, the boundary conditions – mechanical as well as biochemical – can make a dramatic difference. This is in contrast to experiments on tissues, where doing the measurement does not affect the surroundings of the cells inside the sample. As an example, single round cells in suspension (40) show a very different frequency dependence of the shear moduli than cells spreading on a substrate (33). Most likely, this reflects the different internal structures induced in each geometry. Thus, the precise way a cell is probed is of utmost importance in single-cell mechanics, since it defines the mechanical properties of the sample. In this sense, the field reminds of wave-particle duality–the behaviour of the system may depend on the question one poses.

Chapters 3 and 4 describe mechanical measurements on single cells held between two microplates, the “cell-pulling” geometry (38). The measurement probes the response of the whole cell. Fine, regional details cannot be distinguished; only the overall behaviour is recorded. This may be viewed as losing possibly relevant spatial information (41); we will argue that the geometry is actually advantageous, leading to highly reproducible mechanical behaviour. Moreover, the results gained with the cell-pulling geometry can be highly relevant for the modelling of tissues (10, 42), where the “atoms” are whole cells.

The first part of this report is arranged as follows. Chapter 2 introduces the cytoskeleton in some detail and summarises the results in biomechanics most relevant for us. The experimental setup is discussed in Chapter 3. The experimental results obtained with the cell-pulling setup are thoroughly described in Chapter 4. At the end of this chapter, possible explanations for stress stiffening in fibroblasts are given, and the similarity between metal plasticity and fibroblasts mechanics is highlighted.

Osmotically induced shape transformations in axons

Axons are the long cellular processes extended by neurons which transmit the nervous impulse. A $\simeq 1\,\mu$m thick axon of a motor neuron can easily reach a length of 1 meter. This extreme aspect ratio is reflected in their cytoskeletal structure. Axons are filled with longitudinal bundles of filaments, arranged in a given direction, which act as a railway for directional transport of material from one end to the other. This filament array also confers the axon with rigidity and mechanical stability, necessary to withstand the huge forces which may arise even in normal physiological conditions. This highly organised cytoskeletal structure, plus the simple cylindrical geometry, make this system ideal for biophysical studies where the aim is to understand the biologically relevant physics. Unlike the cell-pulling experiment, here the clean geometry is already present thanks to the careful choice of the system.

The experiments described in the second part of this report concern mechanical stability of neurites. They developed out of Pramod A. Pullarkat’s observation of a cylindrical-peristaltic transition of the axonal shape triggered by a sudden dilution of the extracellular medium (43). Similar shape transformations – known as pearling in the physics literature– have been observed in membrane tubes (44) and in cellular extensions (45). They can be well explained as a Rayleigh-Plateau-like instability triggered by elastic tension arising out of membrane stretching. There are several minor differences between the Rayleigh-Plateau instability in liquid jets and pearling in membrane tubes. The instability is driven in the former by interfacial tension, whereas tension in membrane tubes is rather of elastic nature. Moreover, liquid jets are always unstable, whereas membrane tubes are stabilised by their elasticity. Where cytoskeleton is present it provides extra stability, which has to be overcome to trigger pearling. Based on this framework, we argue that the hypoosmotic shock-induced shape transformation obeys a similar mechanism, and that it can be described as a Rayleigh-like instability driven by elastic tension in the membrane, arising out of axon swelling (43), similar to the phenomena described in Refs. (44, 45).

In axons, similar cylindrical-peristaltic shape transformations –known as beading in the biological and medical literature– arise under a wide range of situations. These include neurode-

generative diseases like Alzheimer's (46), brain trauma (47), stretch injuries to nerves (48) and *in vitro* as well as *in vivo* application of neurotoxins or drugs (49, 50). In stretch injuries, tension is responsible for beading, whereas in the other examples the common feature appears to be cytoskeleton disruption. In all of them, the beaded state persists and no recovery has been reported. In our experiments, where the shape transition is triggered by a hypoosmotic shock, the volume is seen to come back to its initial value and the original cylindrical shape is recovered within several minutes. Moreover, the periodic modulation sets in only when the change in osmotic pressure is strong and fast enough. This points towards the existence of regulatory mechanisms acting at slow timescales. Regulatory responses to changes in osmotic pressure have indeed been known for a long time (51–53). They are ubiquitous homeostatic mechanisms found in all kinds of cells. The short term response involves a passive diffusion of specific solutes which opposes the initial flux of water. In the case of a hypoosmotic shock, cell swelling leads to an increase in the conductance of the membrane to potassium, whose diffusion out of the cell lowers the internal osmolarity and reestablishes the original volume (54, 55).

Essential to this response is a "volume sensor" which opens ion channels when the volume deviates from its normal value. The nature of this sensor is at present unknown (51, 53). The change in the internal concentrations itself may act as a trigger (56). Tension in the membrane may also open mechanosensitive channels (57). Though their physiological role is still unclear, mechanosensitive channels are ubiquitously found and may well act as membrane tension sensors. Finally, the cytoskeleton is known to be important in volume regulation (12). Being an interconnected structure spanning over the whole cell and crosslinked to the membrane, changes in cell volume should invariably lead to cytoskeletal strain. This can trigger biochemical signals, but also the stress itself may balance hydrostatic pressure differences across the membrane. Mixed mechanisms can be advanced; for example, membrane tension may open mechanosensitive calcium channels, triggering Ca^{2+} bursts leading to solation or contraction. At present it is not clear which mechanisms are important. This is indeed a general problem in the study of the cytoskeleton, that of distinguishing between its biochemical and mechanical aspects. To complicate matters, different cell types respond differently to cytoskeleton disruption (58). It is therefore important to find model systems showing reproducible behaviour.

Thus, besides the investigation of the pearling instability itself, a certain effort was spent on the volume regulation process, pursuing the question: what role do hydrostatic pressures play in the volume regulation response of axons? In this exceptional system, hydrostatic pressure is opposed by the deformation of a highly organised cytoskeleton. Moreover, thanks to the cylindrical geometry, pressure reveals itself by inducing pearling.

Chapter 5 gives some detail on axons, a simple theoretical background for the Rayleigh instability, and discusses the experimental details. In chapter 6 the results are presented and discussed.

Part I

Nonlinear viscoelasticity of single fibroblasts

Chapter 2

Biomechanics

This chapter begins by presenting the main features of the cytoskeleton, an intracellular filamentous network which defines cell mechanics and architecture. Then cell adhesion and fibroblasts are discussed. Finally the mechanical features of biological materials are reviewed, going from whole tissues down to the sub-micrometer scale.

2.1 On biomechanics

An essential requirement for a living unit is mechanical integrity, as disrupting forces are always present and show up at all length scales. Already a single cell faces viscous shear forces by the surrounding liquid (5); and as a multicellular organism grows in size, it eventually meets gravity. To mantain a structure under constant forces, living matter must behave like an elastic solid. Nevertheless, eucaryotic cells are clearly not simply elastic solids; they manage to change their shapes, divide, crawl. Cells can flow without losing integrity, an ability which in mechanical terms is a signature of *plasticity* (7).

Yet this suffices not. For a cell to move in a viscous environment without slowing down, it must convert energy into movement. Not only must it be stiff to sustain external forces; it has to generate forces itself. This leads to *contractility*, a major function of the cytoskeleton found at all length scales (5). The need for contractility arises in order to move against gravity and overcome friction, or to pump internal fluids such as blood and air. As it turns out, the structures powering single cell movement are also behind muscle contraction–the orchestrated machinery of crawling lets life run, jump, fly.

In fact, living matter displays a permanent desire for tension which distinguishes it strongly from dead matter. Single cells in culture develop stress spontaneously by pulling on the substrates on which they adhere. If they cannot adhere they round up, revealing a surface tension also actively generated. Again, the picture remains at the multicellular level. When cut, important blood vessels and nerves show rest-lengths about 30% shorter than their *in situ* length (59). Soft connective tissues are under tension even during sleep (59).

2.2 The Cytoskeleton

At the heart of cell mechanics stands the cytoskeleton, the intracellular structure behind spatial organisation and mechanical properties in eucaryotic cells. As life on earth began, about $3.5 \cdot 10^9$ years ago, it did not take the first steps by cytoskeleton-powered amoeboid crawling; for the first $2 \cdot 10^9$ years there were only bacteria. When eucaryotes finally appeared, they were the most sophisticated machines ever to roam the earth. They had a nucleus, a cytoskeleton, organelles, and they could form multicellular organisms (13). Conceivably, it was precisely the cytoskeleton what allowed this degree of organisation. A number of reasons for this can be advanced (5). For one, the cytoskeleton allows for mechanical integrity without shape constraints; surface plasticity in turn facilitates phagocytosis, which may have been key to the acquisition of mitochondria, chloroplasts, and maybe even the nucleus. As cell size increases, diffusion is no longer able to transmit material inside the cell, and directional transport becomes essential. This is possible thanks to the cytoskeletal scaffold. Transport of material against viscous forces is performed by motors walking on filaments, precisely directed to the right place. In this way the cytoskeleton allows for the bigger sizes of eucaryotic cells. Spatial organisation of single cells is in turn a prerequisite for complex tissues to arise. Examples are secretory cells, neuronal synapses, muscle cells, etc. In general, tissue architecture requires intracellular architecture (13).

2.2.1 Actin

Actin is a globular protein with a diameter of 6 nm (9). Actin monomers binds to themselves, forming two-stranded filaments with a cross-sectional area of about 20 $(\text{nm})^2$ and a right-handed twist (9). As actin monomers are asymmetrical and actin filaments are double stranded, the microscopic details of the monomer-addition process are different at each filament end. Therefore the polymerisation rate constant k_{on} and the depolymerisation rate constant k_{off} can have different values at each end. The final product after monomer addition, however, is the same regardless on which filament end addition takes place – provided all monomers are equal. Then the ratios $k_{\text{off}}/k_{\text{on}}$ at each end must be equal, since both are equal to the critical monomer concentration. When the free monomer concentration exceeds $k_{\text{off}}/k_{\text{on}}$, both filament ends grow, though they may do it at different rates, as illustrated in Fig.2.1(A). The situation is actually more complex. Actin binds to ATP and catalyses its hydrolisis, so that ATP-actin monomers become ADP-actin monomers after a while. Moreover, ATP-actin fits well into filaments, but ADP-actin does not; thus the critical concentration $k_{\text{off}}/k_{\text{on}}$ of an ATP-actin filament end is lower than that of an ADP-actin filament. In this way the possibility of "treadmilling" arises. If a filament is long enough, the ATP-actin end will grow and the ADP-actin one shrink, material constantly travelling between the two while ATP is hydrolysed. This process is illustrated in Fig.2.1(B).

Mechanically, actin filaments have well defined properties, and can be described as isotropic materials which sustain high stretching or bending forces without breaking. Stretching of single 1 μm long actin filaments has revealed a Young's modulus of 2.3 GPa (9). This agrees well with indirect measurements via thermal undulations, which gave values of 1.7 GPa (9). Recently, the force - length relations of 3–10 μm long single actin filaments have been measured (60). At forces below 50 pN, an entropic stiffening regime is seen, corresponding to wormlike chain

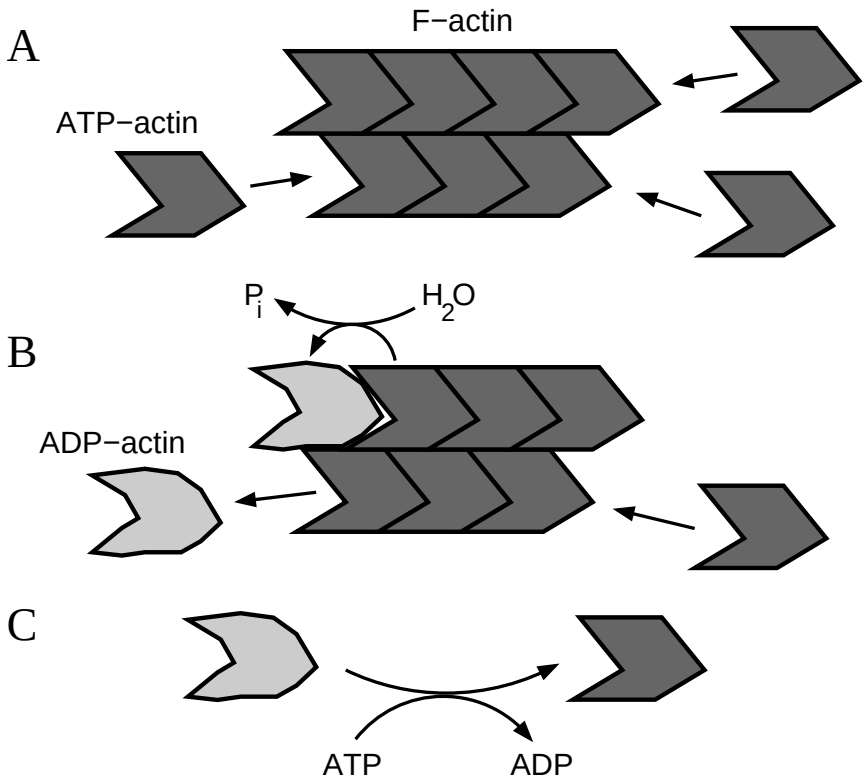

Figure 2.1: *Cartoon illustrating actin polymerisation.* **A:** *ATP-actin monomers polymerise forming two-stranded F-actin filaments.* **B:** *polymerised actin hydrolyses ATP into ADP. ADP-actin monomers do not fit well together and dissociate from the filament.* **C:** *in solution, ADP-monomers exchange ADP for ATP and begin the cycle anew.*

behaviour. Above deformations of $\sim 1\%$, a crossover to an enthalpic linear regime is seen. Forces can then reach up to 200 pN.

2.2.2 Actin binding proteins

To exploit the full power of actin filaments, cells have a plethora of actin binding proteins (ABPs), many of which polyfunctional. These regulate filament growth and crosslink them together or with other proteins.

The concentration of unpolymerised actin in the cytosol of most cells is very high, about 100 μM. Though the *in vitro* critical concentration for polymerisation is a factor of 500 lower, a significant pool of free actin monomers is always present. This is possible thanks to ABPs which regulate intracellular F-actin assembly (61). The most abundant monomer-binding factor in higher animals is thymosin, a small, highly charged protein (5). At a high concentration and with a relatively high dissociation constant of about 1 μM, it rapidly buffers monomeric actin.

An important result from studies of cell motility is the observation that new filaments initiated by extracellular cues are often created by *de novo* nucleation events (61). An ABP which has

become fashion in the last years is Arp2/3, a highly conserved seven protein complex that, when activated, nucleates new actin filaments from the sides of existing filaments, inducing branching at an angle of 70° (62). *In vitro* it also enhances the rate of actin filament nucleation, and crosslinks actin filaments. Additionally it caps the slow-growing ends of actin filaments. In crawling cells, the Arp2/3 complex localises in lamellipodia.

The Arp2/3 complex also binds to the actin-monomer binding protein profilin. The effects of profilin depend on its concentration. At low concentrations, it can enhance actin filament assembly by shuttling monomers from thymosin to the fast-growing ends of actin filaments. At high concentrations, it acts as a monomer-sequestering protein (62). Profilin also catalyses exchange of actin-bound nucleotides (5).

In addition there exist depolymerisation factors such as cofilin, which stimulates disassembly from slow-growing ends (5). Some ABPs "cap" actin filament ends, preventing monomer exchange and stabilising filament length. The situation is indeed complex, yet some progress has been made in *in vitro* experiments. A breakthrough came as *Listeria* propulsion was reconstituted with a minimal system (63). The four proteins needed are actin, the nucleation and crosslinking factor Arp2/3, the depolymerisation factor cofilin and a fast-growing end capping protein. These proteins together generate growing F-actin tails which can propel beads against viscous forces.

As a last example of protein multifunctionality we mention gelsolin. Gelsolin is a compact protein found in most vertebrate cells, which receives its name from its ability to transform an elastic gel into a liquid sol by severing F-actin. Gelsolin 1) binds to actin monomers to promote actin nucleation, 2) caps the fast-growing end of actin filaments, and 3) severs F-actin. Its effects are regulated by Ca^{2+} ions and phosphoinositides, especially PIP_2, opening the door to the control of mechanical properties by signalling pathways. A rise in calcium promotes binding of gelsolin to actin and filament severing, whereas PIP_2 induces its detachment from F-actin (5).

Crosslinking proteins

Non-crosslinked actin, at physiological concentrations and filament lengths (less than 1 μm), is soft and fragile. The mechanical functions of actin filaments require the formation of an elastic gel. Different ABPs generate different crosslinking geometries, so the mechanical properties of the gel depend crucially on the concentration and type of ABPs. It is thus no surprise that crosslinking ABPs of all types exist. The small protein *fimbrin* links filaments in parallel arrays. it α-Actinin is composed of two polypeptide chains, each chain with an actin-binding domain at one end and a flexible central domain. As the two chains are aligned in antiparallel fashion, this forms spacer which binds filaments at a distance of about 40 nm. Along with α-actinin, the most abundant ABP in vertebrate cells is *filamin*, an 80 nm protein which forms a V-shaped, flexible dimer, with an actin-binding domain in each N terminus. In cultured non-muscle adherent cells, filamin localizes to the cortical actin network, the base of cell membrane protusions, and along stress fibers (64). In contractile assemblies of actin and motor proteins (discussed below), the rigid rodlike protein *tropomyosin* binds along actin filaments, stabilizing them and modifying the interaction with other ABPs . It enhances interaction with the motor myosin II, but limits the association with actin-bundling or actin-fragmenting proteins (5).

Myosin

The molecular motor myosin is also an ABP, but outstanding in its ability to move actin filaments against a load. Muscle myosin and myosin II, its homologue in nonmuscle cells, are large proteins consisting of two polypeptides, each one with two domains; a globular head and a long tail. The two polypeptides are joined by the tails, which are intertwined together. The globular myosin heads are actin-activated ATPases, the sites where mechanical and chemical energy are interconverted (5). Near the myosin head we find the Light chains, regulatory subunits belonging to the calmodulin family. In the form of myosin II found in nonmuscle cells, the regulatory light chain is substrate of kinases such as myosin light chain kinase (MLCK). MLCK has a regulatory domain which interacts with the Ca^{2+}-binding protein calmodulin. In this way, when the intracellular calcium concentration rises, MLCK becomes activated and in turn phosphorilates myosin light chains. This activates the myosin heads, by exposing the actin-binding site, and induces a conformational change in the myosin tail which extends. Extended myosin tails bind to other myosin tails, leading to assembly of bipolar myosin minifilaments (65). These rodlike structures have motor heads at each end, facing opposite directions. Hence they can slide antiparallel actin filaments relative to each other. This is the basic unit behind actomyosin contraction. Myosin is also subject to deactivation by a phosphatase, whose activity is independent of calcium. The Rho pathway, responsible for sustained contraction, inhibits this phosphatase as well as activates another kinase (Rho-kinase) which activates myosin (5).

Myosin generates forces by means of a conformational change coupled to ATP hydrolisis. The details of this interaction are object of current research and much reminds to be understood. It is known that myosin acts in a non-processive fashion, i.e. a myosin head only stays bound to actin for a short time (9). Inspired by the observation that muscle liberates more heat when it shortens against a load than in unloaded conditions (66), it has been speculated that the kinetics of force production depend on the load. Recently this so-called “Fenn effect” has been studied at the single molecule level (67). Single crossbridges have been reported to produce movement in two phases, one of them depending in an exponential manner on the applied load, the other one much less load-dependent.

When collections of motors acting simultaneously are considered, collective effects can arise. In particular, actin-myosin motility assays have revealed a discontinuity in the force-speed relation about stalling conditions (68). This phenomenon has been theoretically explained as a dynamical phase transition (69). Above a critical motor activity, the zero-speed state is unstable against two finite, opposite velocities.

2.2.3 Microtubules

Microtubules are similar to actin filaments in being polar and of a dynamic nature, able to switch between growth or shrinkage. Indeed, catastrophic shrinkage is a physiologically important feature of microtubules; in general, their remoteness from polymerisation equilibrium is more important than for actin filaments. Another important difference between the two is size: microtubules have a cross-sectional area of 200 $(\text{nm})^2$, ten times that of actin filaments. Hence they are much stiffer against bending, with a persistence length of about 6 mm (9). The current picture of

microtubules presents them as a central organising unit which controls long-range organisation. Its main functions comprise finding the center of the cell, separating genetic material before cell division, and maintaining cell polarisation during movement. Mechanically, they are essential for axons, as will be shown in the second part of this work. In round cells, however, they seem to be of little importance.

2.2.4 Intermediate filaments

Intermediate filaments have a diameter of 10 nm. They form a tough, crosslinked network extending from the nucleus to the cell membrane (5). Their flexural rigidity seems to be quite low, the persistence length being about 1 μm (9). This suggests that the individual coiled-coils making up the filaments are not heavily crosslinked (9). Thus they are highly resistant to elongation, but yield when twisted or sheared. Unlike actin or microtubules, intermediate filaments are not polar and do not grow actively. Moreover, they are much more varied in sequence and structure. We will only mention *vimentin*, as it is very ubiquitous and strongly expressed in fibroblasts. Vimentin filaments tend to associate with microtubules, and if the latter are disrupted, vimentin collapses close to the nucleus (5). Their physiological functions are very difficult to detect, as many cells can live without them. Knockout mice lacking vimentin develop and reproduce without major problems, but have abnormal wound healing (5).

2.2.5 Actin Cortex

A general feature of eucaryotic cells is the actin cortex, a thin layer (~ 100 nm) of short actin filaments located under the cell membrane, known to be significantly stiff and under active tension. The actin cortex is a major actor behind cell shape transformations and ameboid movement (70), which mediates much of the interaction between the cell and its surroundings. Being at the boundary of the cell, its mechanics have been extensively studied by microrheological experiments. Its elastic properties show it to be highly crosslinked, necessary for the short actin filaments to behave as a gel and to tether them avoiding their dispersion (28).

The importance of actin cross-linking proteins has been highlighted by studies on Dictyostelium mutants lacking α-actinin and ABP120 (71). These cells have smaller sizes and more rounded shapes, exhibit an increased sensitivity towards osmotic shock and a reduced rate of phagocytosis. Mutant Dictyostelium cells lacking conventional myosin have been shown to have a lower resting-state stiffness when probed by indenting the cell surface with a glass stylus (72).

2.3 Mechanotransduction

The mechanical interaction of cells with the environment requires adhesion. Cell adhesion is a prerequisite for essential functions such as movement inside a tissue, tissue architecture and integrity, sensing extracellular tension. If a cell is to exert forces on its surroundings, it must firmly connect the intracellular machinery to the extracellular matrix. Clearly, the adhesion strength of this binding has to be well above the forces to be applied. On the other hand a permanent bond

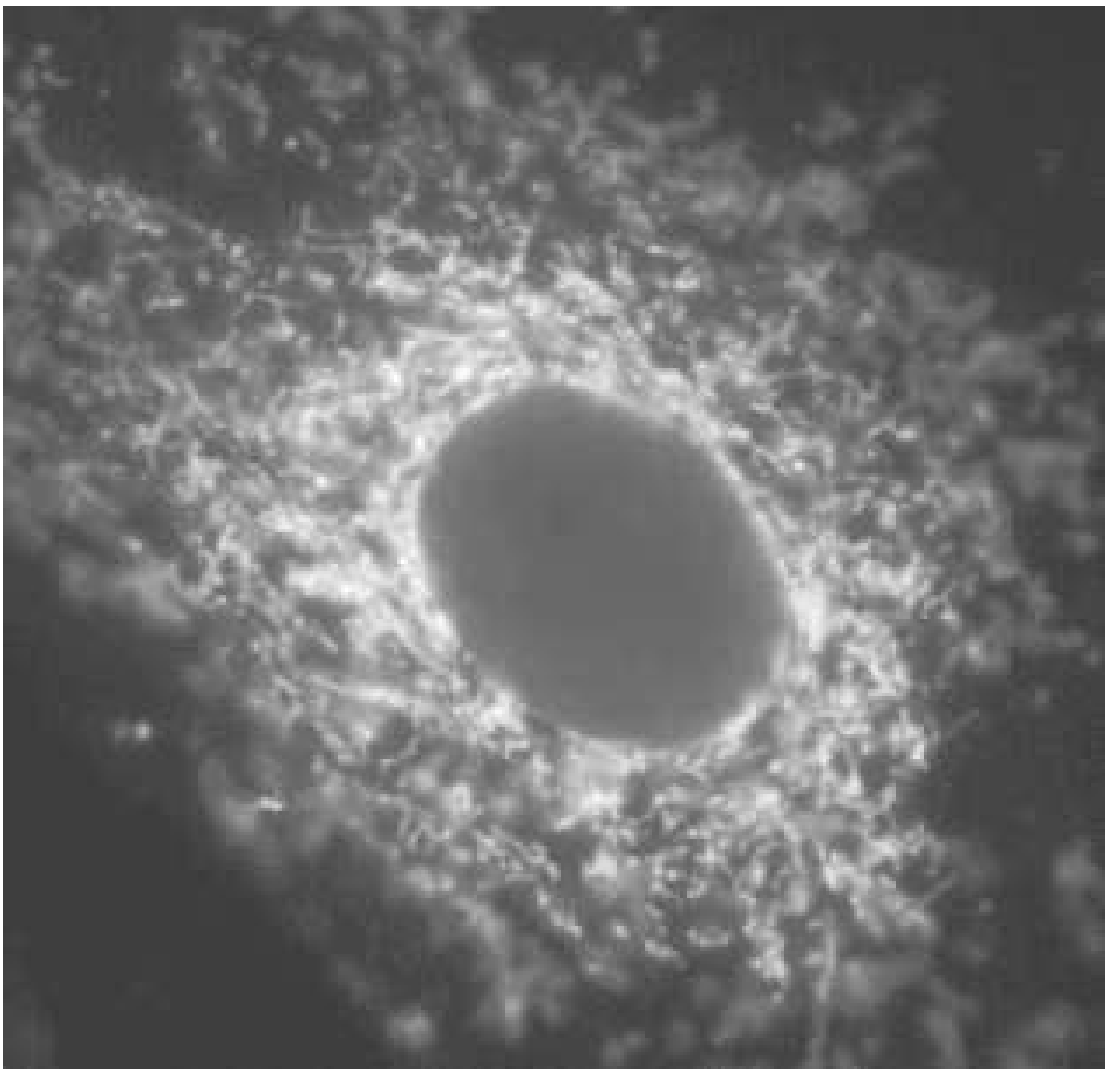

Figure 2.2: *Spreading fibroblast stained for vimentin using a Cy3-conjugated antibody. The dark region in the middle corresponds to the nucleus. Notice the small size of the filaments. In some cases, they seem to be strongly bent.*

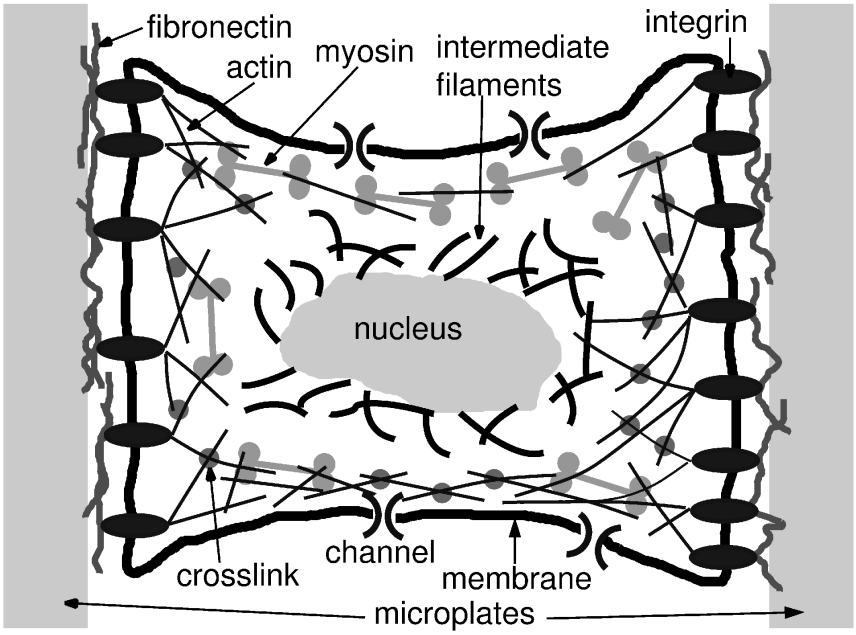

Figure 2.3: *Cartoon illustrating the mechanically relevant features of cell ultrastructure. The cell is adhering between two glass walls, in the cell-pulling geometry used for our experiments. The cell is enclosed by a membrane, to which a cortex of actin filaments is firmly connected. The actin filaments are crosslinked by proteins, among them myosin minifilaments which generate tension. Transmembrane proteins such as integrins connect extracellular matrix proteins to the cytoskeleton. Channels in the membrane are also shown. Mechanosensitive channels are a general feature of animal and plant cells; their physiological role is still unclear.*

is clearly not desirable. One would expect the strength and extent of adhesion to be under the control of the cell.

2.3.1 Focal adhesions

When cells under culture are observed, adhesion can be seen to take place in a discrete fashion at a few places. These are known as focal adhesions. They provide the link between the extracellular matrix and the cytoskeleton (73). These are complex dynamic structures, which change their structure in response to extracellular cues, some of them of mechanical nature. Nascent adhesions, known as focal complexes, can mature and develop into focal contacts in a process which requires actomyosin contraction (74). It is becoming increasingly clear that, besides their static mechanical role as an outside-inside link, focal adhesions function as mechanosensors which interconvert mechanical and biochemical information.

Structurally, three components are always present in focal adhesions: the extracellular matrix (fibronectin), transmembrane receptors (integrins), and an intracellular macromolecular assembly of F-actin, myosin, and ABPs.

Fibronectin

Most experiments described in this work are performed on cells adhering on a fibronectin layer. Fibronectin is a fibrous protein which can be found in connective tissue, as part of the *extracellular matrix* (ECM). Most if not all effects of fibronectin can be reproduced by the aminoacid sequence Arg-Gly-Asp (RGD), present in fibronectins. This is the motive recognized by integrins, transmembrane receptors which inside the cell bind to the cytoskeleton.

Integrins

Integrins are composed of several subunits. These come in two different types, α and β. Each subunit consists of a large extracellular domain, a single transmembrane segment, and a relatively short cytoplasmic tail. Wehrle-Haller and Imhof have suggested classifying focal adhesions according to β-3-integrin density (74), which seems to agree with their physiological functions. Nascent adhesions (focal complexes) have a low integrin density, whereas focal contacts show a high density. Only focal contacts show mobility relative to the substrate. They are very dynamic structures which undergo constant restructuring: complete turnover of β-3-integrins takes place in 5–10 min (74).

On the cytoplasmic side

A number of important actin-binding proteins (ABPs) are known to bind directly to integrins. Among them we find Talin, whose importance is shown by Talin-null ES cells, which exhibit extensive membrane blebbing and defects in cell adhesion and spreading. Many integrin subunits bind to the crosslinking ABPs filamin and α-actinin (75). There are also β_4 integrins, which have a long tail linked primarily to intermediate filaments instead of actin filaments (75).

Focal adhesion formation

Integrins trigger a plethora of signalling cascades. Among the downstream events we find activation of the Ca^{2+} pathway, changes in gene expression leading to growth stimulation, and inhibition of apoptosis (76). Signalling triggering by integrins seems to require conformational changes induced by ligand binding, as well as integrin clustering. Occupancy of α_V-containing integrins by RGD peptides induces their incorporation into previously formed focal adhesions, but no signal transduction involving tyrosine phosphorylation or accumulation of cytoskeletal proteins. Simple integrin aggregation in absence of ligand occupancy, induced by anti-integrin antibodies, induces accumulation of only a subset of cytoskeletal proteins. Aggregation must be accompanied by ligand occupancy in order for integrins to induce a characteristic large accumulation of actin-containing cytoskeleton. Beads coated with fibronectin induce rapid integrin aggregation and accumulation of a variety of cytoskeletal proteins including talin, α-actinin, and tensin within 15-20 minutes (76). The detachment forces have been shown to increase by about an order of magnitude 15 min after contact with fibronectin coated surfaces (77).

Maturation into focal contacts

The maturation of low-density focal complexes into high-density focal contacts depends on the GTPase RhoA and acto-myosin contraction (74). This has been elegantly demonstrated by studying the growth of focal contacts in response to externally applied force by pulling with a micropipette (78). In this way, the presence of fibronectin as an extracellular ligand was shown to be necessary. However, the micropipette did not require any specific coating to induce contact growth, showing mechanical tension to be the relevant parameter. Further, actin was necessary, but not myosin. Thus, focal contacts are stable only under tension, regardless of how this tension is generated, and loss of tension leads to immediate disassembly. A complementary observation is that focal adhesions retract on elastic substrates, whereas they are reinforced and maintained on stiff surfaces (73). The influence of the extracellular stiffness was studied by elegant experiments with optical tweezers, which showed the adhesion strength to depend on the stiffness of the optical trap (11).

The mechanism which couples growth to tension is at present not known. Presumably, the change in protein conformation induced by the strain is recognised by other proteins, leading to signalling cascades. This is supported by the observation that specific signalling molecules bind to focal adhesions after mechanical stretch (19).

2.3.2 Stress fibres

Stress fibres have much in common with focal adhesions. For one, they always go together. On spreading cells stained for F-actin, stress fibres are immediately recognised as long, thin lines extending across the substrate, their ends invariably ending in focal adhesions. In agreement with the fact the latter are only stable under tension, stress fibres are known to constantly exert forces. The force which they exert on the substrate has been shown to be proportional to the focal contact area (78). Their ultrastructure is similar to that of muscle. An important component is α-actinin, which joins actin filaments in bundles. Myosin is seen to be located periodically along stress fibres, with a typical distance of about 1 μm (13).

A dramatic demonstration of the contractile abilities of stress fibres was given by Katoh *et al* as they isolated stress fibres and induced their contraction by adding Mg-ATP (79). This led to 20% shortening at a velocity of several micrometers per second. No significant actin filament depolymerisation was seen throughout. Remarkably, during contraction stress fibres rotated and became thinner. Electron microscopy revealed a more compact structure after contraction. Posterior work from this group showed that MLCK (Myosin light chain kinase, already discussed in 2.2.2) induced more rapid and extensive contraction of isolated stress fibres than Rho-kinase. These authors therefore suggest distinguishing two regulatory systems: the Ca^{2+}-dependent MLCK, and the Rho-kinase (80). The first generates rapid contraction, the second mantains sustained contraction in cells.

2.3.3 Summary

In response to serum, or serum factors such as lysophosphatidic acid (LPA), contractility is activated and sustained via the GTP-binding protein Rho. Rho keeps myosin activated, which polymerises in bipolar minifilaments and interacts with actin. This leads to stress fibre assembly and force generation. For force to arise, however, stress fibres have to hold on something. If the extracellular matrix contains fibronectin and is stiff enough, focal adhesions arise and stress fibres can exert tension. Alternatively, the Ca^{2+} pathway can increase myosin contraction via MLCK, but this effect is temporary.

2.4 Fibroblasts and mechanosensing

Fibroblasts are the experimental system used in the first part of this report. These cells can be found in connective tissue, the architectural framework of the vertebrate body (59), a network of polysaccharides and collagen sparsely populated by cells. Under normal conditions, fibroblasts are sedentary cells which play a synthetic role, secreting collagen fibres and reorganising them into fibres and networks (5). They neither show stress fibers nor form focal adhesions with the ECM. In the presence of mechanical tension or biochemical factors such as fibronectin or *transforming growth factor $\beta 1$* (TGF-β1), fibroblasts differentiate into myofibroblasts. These are characterised by the *de novo* expression of α-smooth muscle actin, the presence of developed stress fibers, supermature focal adhesions, and generate large forces. *In vivo*, differentiated myofibroblasts are found in specialized normal connective tissue, such as bone marrow stroma or the liver capsule, and in late contracting granulation tissues like in open wounds (59).

A physiological function of fibroblasts which highlights their contractile abilities is wound closure. When tissue damage takes place, fibroblasts become motile and migrate into the wounded area, where they proliferate, secrete collagen-containing extracellular matrix, and differentiate into myofibroblasts. Simultaneously, wound contraction takes place (81, 82). Later cells die and scar tissue arises. It is a clinical observation that sustained mechanical tension increases scarring. This connection between mechanics and cell behaviour has been investigated by elegant experiments on fibroblast-populated collagen gels reviewed in Ref. (81). In free gels, where significant stresses cannot arise, fibroblasts remain in the non-activated state. If the boundary conditions allow tension generation (e.g. when one side of the gel is fixed to a rigid wall), tension develops and fibroblasts proliferate. We remark that this tension is generated by the cells themselves.

2.4.1 Mechanosensing

This picture does not pertain exclusively to fibroblasts. In the last years much has been learned about the response of eucaryotic cells to the mechanical properties of the environment. It has been shown that in general cells align along the directions of highest extracellular stiffness (10, 11). We can now see a feedback loop at work. Where the right biochemical cues are present and the surroundings are stiff enough, forces develop due to cellular contraction. Tension in the ECM stiffens it. Cells sense the stiffer directions, aligning and assembling force-exerting

structures along them. The situation is clearly unstable; it is no surprise that contractile cells are highly asymmetrical. The process reflects *mutatis mutandis* the behaviour of stress fibres and focal adhesions. Stiffening of the extracellular matrix can be sensed by other cells, inducing them to align in a given direction and leading to parallel arrangements of cells (10, 42).

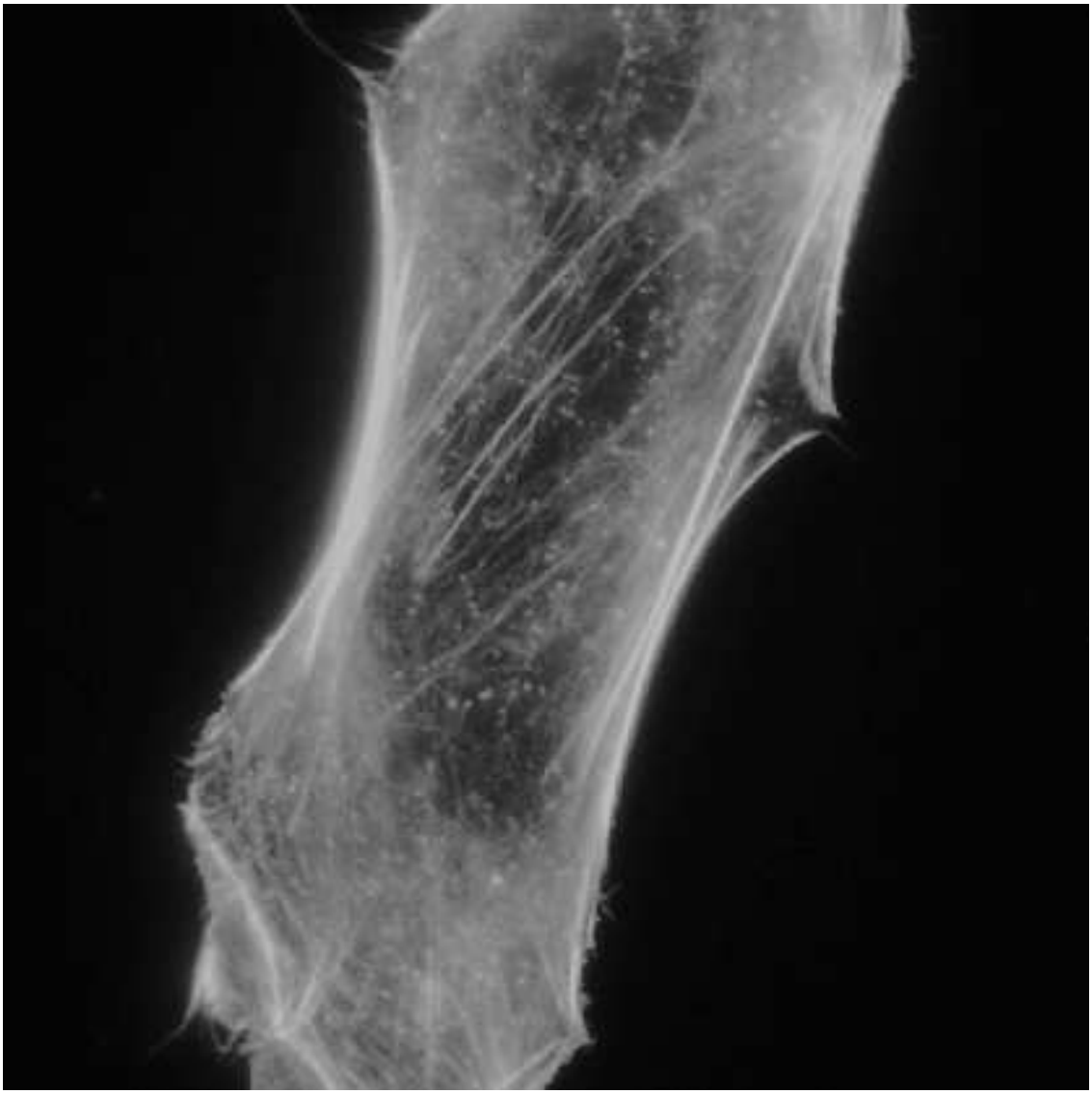

Figure 2.4: *Spreading fibroblast stained for F-actin with phalloidin-rhodamine. The darker region in the middle corresponds to the nucleus. Notice the strong intensity of the actin cortex along the edge of the cell, and the numerous stress fibers.*

2.5 Rheology of soft living matter

Though bewildering in its structural complexity, living matter does show a characteristic mechanical behaviour. Presumably, this is a consequence of sharing a common load-bearing structure. Here we discuss the general rheological features of soft biological materials. This can be summarised in a few keywords: preconditioning / plasticity, rate-independent hysteresis / power-law relaxation spectra, exponential stress-strain relations, active force generation. In this section we will change direction: beginning from whole tissues, we go down to the microrheological scale, following the historical development of the field.

2.5.1 On power law relaxation

Let A, B be conjugate variables. An experimentator perturbs the system by changing A and measures the response B. As to how exactly A is changed, one possible approach is to impose a sinusoidal function at a given angular frequency ω and amplitude Δ_A,

$$A = \Re e \left(\Delta_A \, e^{i\,\omega\,t} \right) \; .$$

If the perturbation is sufficiently small the relation between the two variables is linear, given by

$$B = \Re e \left(\Delta_B \, e^{i\,\omega\,t} \right) \tag{2.1}$$

$$\Delta_B = \chi(\omega)\, \Delta_A, \tag{2.2}$$

with a complex amplitude Δ_B. The linear response function $\chi(\,\omega\,) = \chi'(\,\omega\,) + \mathrm{i}\,\chi''(\,\omega\,)$, the dynamical susceptibility of B to its conjugate A, characterises the inherent dynamics of the system and can be measured without reference to any theoretical model (83, 84).

An alternative to oscillations are relaxation experiments . The perturbation is switched on slowly, from $A = 0$ to $A = \delta A$. This induces a change $\delta B = \chi_T \, \delta A$, characterised by the thermostatic susceptibility χ_T (83). At $t = 0$ the external perturbation is switched off and the free motion of B is observed. In the linear response regime,

$$B(t) = \delta B \, \phi(t) \qquad\qquad (t > 0) \, ,$$

where $\phi(t)$ is called the relaxation function. Both approaches have been extensively used in biomechanics, revealing power law relaxation functions as a common feature of biorheology at all length scales. Phenomenologically, such a behaviour is not a novelty. Von Schweidler emphasized a century ago (84) that many relaxation processes follow over more than two time decades the law

$$\phi(t) = f - (t/\tau)^b \qquad\qquad \text{for} \quad 0 < b < 1.$$

The von Schweidler law holds above the microscopic cutoff time t_c and is proposed to describe the initial part of the decay process only, $t_c << t \leq \tau$. The term f represents an instantaneous response. This relaxation law can be shown to be equivalent (84) to the susceptibility

$$\frac{\chi(\,\omega\,)}{\chi_T} = f + \Gamma(1+b) \, \left(\frac{\mathrm{i}}{\omega\tau} \right)^b \qquad\qquad (1/\tau \ll \omega \ll \omega_c) \tag{2.3}$$

where Γ is the gamma-function. Notice that the loss tangent is frequency-independent,

$$\frac{\chi''}{\chi' - f\chi_T} = \tan\left(\frac{\pi}{2}\,b\right).$$

In passive materials (85), the Kramers-Kronig relations allow the converse conclusion; if the loss angle is independent of ω with $b < 1$, then the susceptibility expressions 2.3 hold (84).

We now argue that power-law spectra reflect a broad continuous distribution of relaxation times. One may always attempt describing relaxation functions as a superposition of exponential functions,

$$\phi(\,t\,) = \int e^{-t/\tau}\rho(\,\tau\,)\frac{d\tau}{\tau}$$

where $\rho(\,\tau\,)$ is the distribution of relaxation times. Addressing *unvollkommene Dielektrika*, Karl Willy Wagner proposed in 1913 a Gaussian function for $\rho(\,\tau\,)$ (86) and showed that the loss angle becomes frequency-independent as the width of the gaussian increases. Thus, as the relaxation spectrum broadens one approaches the von Schweidler law.

Rate-independent hysteresis was subsequently found in magnetic and mechanical relaxation phenomena. An alternative mathematical description was adopted by Neubert in 1963 (87) and by Fung in 1972 (88), assuming $\rho(\,\tau\,)$ to be constant in the range bounded by the cutoff times τ_1, τ_2 and to vanish beyond:

$$\rho(\,\tau\,) = \begin{cases} 1/\ln(\tau_2/\tau_1) & \text{for} \quad \tau_1 < \tau < \tau_2 \\ 0 & \text{for} \quad \tau < \tau_1,\ \tau > \tau_2\ . \end{cases}$$

The assumption of constant $\rho(\,\tau\,)$ can be justified as follows. The relaxation time τ is a scale parameter: $\tau > 0$ must always hold. Therefore complete ignorance of its value is properly described by assigning a constant probability to its logarithm (89), so that a milisecond is as likely as a year. As $d\tau/\tau = d\ln\tau$, this amounts to constant $\rho(\,\tau\,)$.

Taking a ratio between cutoff times $\tau_2/\tau_1 \sim 10^4$, the loss tangent can be shown to remain virtually constant over two decades around its maximum at $\omega = 1/\sqrt{\tau_1\tau_2}$ (87). Its maximum value in this limit is given by

$$\frac{\pi/2}{\ln(\tau_2/\tau_1)}.$$

Again we recover the von Schweidler law 2.3 as the limit of a broad, flat relaxation spectrum. The wider the spectrum of relaxation times, the smaller the exponent b becomes; the material becomes more elastic and less frequency dependent.

2.5.2 Soft tissues

Ramp experiments

A remarkable characteristic of soft tissues is their elongability. They can undergo deformations of about 100% without rupturing and display significant stiffening. Stretch experiments on tissues

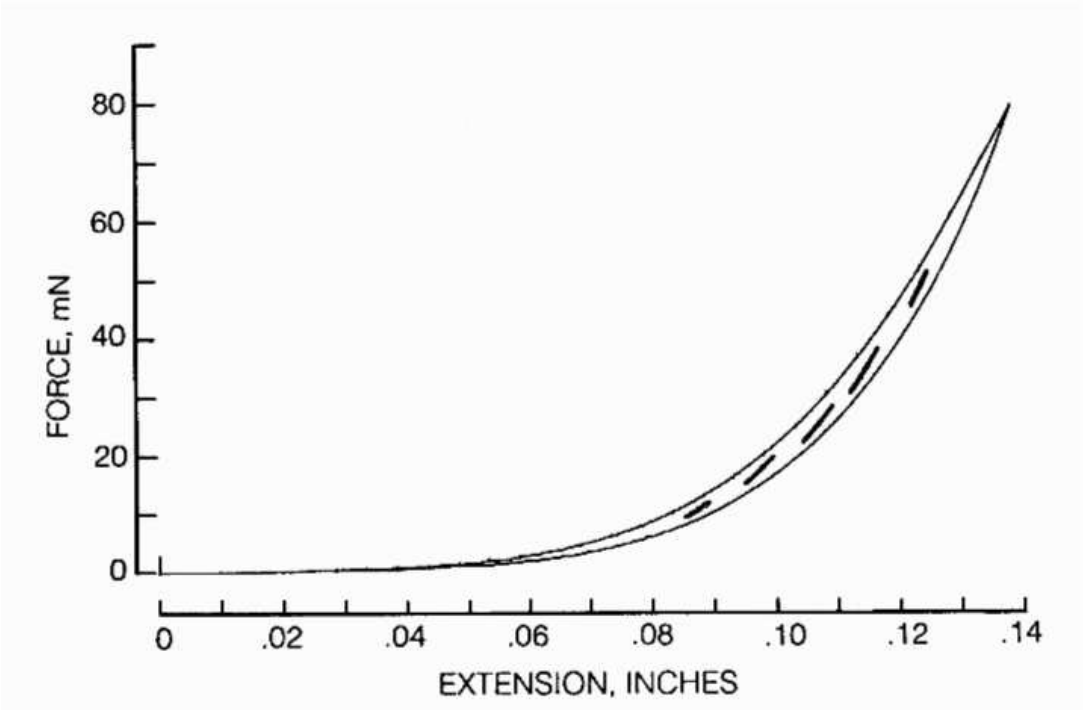

Figure 2.5: *Rabbit mesentery under uniaxial loading: force as a function of extension. The continuous curves corresponds to loading (upper curve) and unloading (lower curve); the small loops corresponds to oscillatory experimens. Notice that the slopes of the loops are not exactly equal to the slope of the loading-unloading curves, though both show stiffening. Taken from Fung (90).*

such as skin, tendon and muscle have revealed highly nonlinear stress-strain relations, often well approximated as exponential. Exponential elasticity was first found in striated muscle in 1955 (91). Later, Y.C.Fung addressed it as a general feature of tissue mechanics (90). Restricting the analysis to the reversible part of the mechanical response, he proposed the equation $dF/d\lambda \sim F$, where F is force and $\lambda = \ell/\ell_0$ the stretch ratio. He showed that this equation could reduce results obtained on mesentery, skin, muscle, myosin fibres, tendons. Fig.2.5 shows an example of exponential elasticity taken from Ref.(90).

Tissues always show some degree of internal dissipation, so that during loading higher forces are obtained than while unloading. The total energy dissipated, e.i. the area enclosed by the force-length curve, does not change significantly as a function of the deformation rate (8). “Preconditioning” is seen when cyclically repeating the loading-unloading experiment. The force-length curves go down during the first few cycles until a stable situation is reached. The specimen is then said to be preconditioned (8).

Oscillatory experiments

A tissue can be characterised by the force-length relation measured in a ramp experiment, where usually a fixed strain-rate is imposed and kept constant throughout. One may however take a different approach: reach somehow a given force–length point, let the specimen stabilize, and then apply small amplitude sinusoidal oscillations. The superimposed deformations must be small enough to remain in a linear regime. The linear response at the given point is characterised by a modulus Θ and a loss angle δ. The frequency dependence of the dynamic moduli is a rather flat power law, the loss angle δ being essentially constant. This reflects the fact that soft tissues cannot be described by a discrete relaxation spectrum. The specimen can then be further stretched, going to a new force–length point, and again the linear response is measured. In this way, the dependence of the moduli on the force and length is obtained. Following Fung's terminology, we shall call this procedure an *incremental* approach (8). Since the modulus Θ amounts to a derivative of the force-length curve, one may be tempted to relate the incremental law to the force-length relation measured in a ramp experiment. More precisely, one might expect $\Theta = dF/d\ln\ell$. This does not work in soft biological materials, as explicitely stated by Fung (90). The incremental approach does indeed reveal stiffening, but the dynamic modulus Θ is not the same as the tangential stiffness $dF/d\ln\ell$, a discrepancy which is not due to differences in deformation rate, but to a dependence on deformation history. Fig.2.5, taken from Ref.(90), shows this point explicitely. For clarity, we shall call this phenomenon *non-integrability*: the F–ℓ relation cannot be obtained by integrating the Θ–F relation. Since preconditioning is also usual, this memory effect is not surprising. Clearly, flow changes the mechanical response; a system which has been flowing for some time has a different structure from one which was oscillating around a steady state.

2.5.3 Muscle

Muscle is not essentially different from other soft tissues in its mechanical properties. It also shows stiffening and nonderivability. The main difference is the presence of force generation. A complication is the presence of passive extracellular material in parallel and in series to the contractile element. Dissecting the response of the tissue into passive and active elements in to some extent arbitrary.

In skeletal muscle, plasticity arises naturally from the sliding between actin filaments and myosin molecules. Oscillatory experiments reveal power-law frequency dependence. Stiffening is also seen, in the form of proportionality between force and stiffness. It is generally accepted that this stiffening arises as both tension and stiffness are proportional to the number of cross-bridges. This is possible due to the processive nature of myosin. A single myosin head stays attached for a time t which is a small fraction of the turnover time T (9); typically, $t \sim T/20$. Thus, the contributions of uncorrelated myosins acting on the same filament add up–as long as there are not more than $T/t \sim 20$ myosins.

Smooth muscle

Smooth muscle is very relevant for us, as it is a close relative of fibroblasts (13). Smooth muscle is found in the digestive, respiratory, urinary, and genital tracts, in the walls of vessels, in the uterus, and in the ducts of liver and spleen. It consists of long cells surrounded by extracellular matrix, disposed with different orientations. Its cytoplasmic organization is complex and not well understood. Actin and myosin filaments are arranged in myofibrils aligned with the cell axis, consisting of a myosin filament surrounded by several actin filaments. Interspersed with them are regions rich in intermediate filaments such as desmin or vimentin containing α-actinin, which seem to act as anchorage points for myofibrils (5).

2.5.4 Cell populated gels

An alternative approach to biomechanics are cell-populated collagen gels (92, 93), where many characteristics of tissues have been traced back to fibroblasts – indirectly, via drug treatment. Such bio-mimetic systems consist of hydrated collagen gels filled with fibroblasts, which remodel and compress the collagen matrix. Elongation experiments performed with such systems (93) show exponential dependency between stress and strain. By treatment with actin-disrupting drugs such as Cytochalasin D or stimulation of the cells via serum addition, the mechanical behaviour can be separated in so-called active and passive parts. Stimulation of the tissue by serum defines the total response. Disruption of F-actin by Latrunculin gives the passive response. The algebraic difference between them is *defined* as the active one. Very clean results are obtained in this way. The passive element resembles tissues such as skin and tendons: the force–length relation is exponential, and the dynamic stiffness is proportional to the force. The active element, on the other hand, reminds of muscle: it shows proportionality between dynamic stiffness and force, but in ramp experiments fact its force-length relation is quite linear, even showing softening at higher forces. Muscle-like behaviour has also been found in this bio-mimetic system by Obara et al (92), who showed that contraction rate and force are related in a hyperbolic manner, as in Hill's equation (8).

2.5.5 Microrheology

Microrheology experiments are performed by perturbing small cellular regions, with sizes of $\sim 1\,\mu$m. Magnetic tweezers have been employed to measure the intracellular viscoelastic parameters (32). Another popular approach is magnetic twisting cytometry, where the shear moduli of the actin cortex are measured by twisting coated ferrimagnetic beads (33, 34, 94). Alternatively, one can measure diffusion of intracellular particles, or use variants of AFM (95). Frequencies in the range 0.1–100 Hz can be explored with high spatial resolution, so one may attempt the study of specific cellular structures (41).

Frequency dependence

Microrheology experiments have conclusively shown that power-law creep functions and power-law frequency dependence of the moduli are still found at the micrometer scale, on cells of several types. Remarkable scaling of results obtained on different cells has been reported (33, 34). These authors have put special emphasis on an interpretation in terms of a phenomenological-mesoscopic theory known as soft glassy rheology (96, 97). Soft glassy rheology indeed successfully describes tecton networks (98) and in general materials with "weak strain overshoot" (99), i.e. when increasing the strain amplitude beyond the linear regime, the loss modulus G'' displays a maximum before falling down. In biomechanics, however, its validity has only been shown in the linear regime, where, as pointed out by Sollich himself (96), there is no real need for the theory; it is simpler just to postulate a flat relaxation spectrum. A real test of the validity of the theory requires going to the nonlinear regime.

The description of cell microrheology in terms of internal damping has revealed an interesting fact. The frequency dependence of the shear moduli remains qualitatively the same after drug treatments such as actin disruption with Latrunculin-A or contractility activation with histamin. Drug treatment changes both the exponent and the stiffness scale factor G_0. Remarkably, the two remain correlated; there is a frequency of the order of GHz where the value of the storage shear modulus is "universal", $G' \simeq 10$ kPa, independently of the drug treatment (33, 95).

Force dependence

Magnetic twisting cytometry experiments have been performed where the overall tension exerted by the cell spreading on the substrate was changed. This has been done "actively", by introducing drugs which stimulate or depress contractility (100). The storage shear modulus G' was compared to the traction exerted by the cell on the substrate, revealing stress stiffening. Remarkably, this is a relation between the shear modulus measured on one side the cell, and the traction force generated on the other side. As an alternative approach, "passive" experiments were done by stretching the substrate in order to strain the cells. In this way a correlation between the amount of stretch and the storage shear modulus was observed (101).

Stiffening in living matter can always arise by major structural rearrangements, such as changes in the amount of compromised cytoskeleton, in filament length, or in type and degree of crosslinking. Since tension is an essential determinant of cytoskeleton restructuring, it is in general very difficult to separate this effect from more "physical" stress stiffening mechanisms. One of the few examples of successful mechanism discrimination is given in Ref. (102), where changes in internal viscoelastic parameters were measured by intracellular microrheology. By treatment with *staurosporine*, which blocks stress fiber formation, the increase in intracellular stiffness upon Rho activation by LPA could be ascribed to actin polymerisation and not to actomyosin contractility. Recently, atomic force microscopy experiments performed on airway smooth muscle cells showed that the stiffening response induced by a contractile agonist could be ascribed to actin polymerisation and was myosin-independent (95).

2.6 Rheology of soft dead matter

In vitro experiments on purified cytoskeletal components have become increasingly popular in the last fifteen years. Though often claimed to be easier to understand than experiments on living matter, they face major reproducibility problems. Sample preparation is absolutely critical, as mechanical properties are extremely sensitive to parameters such as mesh size and filament length. F-actin length for example depends on ATP concentration, polymerisation time, previous mechanical history, etc. An improvement in reproducibility was achieved by including gelsolin, in order to control the length and number of filaments, and to stabilize them (27).

In polymerizing buffer, F-actin forms random networks with a well-defined mesh size, a consequence of the strong thermal bending fluctuations (103, 104). From a biological point of view, crosslinked networks of short actin filaments are probably more relevant. Since different crosslinkers have different binding rates and mechanical properties, each case has to be considered separately. Sato et al (105) studied mechanical properties of actin / α-actinin gels, finding viscoelastic liquid behaviour. This can be explained as α-actinin dissociates from actin relatively fast. The nonlinear regime is therefore difficult to study in this system, as stresses relax quite fast. However, by applying strain steps and studying the force relaxation function as a function of the step amplitude, stress stiffening was observed (29). A detailed study of the different structures which it can adopt as a function of mesh size and temperature can be found in Ref.(106). Janmey and coworkers (27) studied the rheological behaviour of actin filaments in presence of the actin-binding protein ABP1, and showed that such a system is rheologically equivalent to covalently crosslinked gels. The *in vitro* effect of filamin depends on its concentration: below a threshold, it crosslinks actin filaments into orthogonal networks, above it, bundles are formed. In careful studies where filament breakage was avoided, it was shown that below a threshold filamin concentration the behaviour is that of a viscoelastic liquid, whereas at higher filamin/actin ratios the solution behaves as a solid gel (107).

2.6.1 Stress stiffening

Scruin, an ABP found in the sperm cell of the horseshoe crab, both crosslinks and bundles actin filaments, forming isotropic, disordered three-dimensional networks. Scruin bonds are irreversible, and scruin itself is relatively non compliant. Experiments on actin-scruin gels show a constant shear modulus G' at low stresses, and a crossover to a stress stiffening regime where $G' \sim \sigma^{3/2}$ holds (30). Similar stress stiffening curves were later reported for several biopolymers, such as actin / filamin, vimentin, collagen (31). Thus this mechanical behaviour seems to be a general feature of random networks of semiflexible filaments.

2.6.2 Active gels

Fluidization of an actin network by activation of myosin II minifilaments has been recently reported (108). Addition of ADP to the myosin - actin network led to formation of inactive crosslinks, and the sample behaved as a solid gel, with a higher elastic modulus. On the contrary, addition of ATP lowered the storage modulus without significant change in the loss modulus, i.e.

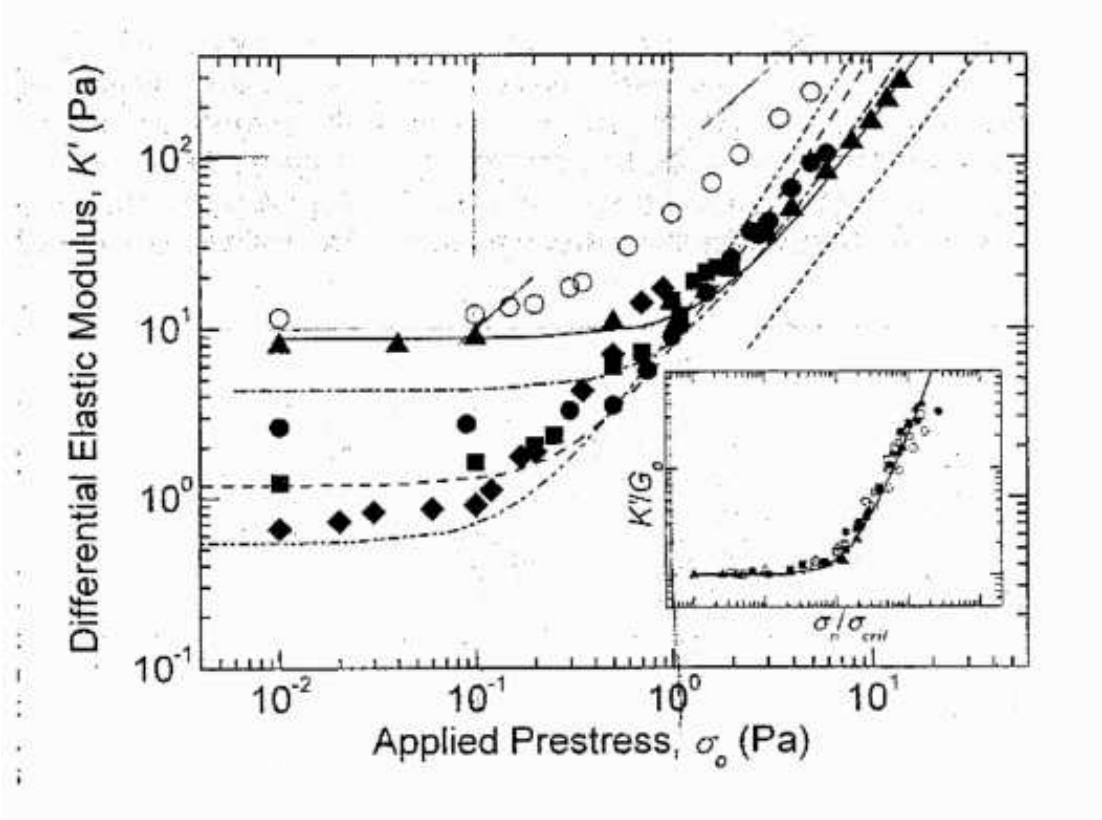

Figure 2.6: *Shear rheology of actin-scruin networks. Storage shear modulus as a function of shear stress. Taken from Ref. (30).*

the sample fluidized. Observation of single actin filaments by means of fluorescence microscopy showed longitudinal sliding upon addition of ATP, with an average sliding speed of 1 μm/s. The local stress relaxation time t, defined as the time it takes a filament to move a distance equal to its length L, was seen to scale as $t \sim L$ in presence of active myosin, and as $t \sim L^3$ for pure actin solutions, according to theoretical expectations.

Slightly different results were later found by another group (104). Here, myosin was in a non-aggregated state, i.e. not forming minifilaments. A slight decrease in both moduli was observed at low frequencies, while above 1 Hz the loss modulus G'' was slightly higher for the active network. The effect on the loss angle depended on the frequency. Above 0.3 Hz, activation of actin increased it; below that frequency, activation made it lower. Thus, rather than fluidization, these experiments gave a solidification.

Chapter 3

Setup and procedures

3.1 Experimental setup

The main features of the cell-rheometer are schematically shown in Fig. 3.1. This is an improved version of the original, home-built micromanipulation set-up previously described in Ref.(38). 3T3 fibroblasts (109, 110) are held between two parallel, coated glass microplates. One of them is rigid and provides a reference point. The other microplate is thin and narrow and therefore flexible, with an effective tip stiffness ~ 100 nN/μm, close to the stiffness of a typical fibroblast. Its bending gives the force acting on the cell along the *y*-axis (see Fig. 3.1). The flexible microplate is translated by means of a piezoelectric actuator, controlled in closed-loop configuration by a P-862 controller. An optical fiber in contact with the flexible microplate couples microplate bending to translation of the emergent laser light. The optical fiber is etched with hydrofluoric acid to a diameter of 6 μm, so that its stiffness is far lower than that of the flexible plate and does not interfere with the force measurement. The cell is illuminated with green light and observed with an Axiovert 135 microscope (Zeiss, Oberkochen, Germany). A dichroic mirror separates the green illumination light from the He-Ne laser light, which reaches a two dimensional position sensitive detector through one of the microscope ports. A personal computer reads the signal from the position detector, calculates the normal force F and the cell length ℓ, and controls the piezoelectric actuator. By controlling the piezoelectric translator, a feedback loop can be used to impose user defined force- or length-histories.

Due to the large length of the flexible microplate, its tip deflects by less than 6 arc min during an experiment. Hence, the experimental geometry can be described as two parallel walls, which can be separated by a translation in the perpendicular direction.

Position detector

The magnification along the path from the sample to the position detector is given by 40 x 2.5 = 100. In a typical experiment, total deformations are at most 20 μm, corresponding to 0.2 mm on the detector. The initial location of the microplates can be chosen at will, so the detector can be as small as 1 mm. A two dimensional position sensitive detector S-2044 (Hamamatsu photonics, Japan) with active area dimensions of 0.9 mm x 0.9 mm was used. With it, the precision in the

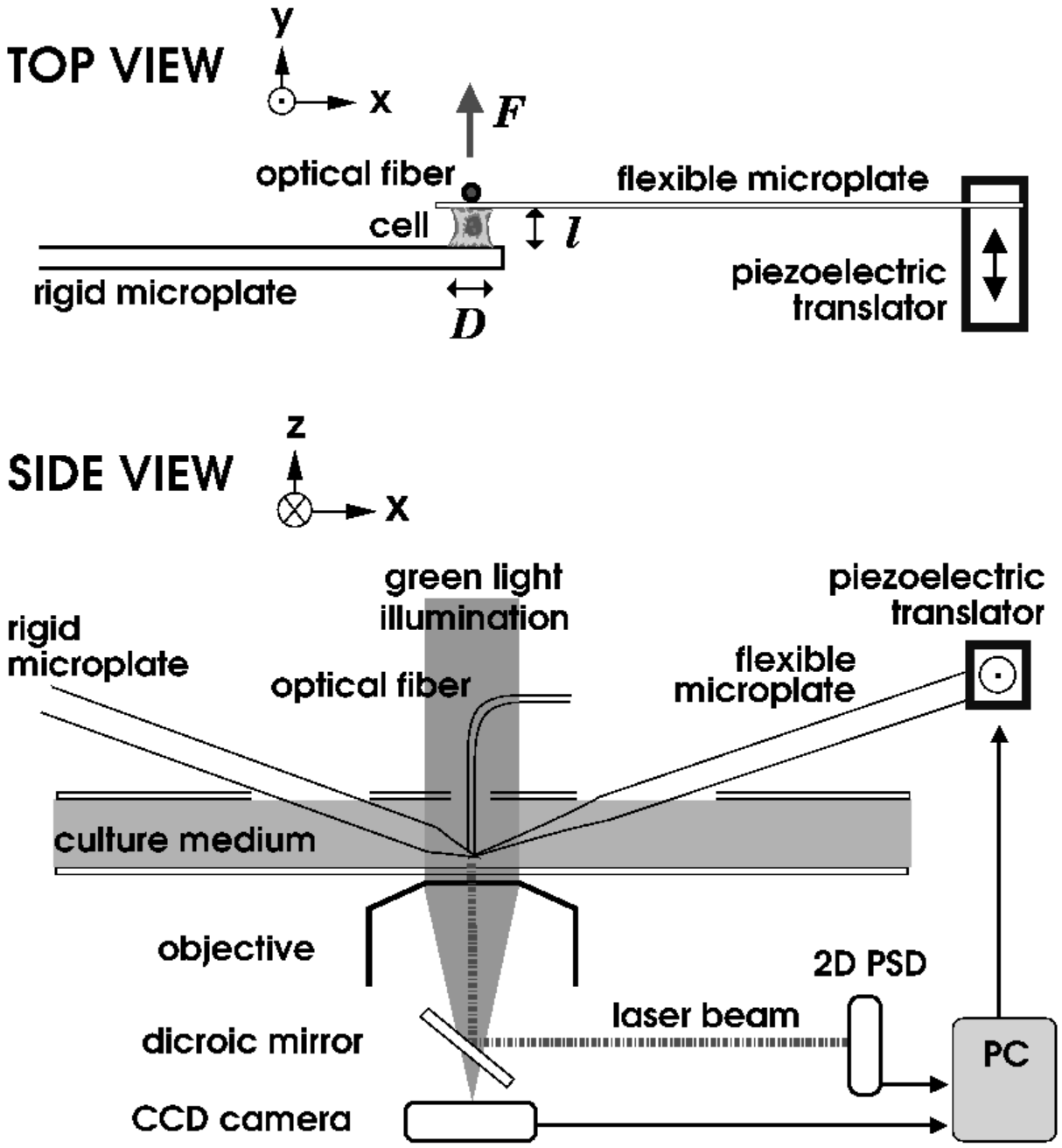

Figure 3.1: Schematic of the micromanipulation set-up. A fibroblast is held between two coated microplates. The deformation of the flexible microplate gives the force F acting on the cell. The position of the laser beam emerging from the optical fiber which is in contact with the tip of the flexible plate is detected using a position sensitive detector (PSD). A personal computer reads the signal from the detector and controls the piezoelectric translator.

measurement is about 100 nm. By integrating ~ 100 data points the resolution can be taken to 10 nm.

Piezoelectric translator

The piezoelectric translator used is a low voltage translator P-841.40 (Physik Instrumente, Karlsruhe, Germany), with a full range of 60 μm and a nominal precision of 5 (50?)nm. The controller is a P-862 controller (Physik Instrumente). Though the DC positioning exactitude is of a few nanometers, when performing oscillations at frequencies in the range 0.1–1 Hz deviations of about 10% arise, depending on the amplitude and frequency. At frequencies beyond 30 Hz, the distorsion in the response precludes the measurement. Therefore a calibration was done by placing an optical fiber directly against the piezoelectric actuator and applying sinusoidal signals at frequencies in the range 0.1–1 Hz and amplitudes in the range 100 nm–10 μm.

3.1.1 Temperature Control

Previously, the whole setup – including microscope – was enclosed by a styrofoam box. The inside of the box was kept at the experimental temperature (35° C), heated by an array of wires placed at the bottom. A window provided communication with the outside. Opening it in order to perform the experiment induced temperature gradients across the microscope, causing significant drift. Moreover, it was difficult to control the temperature in the box, due to its large dimensions; significant spatial and temporal temperature nonuniformities were present, most likely due to convection rolls. A further complication was the presence of the microscope lamp in the box, which heated strongly.

Given these difficulties, we changed the approach and went for a local temperature control. The box was thus disassembled, leaving the microscope and stage at room temperature. The desired temperature for the experiment is imposed only in the chamber, as shown in Fig.3.2. The chamber is made out of teflon. The temperature of the cell-culture medium inside the chamber is controlled by means of two ITO-coated glass slides, one on the bottom of the chamber, the other one above, with holes for the microplates and the optical fiber to pass through. The temperature control is performed by PID-controllers, receiving input from small PT-100 thermometers glued on the ITO-coating. For protection, a layer of PMMA covers the slides including thermometers and heating wires. In order to avoid convection in the medium, these slides are kept at different temperatures, imposing a temperature gradient pointing upwards with a magnitude of ~ 1 °C/cm.

In this way, a steady temperature gradient builds up along the microplates. Drift is seen after introducing the microplates in the chamber, with a relaxation time of about 20 minutes. Because of the way the experiment is performed, one may well let the plates relax for hours before beginning the experiment. After this relaxation phase, the position of the plates is stable within 2–3 μm. A slow drift within this range is always seen, which correlates with the room temperature.

Illumination is absolutely necessary at the beginning of the experiment, in order to prepare the plates, introduce cells, catch a good one, align the plates, etc. However, the focused illumination creates convection. This is undesirable for the experiment as it introduces noise. Moreover, there

is always “junk” in the chamber, such as dead cells or collagen fibers, which can stick to the plates and interfere badly with the experiment; the probability of this is increased by convection as it keeps junk flowing around. Finally, prolonged exposure to light may damage the cell. For these reasons, once the measurent begins it is preferable to turn the light off, and turn it on only ocasionally when taking an image of the cell. Here arises a complication. Though located about 30 cm over the stage, drift of up to tens of microns can be seen after switching off the microscope lamp once it has been on for about ten minutes. This drift showed sharp changes in rate; the plates would move at a constant speed, stop for a while, then resume movement. These movements are clearly due to temperature changes. Insulating the lamp by placing a plexiglas slab below it was not enough. The solution was to replace the lamp by a Dolan-Jenner illuminator, placed about 1 m behind the setup, using an optical fiber to direct its light on the optics of the microscope condenser.

Another factor causing drift were changes in the location of the warm body of the experimentator. As the cell is prepared, the warm body is very close to the setup. Once the experiment begins it is run by the computer and takes several hours; during this time the warm body of the experimentator is far away, usually in some other room. The sudden change causes drift. To minimize this effect, an insulation screen was built around the setup. The insulation also has the advantage of damping fluctuations in room temperature.

3.1.2 Microplates

The glass microplates used for the experiment are obtained by pulling glass strips (Vitrocom, NJ, USA) as described previously (38), using a modified P-97 Flaming/Brown micropipette puller (Sutter Instruments, Novato, CA, USA).

Calibration

The stiffness of the microplate should be close to that of a typical fibroblast, in order to optimize the force measurement. A good value for experiments with fibronectin coatings is 100 nN/μm. Experiments on glutaraldehyde coatings require slightly lower values, about 30 nN/μm. Calibrations were done by placing a silver wire against the microplate and measuring its stiffness. We used wires with a diameter of 50 μm and lengths of $\sim$ 3 cm. For the measurement it is again important to match the stiffness of microplate and wire, easily accomplished by changing the free length of the wire. The deformation imposed should be small, otherwise the wire stick-slips in an uncontrolled way. Good results were obtained by doing “wet” calibrations, i.e. in culture medium, right after a successfull experiment. As a general advice, we suggest not spending too long on microplate calibration; exactitude within an order of magnitude is enough. As will be shown in the next chapter, the precise value of the stiffness of a cell is not very informative.

Fibronectin coating

The microplates are sonicated for 10 minutes in a 5% Decon solution, rinsed thoroughly with millipore water, and coated with fibronectin from bovine plasma (Sigma-Aldrich Chemie GmbH,

Germany) by 1 hour exposure to a 10 μg/ml fibronectin in PBS solution at room temperature. If kept at 4°C in the dark and opened only inside a sterile hood, a 0.1% fibronectin solution is stable for months. Freezing should be avoided.

Glutaraldehyde coating

Alternatively, for a non-specific glutaraldehyde coating, we use 3-aminopropyl triethoxysilane (Sigma-Aldrich) and glutaraldehyde (Fluka Chemie, Buchs, Switzerland). The procedure is the one described in ref.(38). For a perfect silanization, the plates must be cleaned thoroughly as described above. After rinsing with water, it is wise to rinse them once more with ethanol.

The quality of the reagents is essential to achieve good adhesion, in turn essential for the experiments. Silane should be protected from humidity and light. If stored in the dark in a tight bottle filled with argon or nitrogen, it can last for at least 1 year. Similar considerations hold for glutaraldehyde.

Holding the microplates

The size of the microplate is about 1 cm, and one needs the tip to be stable within at least 1 μm. Not surprisingly, the way the microplates are held dramatically affects their stability. Holding the glass plates by clamping them between two metal pieces is not a good procedure. Gluing them gives better results, but since glass has a thermal expansion coefficient at least two orders of magnitude lower than most glues, this must be done properly to avoid an exaggerated temperature sensitivity. We got good results by gluing the plates by their narrow side over a metal piece, using as little glue as possible. Particularly good for this purpose is NOA 61 (Norland Adhesives, NJ, USA), a UV-curable adhesive with a thermal expansion coefficient of about 230 $10^{-6}/\mathrm{K}$.

3.2 Cell culture

3T3 fibroblasts are obtained from the German Collection of Microorganisms and Cell Cultures (DSMZ, Braunschweig, Germany) (111). Standard procedures are followed for the cell culture. Cells are grown adhering on the bottom of culture flasks filled with medium. The medium used for regular culture is Dulbecco's modified Eagle medium (DMEM), with glucose 4.5 g/l and 10% fetal bovine serum (FBS). An appropriate amount is $\sim 200\,\mu\mathrm{l}$ of medium per $(\mathrm{cm})^2$ of covered surface. Each 2-3 days cells are split. The culture medium is removed from the flask, cells are washed with Ca^{2+}-free HBSS in order to remove non-adherent cells and extract calcium, then trypsin solution is introduced and left for 5 minutes to detach cells. Ocasional tapping of the flask helps. Then, a fraction of the cell suspension is introduced in a new flask with fresh culture medium. All cell culture reagents are from Gibco (Invitrogen, Carlsbad, CA, USA).

3T3 fibroblasts are very sensitive to contact inhibition; when confluence is reached they leave the cell cycle and become quiescent. Experiments attempted on such cells almost always fail. Resting fibroblasts seemingly do not adhere readily on fibronectin. Thus, previous to an experiment the density of the culture should not be too high.

3.3 Experimental procedures

Fibroblasts are detached from the culture flasks by 5 min treatment with a solution of Trypsin in HBSS-based dissociation buffer (GIBCO). Then, they are introduced into the chamber. The previous protocol was to throw cells inside and catch them while they sank. Such a procedure is far from ideal. Introducing the cells has to be done very precisely in the field of view, which is complicated by convection due to the illumination. Moreover, as fibroblasts sink relatively fast, the experimentator has only a few seconds to choose the cell. As selecting the cell is important in order to do a good experiment, the procedure was modified. The bottom slide was coated with a hydrophobic layer of dichlorodimethylsilane (Fluka) by a brief exposure to fumes, then washed with tap water. Fibroblasts cannot stick to this hydrophobic coating; once they fall on it, they stay round and alive for many hours (112). In order to look for a good cell, the experiment chamber is designed so that the bottom slide can be moved around. This is shown in Fig.3.2. The top ITO-coated slide and the teflon chamber are fixed relative to the stage. The bottom ITO-coated slide is fixed with vacuum grease on the lower side of a makrolon piece (*coloured black in Fig.3.2*), shaped as an open box. This part can be displaced by hand, thereby moving the bottom slide relative to the microscope. To avoid the medium from flowing out, the top and bottom parts are pressed together and there is a thin layer of vacuum grease (Baysilone-Paste hochviskos, GE Bayer) between them, which allows for relative movement while preventing leakage.

The whole procedure is as follows. Cells are introduced in the chamber and let fall on the bottom slide. As this is coated with hydrophobic silane, they stay round without adhering to the slide. The bottom slide is moved around, until an appropriate cell is found. This usually meant a non-blebbing, middle sized, as round as possible cell. The flexible plate is then brought down, rotated so that its wide side faces the bottom, and the cell lightly pressed from above with the plate. For a fast-adhering cell, a few seconds of contact are enough. Then the plate is lifted carefully and rotated by 90 degrees. This procedure is performed best with a low magnification objective. Then, we switch to the 40X objective and position the optical fiber against the flexible microplate. The initial position of the fiber should roughly match the zero of the position detector, to avoid going beyond the active area during the experiment. Before contact with the second plate, the zero force position of the microplate has to be recorded by the software. Only then can one bring in the rigid plate and press the cell. An initial compressive phase of about 5 minutes is essential. The cell should be well compressed, to a diameter/length aspect ratio of ~ 5. The compressive force should not go beyond -400 nN, least the cell explodes. After this compressive phase the force can be taken close to zero and the cell left for about half an hour. Cells often try to contract during this phase; it is wise to impose a constant length throughout, to avoid extensive spreading. If kept at constant length, cells develop strong pulling forces, as shown in the next chapter.

A big advantage with the procedure as described is that many experiments can be tried without changing medium or microplates or introducing new cells. The fibronectin coating stays active through the experiment. Moreover, the cells lying on the hydrophobic coating do not spread. Thus, once an experiment is over, one can bring the plate down, choose a second cell, catch it, and begin anew.

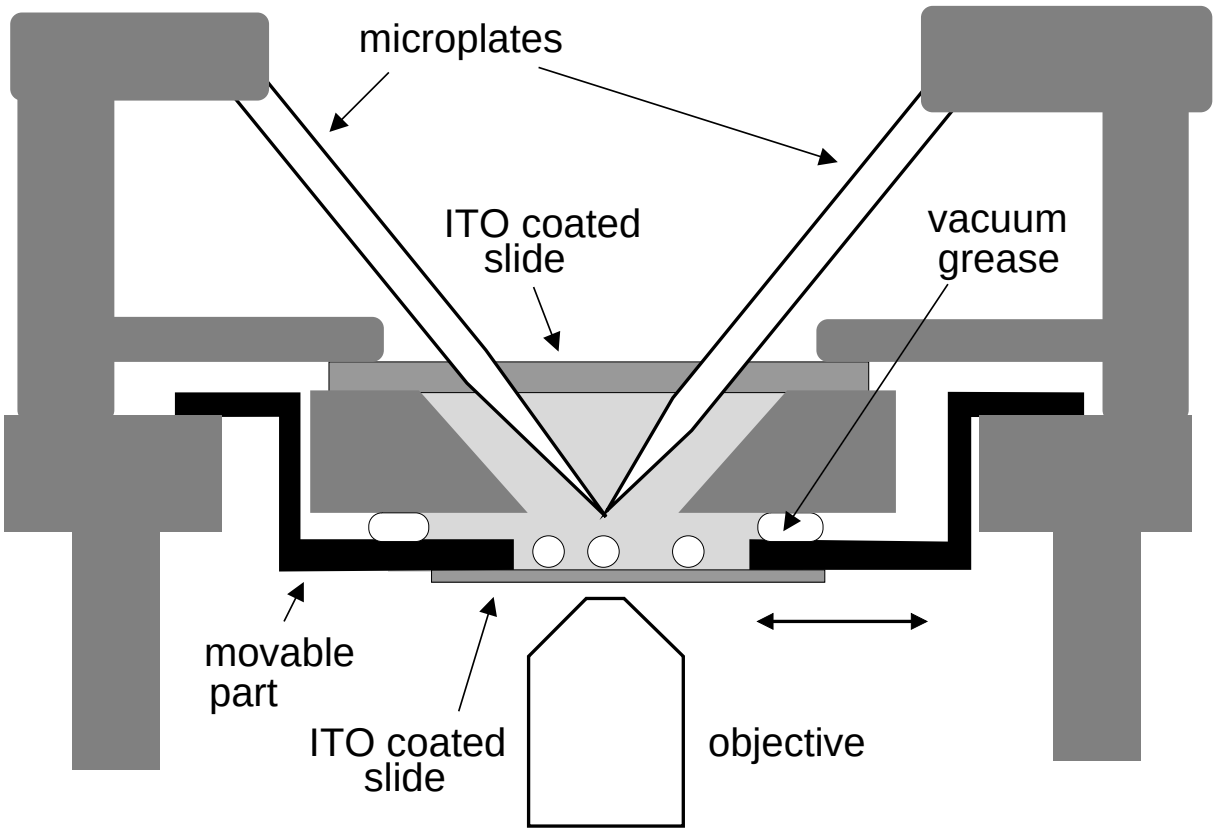

Figure 3.2: *Experiment chamber. The microscope stage, microplate manipulators, and the chamber are coloured dark gray. Cells are resting over the bottom slide, itself sticking on a makrolon piece (coloured black). This part can be moved relative to the microscope, in order to look for a nice cell.*

A major disadvantage of the procedure is the following. After years of observations, it has become clear that the faster a cell spreads on fibronectin, the better it is for the experiment. Spreading on fibronectin implies cytoskeletal compromise and is largely an irreversible process. With the described procedure, the cells contacts one plate first, and only 1-2 minutes later the second. Above 30°C, by the time the second plate is brought in, a significant fraction of the cells has already spread extensively on the first one. This situation does not revert by the presence of the second plate (at least within a few hours); the adhesion to the first plate is strong, but weak to the second one. These cells cannot be used for the experiment, as the weakly-binding side does not sustain strong pulling forces. Yet these fast-spreading cells presumably would have been very good for the experiment. I have not managed to solve this problem. The process of lifting the cell and rotating the plate cannot be sped up enough. I strongly suggest including a micropipette in the setup, which can be used to lift the cell and place it between the microplates.

Fibronectin coating

Experiments where the cells stick to fibronectin-coated plates are performed in ISCOVE medium, with 25 mM HEPES buffer and 10% fetal bovine serum (FBS). For the cells to stick to fibronectin coated plates, some contractility-inducer like serum is absolutely necessary.

Glutaraldehyde coating

Unlike the fibronectin coating, adhesion to glutaraldehyde coated plates does not require any biochemical promotor. In fact, serum has to be avoided, as it has a large amount of albumin and other proteins which passivate the plates. In general, amino groups should be absent as they react with glutaraldehyde. Thus, one cannot use nutritive culture media such as ISCOVE or DMEM, which have aminoacids and vitamins. Pure saline solutions such as HBSS or PBS must be used instead for the experiment. Alas, experiments in absence of serum are very inefficient. Most cells were very fragile under such conditions, and tended to burst. Thus, we did experiments in pure saline solution (HBSS), but added serum to a low concentration (2%) once the cell was sticking between the glutaraldehyde-coated plates. Though this procedure works, it is tedious and risky as serum has to be introduced very slowly to avoid losing the cell. As an alternative, I suggest using liso-phosphatydic acid (LPA) instead of serum, which does not react with the glutaraldehyde coating and hence can be present from the beginning.

...live cells are seen to adapt to step stretching. The authors attempted to bypass this complexity by applying oscillatory stretching for the rest of the experiments.
However, this merely masks the complexity and allows the authors to apply defined theories, but does not change the nature of the materials.

– a negative reviewer

Chapter 4

Results and discussion

4.1 Isometric force generation

We first perform experiments to characterise the response of fibroblasts to their presence in the rheometer. To stimulate contractility, we use high serum concentrations of 10%, and fibronectin mediated adhesion using coated microplates. As discussed in chapter 2, fibronectin binding to integrins is known to trigger the formation of focal complexes, which connect the extracellular matrix to the actin cytoskeleton (11, 113). To minimise the mechanical perturbation to the cell, we keep constant the cell length ℓ, given by the distance between the rheometer microplates, and measure the force F.

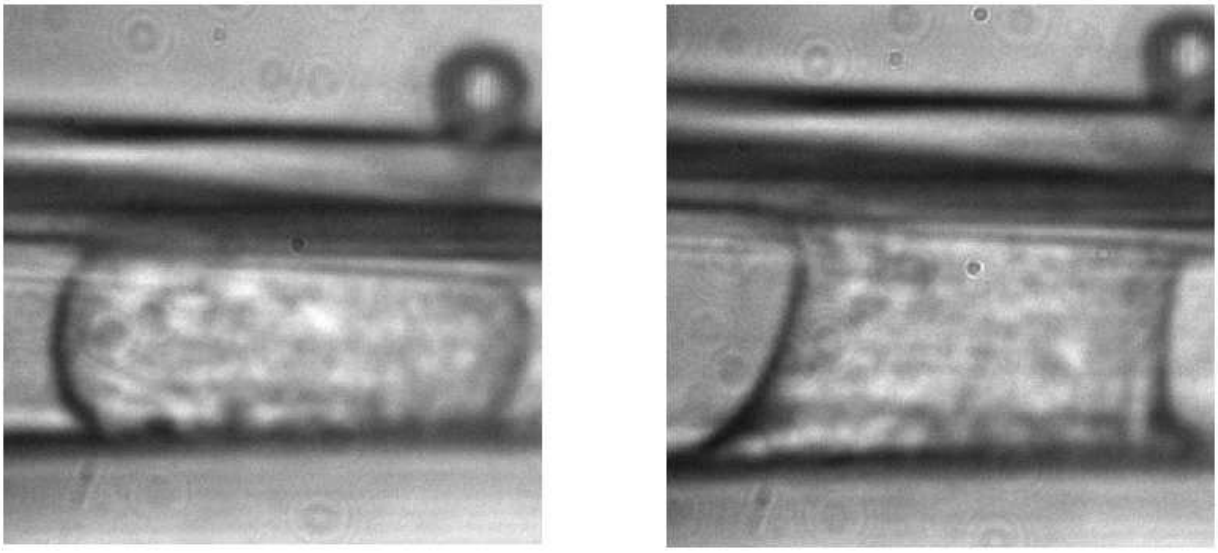

Figure 4.1: *Typical change in cell shape after contact with the fibronectin coated plates.* **Left:** $t = 0$. **Right:** ~ 20 *minutes later, the cell has adhered and spread symmetrically.*

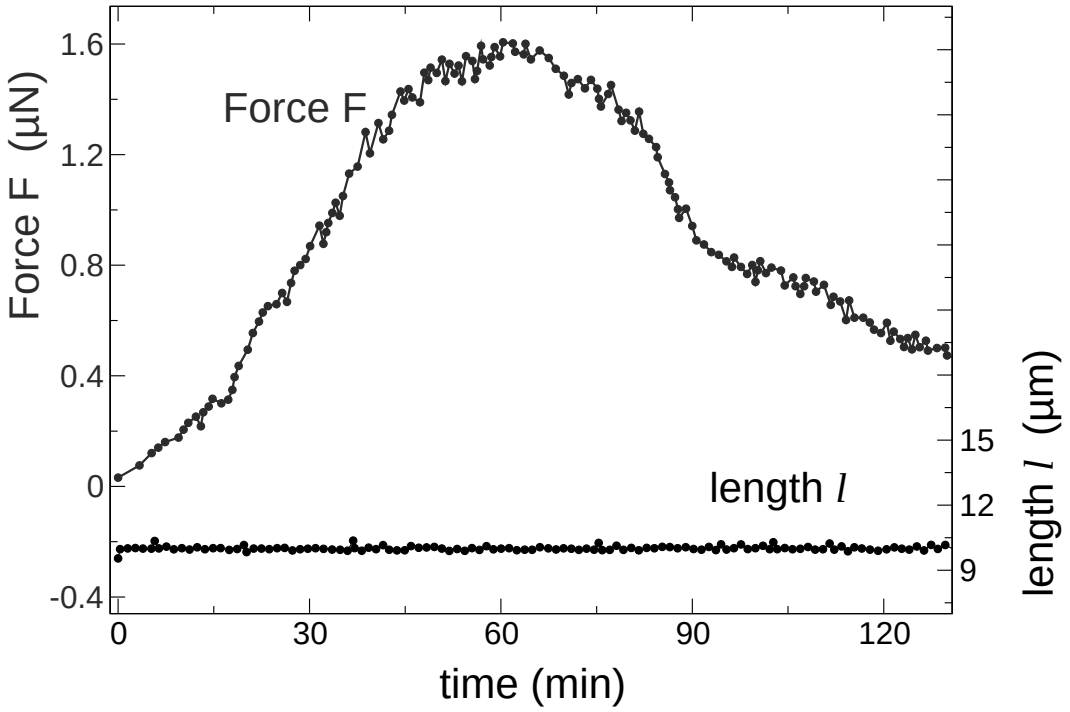

Figure 4.2: *Force as a function of time at constant cell extension, recorded immediately after incorporation of the fibroblast into the rheometer. The force change is due to active behaviour. No significant cell shape alterations are seen throughout. The experiment is performed at* $27°C$ *using fibronectin mediated adhesion.*

The experiment is began by placing the cell between the fibronectin coated plates and compressing it for about 1 hour. During this time, a significant fraction of the cells spread symmetrically between the plates, their shape changing from the initial spherical form to a concave one, as illustrated in Fig.4.1. This process, which at a temperature of $30°$C requires compression for ~ 30 min, is invariably associated with the ability to generate strong contractile forces. Once this concave shape is reached, the cell is stretched until the force F becomes zero, and the respective length ℓ is then imposed constant for several hours. The cell shape is then usually stable, with no further geometrical changes taking place during the rest of the experiment. Often, while the length ℓ is kept constant, strong forces develop. An example is given in Fig4.2. The force F reaches values in the range 0.1–1 μN and eventually decays to zero. The force relaxation seems to be an adaptation to the constant length condition, since active contraction can be induced again by a sudden change in cell length ℓ. The behaviour is reproducible only in its broad, qualitative features. The force and time scales are strongly cell-dependent. Such experiments are interesting in that they reveal the contractile potential of fibroblasts in the experimental conditions. However, the large variability between cells difficults a quantitative analysis.

4.2 Superimposed small amplitude oscillations

In order to probe cell rheological properties during these complex force regulation processes, we superimpose sinusoidal length oscillations at small amplitudes and high frequencies. These are chosen so that the corresponding maximum rate of change of force is at least two orders of magnitude above the values typically seen in active contraction.

When sinusoidal length oscillations are superimposed, the cell length ℓ can be written as

$$\ell = \langle \ell \rangle + \Re e \left(\Delta_\ell \, e^{i\omega t} \right),$$

where $\langle \ell \rangle$ is the average length over an oscillation period, and Δ_ℓ is a complex amplitude for the superimposed length-oscillations. At small amplitudes $|\Delta_\ell| < 0.05 \langle \ell \rangle$ a linear regime exists, as will be shown later, where a similar equation holds for the force F :

$$F = \langle F \rangle + \Re e \left(\Delta_F \, e^{i\omega t} \right).$$

The complex amplitudes are then related by

$$\frac{\Delta_F}{A_0} = (\Theta' + i\,\Theta'') \, \frac{\Delta_\ell}{\langle \ell \rangle},$$

which defines a formal stretching modulus $\Theta' + i\,\Theta''$, independent of the amplitudes as long as these are small. As long as one applies small amplitude deformations, cells can be described as viscoelastic media (8, 114). As the viscous response depends on deformation rate instead of absolute deformation, it causes a phase-shift between length and force. The storage modulus Θ' reflects the purely elastic (non-dissipative) part of the cell reaction, and the loss modulus Θ'' the viscous (dissipative) contribution. In order to compare cells of different sizes and with biological gels, we use formal engineering stress units for the moduli. Accordingly, stress is taken as $\sigma = F/A_0$.

The differential stretch moduli Θ' and Θ'' should not be confused with material parameters like the Young's modulus. The spatial distribution of force bearing structure inside the cell is unknown. Rather than introducing ad hoc hypotheses, such as assuming a uniform material, we simply treat the cell as a mechanical black box. The unconventional symbol Θ for the moduli intends to emphasise their experiment-specific nature. Further, these moduli characterise the response of the material to small perturbations around a situation which may be far away from the resting state. Indeed, we show below that it is suitable to study Θ' and Θ'' as a function of the average force $\langle F \rangle$. As described in chapter 2, a similar approach has been successfully used in stretching experiments on whole tissues, such as skin or muscle (8). Equivalent procedures have recently been applied to biopolymer gels under shear deformations, where the differential shear moduli are measured as a function of the average stress or strain (30, 31).

Instead of the loss and storage moduli Θ', Θ'', it will be more convenient to regard the absolute modulus $|\Theta|$ and the loss angle δ, defined as

$$|\Theta| = \sqrt{\Theta'^{\,2} + \Theta''^{\,2}}$$

$$\delta = \arctan\left(\frac{\Theta''}{\Theta'} \right)$$

Amplitude dependence of the Θ-moduli

Fig. 4.3 shows the dependence of the stiffness $|\Theta|$ as a function of the strain amplitude $\Delta_\ell/\langle\ell\rangle$. In general, at strain amplitudes in the range 0.02–0.06, the effective moduli do not change by more than 20%.

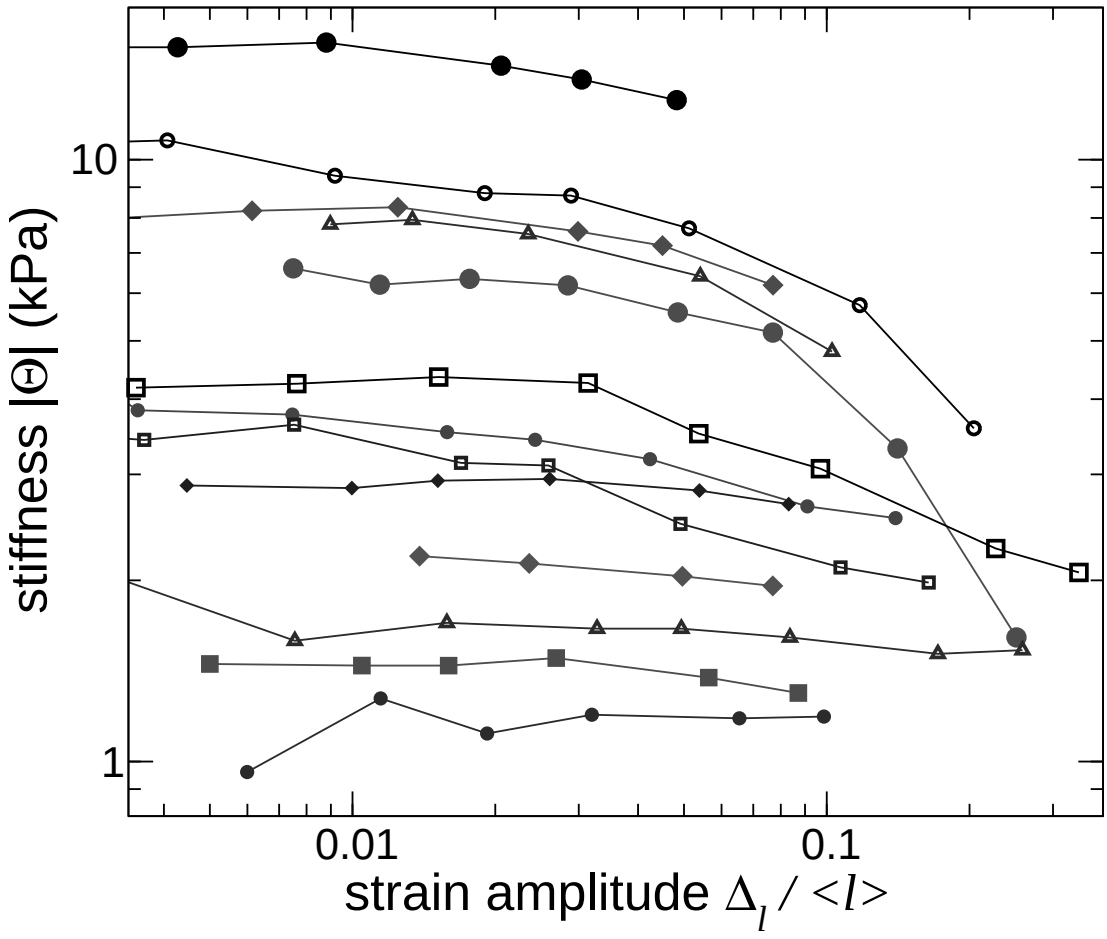

Figure 4.3: *Amplitude sweep. Stiffness $|\Theta|$ as a function of the strain amplitude $\Delta_\ell/\langle\ell\rangle$ for an arbitrary selection of cells. Each curve is a different experiment. All frequencies are 0.2 Hz.*

Moreover, no significant distortion of the response is seen below relative deformations of 0.1, as illustrated by the Lissajoux figures shown in Fig. 4.4. This holds irrespective of the frequency in the range 0.1–1 Hz. Thus, in subsequent experiments the amplitude is kept small, $\Delta_\ell = 0.5$ μm, which corresponds for all cell length values to 0.02–0.06 strain amplitudes.

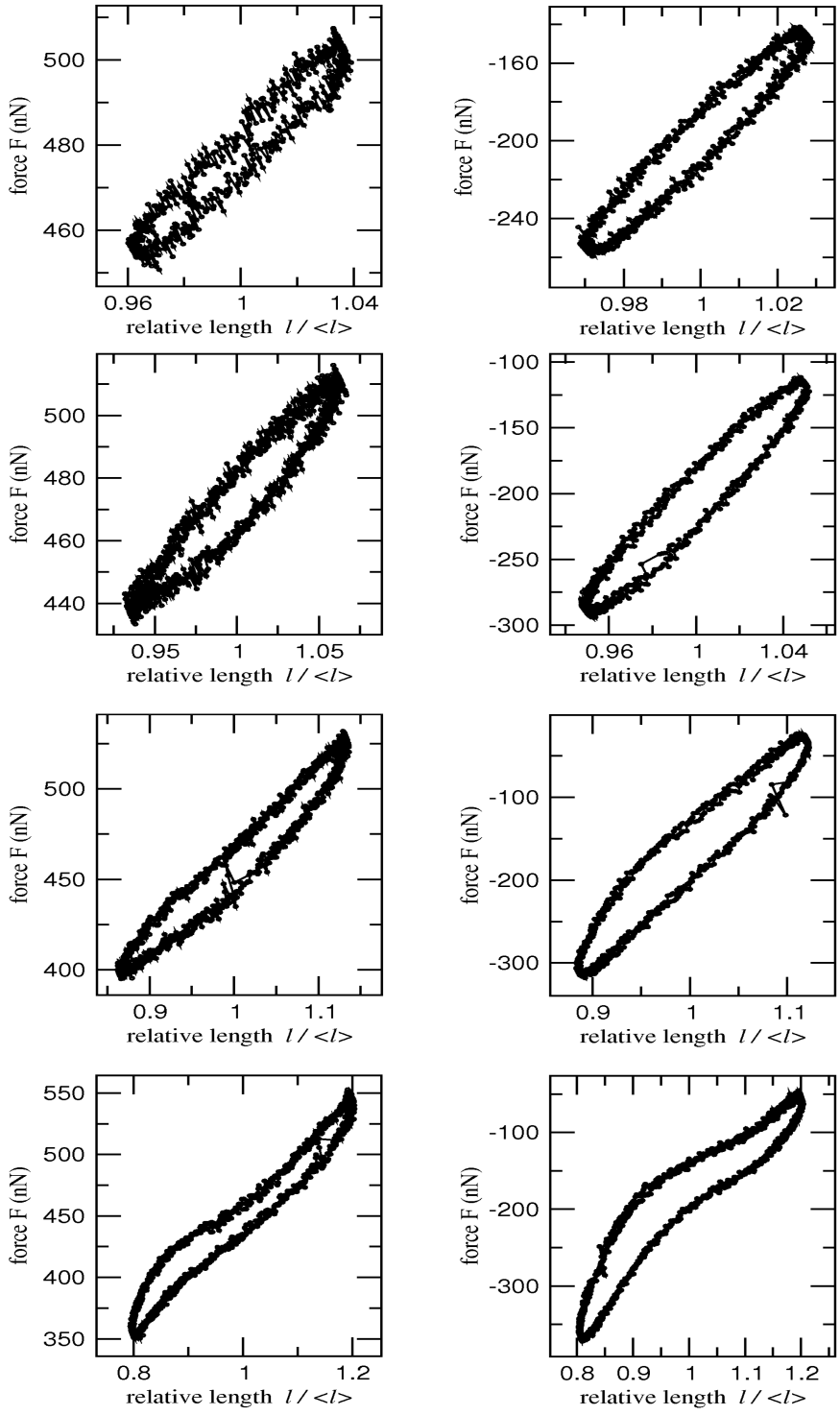

Figure 4.4: *Lissajoux figures for different amplitudes.* **Left:** *Typical response under tension, at forces above crossover. Force F as a function of relative cell length $\ell/\langle\ell\rangle$ for strain amplitudes 3.5% (**T1**), 6% (**T2**), 13% (**T3**), and 20% (**T4**). The oscillation frequency is 0.2 Hz.* **Right:** *Typical response under compression. Force F as a function of relative cell length $\ell/\langle\ell\rangle$ for strain amplitudes 3% (**C1**), 5% (**C2**), 12% (**C3**), and 20% (**C4**). The oscillation frequency is 0.2 Hz.*

Frequency dependence of the Θ-moduli

In Fig. 4.5 we show results on the frequency dependence of the modulus $|\Theta|$ and the loss angle δ, in the range 0.1–1 Hz. Keeping in mind that our frequency range spans only one decade, our results are consistent with the results on biomechanics discussed in chapter 2 (8, 33, 93, 95). The modulus $|\Theta|$ increases weakly with the frequency for all cells studied, whereas δ is roughly constant when averaging over cells. If the frequency dependence of the modulus $|\Theta|$ is described as a power-law, exponents are in the range 0.1–0.3. Such a frequency dependence is the signature of a flat, broad continuous spectrum of relaxation times (8).

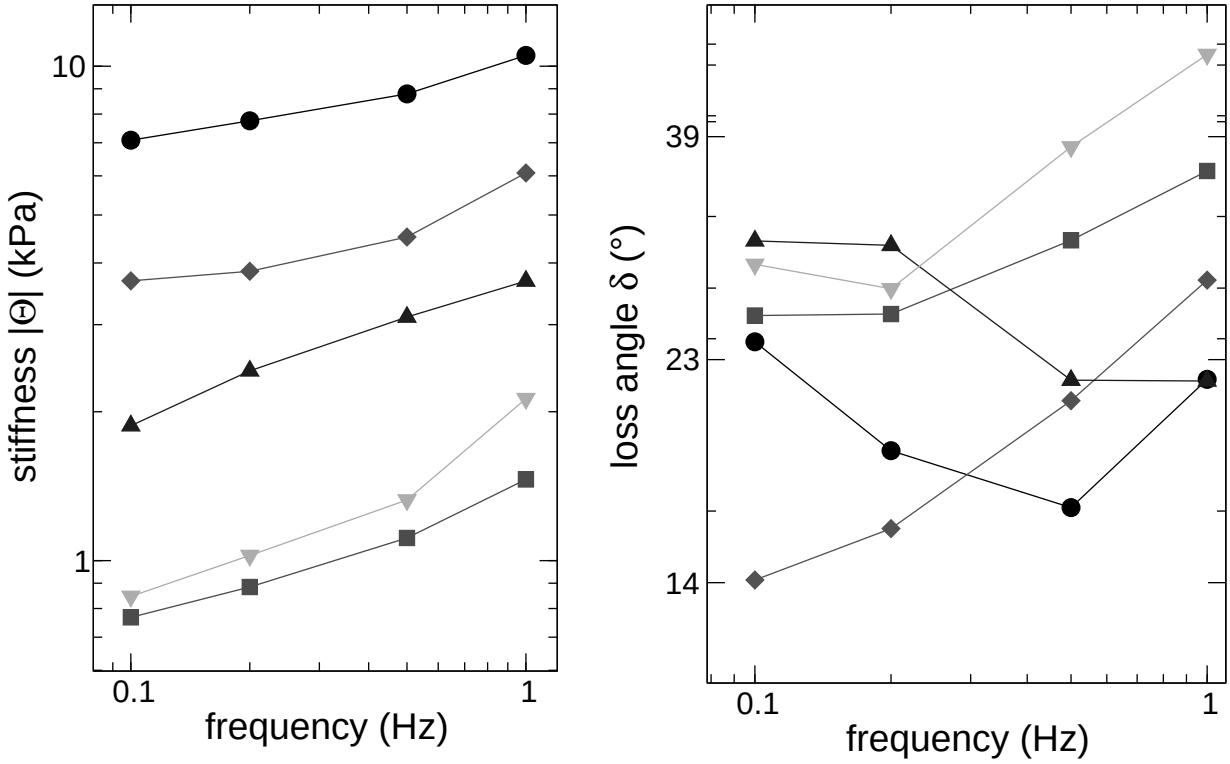

Figure 4.5: *Frequency sweep. Modulus $|\Theta|$ and loss angle δ as a function of frequency. Each curve is obtained using a different cell.*

4.3 Length-independent stress stiffening

This section conveys one of the major results of this work. We show that the viscoelastic Θ-moduli are a well-defined function of the average force $\langle F \rangle$, independently of the cell length.

4.3.1 Stiffening at constant length

During the initial phase of force development after contact with the fibronectin-coated microplates, the cell sweeps force-space at a constant length. We superimpose sinusoidal oscillations to the constant average length, in order to probe the temporal evolution of the moduli Θ' and Θ''. The frequency of the oscillations is cyclically changed in the range 0.1 – 1.0 Hz. As shown in Fig. 4.6, as the average force increases with contractile activity of the cell, so does the modulus $|\Theta|$. Figs. 4.6 *c, d* show the dependence of the response parameters $|\Theta|$ and δ on the average force $\langle F \rangle$ for different frequencies. The relation between the modulus $|\Theta|$ and the force $\langle F \rangle$ can be seen to be independent of the frequency. This can be seen as an unusual example of stress stiffening, since it takes place *at an average constant length*.

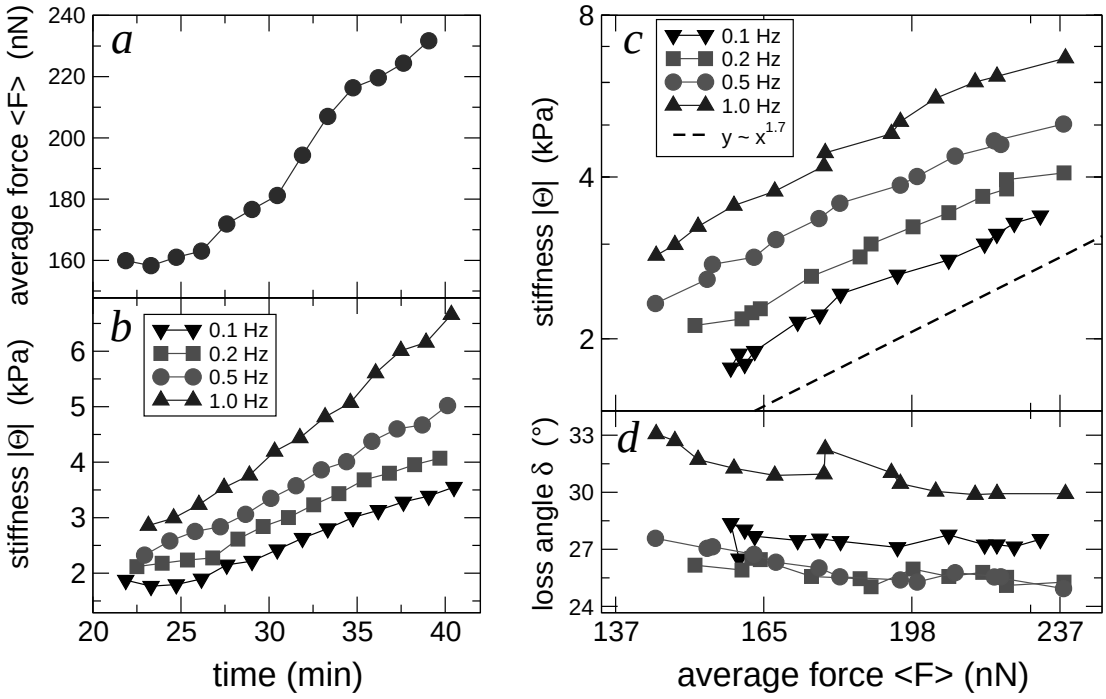

Figure 4.6: *Stress stiffening at constant length. The average cell length is kept constant throughout,* $\langle \ell \rangle = 9\mu m$. *Sinusoidal oscillations are superimposed with a strain amplitude* $\Delta_\ell / \langle \ell \rangle = 0.03$. *The frequency of the oscillations is cyclically changed from* 0.1 *to* 1.0 *Hz.* **a)** *The average force* $\langle F \rangle$ *is seen to increase in time.* **b)** *The modulus* $|\Theta|$ *increases in time for all frequencies.* **c)** *Stiffness* $|\Theta|$ *as a function of average force* $\langle F \rangle$*, for different frequencies. The line shows a power-law function* $y \sim x^{1.7}$. **d)** *Loss angle* δ *as a function of average force* $\langle F \rangle$

4.3.2 Stiffening probed by length/force steps

Not all fibroblasts generate such high forces as in the experiment shown in Fig. 4.6. In order to span a larger range of average force $\langle F \rangle$ and length $\langle \ell \rangle$, we step-stretch the cell and then keep the average length constant, superimposing oscillations to record the moduli Θ' and Θ''. The procedure is periodically repeated, as shown in Fig. 4.7. We have confirmed that the presence of the oscillations does not significantly alter the overall behaviour of the cell. Like in the step-experiments shown at the beginning of the chapter, as a reaction to a sudden change in length a force relaxation always occurs, usually followed by active contraction. As the average force $\langle F \rangle$ evolves at a fixed length $\langle \ell \rangle$, the viscoelastic moduli are continuously recorded. We also perform step experiments controlling the average force $\langle F \rangle$. In this way, it is possible to span large areas in the $\langle \ell \rangle$ – $\langle F \rangle$ diagram.

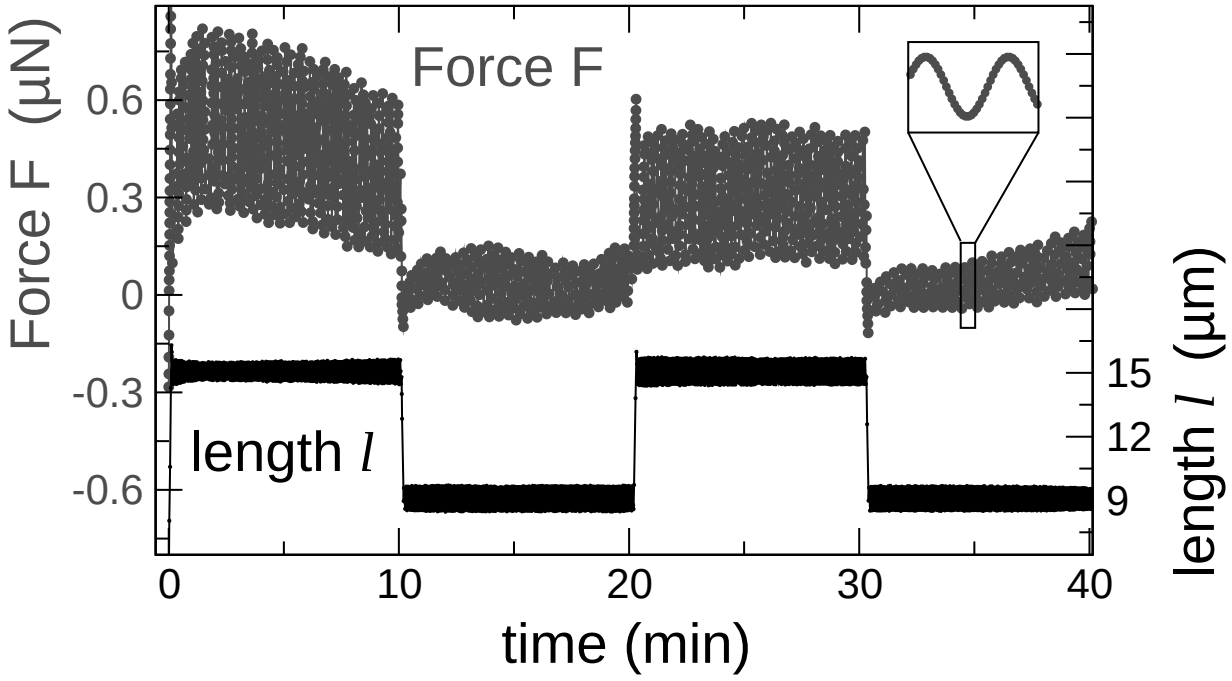

Figure 4.7: *The force response as result of imposed length changes with superimposed oscillations. We step-strain the cell by about 50% at a rate of* $1.5\ \mu$*m/s, and apply length oscillations (as shown in the* **inset***) at an amplitude of* $0.5\ \mu$*m and a frequency of* 0.2 *Hz. The experiment was performed using fibronectin mediated adhesion.*

In the experiment shown in Fig.4.8, the deformation rate during the ramps is increased progressively. At high rates, the force F barely changes during the ramp, and increases later isometrically. Simultaneously the modulus $|\Theta|$ increases. Fig.4.8(b) shows the relation between the modulus $|\Theta|$ and the average force for the initial part of the experiment. In the second part of the experiment shown in Fig.4.8(a) the force is controlled, the average $\langle F \rangle$ kept constant at various plateau values. In Fig.4.8(c) the $|\Theta|(\langle F \rangle)$ relation so obtained is compared to the one measured during isometric pulling.

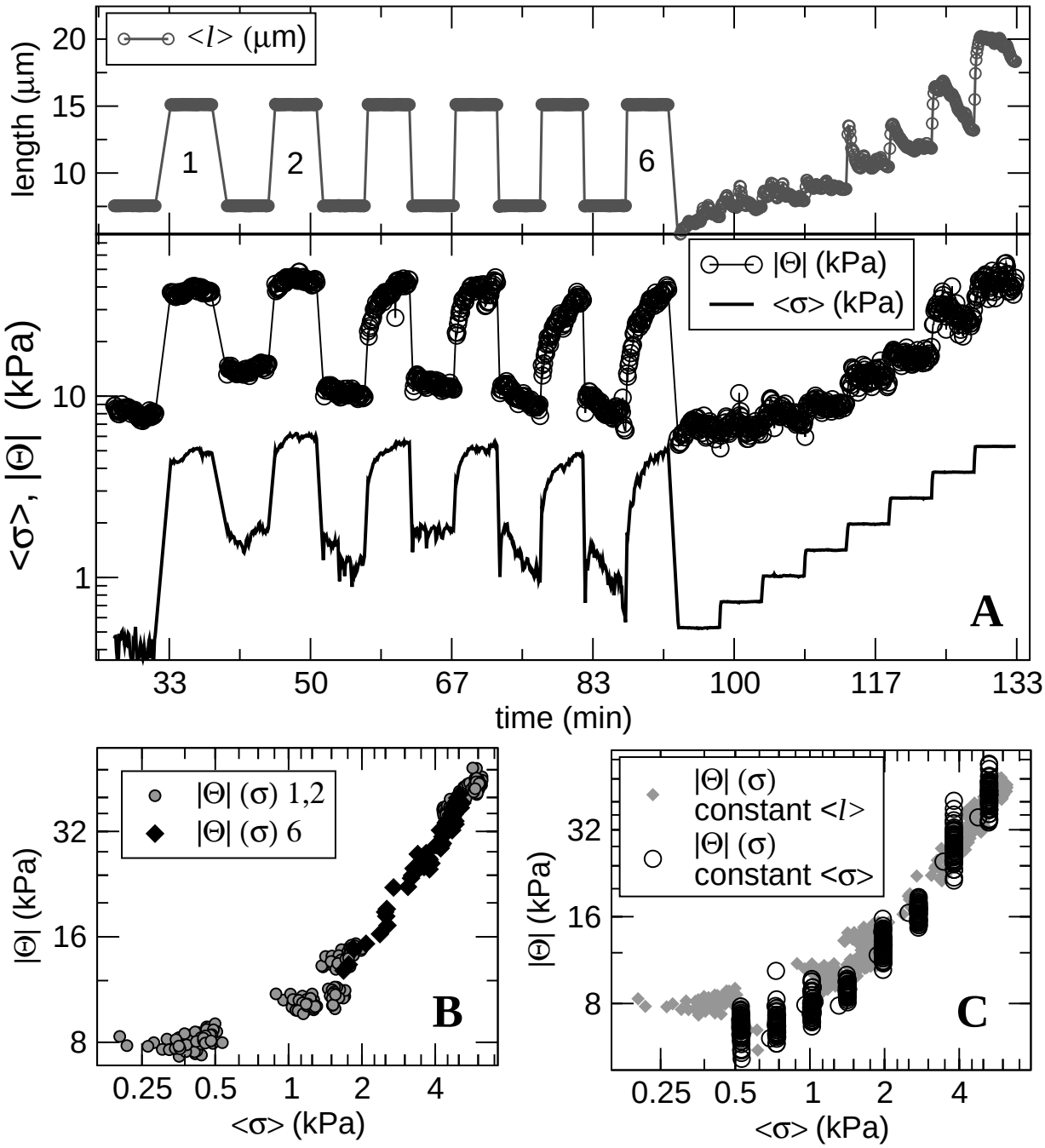

Figure 4.8: *Experiment with fibronectin coating at 35°C. First the cell length ℓ is stepped between 7.5 μm and 15 μm. The deformation rate $\dot{\ell}$ during the ramps is increased progressively. During each plateau, oscillations at 0.2 Hz are superimposed to the constant average length $\langle\ell\rangle$. In the second part of the experiment, force is controlled. The average force $\langle F\rangle$ is kept constant for about 5 min, then step-increased to a new value. Oscillations at 0.2 Hz are superimposed throughout.* **A:** *average length $\langle\ell\rangle$, modulus $|\Theta|$, and average stress $\langle\sigma\rangle$ as a function of time.* **B:** *Modulus $|\Theta|$ as a function of the average stress $\langle\sigma\rangle$ for the data points corresponding to the steps 1,2, (symbols....) and 6.* **C:** *the same data from* **B**, *plus all $|\Theta|(\langle\sigma\rangle)$ data points from the second part of the experiment where the average force $\langle F\rangle$ was imposed constant* **(open circles)**.

4.3.3 A master-relation characterises stress stiffening

By the procedures just described, a remarkably simple picture arises. We see that both viscoelastic moduli depend only on the average force, essentially independent of the average length. The dependence of the loss angle $\delta = \arctan(\Theta''/\Theta')$ on the average force $\langle F \rangle$ is erratic and weak, at most decreasing about 20% in the whole force range. As a function of the individual cell, it is within the range 10-30°. The absolute modulus $|\Theta| = [(\Theta')^2 + (\Theta'')^2]^{1/2}$ remains constant at low forces, in a 1–30 kPa range depending on the individual cell. Above a cell-dependent crossover force, we observe stress stiffening: $|\Theta|$ increases as a function of the average force $\langle F \rangle$. This dependence of $|\Theta|$ on the average force can be well approximated by a power-law, as shown in Fig. 4.9 *(inset)*. More than one stress decade above crossover, most cells deform significantly and begin to detach or yield.

A collapse of all data to a single master-relation can be achieved by introducing cell-dependent scaling factors, the zero force stiffness Θ_0 and the crossover stress σ_C. On the average,

$$|\Theta| = \begin{cases} \Theta_0 & \text{for} \quad \langle \sigma \rangle < \sigma_C \\ \Theta_0 \left(\dfrac{\langle \sigma \rangle}{\sigma_C} \right)^{\gamma} & \text{for} \quad \langle \sigma \rangle > \sigma_C \end{cases}$$

The exponent γ is independent of the scaling factors. At $26°$C, 0.2 Hz, and 5% deformation amplitude, it is approximately 1, as shown by the collapsed data in Fig. 4.9. The scaling factors are roughly related by $\Theta_0 \propto \sigma_C^{1.3}$. Thus, an approximate collapse can be reached with a single parameter. This "collapsability" should not be overemphasised, as the exponent does vary from one cell to the other.

This master-relation is consistently found in all cells strong enough to reach average stresses above $\sim 0.1\ \Theta_0$. This reproducibility shows that oscillatory measurements are indeed effective in probing cell mechanical properties, even in presence of an underlying slow active behaviour.

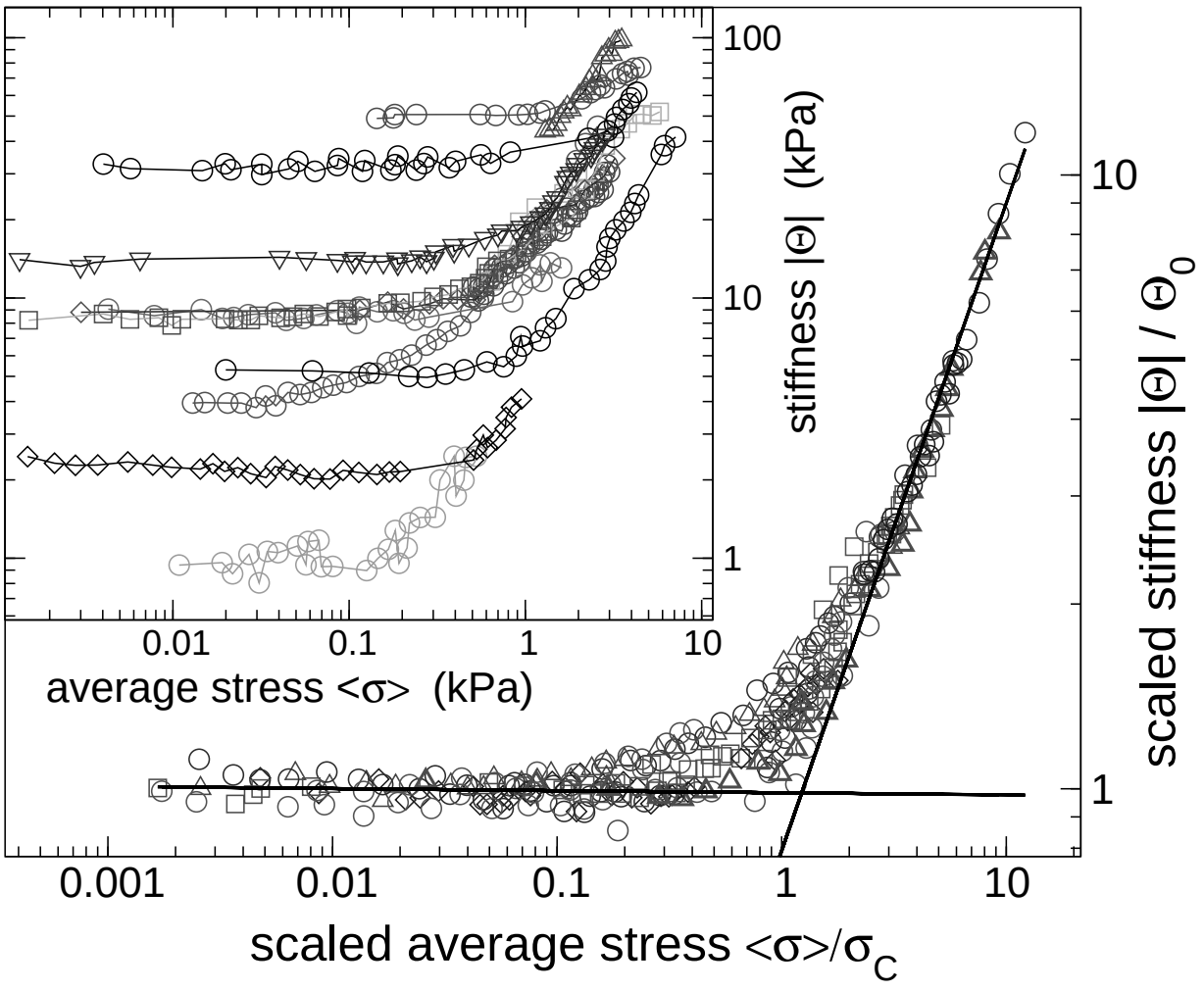

Figure 4.9: *The inset shows the elastic modulus $|\Theta|$ as a function of average stress for 13 cells, measured using length steps plus oscillation experiments such as in Fig. 4.7. The main plot shows the data scaled using 2 factors, which gives an exponent $\gamma \simeq 1.0$. All experiments are performed at 26°C and using fibronectin mediated adhesion.*

4.4 Stress relaxation function

If the cell length ℓ is kept constant after a fast step deformation, force relaxation can be observed. Measurement of the force relaxation curve after an *increase* in length is difficult, since often active behaviour sets in before the relaxation is over. On the contrary, after a fast *decrease* in ℓ the subsequent force relaxation curve has a reproducible, simple shape. As shown in Fig.4.10, a good fit can be obtained with a Kohlrausch function

$$F = F_\infty + (F_0 - F_\infty)\ \exp[-(t/\tau)^\beta]\ .$$

Neither exponential nor power-law functions describe well the data over the three time decades available.

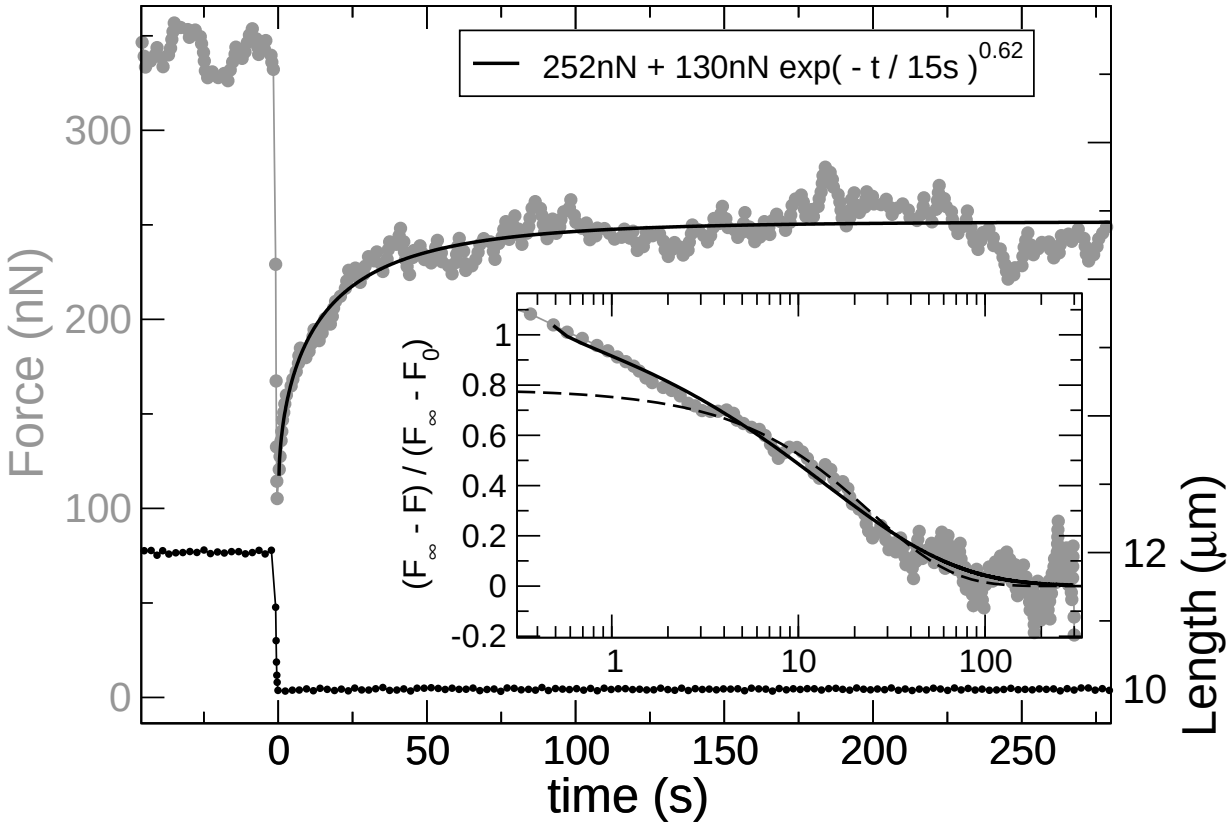

Figure 4.10: *Force relaxation after a length step downwards. The* **solid line** *is a fit to a stretched exponential with parameters* $\beta = 0.62$, $\tau = 15s$, $F_\infty = 252$ *nN, and*$F_\infty - F_0 = 130$ *nN.* **Inset:** $(F_\infty - F)/(F_\infty - F_0)$ *using the data from the main plot. For comparison, a least-squares simple exponential fit is also shown (***dashed line***).*

4.5 Ramp experiments

Now we take a closer look at the mechanical behaviour of cells when stretched at a constant rate. We stretch the cell at a rate $\dot{\ell}_1$, keep ℓ constant for 5 min, then bring it back at the rate $-\dot{\ell}_1$ and let relax again for 5 min. The procedure is repeated, increasing the deformation rate each

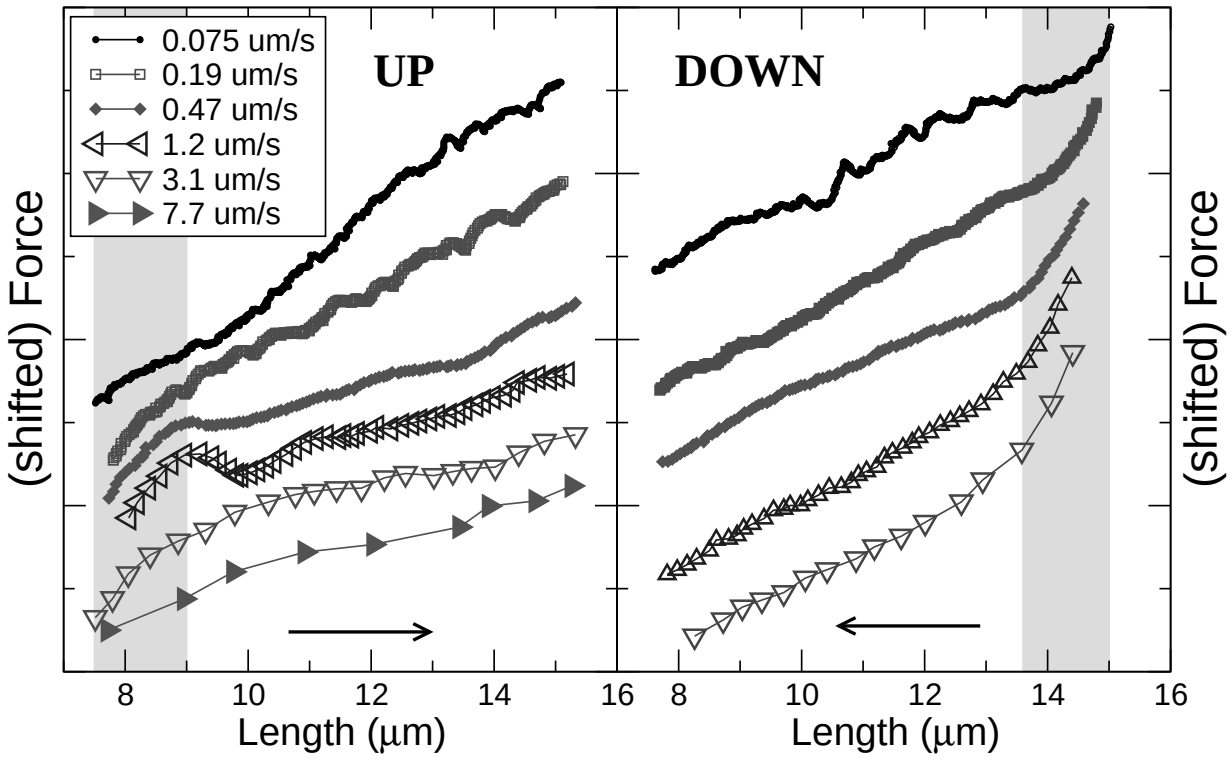

Figure 4.11: *Ramp experiments at different rates performed on the same cell.* **For clarity, the curves have been arbitrarily shifted along the F axis to separate them.** *The stretch rate $\dot{\ell}$ is kept constant during each ramp.* **UP** *: ramps upwards, $\dot{\ell} > 0$.* **DOWN** *: ramps downwards, $\dot{\ell} < 0$. Both plots have exactly the same size and scale, to ease the comparison of the slopes. Notice how beyond a crossover deformation the tangential stiffness $\partial F/\partial \ell$ drops and becomes approximately constant. The shaded regions signal the beginning of the deformation.*

The most remarkable feature of these curves is their linearity, even though the total deformation amounts to 50%, a very large stretch. A careful look shows that this linearity is reached only after ℓ has changed by $\sim 10\%$. This holds for the ramps up as well as down, and for all rates within over a decade range. Hence, the initial drop in the tangential stiffness $\partial F/\partial \ell$ is not a *time* effect; the relevant parameter is rather the extent of deformation. One can therefore talk of a crossover amplitude, and of a tangential stiffness beyond crossover $\Psi = \partial F/\partial \ell$.

The curves in Fig.4.11 show a clear dependence on the sense of deformation. When going down ($\dot{\ell} < 0$), the tangential stiffness beyond crossover is essentially rate-independent, $-\Psi^- = \Psi_0$. At low deformation rates, the upward stiffness has a similar value, $\Psi^+ \simeq \Psi_0$; but increasing the rate $\dot{\ell}$ beyond 200 nm/s leads to a drop in Ψ^+. The dependence on the deformation sense is more pronounced in the experiment shown in Fig.4.12. Here, before and after the ramp sinusoidal oscillations are superimposed. The decreasing trend of Ψ^+ with deformation rate $\dot{\ell}$ is here very clear. In fact, at $\dot{\ell} = 0.44\,\mu$m/s an almost "flow" state is reached where the cell extends at a constant force. Remarkably, the ramps downwards do not show such an effect at all.

As revealed by the sinusoidal oscillations imposed right after the ramp, the cell has not been irreversibly disrupted by the fast ramps shown in Fig.4.12. As soon as the ramp finishes and an oscillation begins, the force-length relation changes: the slope $\partial F/\partial \ell$ jumps to a value similar to that of the first set of oscillations, as suggested by the dotted lines.

Incidentally, this behaviour strongly resembles strain-hardening in plastic materials (7, 115). When deformed beyond the yield stress, the slope goes down as the material strains plastically. The moment the deformation is reversed, elastic behaviour is recovered and the slope jumps back to the initial value.

Figure 4.12 : *Ramp experiment at different rates.* **a, b, G:** *deformation rate* $|\dot{\ell}| = 0.069\,\mu$*m/s.* **a:** *upward ramp,* F *and* ℓ *vs. time.* **b:** *downward ramp,* F *and* ℓ *vs. time.* **G:** F *vs.* ℓ *using the data from* **a, b**. *The* **dashed line on the left in G** *indicates the elastic region. Beyond an amplitude* $\sim 1\,\mu$*m the tangential stiffness* $\partial F/\partial \ell$ *drops and becomes approximately constant (***arrow***). The oscillations performed after the ramp show that no irreversible disruption has taken place. Notice how the slope jumps to its elastic value (indicated by the* **dashed line on the right***) as soon as the deformation sense is reversed. Notice also that the tangential stiffness beyond crossover* Ψ *has a similar value in the downward as in the upward ramp.*
c, d, H: *deformation rate* $|\dot{\ell}| = 0.17\,\mu$*m/s.* **c:** *upward ramp,* F *and* ℓ *vs. time.* **d:** *downward ramp,* F *and* ℓ *vs. time.* **H:** F *vs.* ℓ *using the data from* **c, d**.
e, f, J: *deformation rate* $|\dot{\ell}| = 0.44\,\mu$*m/s.* **e:** *upward ramp,* F *and* ℓ *vs. time.* **f:** *downward ramp,* F *and* ℓ *vs. time.* **J:** F *vs.* ℓ *using the data from* **e, f**. *At this fast rate there is a clear difference between the upward and the downward ramp. Whereas the downward ramp is still approximately linear and the slope* Ψ *does not change noticeably, in the upward ramp a "flow" state is reached where the cell extends at constant force. Yet again no irreversible disruption has taken place, as indicated by the oscillations imposed afterwards.*

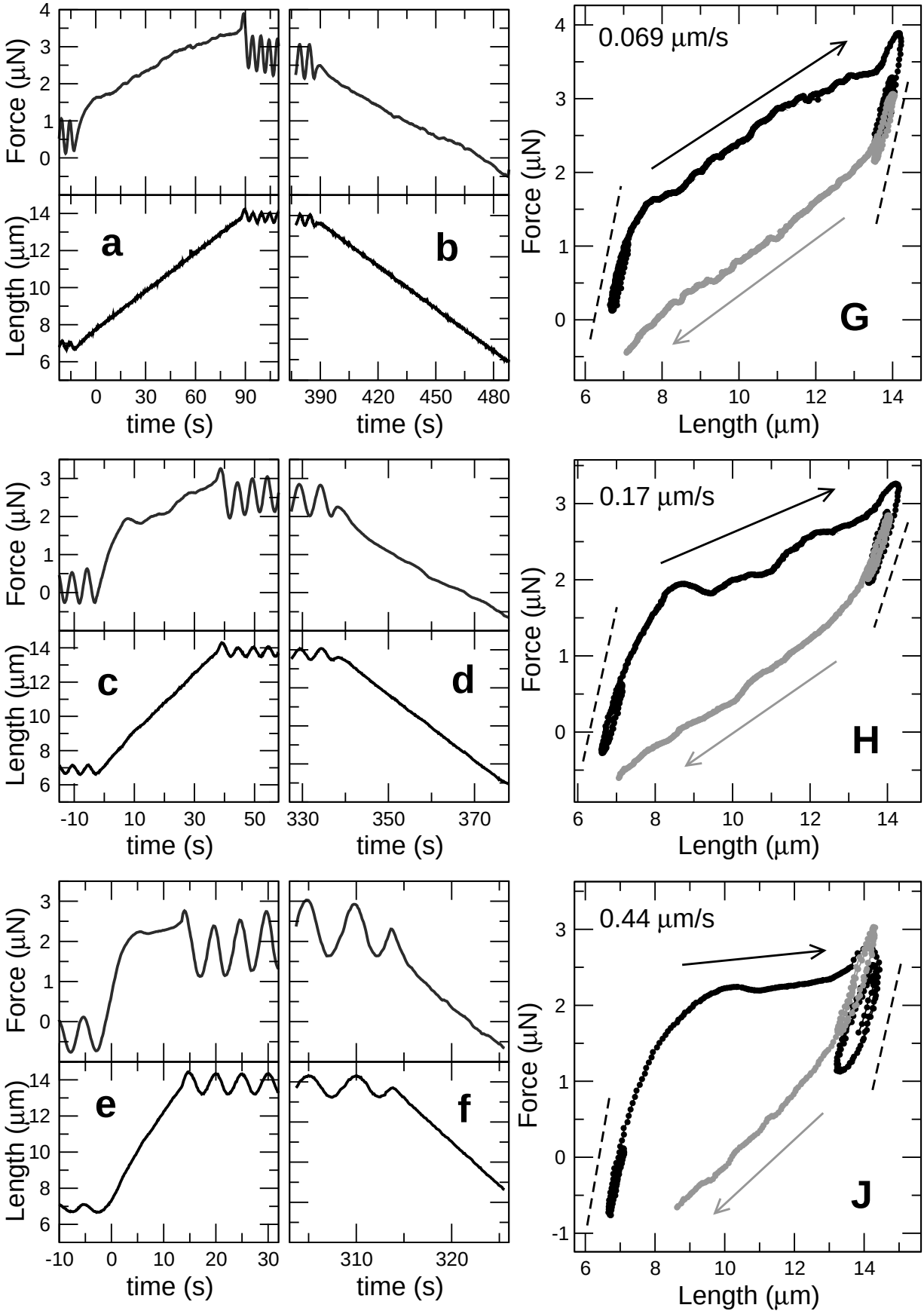

Figure 4.12: **See the caption on the left**

4.6 Ramp experiments with superimposed oscillations

The master-relation holds at a constant cell length $\langle \ell \rangle$ while an underlying active contraction occurs, i.e. the cell itself sweeps $\langle F \rangle$–space. This requires the good will of the cell. Another procedure is available: the experimentator can force the exploration of force space by stretching the cell and superimposing small oscillations. Fig.4.13 shows such an experiment. In the first case, the rate of change of the average force is set by the cell. By stretching the cell different rates can be imposed.

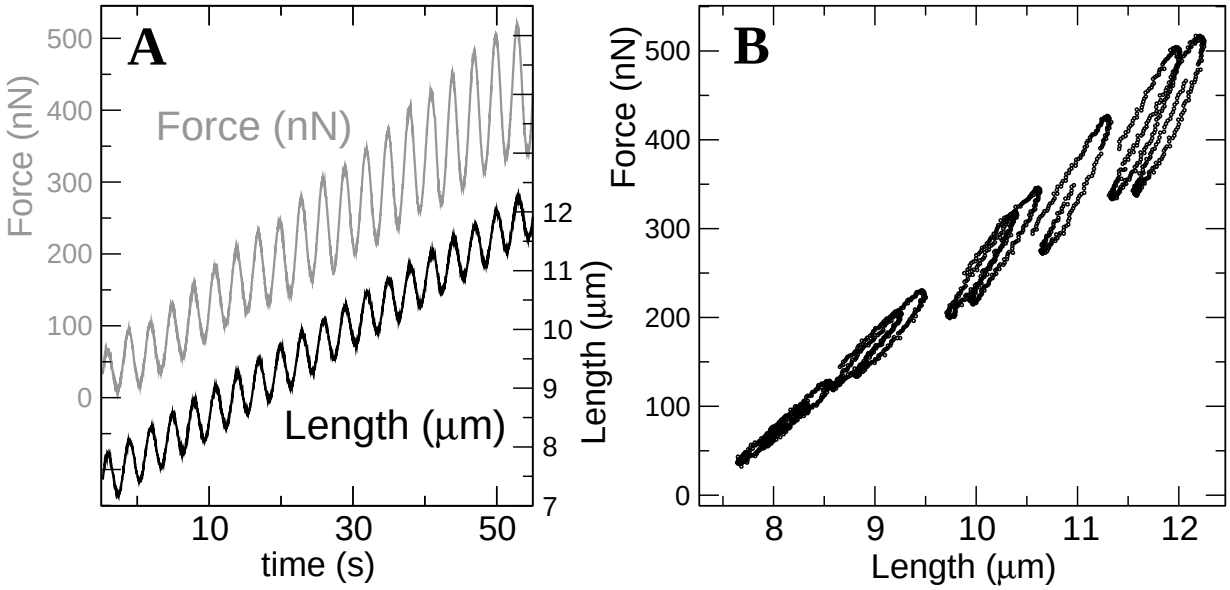

Figure 4.13: *A typical ramp experiment with superimposed oscillations.* **A:** *Force and length as a function of time.* **B:** *Force–length relation using the data in* **A**. *For clarity,* **only a few of the oscillatory loops are shown**. *Notice the roughly linear relation between the average values* $\langle F \rangle$, $\langle \ell \rangle$, *as well as the simultaneous stiffening given by the loops tilting upwards.*

4.6.1 Stiffening during a ramp

Now we show that ramping the average force is equivalent to having the cell pull on its own, as far as the master-relation goes. We increase $\langle \ell \rangle$ at a constant rate in the range 0.1 – 2 μm/s, and simultaneously superimpose small oscillations at an amplitude $\Delta_\ell \simeq 0.5\ \mu\mathrm{m}$ and a frequency of 1 Hz, to measure the dynamic moduli Θ' and Θ''. As shown in Fig. 4.14 *a*, by stretching the cell, a change in average stress is induced. As in the pure ramp experiments discussed at the beginning of the chapter, the average stress $\langle \sigma \rangle$ depends roughly linearly on the average length $\langle \ell \rangle$ throughout a ramp with superimposed oscillations. Remarkably, stress stiffening of the dynamic moduli is simultaneously observed. The master-relation between $|\Theta|$ and $\langle \sigma \rangle$ is seen to remain valid at low deformation rates. These experiments show that the particular way of sweeping force space is not relevant, since the $|\Theta|(\langle \sigma \rangle)$ function is qualitatively the same as that found in active contraction experiments. As can be seen in Fig. 4.14, *a* and *b*, only at

rates higher than a cell-dependent value in the vicinity of 200 nm/s does $|\Theta|(\langle\sigma\rangle)$ fall below the master-relation. The cell then becomes more fluid as evidenced by an increase in the loss angle δ. This also happens during the ramps down, though to a lesser extent.

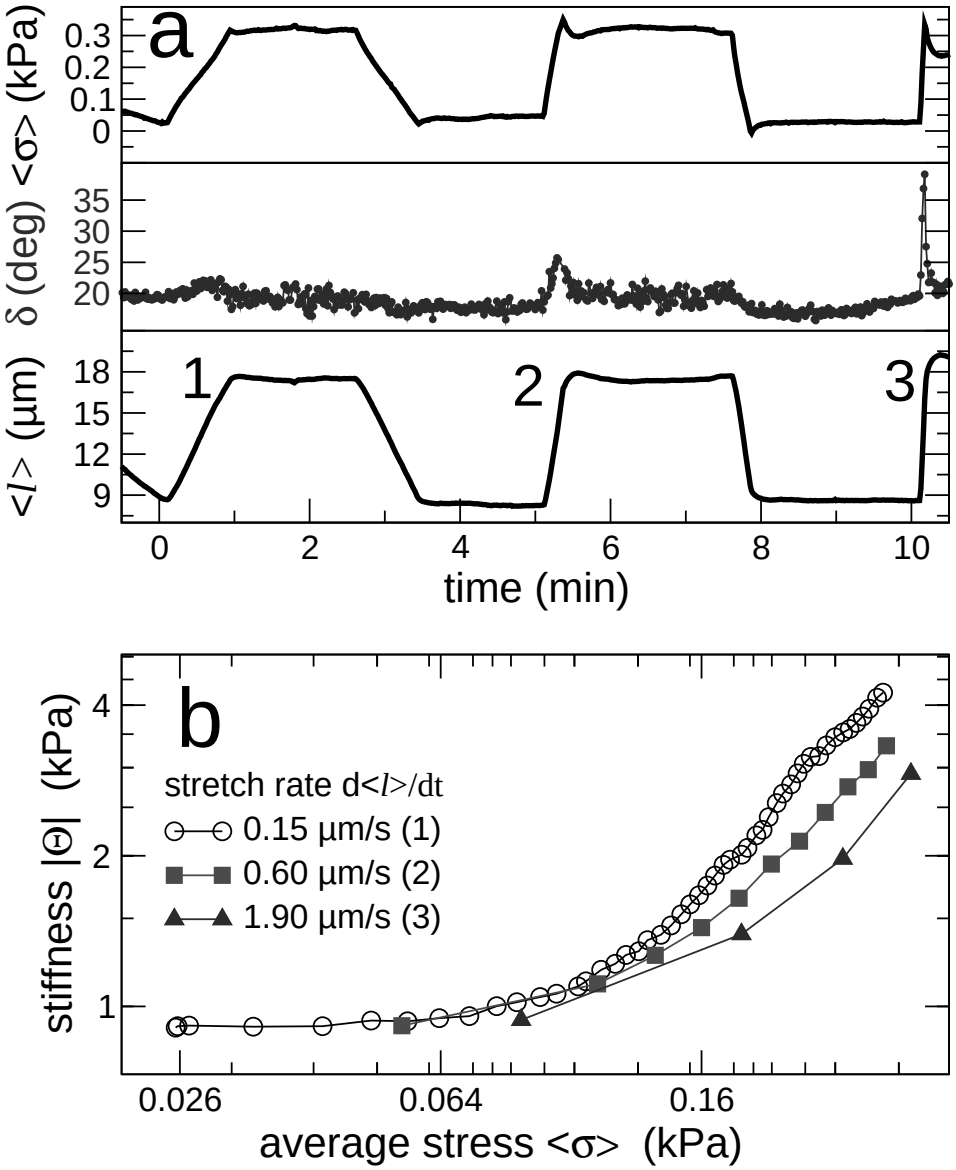

Figure 4.14: **a)** *Ramp experiment with glutaraldehyde coating. Average stress* **(top)**, *loss angle* **(middle)** *and average length* **(bottom)** *as a function of time. Oscillations at 1 Hz, 5% amplitude are superposed throughout, also during the ramps. The phase difference δ increases with the deformation rate.*
b) *Stiffness as a function of average stress. The relationship between $|\Theta|$ and $\langle\sigma\rangle$ depends on the deformation rate. The curves correspond to the ramps upwards 1, 2, 3 in Fig. 4.14* **a**.

4.6.2 Non-integrability

In general, the master-relation between the dynamic moduli and the force cannot be deduced from the force–length relation obtained in a ramp experiment without superimposed oscillations. The former shows stiffening; the latter is linear. We now regard this somewhat paradoxical issue in more detail. From the results of a ramp experiment with superimposed oscillations we calculate the relative tangential stiffness $\Psi\,\langle\ell\rangle = \partial\langle F\rangle/\partial\ln\langle\ell\rangle$, and compare it to the dynamic modulus $|\Theta|$.

We briefly motivate the comparison. Picture a cell at rest, with length ℓ_0 and force F_0. A ramp experiment with superimposed oscillations begins: $\ell(t) = \ell_0 + \dot{\langle\ell\rangle}\,t + \Delta_\ell \sin(\omega t)$. As long as the relative change in the average length is below the critical value, $\langle\ell\rangle/\ell_0 - 1 < 10\%$, the time evolution of $\langle\ell\rangle$ is indistinguishable from that of a small amplitude oscillation. Neglecting rate dependences, the response is given by $\langle F\rangle - F_0 = |\Theta|\,(\,\langle\ell\rangle/\ell_0 - 1\,)$. Thus, $\Psi = |\Theta|/\ell_0$, so that the two stiffness measures are equal at the beginning of the deformation: $\hat{\Psi} = |\Theta|$. As the deformation increases, $\langle\ell\rangle/\ell_0 - 1 > 10\%$, we leave the small amplitude oscillation scenario and the two stiffness may decouple. Indeed, as Fig.4.15 shows, the two stiffness measures are different at large deformations. The modulus $|\Theta|$ is seen to be a well-defined function of the average force, regardless of whether $\langle F\rangle$ increases or decreases. The relative tangential stiffness $\partial\langle F\rangle/\partial\ln\langle\ell\rangle$ instead shows a clear dependence on the deformation sense, falling down at the beginning of the ramp and eventually reaching a roughly constant value. Particularly revealing is the ramps upwards, where as the tangential stiffness becomes constant, the modulus $|\Theta|$ *simultaneously* increases according to the master-relation.

These experiments are very informative as the two stiffness measures are probed simultaneously, an advantageous feature in such highly adaptive-evolving-aging systems as living cells. However, this necessarily entails a separation of timescales. The rate of change of the average magnitudes $\langle\ell\rangle$, $\langle F\rangle$ is always lower than the deformation rates of the superimposed oscillations. One may wonder whether this can be neglected. In particular, if the crossover stress σ_C was much larger at low deformation rates, that would explain the absence of tangential stiffening. Taking all our results together, however, this can be ruled out. Absence of tangential stiffening can be seen in pure ramp experiments at all deformation rates in the range 0.05 – 5 μm/s. The master-relation holds for frequencies in the range 0.1 – 1 Hz and amplitudes 0.1–1 μm, which corresponds to deformation rates $\omega\Delta_\ell \sim$ 0.06 – 6 μm/s. The relevant parameter is thus seen to be the extent of deformation.

As discussed in chapter 2, this "non-integrability" phenomenon has been identified as a general feature of tissue mechanics a long time ago (8, 90). Whole tissues such as tendons do show a certain degree of tangential stiffening, though. Complete absence of tangential stiffening, i.e. a linear $\langle F\rangle\,(\,\langle\ell\rangle)$ relation, agrees very well with results from ramp experiments on fibroblast populated collagen gels (93).

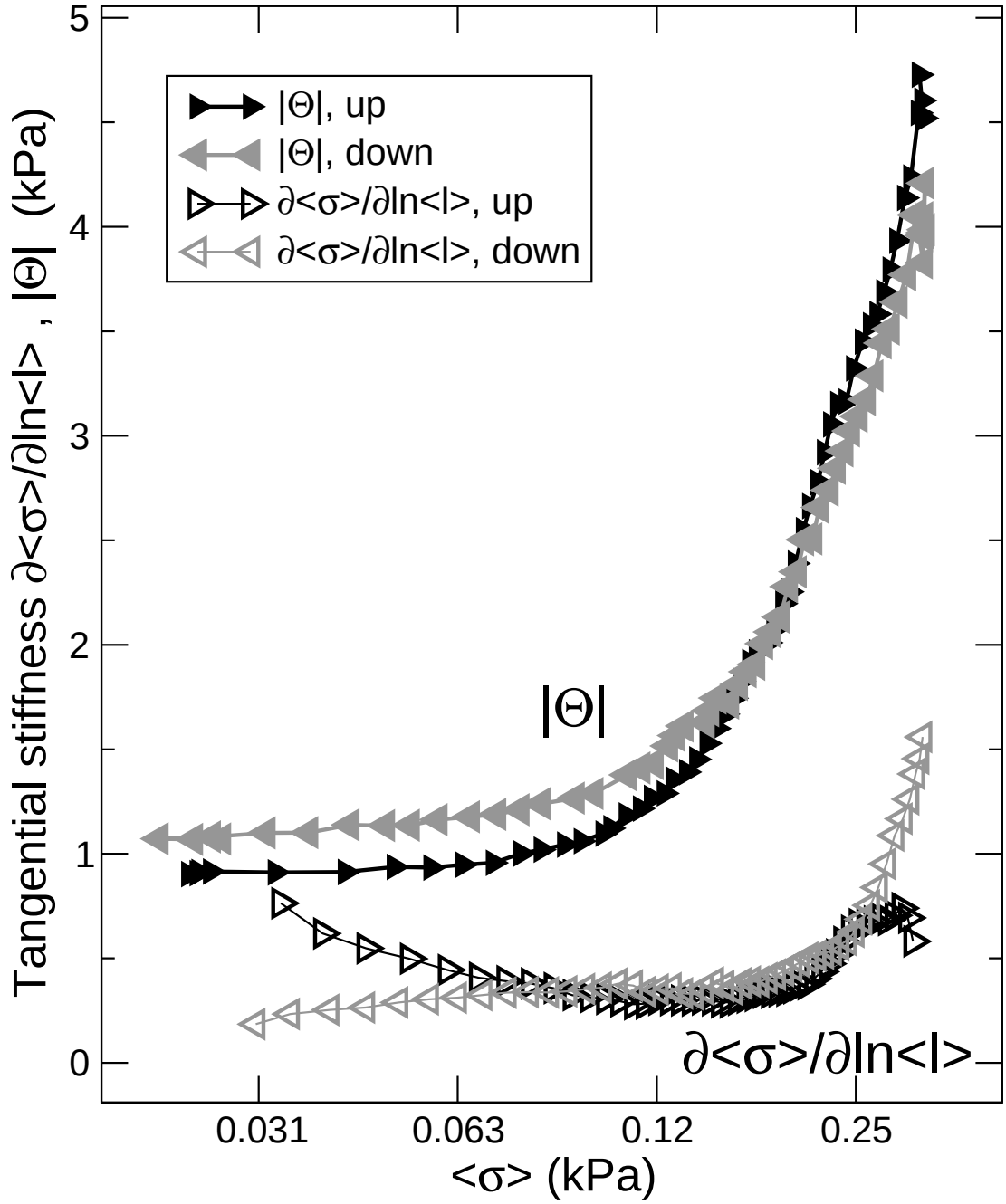

Figure 4.15: *Ramp experiment with superimposed oscillations, performed with fibronectin coatings. The average cell length $\langle \ell \rangle$ is increased linearly in time at a rate $\dot{\ell} = 0.18\,\mu$m/s. After a resting pause of a few minutes, $\langle \ell \rangle$ is lowered back to the initial value at the same absolute rate. Small amplitude oscillations are superimposed throughout, to measure the Θ-moduli.* ▶**:** *modulus $|\Theta|$, upward ramp.* ◀**:** *modulus $|\Theta|$, downward ramp.* ▷**:** *relative tangential stiffness $\partial\langle\sigma\rangle/\partial \ln\langle\ell\rangle$, upward ramp.* ◁**:** *relative tangential stiffness $\partial\langle\sigma\rangle/\partial \ln\langle\ell\rangle$, downward ramp.*

4.7 Large amplitude oscillatory experiments

As mentioned in section 4.6, the average force and length are related in a roughly linear way, in spite of the stiffening behaviour implied by the master-relation. To analyse this systematically, oscillatory experiments were performed sweeping the amplitude in the range 5%–50% were performed. Fig.4.16 shows a large amplitude oscillatory experiment. The average length $\langle \ell \rangle$ is kept constant and oscillations at a fixed frequency of 0.33 Hz are superimposed. The amplitude Δ_ℓ is stepwise increased in the range $0.3\,\mu$m – $5\,\mu$m, performing about 10 oscillations at each amplitude. Then the average length is increased at a constant rate, superimposing oscillations throughout. A second amplitude sweep is performed. The procedure is repeated several times.

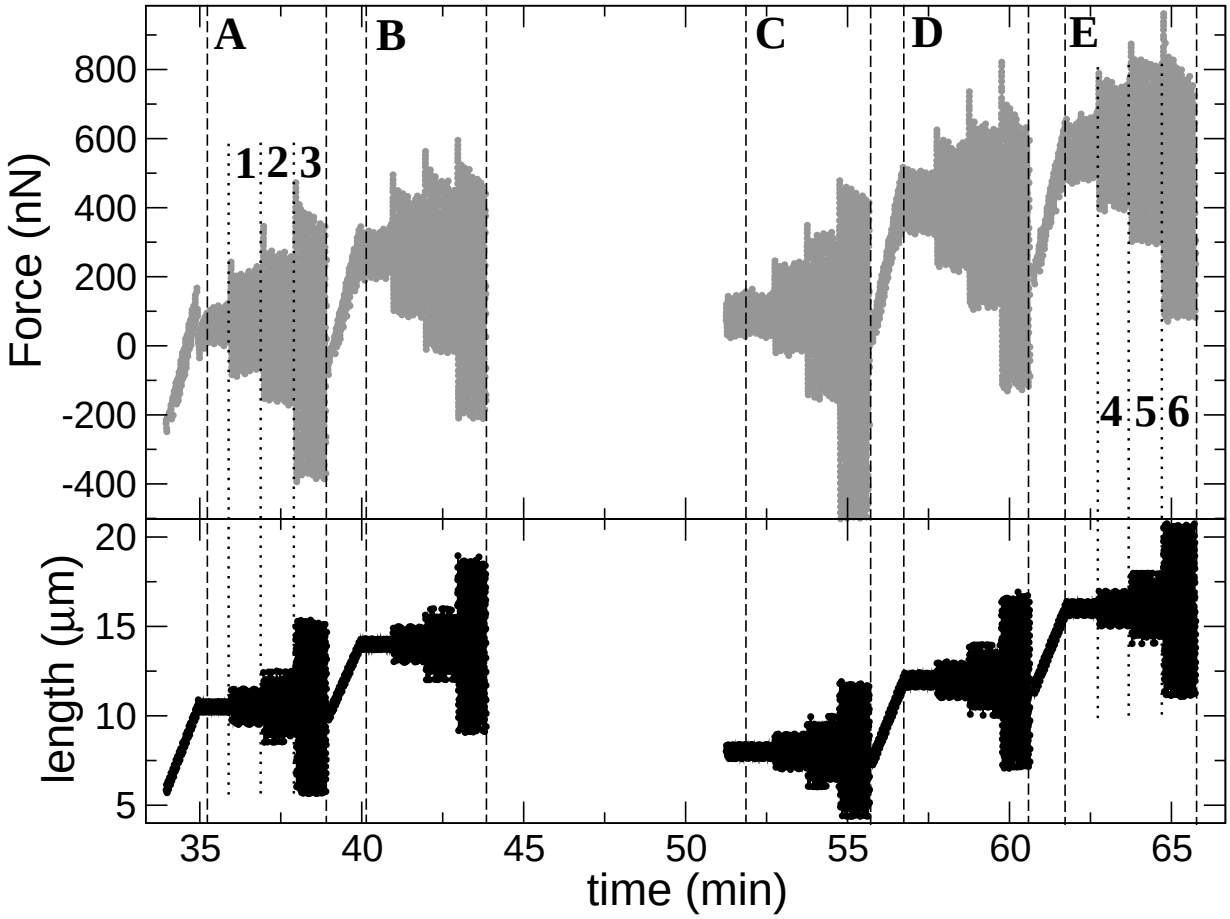

Figure 4.16: *Force F and length ℓ as a function of time. Oscillations are superimposed throughout. The amplitude is stepwise increased in the range $0.3\,\mu m$ – $5\,\mu m$, performing about 10 oscillations at each amplitude. Notice the drop in the average force $\langle F \rangle$ as the amplitude is increased.*

The force-length curves obtained in this way are shown in Fig.4.17. The following reproducible features can be observed.

1. As the amplitude Δ_ℓ is increased at a constant average length $\langle \ell \rangle$, the average force $\langle F \rangle$ falls down.

2. As the amplitude Δ_ℓ is increased at a constant average length $\langle \ell \rangle$, the force-length relation tilts down, i.e. the overall stiffness falls down.

3. When the amplitude is increased, the first oscillation at the new amplitude is markedly different from the subsequent ones, whereas the 2nd oscillation is already very close to the 10th.

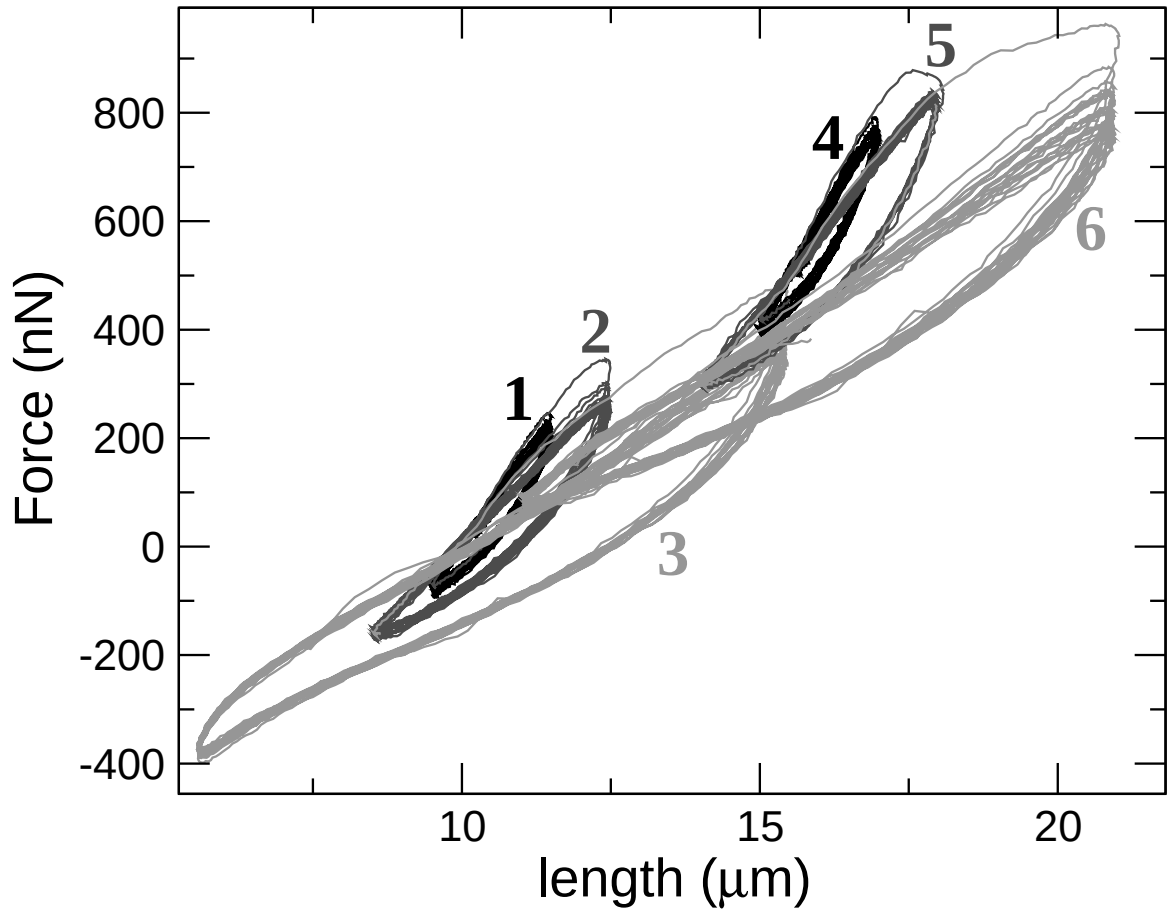

Figure 4.17: *Force as a function of length using the data marked* **1, 2, 3, 4, 5, 6** *in Fig.4.16. Notice how the average force* $\langle F \rangle$ *as well as the overall slope decrease as the amplitude is increased in* **1,2,3**. *This effect is clearly reversible, as shown by the high slope in* **4**. *This "softening" is seen again in* **4,5,6**.

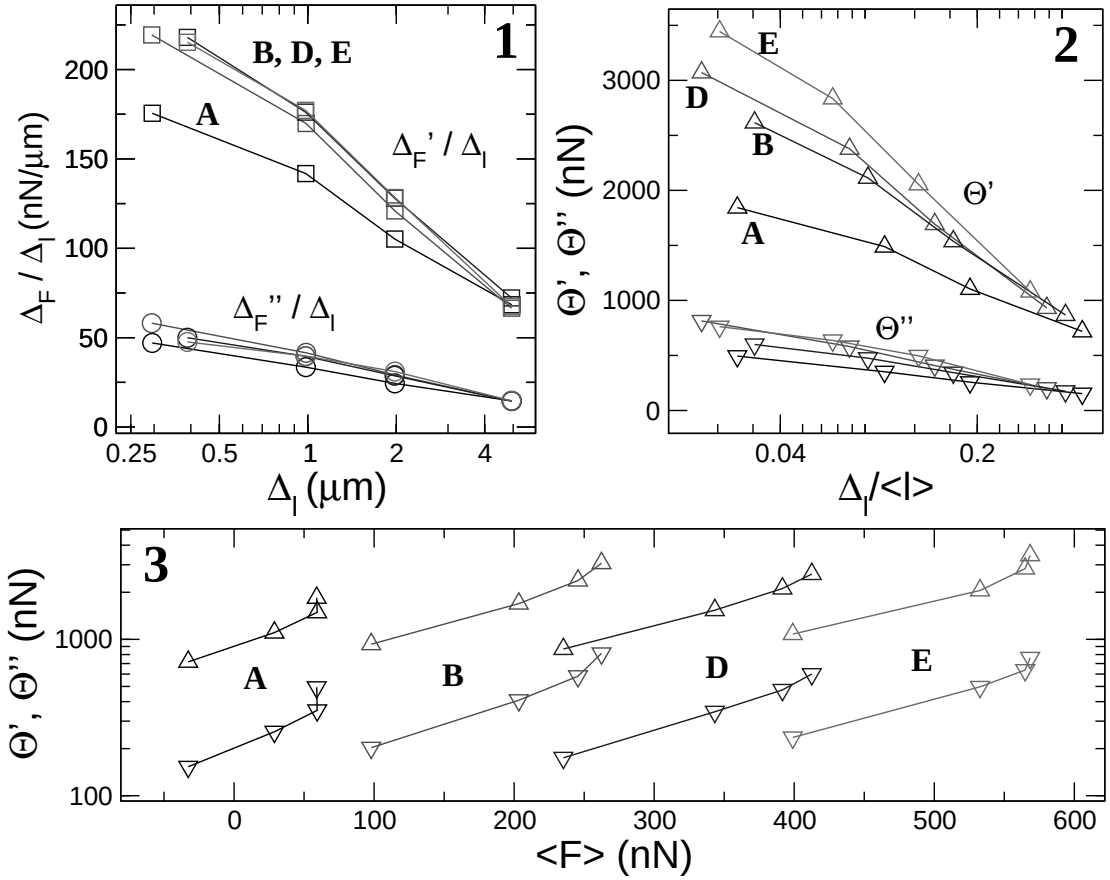

Figure 4.18: **1:** *Storage stiffness Δ'_F/Δ_ℓ (squares) and loss stiffness Δ''_F/Δ_ℓ (circles) as a function of the absolute deformation amplitude Δ_ℓ, for the amplitude sweeps* **A,B,D,E** *in Fig.4.16.* **2:** *Loss modulus $\Theta' = \Delta'_F \langle\ell\rangle/\Delta_\ell$ (up triangles) and storage modulus $\Theta'' = \Delta''_F \langle\ell\rangle/\Delta_\ell$ (down triangles) as a function of the relative deformation amplitude $\Delta_\ell/\langle\ell\rangle$, for the amplitude sweeps* **A,B,D,E** *in Fig.4.16.* **3:** *Moduli Θ' and Θ'' as a function of the average force $\langle F\rangle$.*

In order to characterise the response curves in the nonlinear behaviour, the spectrum of the $F(t)$ curves is calculated. The contribution of the imposed frequency is then taken, which defines the in-phase and out-of-phase amplitudes Δ'_F and Δ''_F of the fundamental response mode. The procedure amounts to removing from $F(t)$ all frequencies except the one imposed to the length oscillation. We show the dependence on the deformation amplitude in Fig.4.18. Fig.4.18 (*top left*) shows the absolute stiffness Δ_F/Δ_ℓ as a function of absolute deformation Δ_ℓ, whereas Fig.4.18 (*top right*) shows the moduli $\Theta' = \Delta'_F \langle\ell\rangle/\Delta_\ell$ as a function of the relative deformation amplitude $\Delta_\ell/\langle\ell\rangle$. Though the difference is small, the data seems to be better described in terms of absolute rather than relative deformations. This agrees with the linear F–ℓ relation found in ramp experiments.

As remarked before, increasing the deformation amplitude Δ_ℓ induces a drop in the average force. This can be observed in Fig.4.18 *bottom*, where the moduli are shown as a function of $\langle F\rangle$.

4.8 Stress stiffening with glutaraldehyde coatings

In order to reduce active responses, we use glutaraldehyde-aminosilane coated walls, where accessible membrane proteins are covalently and non-specifically bound through imine-groups. Further, the serum concentration is reduced to 2%. In this way, the biochemical conditions are changed, but the experimental cell geometry remains the same. Active responses are indeed found to be weaker in these conditions. In general, these experiments are a very inefficient since serum has to be added once the cell is sticking to the plates, a procedure which often leads to cell bursting with the unavoidable loss of the experiment. However, the master-relation between $|\Theta|$ and $\langle\sigma\rangle$ can still be observed, as shown in Fig.4.19.

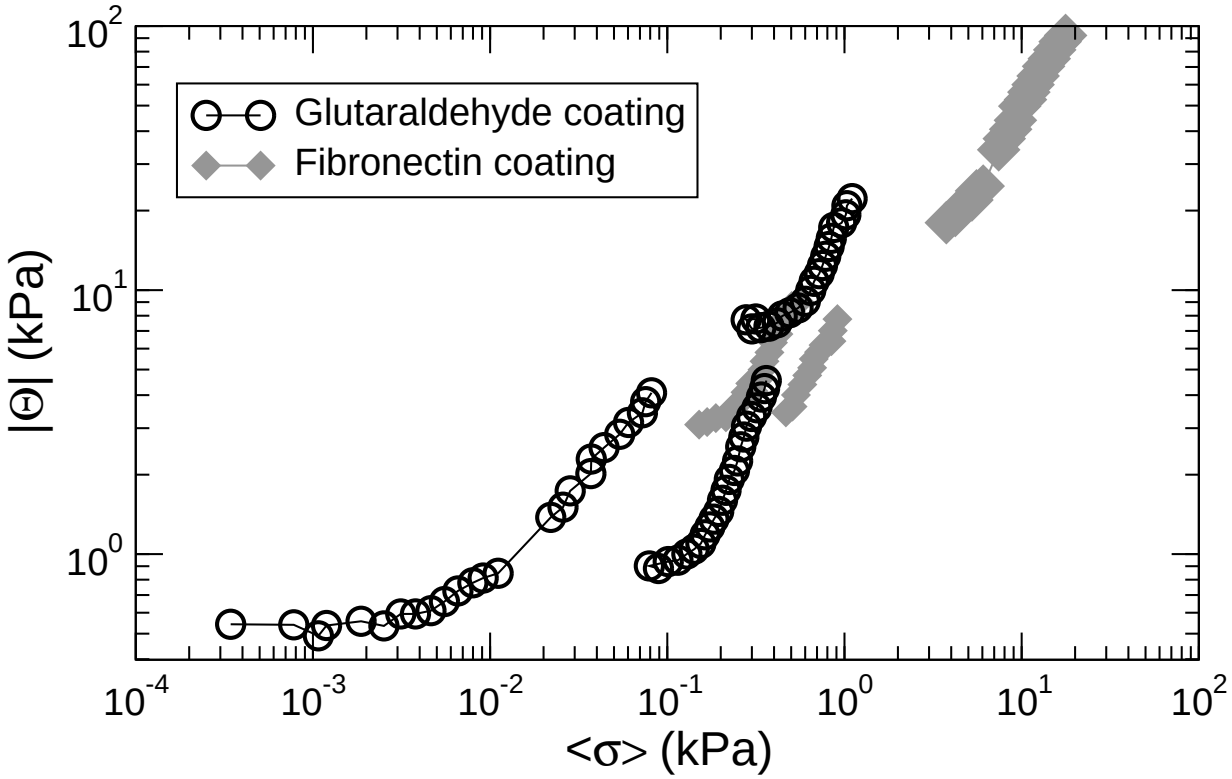

Figure 4.19: *Modulus $|\Theta|$ as a function of average stress σ, obtained via upward–ramp experiments with superimposed oscillations performed at $30°$. Each curve is a different cell. Black circles are glutaraldehyde coatings. Grey diamonds are fibronectin coatings. For technical reasons, in this set of experiments emphasis was put on the nonlinear regime; the linear regimes were not studied.*

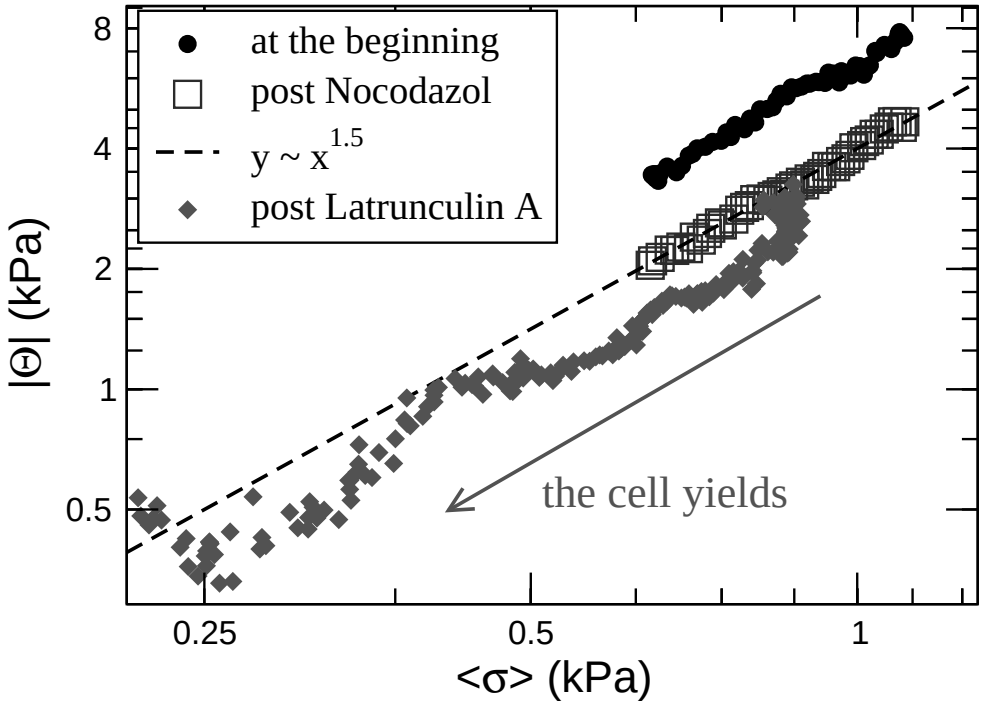

Figure 4.20: *Effects of Nocodazol (10 μg/ml) and Latrunculin-A (0.3 μg/ml) on the stress stiffening curve. Experiment performed using fibronectin coatings. Whereas nocodazol treatment does not affect the cell strongly, addition of Latrunculin-A leads to irreversible weakening and detachment.*

4.9 Drug-perturbation of the cytoskeleton

In order to distinguish between different cytoskeletal subcomponents, experiments are performed in presence of drugs, which disrupt specific filament types. Only cells able to sustain tensions above σ_C are subsequently treated with drugs.

We observe sudden detachment of the cells from glutaraldehyde-coated microplates with the actin depolymerisation inducer Latrunculin-A at 1 μg/ml (116). The same effect is seen with the myosin heavy chain ATPase inhibitor 2,3-butanedionemonoxime at 2 mg/ml (117), as well as with the myosin light chain kinase inhibitor ML-7 at 100 μM (118). Since transmembrane proteins are covalently bound to the glutaraldehyde coating, they must rip off from the membrane during drug-induced cell detachment. Thus, the cell membrane alone is not able to hold transmembrane proteins under significant tension. An internal structure must bear the load under normal conditions. After disruption of either actin or myosin activity, this structure cannot sustain strong forces anymore. At 4-fold lower concentrations, Latrunculin-A and ML-7 reduce $|\Theta|$ up to a factor of 5, while $\langle\sigma\rangle$ goes to zero. No significant effect is seen with the microtubule-disrupting drug Nocodazol (119) at 10 μg/ml, as shown in Fig.4.20. Taken together, these results show that the actomyosin system bears the tension, without any other significant force-bearing structure in parallel.

At its standard concentration 100 μM, ML7 has no effect on fibroblast adhering to fibronectin coated plates. Neither detachment nor significant weakening is observed. This can be confirmed by treating cells spreading on substrates. Cells spreading on normal, non-coated glass or plastic substrates round up in a few minutes as an effect of ML7 treatment, leaving thin extensions behind. When spreading on fibronectin coated substrates, however, no significant change in geometry can be observed.

Lysophosphatidic acid can scale the master-relation

Fig.4.21 shows a dramatic example of the effects of the contractility-inducer Lysophosphatidic acid (LPA). Addition of LPA at a concentration of $0.5\,\mu$M triggers an increase in stiffness and average force of about two orders of magnitude. The master-relation connecting $|\Theta|$ and $\langle F \rangle$ holds throughout. A slight drop in the loss angle is observed.

Such an experiment pushes the setup to its limits. In general, one is limited to probes with a rigidity similar to that of the microplates. Since the microplate stiffness cannot be changed during the experiment, orders of magnitude variations in the mechanical properties of the cell are undesirable.

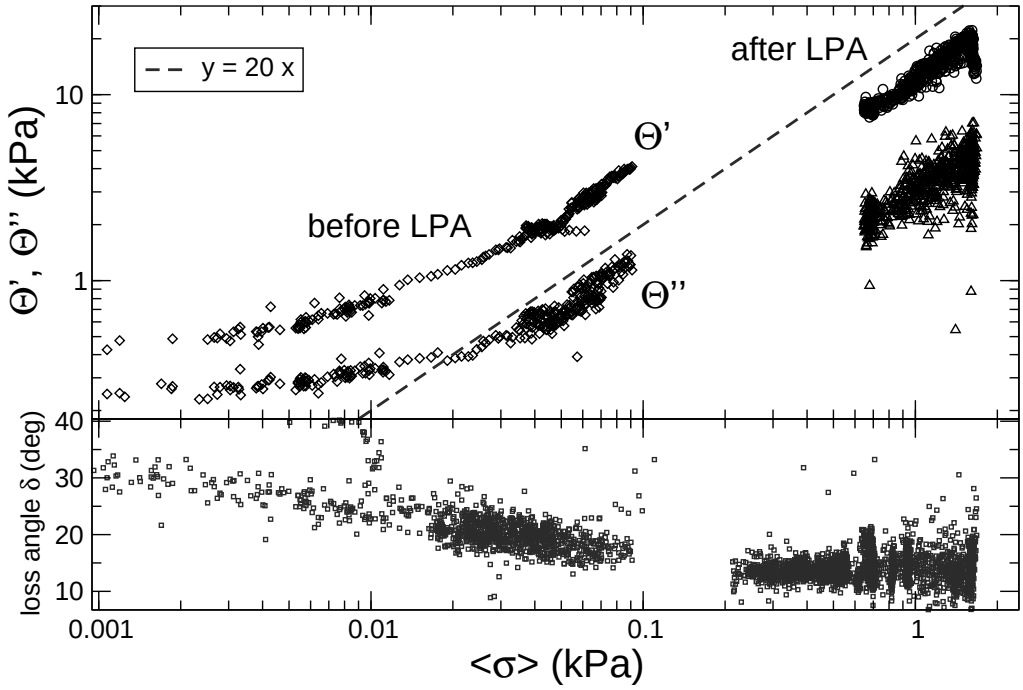

Figure 4.21: *Ramp experiment with superimposed oscillations performed with glutaraldehyde coatings, at a temperature* $30°C$*. The data* **on the left**, *in the low force and stiffness region, is the initial measurement of the master-relation. Then, the contractility inducer LPA is introduced at a concentration of* $0.5\,\mu M$*. After 30 minutes the experiment is repeated (***on the right***). A dramatic increase both on force and stiffness can be seen. For comparison, the dotted line corresponds to* $y = 20x$.

4.10 Strain-steps : force regulation

We now show that fibroblasts behave as elastic *solids*. We step-stretch the cell from a length ℓ_1 to ℓ_2 at a moderate rate $\dot{\ell}_A = 0.3\,\mu m$/s, and then keep ℓ constant in time, for ~ 10 min. We purposely keep the longest times of this order, to avoid slow erratic changes as those in Fig.4.2. The length ℓ is then taken back to the previous value ℓ_1 at a rate $-\dot{\ell}_A$, and held for ~ 10 min. Again the cell is stretched, but now at a much faster deformation rate $\dot{\ell}_B = 20\,\mu m$/s; we wait and come back at the rate $-\dot{\ell}_B$. The whole procedure is repeated several times. Fig.4.22 shows such an experiment.

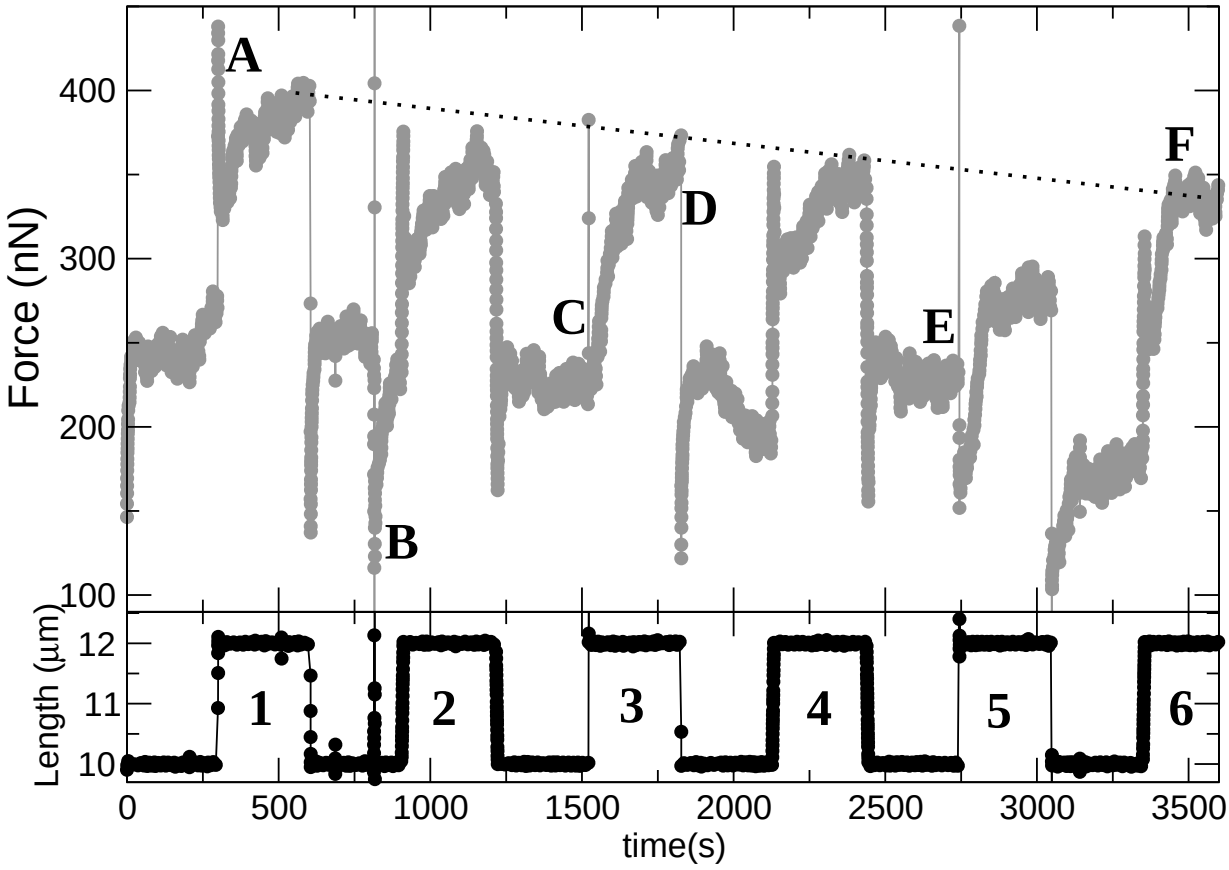

Figure 4.22: *Step-stretch experiment. Force F and cell length ℓ as a function of time. The length is cyclically changed between 10 and $12\,\mu m$.* **Steps 1,3,5:** *deformation rate $|\dot{\ell}| = 0.34\,\mu m/s$.* **Steps 2,4,6:** *deformation rate $|\dot{\ell}| \simeq 20\,\mu m/s$. Notice that during the fast upward steps* **3,5** *the force does not increase.*

1. During a slow ramp, the cell behaves in the linear fashion previously discussed. Once the deformation is over and the length imposed constant, force relaxation follows. The steps upwards trigger active behaviour: shortly afterwards, isometric force increase can be seen. The shapes of these active curves are significantly more irregular than those of the relaxations. About a few minutes after the step perturbation, the force F reaches a roughly steady value.

2. A remarkable phenomenon is sometimes observed during fast steps upwards. Fig.4.22 **C** shows it clearly. Just before the step, the force has reached a steady state. The cell is then suddenly stretched by 2 micrometers at $20\ \mu$m/s. The length ℓ increases, but not the force F – it stays at its previous value. Only later it rises at a slow rate. We stress that the force has a non-zero value throughout the jump. Notice that this does not happen at **D**, where the length is *reduced* at a similar fast rate.

3. Remarkable is also the "steady" value that the force finally reaches after slippage, in **D** : it is roughly the value corresponding to ℓ_2 in the previous steps.

4. In **B**, without any noticeable change in the cell, the force F suddenly drops, to rise again later at a slow rate. Such events are only rarely observed. They are always a sudden *lowering* of the force. Notice how afterwards F approaches its value previous to the drop.

5. In **E** we see a slipping event similar to the one in **C**, but this time F goes down significantly. Afterwards we see again isometric pulling, though the force does not reach the value attained previously at the length ℓ_2. Only after the fast step down and a subsequent slow step up, at **F**, does the force F come again close to the value indicated by the dotted line.

Looking at the whole experiment, a well-defined relation connecting the "asymptotic" force and length values is observed, as indicated by the line of points. On the long term the cell behaves effectively as an elastic solid, even though drastic deformations take place in between, such as those marked in **B**, **C**, **E**.

4.11 A slipping instability?

At large deformation rates of about $10\,\mu$m/s, a remarkable phenomenon is often observed: the cell can be stretched without any noticeable change in force F or in the viscoelastic moduli. After the stretch, a burst of isometric force development invariably follows, taking the force to a higher steady value. Due to low time resolution, at present it is not clear what happens while the fast stretch takes place. However, the essential feature of the phenomenon concerns the values before and after the stretch, and thus can be captured in spite of the low resolution. It reminds of a stick-slip instability: at a given force, the cell can be in two different states– sticking, or slipping.

Fig.4.23 shows an example of the putative slipping instability. Here, the time spent at the smaller length ℓ is shorter, so that the relaxation is not over when the fast step up takes place. The first two fast steps up give a neat slippage, without significant change in force. Also the

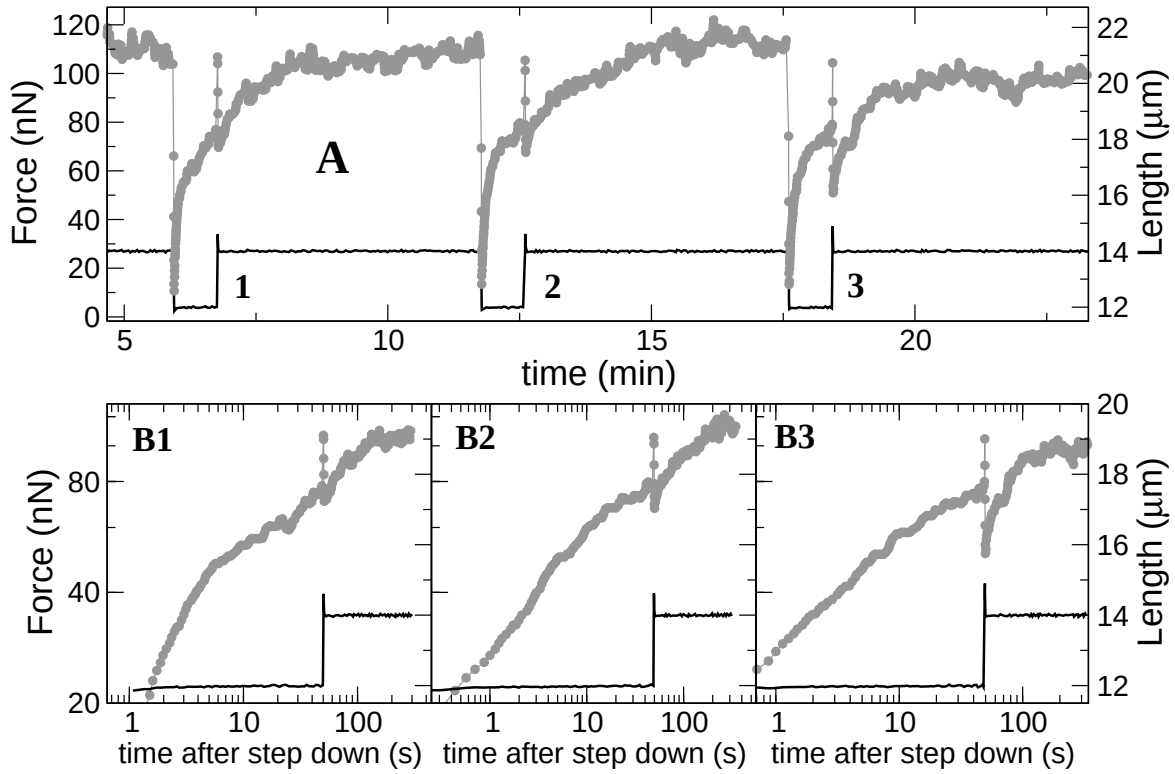

Figure 4.23: *Three examples of slipping.* **A:** *Force F and length ℓ as a function of time. The length ℓ is step-changed at a rate $6\,\mu$m/s between the values $12\,\mu$m and $14\,\mu$m. Notice how during the upward steps the force does not increase. On the contrary, during the downward steps force decrease is seen in all cases.* **B1:** *close-up of the step marked as* **1** *in* **A**. **B2:** *close-up of the step marked as* **2** *in* **A**. **B3:** *close-up of the step marked as* **3** *in* **A**. *Notice that the overall time evolution of the force does not change significantly after slipping.*

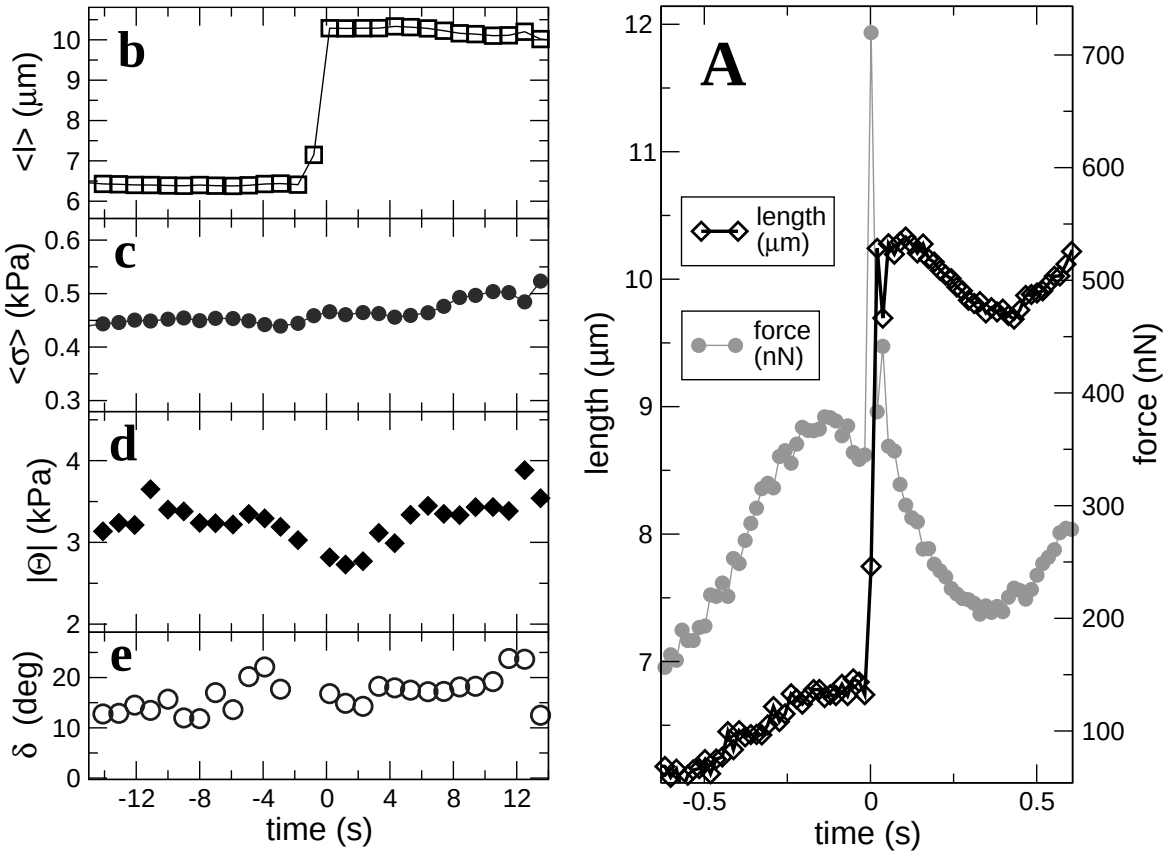

Figure 4.24: *Slippage event, revealed by a steps plus oscillations experiment performed on fibronectin coatings.* **A:** *force F and length ℓ as a function of time. At time 0, the length is increased at a rate $100\ \mu$m/s and then kept constant. Oscillations are superimposed throughout. Notice that the force rises and falls back very close to its previous value, and resumes the oscillation.* **b:** *average length $\langle\ell\rangle$,* **c:** *average stress $\langle\sigma\rangle$,* **d:** *modulus $|\Theta|$, and* **e:** *loss angle δ as a function of time. The time axis is centred on the step but covers a larger interval than in* **A**. *Notice that the only variable which noticeably changes after the step is the average length.*

rate of change of force does not change much during the steps. In the third step, the degree of slipping is higher; the force goes down noticeably.

That the fast step disrupts the cytoskeleton is unlikely – if so, why should the force after the step be so close to its previous value? The experiment in Fig.4.24 shows more direct evidence against disruption. Here oscillations are superimposed before and after the step. Within the 1 s time resolution given by the oscillation periode there is no significant change in the response parameters $|\Theta|$, δ.

Finally, it should be remarked that *slipping has been observed only while stretching*, i.e. always when increasing ℓ, never when decreasing ℓ. This asymmetry mirrors the dependence of the tangential stiffness Ψ^+ on the deformation rate, as previously described in section 4.5: only during a fast *upward* ramp does the tangential stiffness go down.

4.12 Summarising

This cartoon intends to give a crude summary of our results. It shows how a cell at rest with length ℓ_0 will respond to a length perturbation $\delta\ell$. The column on the left corresponds to the master-relation, which holds as long as the relative deformation $\delta\ell/\ell_0$ stays below $\sim 10\%$. The force response is then given by $\delta F = |\Theta|\,\delta\ell/\ell_0$. The middle column gives the behaviour when the deformation progresses beyond the $\sim 10\%$ limit. This is the plastic region where the tangential stiffness $\Psi = \partial F/\partial\ell$ is essentially constant, independent of the extent of deformation:$\Psi = \Psi_0$. At high positive deformation rates beyond ~ 200 nm/s, Ψ^+ drops, sometimes reaching zero. At very high rates this may become a slippage event. Both effects are absent when going down, $-\Psi^- \simeq \Psi_0$. Finally, the column on the right corresponds to ramp experiments with superimposed small amplitude oscillations. As the superimposed oscillations do not affect the relation between the average values, the latter is linear, i.e. the tangential stiffness is constant, $\partial\langle F\rangle/\partial\langle\ell\rangle = \Psi_0$. Simultaneously, the master-relation holds for the superimposed oscillations as long as $\langle\ell\rangle$ does not change too fast. At absolute deformation rates $|\dot{\ell}| > 200$ nm/s, the master-relation breaks down, which shows up in the loss angle δ increasing.

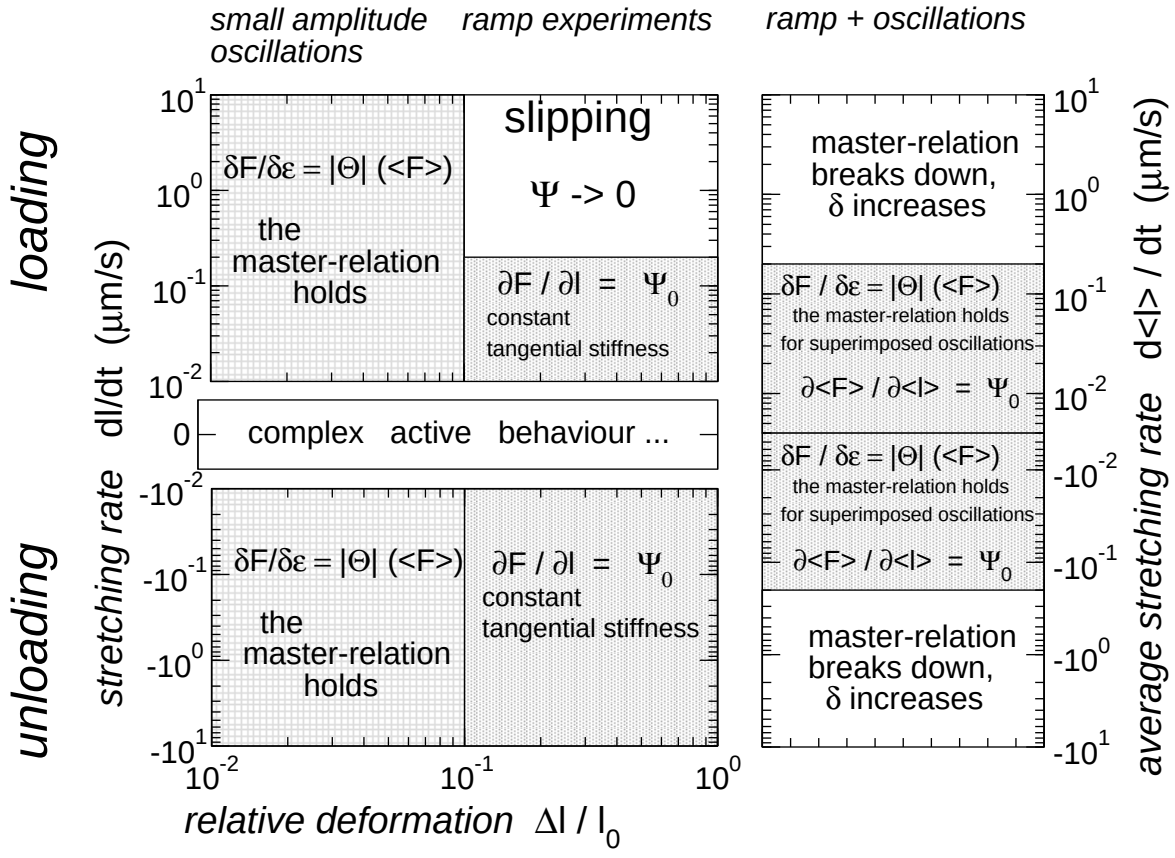

Figure 4.25: *A crude summary of our results. All numerical values should be taken as order of magnitude estimations.*

4.13 Discussion

4.13.1 Stress stiffening

The master-relation is a reproducible feature in our experiments. It holds during active contraction and adaptive responses, such as those seen in Figs. 4.2, 4.6 and 4.7, as well as in ramp experiments with superimposed oscillations, as in Fig. 4.14 *b*. It is observed in different biochemical environments, which change the intensity of active responses. From this generality of the master-relation, we conclude that it reflects a fundamental property of the cell force-bearing elements (35).

Stress stiffening in actin networks

Our cytoskeleton perturbation experiments point towards the actin network as the main component responsible for stress stiffening. Actin filaments, with a persistence length of 15 μm (9, 120), behave as semiflexible filaments in vivo, where typical filament lengths are about 1 μm. As discussed in chapter 2, crosslinked networks of semiflexible filaments show characteristic nonlinear mechanical behaviour. In vitro prestressed biopolymer gels under shear deformation, including crosslinked actin networks, generally show a transition from a linear regime to power-law strain stiffening (26, 27, 29–31, 121). Certainly, the connection to our results has to be established with care; *in vitro* gels are passive minimal systems, moreover studied under shear deformations. Instead, the living cell is a complex entity where a multitude of crosslinking proteins is available, many of them of dynamic nature. Cytoskeletal restructuring might take place within an oscillation period. Bearing this in mind, the similarity between the stiffness-force relations is very suggestive. In scruin-crosslinked actin networks (30) (shown in Fig.2.6), the ratio between the crossover stress and the zero force modulus is of the order of 10^{-1}, and the stress-stiffening exponent is in the range 1–1.5, in remarkable agreement with our results. In experiments on filamin-crosslinked actin gels (31), where the storage modulus G' is actually studied as a function of strain, the crossover strain is also of this order.

Stress stiffening in living systems

As mentioned in chapter 2, stress stiffening in oscillatory experiments, typically in the form of proportionality between stiffness and force, is a general feature of biomechanics. It has been observed over many decades in length scale, corroborating our interpretation of the master-relation as a general feature of the force-bearing elements in the cell. Uniaxial stretching experiments performed on skin, myosin fibres, tendons (8, 39, 90) and on fibroblast-populated collagen gels (93) show proportionality between oscillatory stiffness and force. At the subcellular scale, microrheology experiments performed on adhering cells show proportionality between the shear storage modulus G' of the actin cortex and the force applied by the cell on the substrate (100). Here, the force was increased by stimulating cell contractility with histamine, or decreased by the relaxing agonist isoproterenol. The result compares well to our observation of stress stiffening at constant length, though no crossover to a linear regime is reported here. Simultaneous increase

of both the storage and loss shear moduli G' and G'' of the actin cortex after stretching epithelial cells has been observed (101). Accordingly, we see stress stiffening of both longitudinal moduli Θ' and Θ'' when stretching the cell in a ramp experiment with superimposed oscillations. These microrheological studies taken together agree with our main result: the master-relation holds regardless of the way force-space is explored.

4.13.2 Stiffening mechanisms

Stress stiffening in muscle

Our results are also similar to stress stiffening in skeletal and smooth muscle, where stiffness is proportional to force. The generally accepted explanation for stiffening in muscle is that both stiffness and force are a function of the variable number of actomyosin crossbridges (122). Although such an explanation is attractive, it does not seem to apply to our case. We have measured forces up to $1\ \mu$N, in agreement with total forces exerted by spreading fibroblasts of $\sim 2\ \mu$N (123, 124). This corresponds to $\sim 10^6$ myosins working in parallel, very close to the total amount reported in fibroblasts (125). Taking crossbridge stiffness as 0.6 pN/nm (9), an arrangement of 10^6 myosins in parallel would be a factor of 100 stiffer than the maximum $|\Theta|$ we have measured in fibroblasts.

Stiffening in biopolymer networks

Aiming at describing crosslinked biopolymer networks, two-dimensional random networks of semiflexible filaments have been introduced as a theoretical framework (103). Temperature effects are addressed by including an effective entropic stretching modulus (126–128). The mechanical response of 2-D random networks depends strongly on the length scales involved, the filament length and diameter and the average distance between filaments. For small strains, the different regimes have been thoroughly explored (103, 126, 127, 129–131). Taking a persistence length of $\sim 10\,\mu$m and a mesh size of 100 nm, mimicking a real F-actin network, a non-affine regime dominated by filament bending is predicted (131). Extrapolating to three dimensions, the magnitude of the shear modulus is of the order of 10 kPa.

At large deformations the situation is far less well understood. Stiffening in crosslinked biopolymer networks has been explained in terms of an affine stretching-dominated regime where the macroscopic response is given by single-filament entropic stretching (30, 31). As mentioned in chapter 2, at high forces, the stiffness-force relation becomes a power-law with exponent $3/2$. However, the crucial assumption that the deformation remains affine beyond the linear regime has not been demonstrated in this work. Moreover, the speculation that the non-affine bending regime does not show stiffening (132) has been proved as utterly false by recent simulations. According to Onck et al (133), stiffening arises as a transition from bending to stretching. Thermal effects are mostly irrelevant; increasing the temperature from 0 to 300K increases the crossover strain, but does not affect the stiffening regime. Conclusions concerning thermal effects may however be wrong, since the way temperature is modelled is not entirely correct and the validity of the approximation used is not discussed.

These discrepancies show that even this simple "toy theory" displays complex behaviour which at present is not fully understood; undoubtedly, rigorous theoretical work is necessary. Here we would like to discuss the nonlinear mechanics of beams. Though overlooked by the community, they may be relevant for the problem; in fact they already reproduce many features of fibroblast stiffening.

4.13.3 The bending response of an inextensible filament

Here we address the bending mechanics of an inextensible filament, with emphasis to the nonlinear response. We model the problem as physically linear, geometrically nonlinear. That is, locally we assume the torque to be simply proportional to curvature. The nonlinearity arises for geometrical reasons, as a consequence of the high aspect ratio of the filament.

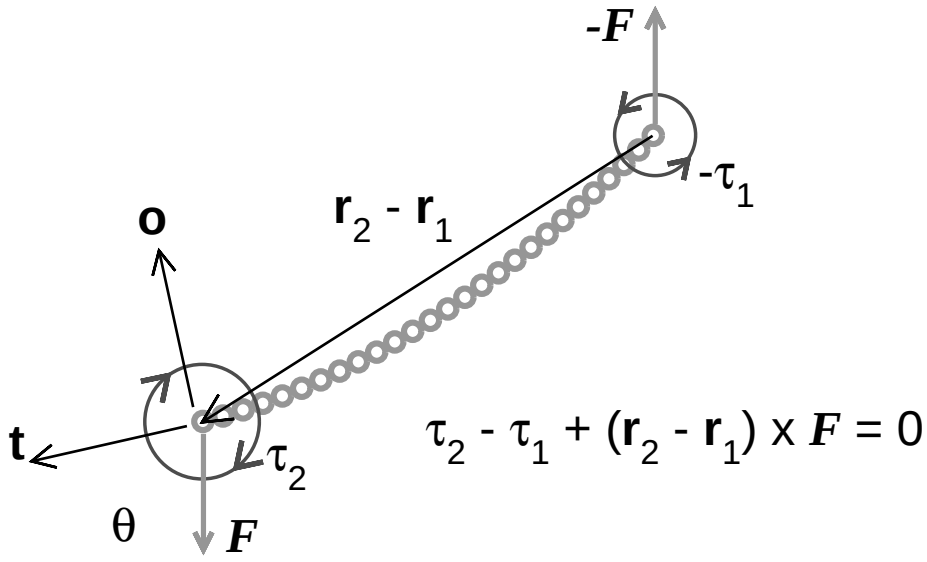

Figure 4.26: *Cartoon showing the forces and torques acting on the filament segment between* s_1, s_2. *Since it is in equilibrium, it experiences a total force* 0. *The torque balance equation is* $\boldsymbol{\tau}(\, s_2\,) - \boldsymbol{\tau}(\, s_1\,) + (\boldsymbol{r}_2 - \boldsymbol{r}_1) \times \boldsymbol{F} = 0$,

We describe the stress field $\boldsymbol{\sigma}$ inside the filament by two vectorial functions of the arclength, $\boldsymbol{F}(\, s\,)$, $\boldsymbol{\tau}(\, s\,)$ (6). $\boldsymbol{F}(s)$ gives the force and $\boldsymbol{\tau}(s)$ the torque exerted on the segment (0,s) by the segment (s, L). We are interested in mechanical equilibrium in absence of body forces. Consider a small filament segment with ends s_1, s_2, as shown in Fig.4.26. It is in equilibrium; thus, the total force acting on it, $\boldsymbol{F}(\, s_2\,) - \boldsymbol{F}(\, s_1\,)$, must be zero. Therefore $\boldsymbol{F}$ is a constant, independent of the arclength s. Now we consider the torque balance. The segment between the point $\boldsymbol{r}_1$ at $s = s_1$ and the point $\boldsymbol{r}_2$ at $s = s_2$ experiences a total torque (equal to zero in equilibrium)

$$\boldsymbol{\tau}(\, s_2\,) - \boldsymbol{\tau}(\, s_1\,) + (\boldsymbol{r}_2 - \boldsymbol{r}_1) \times \boldsymbol{F} = 0 \ ,$$

where we already introduce the constant value for $\boldsymbol{F}$. As $s_1 \to s_2$, the vector connecting the ends of the segment becomes $\boldsymbol{r}_2 - \boldsymbol{r}_1 \to (s_2 - s_1)\, d\boldsymbol{r}/ds$. By definition of arclength, the tangent vector $\boldsymbol{t} := d\boldsymbol{r}/ds$ is already normalised, $|\boldsymbol{t}| = 1$. The local torque balance equation becomes

$$\frac{d\boldsymbol{\tau}}{ds} + \boldsymbol{t} \times \boldsymbol{F} = 0 \; .$$

We now need a constitutive equation relating the torque to the deformation field. The simplest approach is given by the Bernoulli expression: torque is proportional to curvature,

$$\boldsymbol{\tau} = \kappa\, \boldsymbol{t} \times \frac{d\boldsymbol{t}}{ds} \; ,$$

where the bending modulus is given by the crosssectional moment of inertia and the Young's modulus, $\kappa = EI$. This equation can be replaced in the previous one. Since $d\boldsymbol{t}/ds \times d\boldsymbol{t}/ds = 0$, we get

$$\boldsymbol{t} \times \left(\kappa\, \frac{d^2\boldsymbol{t}}{ds^2} + \boldsymbol{F} \right) = 0 \; . \tag{4.1}$$

Since $\boldsymbol{t}$ is a vector with a fixed length, one may identify it with the position of a mass hanging from an inextensible string. We can further regard s as a time, and the constant vector $\boldsymbol{F}$ as a gravitational force. Then, the equation becomes Newton's law for a pendulum projected in the direction perpendicular to the string, where the only force acting on the mass is gravity.

Now we consider the problem constrained in the plane. As the force $\boldsymbol{F}$ fixes a direction in space, it is natural to take it as a reference for the tangent angle θ, given by

$$\boldsymbol{F} \cdot \boldsymbol{t} = F \cos(\theta) \; ,$$

where $F = |\boldsymbol{F}|$ is the magnitude of the external force. The equilibrium equation 4.1 for the problem in the plane can then be written as

$$\frac{d^2\theta}{ds^2} = -\frac{F}{\kappa}\, \sin\theta(s) \; . \tag{4.2}$$

Finally we introduce a length scale $\Lambda(\, F\,) = \sqrt{\kappa/F}$. In terms of the dimensionless arclength s/Λ equation 4.2 becomes $\ddot{\theta} = -\sin\theta$. The curves described in space by Euler-Bernoulli filaments in absence of body forces are called *elastica*. Setting "initial conditions" $\left[\theta_0,\, \dot{\theta}_0\right]$ at an "initial point" $s = 0$ defines a unique solution

$$\theta\left(\frac{s}{\Lambda(\, F\,)};\, \theta_0,\, \dot{\theta}_0\right)$$

for the *elastica* shape. Here we have explicitely indicated the dependence on the "initial conditions". However, for our purposes the problem is rather one of fulfilling boundary conditions. This arises naturally in the situations to be modelled, where the filament length is assumed constant and the conditions at a given filament end are only partially prescribed. For example, in

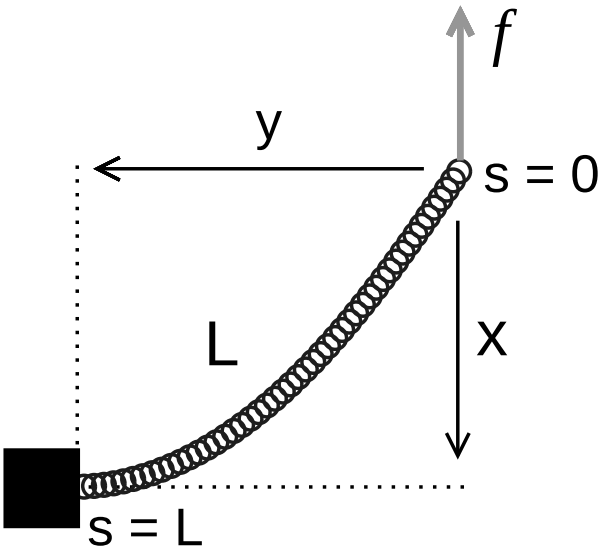

Figure 4.27: *Cartoon showing the boundary conditions used for the calculation of the force-extension relation* $F(\,x/L\,)$.

a network of rigidly crosslinked filaments, all angles θ_0, θ_L, and lengths L are prescribed; the curvatures at the filament ends have to be solved for in order to find the macroscopic deformation.

The boundary conditions used for the calculation are illustrated in Fig. 4.27. One end ($s = 0$) is joined to a free hinge, which implies zero curvature, $\dot{\theta}_0 = 0$, and leaves the angle θ_0 free to take any value. The other end ($s = L$) is clamped perpendicular to the force, which fixes $\theta_{s=L} = \pi/2$ but does not put any restriction on the curvature $\dot{\theta}_{s=L}$. Fix now the force F and complete the "initial conditions" by arbitrarily choosing an angle θ_0. This univocally defines the angle at the clamped end $\theta_{s=L}$. To fulfil the clamped-end condition,

$$\theta\left(\frac{L}{\Lambda(\,F\,)};\,\theta_0,\,0\right) = \frac{\pi}{2}$$

must hold. This equation must be solved for the function $\theta_0(\,F\,)$. Then, for any F one can calculate the filament shape taking as initial conditions $\big[\theta_0(\,F\,),\,0\big]$; finding the filament deflection is straightforward and the problem is solved.

We now write down the explicit solution to the problem. Taking as origin an inflexion point, i.e. $\dot{\theta}_0 = 0$, the solution to eq.4.2 can be shown (6) to be given by

$$\sin(\theta/2) = k\,\mathrm{sn}\big[\,s/\Lambda + \mathcal{K}\,;\,k\,\big], \tag{4.3}$$

where sn is the Jacobi elliptic sine function. This is a periodic function, sort of a "stretched sinusoidal", with a period $4\,\mathcal{K}$. The parameter k can be seen as controlling how distorted the elliptic functions are. When $k = 0$, sn becomes simply the $\sin$ function; in the limit $k \to 1$, the period diverges, $\mathcal{K} \to \infty$. Since $\mathrm{sn}\big[\mathcal{K}\,;\,k\big] = 1$, from eqn.4.3 we have

$$k = \sin(\theta_0\,/2)\,.$$

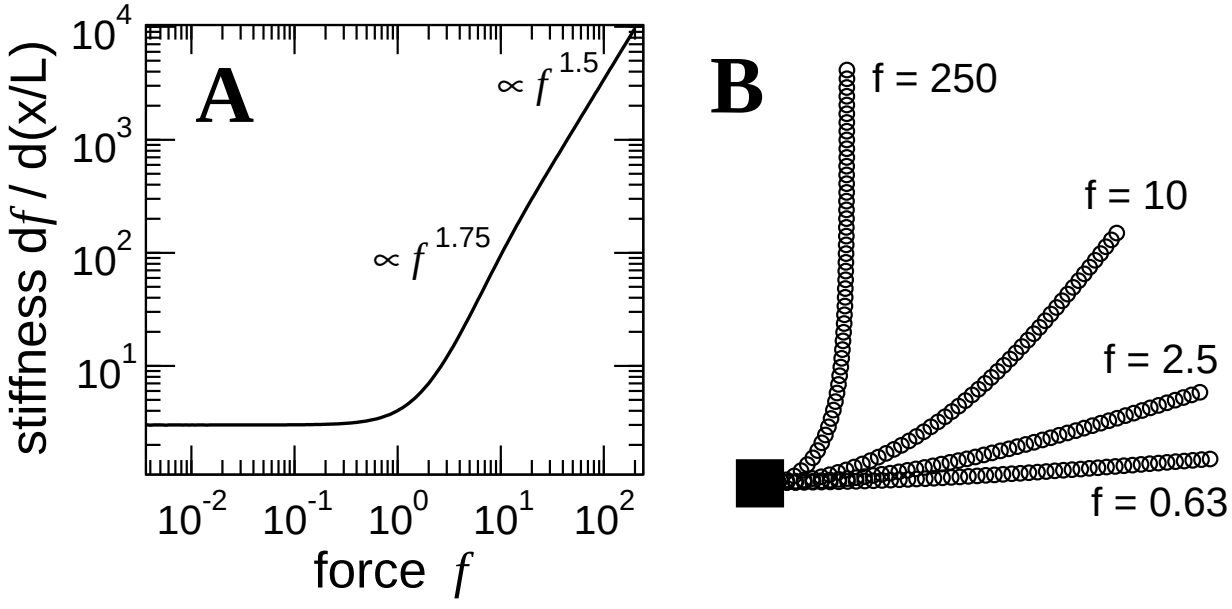

Figure 4.28: *Stiffness-force relation for a beam held as shown in Fig.4.27.* **A:** *dimensionless stiffness* $df/d(x/L)$ *as a function of dimensionless force* f. **B:** *filament shapes for different forces.*

Thus the initial conditions enter through the parameter k. For our purposes we need to describe the *elastica* curve in cartesian coordinates. Introducing coordinates x, y satisfying $dx/ds = \cos(\theta)$, $dy/ds = \sin(\theta)$, the solution can be written as

$$x = -s + 2\Lambda \left(\mathcal{E}\,\mathrm{am}\big[s/\Lambda + \mathcal{K}\,;\,k\big] - \mathcal{E}\,\mathrm{am}\big[\mathcal{K}\,;\,k\big] \right) \tag{4.4}$$

$$y = -2\Lambda\, k\,\mathrm{cn}\big[s/\Lambda + \mathcal{K}\,;\,k\big] \tag{4.5}$$

where $\mathcal{E}$ is the elliptic function of the second kind and am the Jacobi amplitude function (134, 135). Writing down the *elastica* solution explicitely, we get for the clamped-end condition

$$\sin(\frac{\pi}{4}) = \frac{1}{\sqrt{2}} = k\,\mathrm{sn}\big[\,L/\Lambda + \mathcal{K}\,;\;k\,\big]\,.$$

The function $\theta_0(\,F\,)$ appears as a relation between k and the parameter L/Λ. If we take κ/L^2 as force unit and define a dimensionless force $f := FL^2/\kappa$, we can write $L/\Lambda = \sqrt{f}$. The deformation along the force direction is given by

$$x_{s=L} = -L + 2\Lambda \left(\mathcal{E}\,\mathrm{am}\big[\sqrt{f} + \mathcal{K}\,;\,k\big] - \mathcal{E}\,\mathrm{am}\big[\mathcal{K}\,;\,k\big] \right)\,.$$

The force-extension relation is given by $f(\,x_L\,)$. Numerically solving for $k(\sqrt{f})$ we get the results shown in Fig.4.28(A) for the relation between the stiffness df/dx and the force.

As a check of the numerical calculation, the stiffness df/dx in the limit $f \ll 1$ agrees with the analytical result $dF/dx = 3\kappa/L^3$ of the linearised problem (9). In the nonlinear regime we find a relatively sharp crossover to a strain-stiffening regime at strains $x/L > 0.3$, as shown in Fig. 4.26(A).

At large strains, the stiffness-force relation asymptotically becomes a power-law with an exponent 1.5. This regime can be intuitively understood as follows. As the force diverges, $F \to \infty$, the filament shape tends to a straight line along the force direction, with a sharp kink at the clamped end (see Fig. 4.26(B)). At large forces, the effect of increasing F is a scaling of the filament shape at the clamped end. It can be shown that

$$L - x \;\propto\; 1/\sqrt{f} \qquad \text{when } f \to \infty \,,$$

which gives power-law stiffening,

$$\frac{d\,f}{dx} \propto f^{\,3/2} \,.$$

In general, entropic contributions to the effective elasticity of semiflexible filaments must be considered. At small deformations, such thermal effects have been thoroughly studied (136). In particular, when the force is parallel to the end-to-end vector one has the well known expression $k_T = 90\kappa^2/(k_B T L^4)$ for the thermal longitudinal modulus (128). One may ask whether thermal effects affect the bending response. For a distance between crosslinks $L \sim 100$ nm, the mechanical bending energy exceeds the thermal energy at strains beyond $\sim 4\%$, well within the linear regime which extends up to 30%. Thus, thermal effects are not relevant for the bending response.

Comparison between filament and fibroblast mechanics

The experimental fact that a single parameter is sufficient to obtain the master relation is captured by both the force and stiffness scales varying as κ/L^2. The bending response of an Euler-Bernoulli beam shows a crossover to stiffening above a crossover strain $\simeq 0.25$; the magnitude of the experimental crossover stress, when expressed as a strain σ_C/Θ_0, is of the order of 10^{-1}. As Fig. 4.26(A) shows, the first force decade above crossover of the beam stiffness-force relation is an approximate power-law with exponent 1.75; the experimentally observed range for the stiffening exponent is 0.8–1.8. Finally, the magnitude of the force scale is the right one if one assumes a realistic cytoskeleton mesh size of 100 nm (9, 137, 138) and an actin bending modulus of $\kappa = 60$ nN$(\mathrm{nm})^2$ (9). In the linear regime, this corresponds to the open-cell foam geometry proposed by Satcher and Dewey as a general model for the cytoskeleton (138), which gives a zero-force stiffness $\Theta_0 \sim 10$ kPa, in good agreement with our measurements and with the literature on biomechanics (33, 39, 138).

As a final remark, at large forces the beam stiffness-force relation approaches a power-law with exponent $3/2$, equal to the entropic *stretching* response. Therefore, observation of a stiffening exponent close to $3/2$ is far from warranting an entropic mechanism.

4.13.4 Intrinsic stress stiffening

The master-relation connects the viscoelastic moduli to the average force independently of cell length. Rather than strain stiffening, fibroblasts exhibit intrinsic *stress* stiffening. To reconcile this to our interpretation of the master-relation, we postulate that the internal strain of the gel, i.e., the stress, uncouples from the cell length ℓ as a result of crosslink rearrangements.

In ramp experiments on fibroblast-populated collagen gels, approximately linear force-length relations are observed (93), which agrees well with the results of our ramp experiments. Remarkably, most tissues with the exception of muscle show exponential force-length relations (90). Since extracellular matrix itself displays an exponential force-length relation, its presence in parallel to the cellular component is a possible explanation for this discrepancy.

4.13.5 Hardening

Regardless of microscopical interpretations, if we accept that the master-relation is an *elastic* response, then we must regard large-amplitude deformations as *plastic* strains. Indeed, when going over the literature on plasticity a number of striking similarities show up between fibroblasts and metals. We argue here that the proper phenomenological framework to address cell- and cytoskeletal-mechanics has already been developed, albeit for materials about 6 orders of magnitude tougher.

Plasticity is nowadays modelled in terms of internal variables (7, 115, 139). The most fundamental one is the separation of the strain in elastic and plastic. Keeping our experiment-specific notation, we separate the (measurable) cell length ℓ in two parts, the *rest length* ℓ_0 and the elastic deformation $\ell - \ell_0$. If our interpretation of the master-relation as an elastic response is correct, the force must be a function of the relative elastic deformation, $F = \mathfrak{E}\big[\,\ell/\ell_0\,\big]$. The (unmeasurable) elastic-response function $\mathfrak{E}$ must be approximately exponential at large forces $F > F_C$, since its derivative is the stiffness, $d\mathfrak{E}/d\ell \propto \Theta' \sim \mathfrak{E}$. This exponential force-length relation cannot be measured in a ramp experiment since at deformations beyond $\sim$10% plastic flow arises. This changes the rest length ℓ_0, decoupling the total length ℓ from the elastic deformation – and thus from the force.

The problem becomes finding the plastic-flow relation $\dot{\ell_0}\big[F, \ell_0, ...\big]$ between the plastic strain and the other internal variables. This involves introducing internal variables with their respective evolution equations, until satisfactory agreement with the results is reached.

Strain (or isotropic) hardening

In the field of biopolymer networks, hardening is often used as a synonym for stiffening, meaning a positive curvature in the stress-strain relation *within the elastic response*. The terms strain- or stress-hardening are used indistinctly, since strain and stress are biunivocally related in an elastic deformation. In the field of metal plasticity, however, strain-hardening (also called work-hardening) has a different meaning: it describes the increase in yield stress –i.e., in the size of the elastic region– induced by a *plastic strain*. When an ideal strain-hardening material which has been loaded beyond the yield stress is unloaded, it deforms *elastically* to a new rest length larger

than its initial one. If the material is loaded again, the yield stress is seen to have become higher. Such *reversals* in the sense of deformation are absolutely essential to distinguish elasticity from plasticity.

Bauschinger effect

The Bauschinger effect is the decrease in yield stress upon deformation reversal. In materials showing Bauschinger effect, plastic straining in one direction increases the yield stress only in that direction. If the deformation sense is reversed, the yield stress in the new direction is lower. An example is shown in Fig.4.29. The essential point is that unloading does not affect the structure of the material, as it is an elastic process. If plastic flow has induced alterations of *directional* nature, they will remain during unloading. Thus, when reloading in the opposite direction for the first time, the material shows a low yield stress. The Bauschinger effect is intrinsically related to such asymmetric structural changes.

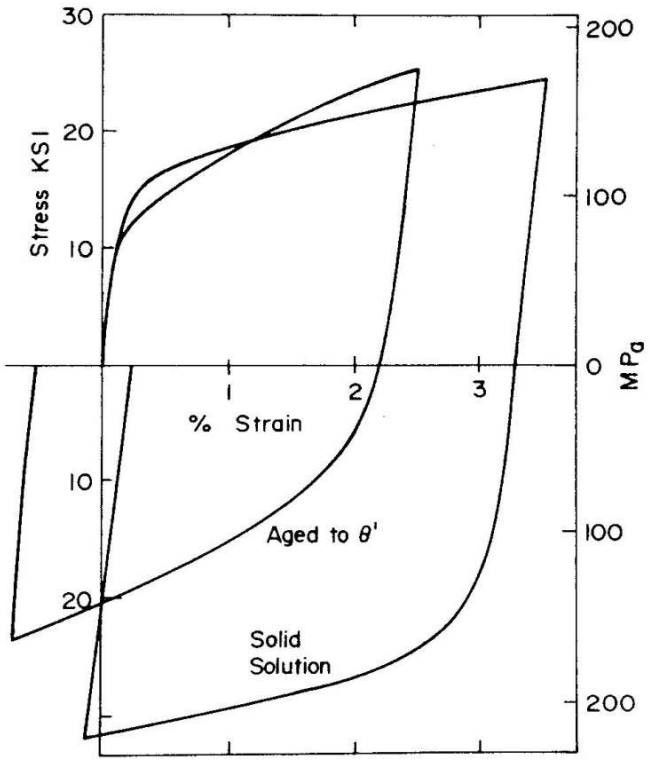

Figure 4.29: *Bauschinger effect. Stress vs. strain in an uniaxial extension experiment. Stress reversal behaviour of single-phase ("solid solution") and two-phase ("aged to θ'") Al-Cu alloy. Only the latter is a permanent Bauschinger effect, the former is a strain-hardening transient. Taken from Moan and Embury (140).*

Kinematic (or directional) hardening

To describe phenomena like the Bauschinger effect the concept of kinematic (or directional) hardening was introduced (115, 141–143). Kinematic hardening amounts to a *translation* of the elastic region induced by plastic strain. It can be described by introducing a new internal variable, the equilibrium or back stress (7, 144). Common notations are σ_b, ER, α. To keep an experiment-specific notation we introduce a rest force F_0. When the force F departs from the (unmeasurable) rest force F_0 by a significant amount, plastic strain develops. The force scale is defined by yet another internal variable, the drag force $\mathfrak{D}$ (115). The basic equation is of the form

$$\dot{\ell}_0 = \mathrm{sgn}(F - F_0)\ \Phi\left(\ \frac{|F - F_0|}{\mathfrak{D}}\ \right)\ ,$$

where $\Phi(\ )$ is a plastic flow function. In some metals this is well approximated by a power-law $x^{\mathfrak{p}}$ with large exponents $\mathfrak{p} \sim 50$ (115). This gives a sharp transition to plastic flow at $|F - F_0| \simeq \mathfrak{D}$. These internal variables F_0, $\mathfrak{D}$, require evolution equations. In absence of recovery processes, the rest force follows closely the inelastic strain, $\ell_0 \propto F_0$. More generally, recovery terms, both dynamic and static, have to be added. A typical evolution equation for the rest force would be (145)

$$\dot{F}_0 = H\,\dot{\ell}_0 - |\dot{\ell}_0|\,d[F_0] - r[F_0,\,T]\ . \tag{4.6}$$

The second term on the right hand side involves a dynamic recovery function $d[\ ]$ which, in presence of plastic flow, takes F_0 to zero. The last term represents thermally activated static recovery, explicitely depending on the temperature T.

The essence of fibroblast mechanics is kinematic hardening, not strain-hardening. Within the force ranges explored, fibroblasts cannot be characterised by an absolute yield stress. They can be stretched up to very large forces and left there – they do not yield. They yield *during* a large deformation; *afterwards* they are stable. The results shown in Figs.4.22 and 4.12 are examples of this.

During a plastic deformation, a kinematic hardening material develops an equilibrium force F_0. Once the ramp is over, the material remains in equilibrium *only under tension*, $F = F_0$. Suppose we suddenly release it free, $F \Rightarrow 0$. First there will be an instantaneous elastic contraction, the length ℓ going from $\ell_0\,\mathfrak{E}^{-1}\big[F_0\big]$ to $\ell_0\,\mathfrak{E}^{-1}\big[\,0\,\big]$. If left at zero force, the material will then *plastically* contract: it will creep according to $\dot{\ell} = \dot{\ell}_0 = -\Phi\big[\,F_0/\mathfrak{D}\,\big]$. If instead the total length ℓ is held constant, an interplay between rest length and elastic strain arises. As the rest length ℓ_0 becomes smaller, elastic strain – i.e. force – develops. The material shows "negative force relaxation", which can also be called "active contraction". This is a possible interpretation of the force relaxation curves shown in Fig.4.10.

Cyclic softening

Another strong resemblance between fibroblasts and metals is the softening induced by repeated loading-unloading cycles. This is a highly reproducible feature of fibroblast mechanics. An

example is given in Fig.4.17. Oscillations at large amplitude lead to a decrease in the tangential stiffness as well as in the average force. The effect reverts once the oscillations stop. Essentially similar behaviour is seen in metals in loading-unloading cycles, though cyclic softening is not as common as cyclic hardening. Phenomenologically, the decrease in the average force $\langle F \rangle$ as the stretch amplitude is increased may be described by Eq.4.6. As the extent of plastic flow increases, the dynamic recovery term has more time to act. The change in the tangential stiffness is treated as a coupling between the rest force F_0 and the drag stress $\mathfrak{D}$ (145). The cyclic deformation induces a periodic change in F_0, which changes the steady value of the drag stress. A skeleton form of the evolution equation for the drag stress is

$$\dot{\mathfrak{D}} \propto |\dot{\ell}_0| \big(F_0 - g[\mathfrak{D}] \big) \; + ...$$

where $g[\,]$ is an arbitrary function. In presence of cyclic plastic flow, a steady state is reached where the two terms cancel each other within an oscillation period. The drag stress $\mathfrak{D}$ approaches a steady value $\mathfrak{D}_\infty$, related to the average rest force by $\langle F_0 \rangle = g[\mathfrak{D}_\infty]$. In this way the decrease in the average force $\langle F \rangle$ is coupled with that of the tangential stiffness.

4.14 Conclusions

The fundamental parameter defining the response of fibroblasts to oscillatory experiments is the deformation amplitude. If the amplitude is kept small, a stress stiffening master-relation relating stress and cell stiffness is found. This relation is obtained by a simple scaling of data from different cells. For the measurement one can use the fact that cells are active: as a reaction to a sudden perturbation the cell sweeps a range of mechanical stresses. In spite of this underlying complex behaviour which may involve multiple biochemical pathways, the master relation is surprisingly simple and reproducible. If the average force is externally changed, by slowly stretching the cell in a ramp experiment while superimposing small-amplitude oscillations, the master-relation between $\langle F \rangle$ and the stiffness $|\Theta|$ is seen again. Thus, a distinction between active and passive stress is artificial – regardless of deformation history, the response to small perturbations is always given by the average force. In view of this generality, and the remarkable agreement with the mechanic behaviour of biopolymer networks, we interpret the master-relation as revealing the nonlinear response of the actin network.

Amplitude is a "historical" concept, a function of the previous deformation history; the response cannot be described solely in terms of the local variables F, ℓ, $\dot{F}$, $\dot{\ell}$, $\ddot{F}$, $\ddot{\ell}$.... Extra, "internal" variables and their evolution equations are required to univocally define the mechanical state of the cell. This approach is in the spirit of the modern phenomenological description of metal plasticity (7, 115, 139). Remarkably, metal plasticity resembles the most reproducible features of fibroblast mechanics. Power-law creep, rate-independent transition from elastic to plastic flow, linear force-length relation during plastic flow, directional hardening, cyclic softening; these features are always present in strong fibroblasts. Though a clean characterisation of the response of fibroblasts to large deformations is still to be achieved, a promising phenomenological framework has been found. The whole body of knowledge from metallurgy is available,

and the microscopic mechanisms of metal plasticity might be partially extrapolated to the cytoskeleton.

An experiment revealing reproducible, nontrivial mechanical behaviour has been developed. Key to this are the experimental geometry, as well as good fibroblasts in a stable, highly adhesive state, which can be stretched by large amounts ($\sim 100\%$) without detaching or breaking. At 30°C, reaching this situation requires about 20 minutes between the coated plates. If an experiment is attempted immediately, the cell cannot be deformed; it simply detaches. Clearly, the cytoskeleton has to become involved and this takes time. Alas, not all fibroblasts are good; on the average, about 30% stick strongly, though this can change strongly from one culture to another and as weeks go by. Though low from the point of view of data acquisition, the percentage is high enough not to rule out biological significance. Significantly higher is the percentage of well-sticking, strongly pulling fibroblasts which show stress stiffening and plastic behaviour: essentially 100%.

4.15 Outlook

The large deformation regime clearly deserves a systematic analysis following the procedures of metallurgy. Large amplitude sinusoidal oscillations seem to miss the point; much better are ramps at constant speeds, which provide surprisingly clean linear force-length relations. Especially important are reversals of the deformation sense, as well as carefully distinguishing between transients and steady responses to cyclic loading. The asymmetry in the responses to loading and unloading, as in Figs.4.11 and 4.12, is an interesting reproducible feature. Within our interpretation, it should show up only in the plastic flow regime; the elastic response should be symmetric. This seems to be the case, but a systematic study has yet to be undertaken.

An essential difference between fibroblasts and metals is the strong stress stiffening of the former. The procedures used to investigate the large deformation regime should take this into account, using the average force $\langle F \rangle$ as a control parameter. The experiment should be repeated at different forces. In this way, it can be decided exactly what triggers plastic flow: whether a critical forcing, or a critical strain. In metals, it is a strain (146).

Armed with this phenomenological framework, the next step are *mild* biochemical perturbations of the cytoskeleton. It would be interesting to study the transition to plasticity after treatment with the myosin-blocking drug blebbistatin at low concentrations (147), or after fixing the cell with glutaraldehyde. For the latter I suggest very low concentrations, not higher than 1/1000. It may be speculated that the dependence on the deformation sense has to do with stretch activated Ca^{2+} channels, which would open up only when stretching the cell (148, 149). Therefore, blocking the fast MLCK pathway for myosin activation would be desirable. Blocking calcium channels with Gadolinium (150, 151) is a possibility.

Part II

Osmotically driven shape transformations in axons

Chapter 5

Background and setup

This chapter begins by introducing axons and PC12 neurites, the experimental system under study. Since in the experiments described here cells are perturbed by changes in osmotic pressure, the process of osmosis is described. Immediately after a hypo- or hyperosmotic shock, the axon volume changes as water flows down its chemical potential. Within several minutes, regulatory mechanisms drive the volume back to its initial value. This short-term volume regulation process, an ubiquituous feature in biology, is at present not fully understood. The state of the field is briefly reviewed. At fast and strong hypoosmotic shocks, neurites lose their normal cylindrical geometry and a peristaltic shape modulation sets in. Later we show that it can be explained as a Rayleigh-like instability driven by elastic tension. The relevant theoretical background is given in this chapter.

5.1 Neurites

The term *neurite* comprises real axons, dendrites, and PC12 neurites. The latter are axon-like cylindrical protusions extended by cell types such as PC12 cells (152), structurally very similar to the axons produced by neurones in culture (13, 153). The physiological function of an axon is to allow for the propagation of an action potential, enabling for communication between distant neurons. Axons sometimes become very large. An extreme case are motor neurons, which extend axons which propagate inside whole extremities, e.g. from the spinal cord to a foot– which corresponds to an aspect ratio of $\sim 10^6$. These amazingly long and thin structures grow following extracellular cues. This is accomplished by the *growth cone*, a highly dynamic unit located at the end of the axon. The growth cone crawls away from the cell body and keeps the axon under tension, making it grow (154, 155). To a first approximation, an axon is a cylindrical membrane tube with a central array of longitudinally arranged microtubules, interconnected by several types of proteins. The outer section of this cytoskeletal gel is the actin cortex, a network of actin filaments connected by crosslinking proteins and myosin motors. The actin cortex has already been discussed in 2.2.5.

Since axons can become so long, material must be transported by means other than diffusion from the cell body to the end. This is accomplished by motors walking on a scaffold of

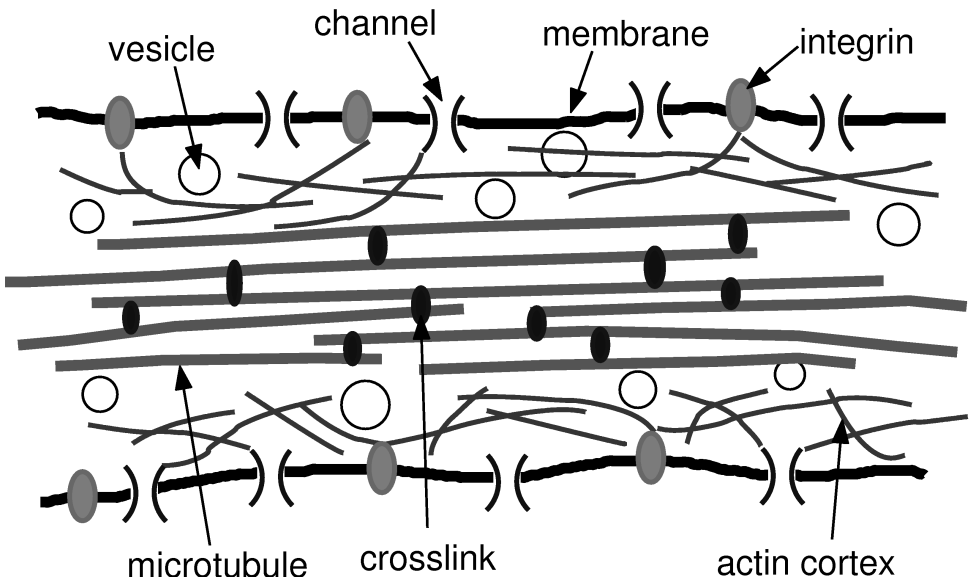

Figure 5.1: *Cartoon illustrating the main structural features of neurites. Little is known about the connections between the composite membrane (membrane + actin cortex) and the microtubule array.*

microtubules. Clearly, a thin tube extending over such enormous distances must be very tough. Specialized intermediate filaments confer axons with the required integrity. For our experiments, however, we always work on young neurites, not more than 5 days old, which are known not to have intermediate filaments (153). In these neurites the role of intermediate filaments is taken up by the microtubule core. Though the essential features of axonal ultrastructure are known, sufficient information on the interaction between its subcomponents and on their dynamic behaviour is still lacking. For example, it is not known whether microtubules are directly connected to the membrane or to the actin cortex. Below we will show results which strongly point towards a mechanical connection between microtubules and membrane.

5.2 Osmosis

In all of these experiments, hypoosmotic shocks are used in order to perturb axons. Osmosis is a phenomenon inextricably linked to the presence of a semipermeable membrane which lets water through but not the solutes (156, 157). The presence of the solutes will modify the chemical potential $\mu_W := \partial G/\partial n_W|_{T,P}$. Thus water will flow towards the phase with lower μ_W, until equilibrium is reached, $\Delta\mu_W = 0$. Having a closed vesicle in mind, we define the symbol Δ as the difference between the internal and the external concentrations : $\Delta = \mathrm{internal} - \mathrm{external}$.

At the low total solute concentrations typical of biology, ideal behavior can be assumed: the dependence of μ_W on n_W is purely entropic. As a function of the molar fraction $\phi = n_W/\Sigma n$,

we can write

$$\mu_W = \mu_W^0 + \mathrm{RT} \ln \phi_W \ . \tag{5.1}$$

In general, in a hypoosmotic shock experiment the total solute concentration will change at most by 100% (by a physicist trying to drive the system well beyond the linear regime). Since the molarity of pure water is 55 M and the physiological osmolarity is about 0.3 M, the water fraction ϕ_W changes at most by 1%. It is therefore reasonable, especially if one is planning "dirty" experiments on living cells, to keep only the linear term. Since $\phi_W - 1 = -\phi_{\mathrm{solutes}}$, we get

$$\mu_W \simeq \mu_W^0 - \mathrm{RT}\phi_{\mathrm{solutes}} \ .$$

Being essentially incompressible, the movement of water across compartments always leads to important changes in volume. Where these compartment are bound by stiff membranes, hydrostatic pressures can arise (balanced by tension in the bent membranes). Now, changes in hydrostatic pressure also modify the Gibbs' energy of the solution, according to $V = \partial G/\partial P|_{T,n_W}$ (for the rest of the discussion we implicitely use P, T, n_W as independent variables). We have $\partial \mu_W/\partial P = \partial_P(\partial G/\partial n_W) = \partial_{n_W}(\partial G/\partial P) = \partial V/\partial n_W$. In physiological conditions we can take $\partial V/\partial n_W$ as constant and replace it by the molar volume V/n_W. The change in chemical potential due to pressure is then given by $\partial \mu_W/\partial P = \partial V/\partial n_W \simeq V/n_W$. Since water can be regarded as incompressible, i.e. V/n_W is independent of the pressure P, we get $\mu_W(P_0 + \Delta P, C) = \mu_W(P_0, C) + \Delta P \ V/n_W$. The equilibrium across the membrane is now given by

$$\mu_W(P_0, C_0) \ = \ \mu_W(P_0 + \Delta P, C_0 + \Delta C) \ = \ \mu_W(P_0, C_0) + \Delta P \frac{V}{n_W} - \mathrm{RT}\ \Delta\phi_{\mathrm{solutes}},$$

where we approximate both the pressure and concentration dependence of μ_W as linear, according to 5.1. Finally, we can assume $n_W \simeq n_W + n_{\mathrm{solutes}}$, so that $\phi_{\mathrm{solutes}} n_W/V \simeq n_{\mathrm{solutes}}/V = C$, and we get the well-known equation describing equilibrium :

$$RT\ \Delta C = \Delta P.$$

The left hand side is pintorescally called the difference in osmotic pressure $\Pi = RTC \simeq (\mu_W^0 - \mu_W)\, n_W/V$. It is essentially the change in Gibbs' energy per unit volume obtained by adding a concentration C of solutes.

To reach equilibrium, water must move down its chemical potential gradient. Within linear irreversible thermodynamics one expects the difference in chemical potential to be the parameter defining the flux, i.e. $J_W \propto \Delta\mu_W$. Introducing the water permeability per unit area $\mathcal{L}_W$ (157), the generally accepted equation is

$$J_W = \mathcal{L}_W(\Delta\Pi - \Delta P) \tag{5.2}$$

Though the thermodynamics of osmosis are transparent, its kinetics are still far from understood (158).

5.3 Volume Regulation

The ability of living cells to regulate their volume is a fundamental and ubiquitous homeostatic feature in biology. Water and ions can permeate through the cellular membrane with timescales of the order of minutes. Therefore, any alteration in the ionic composition of the extracellular medium leads to changes in the cytosolic concentrations. In particular, osmolarity alteration produces fast movements of water and therefore changes in cell volume. Actually, regulatory mechanisms are at work even in normal conditions. A cell is never at equilibrium with respect to movement of ions; ionic compositions inside and outside are very different, so that steady states require the presence of pumps. Due to the presence of fixed charges inside, cations tend to enter the cell and hence rise the osmolarity, leading to swelling. By extruding one solute per cycle, the Na^+ K^+ pump is believed to be the most important factor in avoiding this so-called Donnan equilibrium (157, 159).

Regulatory Volume Decrease / Increase

Cells have a common short-term response to changes in volume triggered by alterations of extracellular osmolarity. Cell swelling leads to an increase in permeability for particular ion species, which diffuse out of the cell. This in turn makes water flow out to keep osmotic pressures balanced, $\Delta\Pi = 0$; thus the volume decreases. Once the volume is near its initial value, the channels close. This process is known as regulatory volume decrease (RVD) (51, 54). Afterwards, the normal ionic composition is slowly recovered by the action of pumps. An equivalent mechanism operates when the cell shrinks after an increase in the extracellular osmolarity; channels open letting a ionic species flow into the cell, thereby increasing the volume. This is called regulatory volume increase (RVI). The osmotic effector is K^+ in RVD, and Na^+ in RVI. The accompanying anion is usually Cl^-, and sometimes HCO_3^-. Increases in K^+ and Cl^- permeabilities after hypotonic shock-induced cell swelling have been observd in several cell types such as Ehrlich ascites tumor cells, lymphocytes, epithelial cells including turtle colon and frog urinary bladder (55).

5.3.1 Sensing swelling

Clearly the cell senses somehow its volume in order to perform RVD / RVI. At present, the underlying mechanism remains obscure (58). Several possibilities can be advanced. Tension in the membrane may directly open channels. Indeed, mechanosensitive ion channels exist and have been proposed as swelling detectors (57, 150). An objection raised is that such a mechanism would only apply to the swelling of a cell which already has the minimal area for its volume; e.g., red blood cells, which are far from being spherical, can increase their volume significantly without changing surface area (53). This argument is however oversimplified, as it does not consider the presence of cytoskeleton connected to the membrane, or the adhesive boundary conditions.

Another possibility is a real “volume measurement” by means of the cytoskeleton, as this is an interconnected unit spanning across the whole cell. Actin filaments and intermediate filaments are known to bind indirectly to transmembrane proteins, so swelling may either strain

the cytoskeleton or break these bonds; and cytoskeleton strain, as discussed in chapter 2, is well known to trigger signaling pathways (12). Indeed the cytoskeleton is known to be important in volume regulation. For one, it seems to act as a physical barrier which slows down the flow of water (160). But evidence also points towards a direct role of actin in RVD. A common observation is that the actin cortex is disrupted when swelling begins (161, 162). This effect seems to be partially secondary to an increase in intracellular Ca^{2+} (149), which activates gelsolin (51). This calcium influx may well be through mechanosensitive ion channels activated by membrane stretching (148, 151). Since there is much evidence for biochemical interactions between actin filaments and ion channels (51, 163), disruption of the actin cortex is expected to lead to changes in channel activity. This disruption is temporary; the actin cortex reforms soon. As its reappearance coincides in time with RVD, it has been speculated that the latter is needed to allowe fusion with the membrane of transporter-containing vesicles (160). The role of other cytoskeletal components is less clear. Experiments with keratynocites show that microtubules also depolymerize during swelling, to repolymerize within a few minutes (162). Disruption of microtubules abolishes RVD in leukocytes (164), but has no effect at all in PC12 cells (161).

Yet another possibility is that the cell does not directly measure its volume, but rather the change in protein concentration. A global concentration change of all components in all signaling pathways would certainly have some dramatic effect; one might naively expect it to kill the cell, but several authors expect it to trigger cascades leading to RVD / RVI (51). According to experiments done with resealed ghosts from red blood cells (56), KCl cotransport correlates with cytosolic protein concentration and not with the total cell volume. Evidence against direct sensing of volume is that potassium currents are observed in *Lymnaea stagnalis* neurons after application of hypoosmotic shocks, but they are absent when the cells are mechanically inflated (165). These authors remark that these cells express stretch activated K^+ channels. A different conclusion was reached by Craelius *et al* when studying rat mesangial cells, who found that swelling due to hypoosmotic exposure as well as due to mechanic pressure induced K^+ currents (166).

Summarising, we are still far away from understanding how cells measure their volume. The precise cell type makes a huge difference, and for no particular cell type is the situation well understood (58).

5.3.2 Modelling short-term volume regulation

The short-term volume regulation responses RVD / RVI are often modelled as follows. Water flow through the membrane is assumed to be given by $J_W = \mathcal{L}_W(\Delta\Pi - \Delta P)$, as discussed above. The main osmotic effectors are usually Na^+, K^+, Cl^- (157). The i-esime ion has a charge $z_i q$, is present at an extracellular concentration c_i^{out}, and at an intracellular concentration $c_i^{\text{in}} = n_i/V$, where V is the volume of the cell. The number of ions per unit time and unit area which flow through the membrane is the total flux J_i, where positive flux means *into the cell*. Several transport mechanisms for each ionic species are present in cells. Among them are passive basal electrodiffusive fluxes as well as pumps (54, 167). Volume regulation is achieved by specialised channels with volume-dependent permeabilities. Hernández and Cristina (54) have introduced KCl(NaCl) cotransports for RVD(RVI) with permeabilities depending linearly

on the volume. Their equation for a RVD flux is

$$J_i = \mathcal{P}_i \left(c_{\mathrm{K}}^{\mathrm{out}} \, c_{\mathrm{Cl}}^{\mathrm{out}} - n_{\mathrm{K}} \, n_{\mathrm{Cl}} \, / \, V^2 \right)$$

The permeability is assumed to depend on the volume as $\mathcal{P} = \mathcal{P}^0(1 - V/V^{reg})$ when $V > V^{reg}$, where V^{reg} is the volume above which the channels open. In general, the precise dependence of the permeabilites on cell volume is unknown. Strieter et al (55), modelling tight epithelium, have assumed a threshold-like volume dependence. A less realistic model has been used by Lucio *et al* (168), modelling RVI response of round kidney cells. These authors considere only one osmolite species, which flows with a volume dependent flux $J \propto (V^{reg} - V)$.

5.3.3 Hydrostatic pressure in short-term volume regulation

In general, little attention is paid to hydrostatic pressures in volume regulation (52). The membrane is often assumed to be unable to sustain pressure differences (157). One of the first authors to discuss a role for mechanical forces in RVD was Kleinzeller, proposing his mechano-chemical hypothesis about thirty years ago (169). Similar suggestions were made later (170, 171). Strieter *et al* included an elastic restoring force in their model of tight epithelium – though only for the sake of completeness, as the effect of this elastic term is not considered (55). Experimentally, the evidence sustaining these ideas in animal cells is rather indirect. It has been observed that *Lymnaea stagnalis* CNS neurons, which survive for hours after the extracellular medium is replaced by distilled water, eventually explode indicating strong pressure differences (165). Experiments with melanoma cells which lack an actin-crosslinking protein and are unable to perform RVD normally indicate that actin stucture can be important (170). Erythrocytes have been reported to swell more after disruption of the spectrin-actin cytoskeleton (172).

5.3.4 Regulatory Volume Decrease in round PC12 cells

Several authors have studied volume regulation on *round PC12 cells without neurites*. Since we study volume regulation on neurites from PC12 cells, this information is relevant. Disruption of the actin cytoskeleton by Cytochalasin B changes dramatically RVD (161, 173). Normally, after a hypotonic shock these cells swell, reach a maximum, and then relax to a final volume V_∞ about $\sim$15% higher than the initial volume. As the concentration of Cytochalasin B is increased, KCl efflux becomes faster and cells swell less. At large drug concentrations, no maximum is observed; the volume goes monotonically to the final volume V_∞. On the contrary, disruption of microtubules in round PC12 cells has no effect on volume regulation after hypo-osmotic shocks (161).

5.4 Pearling instability

We give here a simple analysis of the pearling instability. More careful studies can be found in Refs.(43, 174–176). For the membrane shape we will consider revolution surfaces about an axis $\hat{\mathbf{z}}$, given by an equation $r = r(z)$. The membrane is the locus of the points

$$\mathbf{r}(z,\, \phi) = z\, \hat{\mathbf{z}} + r(z)\, (\cos(\phi)\, \hat{\mathbf{x}} + \sin(\phi)\, \hat{\mathbf{y}})$$

where z, ϕ can take any value. A most important entity for membrane mechanics is the mean curvature $\mathcal{H}$, which connects the membrane tension γ to the pressure difference ΔP according to Laplace's law,

$$\Delta P = \gamma\, 2\mathcal{H}\ .$$

The mean curvature of a revolution surface can be written as

$$\mathcal{H} = \frac{\left(1 + (\partial_z r)^2\right)/r - \partial_z^2 r}{2\left(1 + (\partial_z r)^2\right)^{3/2}}\ .$$

In general, if we consider a perturbation to a cylindrical tube given by $r(\,z\,) = r_0 + \delta r(\,z\,)$, where $\delta r \ll r_0$, we can linearise the mean curvature in δr and get

$$2\,\mathcal{H} \simeq \frac{1}{r_0} - \frac{\delta r}{r_0^2} - \partial_z^2 \delta r\ .$$

For the linear stability analysis we need only consider a shape of the form

$$r = r_0 + \epsilon\, \sin(kz)\ ,$$

where the amplitude ϵ is small. The volume enclosed by the sinusoidal modulation is

$$V \;=\; \int dz\, \pi r^2 \;=\; L\pi \left(r_0^2 + \frac{\epsilon^2}{2} \right)\ .$$

We see that if the average radius r_0 remains constant, a peristaltic modulation increases the enclosed volume, but only to second order in the amplitude ϵ. Similarly the area is given by

$$A \;=\; \int dz\, 2\pi\, r \sqrt{1 + (\partial_z r)^2} \;=\; L\, 2\pi r_0 + O(\epsilon^2)\ .$$

As will be discussed in the next chapter, we believe the tension γ to be a function of the area, arising out of membrane stretch. Since the area does not to change to first order in the amplitude, for the linear stability analysis the tension γ can be taken as constant.

Now we consider hydrodynamics inside the membrane tube. First we need a continuity equation. At a given location z the cross-sectional area πr^2 can change in two ways: either by cytosol flowing in from the sides, or by water permeating through the membrane. In terms of the cross-sectional average of the flow velocity $\langle \mathbf{u} \rangle = u(z)\, \hat{\mathbf{z}}$, we have

$$\partial_t(\pi r^2) = 2\pi\, r\, \mathcal{L}_w(\Delta\Pi - \Delta P) - \pi r^2 \partial_z u\ ,$$

which can be written as

$$\partial_t r = \mathcal{L}_w(\Delta\Pi - \Delta P) - \frac{r}{2}\partial_z u \ . \tag{5.3}$$

In standard treatments of this instability, permeation through the membrane is neglected and only the second term is considered (45, 174, 176). In the next chapter this will be shown to be indeed a good approximation. For the flow inside the tube we assume for simplicity a Poisseuille flow,

$$\partial_z P = -\frac{8\eta}{r^2}\, u \ .$$

Neglecting permeation through the membrane in the continuity equation 5.3, it is straightforward to find the dispersion relation

$$-\big(k\, r_0\big)^4 + \big(k\, r_0\big)^2 = \omega\, \frac{16\, \eta\, r_0}{\gamma} \ .$$

The fastest mode can be shown to be given by $k\, r_0 = 1/\sqrt{2} \simeq 0.707$, independently of membrane tension or viscosity. A more exact analysis of the flow geometry (176) gives $k\, r_0 \simeq 0.68$. This dispersion relation is very similar to the one describing the Rayleigh-Plateau instability in inviscid jets driven by interfacial tension (177, 178). An essential difference between liquid jets and membrane tubes is that the former are always unstable, whereas the cylindrical shape of membrane tubes is stabilised by bending elasticity. Thus, a critical tension is necessary in order to induce the instability (44, 174). Moreover, to describe pearling in cells, the presence of the cytoskeletal gel has to be accounted for (45). An analysis addressing pearling in axons is given in Ref.(43). The neurite is found to be unstable above a critical tension

$$\gamma_1 = \frac{6K\mu\, r_0}{K + 4\mu/3} \ + \ O(kr_0)^4 \ ,$$

where K is the compression and μ the shear modulus of the cytoskeleton. Close to γ_1 the fastest growing mode is given by

$$kr_0 = \sqrt{\frac{\gamma - \gamma_1}{2\gamma_1}} \ ,$$

and the instability growth is dominated by the slow compression modes (43). Above a second tension $\gamma_2 = 6\mu\, r_0$, the instability grows much faster, via a peristaltic shear deformation.

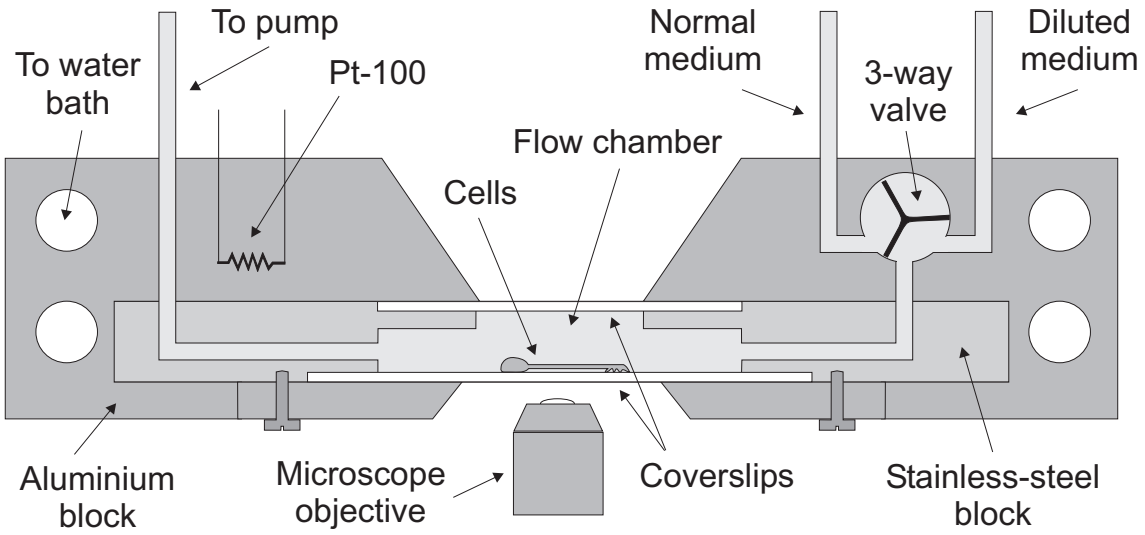

Figure 5.2: *Schematic of the milifluidic flow-chamber. The medium flows sucked by a pump from right to left. A three-way valve lets the user choose which medium flows in. The aluminium block is kept at a constant temperature.*

5.5 Experimental setup and procedures

The experiments were carried out using a milifluidic flow-chamber technique developed earlier in the lab (43). A schematic of the set-up is shown in Fig.5.2. A specially designed stainless-steel block and two coverslips are used to form a 10x5x1(mm)^3 chamber. The bottom coverslip holds the cells under study. One duct of the chamber is connected to a peristaltic pump by means of long, soft silicone-rubber tubing that minimises pressure fluctuations arising from the pump. The other duct is connected to a 3-way-valve to select between the two different media. The chamber is intentionally made small to ensure a quick switching from one medium to the other at low flow rates, in the range of 2–4 μl/s. The chamber, the 3-way-valve, and the stainless-steel tubes are placed inside an aluminium block with godd thermal contact between each other. A water bath maintains the temperature of the block with a maximum variation of ± 0.2 °C. Thus, the liquid pumped into the chamber is at the same temperature as the aluminium block before reaching the chamber. In addition, the continuous flow of medium keeps the chamber at constant temperature despite some heat loss through the coverslips.

5.5.1 Cell culture

Two different experimental systems have been investigated: axons from chick embryo neurons and neurites from PC12 cells. The former have the advantage of resembling closely real *in vivo* neurons, as they are extracted from a living embryo, let grow only for a few days and then used in an experiment (179). The disadvantage is that a laborious dissection procedure is needed in order to obtain the cells, which has to be repeated each time. PC12 cells are an

established cell line which multiplies in culture (152, 180), simplifying experiments enormously. As a drawback, it is not clear to what an extent their neurites resemble real axons. Therefore most quantitative experiments were done on PC12 neurites; only a few and of rather qualitative nature were performed on chick embryo axons, in order to confirm the generality of the phenomena.

Chick embryo neurons

Embryos are from VALO SPF fertilized chicken eggs (Lohmann Tierzucht GmbH). As soon as they arrive they are put in the refrigerator at 12 °C and stored for up to 1 week. Each day a few eggs are taken out and introduced in an oven at 35 °C. After 6-7 days the embryos are removed and dissected. The dorsal ganglia are removed with scalpel and trypsinized in order to dissociate the neurons. These are plated on laminin-coated slides and allowed to grow for 2-3 days (179).

PC12 cells

PC12 cells are from the DSMZ (111). These cells normally grow in suspension forming large clumps. To induce neurite growth, they are plated on collagen coated slides and allowed to grow in presence of nerve growth factor (NGF) for 4–5 days (180). Both rat-tail collagen and NGF are from Sigma. The quality of the neurites depends strongly on the collagen coating. Significant improvement was achieved by first coating the slides with 3-aminopropyl triethoxysilane (Sigma-Aldrich) and afterwards with collagen. The silanization protocol used for the microplates described in Chapter 3 works well. Collagen is prepared at 10% concentration in a 70% ethanol – 30% water solution. The silanised slides are covered with about 1 mm of collagen solution and let dry overnight.

During the 5 days of neurite growth on the collagen coating, cells also multiply and their surface density increases. If the cell density at the time of the experiment is very high, the free neurite portions are short and overlap with other neurites. If the final cell density is too low, most neurites will not have established contact with other cell bodies. Growth for a longer period of time is not desirable, as PC12 neurites are known to develope intermediate filaments after one week (153). Thus, there is an optimal window for the initial cell density.

5.5.2 Neurite selection

A successfull experiment requires a strongly adhering neurite. Small growth cones adhering on the substrate are often too weak to resist a strong hypoosmotic shock. Ideally, we chose neurites whose growth cone is sticking to the body of another cell, as the adhesion strength is then at its highest. The neurite should be perpendicular to the optical axis; otherwise only a small portion will be properly focused. It is also desirable to choose regular neurites, with a uniform radius, to ease the image analysis. Some neurites can be seen to stick on the substrate at isolated points along their lengths; such neurites are discarded, since these connections may move erratically during a hypoosmotic shock, altering the boundary conditions. As only a small fraction of the neurites satisfy all these requirements, it is crucial to keep the culture in optimal conditions so

that enough nice neurites be produced. Not too many, however–for then they overlap and stick to each other. An example of a good neurite is shown in Fig.5.3.

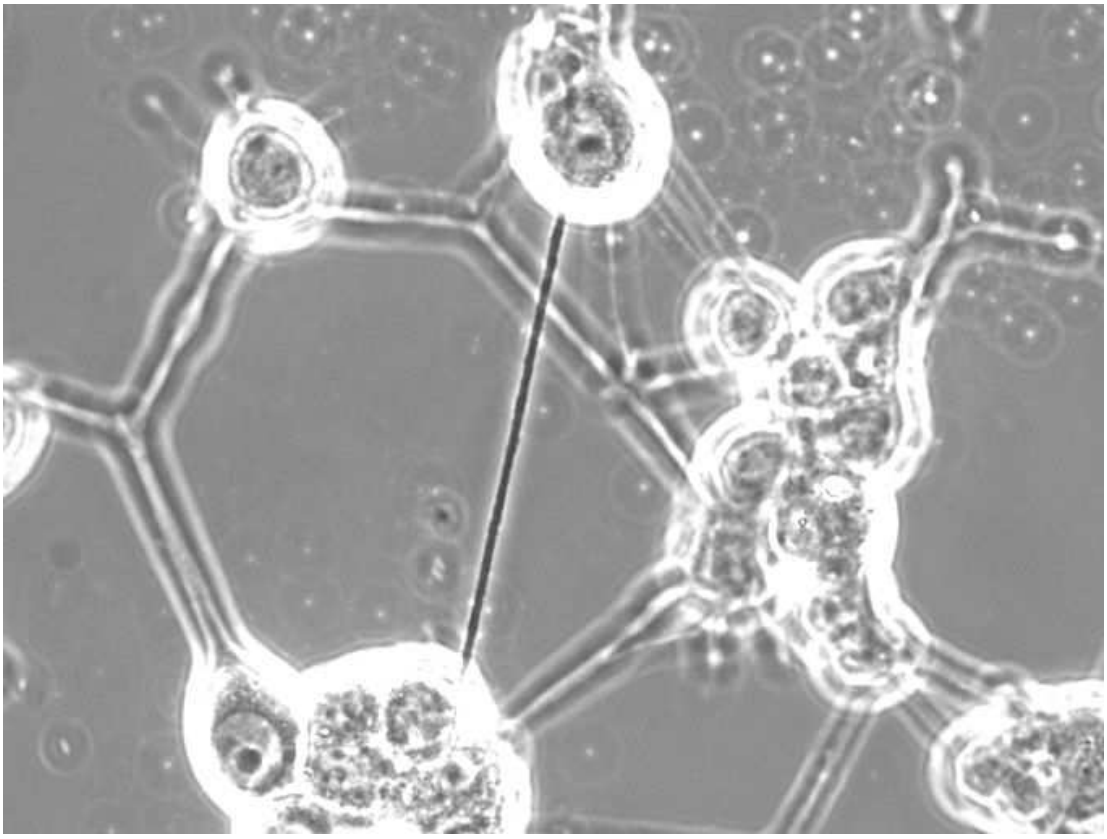

Figure 5.3: *Example of a probably good neurite for a hypoosmotic shock experiment. The neurite is straight and uniform, well attached between two cell bodies, at a considerable height above the substrate.*

5.5.3 Image analysis

The volume and area of the neurites are analysed from the recorded images using an edge detection program which we developed using Matlab programming language. Edge detection using a threshold for intensity is unreliable due to the "halo effect" present in phase-contrast images (see Fig.5.4(A)) and also due to the dependence on the illumination intensity. To avoid such complications, the edge is estimated by detecting the local maxima in the gradient of intensity.

Complications in finding the edge arise mainly because of the "dirty" nature of the experiments. The constant flow removes weak or dead cells from the surface and pushes them around; often this "junk" passes by the neurite during the experiment. The presence of these extra edges difficults finding the right one. Moreover, neurites often have irregular regions where the edge

changes abruptly. The following procedure was used. In the first frame of the sequence, the user locates the axon by drawing a spline over the image. This is taken as an initial condition for the edge-finding algorithm. The algorithm then analyses each column in the image independently, looking along the **y** direction for the position where the intensity gradient is maximal. Since this works on a column-basis, in the image the axon must be roughly oriented in the perpendicular **x**-direction. This is easily accomplished by placing the camera at the right angle during the experiment. Finding the gradient maxima is done in two steps. In the first step, the derivative along the **y**-direction, $\partial_y I$, is maximised. The advantage is that the two neurite edges can be trivially distinguished: one is an absolute maximum, the other one an absolute minimum. In contrast, when looking at the norm of the gradient, one edge is a global- but the other one a *local*-maximum. A bonus is that pieces of junk floating near a given axon edge do not interfere much, as their nearest edge has an opposite sign. These maxima are then taken as initial conditions for a new search, this time maximising the absolute value of the gradient $\sqrt{(\partial_x I)^2 + (\partial_y I)^2}$ in a steepest-ascent way. An example of the intensity profile across the neurite cross-section is illustrated in Fig.5.4(B). Once the edge is found, volume and apparent surface area are computed assuming axial symmetry for the neurite shape. This should be a good approximation for straight neurites which are attached only at the two extremities. The edge is then used as the initial condition for the next frame.

As will be discussed in the next chapter, we trigger periodic peristaltic modulations of the neurite shape in our experiments. It is interesting to characterise the modes present and their growth rates, for which we undertook Fourier-analyses of the neurite shapes. This was not entirely straightforward. Due to the extreme aspect ratio of neurites, a compromise must be found between resolution and total length measured. In most cases, this implied recording a total of about 6–7 waves. The total length sampled is given by the magnification and camera size and hence bears no relation with the dominant wavelength. Standard algorithms for discrete Fourier transforms receive a N-uple as input and return the modes at the wavenumbers $k/2\pi = 0,\, 1/N,\, 2/N,\, 3/N,\, ...$ Therefore a problem arises when the fine structure of the spectrum is of the order of the separation between the calculated modes. In particular, the dominant mode k_D may be located between the calculated modes, e.g. at $k_D/2\pi = 6.5/N$. As a way out, we decided to analyse slightly smaller regions. One might choose N' so that $6/N' = 6.5/N$, which amounts to $N' = N\,12/13$. This entails of course a loss of exactitude as one is now discarding $1/13$ of the data. We did a "N'-sweep", taking ratios N'/N between $16/17 \simeq 0.84$ and 1. As a control, for each N' value we did two analysis; one removing from the left, another one from the right. The difference between the two gives an idea of the error made by discarding the end regions.

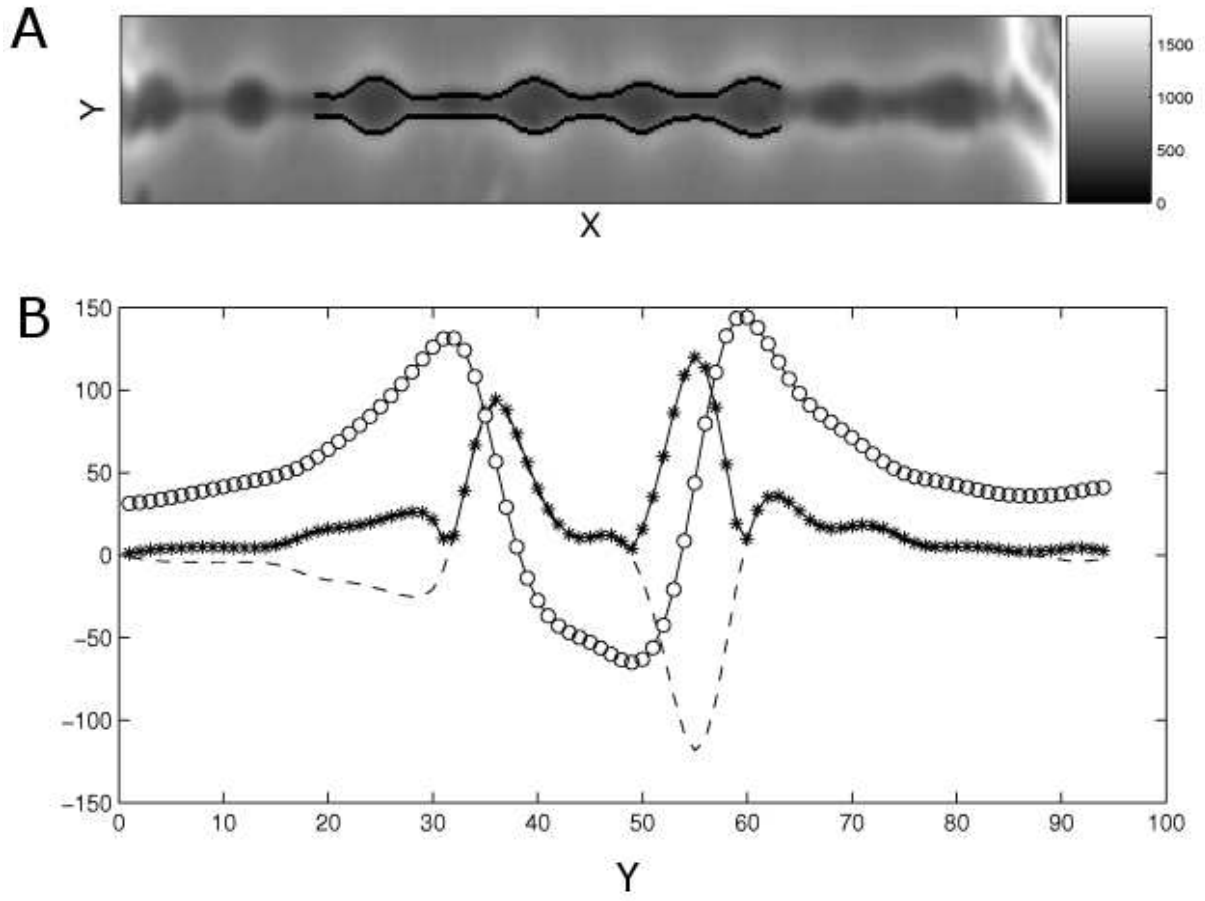

Figure 5.4: *Finding the edge of the axon.* **A:** *image of the neurite. The peristaltic modulation is the "pearling" instability, which will be discussed in the next chapter. The edge found by the algorithm is coloured black. For clarity, only a small portion in the middle was analysed.* **B:** *Cross-section of the axon.* **Open circles:** *profile of the intensity* I. **Asterisks:** *absolute value of the intensity gradient* $\sqrt{(\partial_x I)^2 + (\partial_y I)^2}$. **Broken line:** *derivative* $\partial_y I$.

Chapter 6

Results and discussion

After a dilution of the extracellular medium neurites initially swell. If the dilution is strong and fast enough, a standing peristaltic modulation sets in. After a time of the order of 100 seconds, the neurite volume reaches a maximum and relaxes back to its initial value; with similar timescales the amplitude of the modulation reaches a maximum and relaxes to zero. Fig.6.1 shows a typical response. The study of these phenomena lends itself to a separation in two aspects. On one hand, the shape instability can be successfully explained without regarding all details of the evolution in time of the volume. On the other hand, the hypoosmotic shock triggers a volume regulation process which recovers the intial volume regardless of shape changes. We take advantage of this natural separation for the presentation of results.

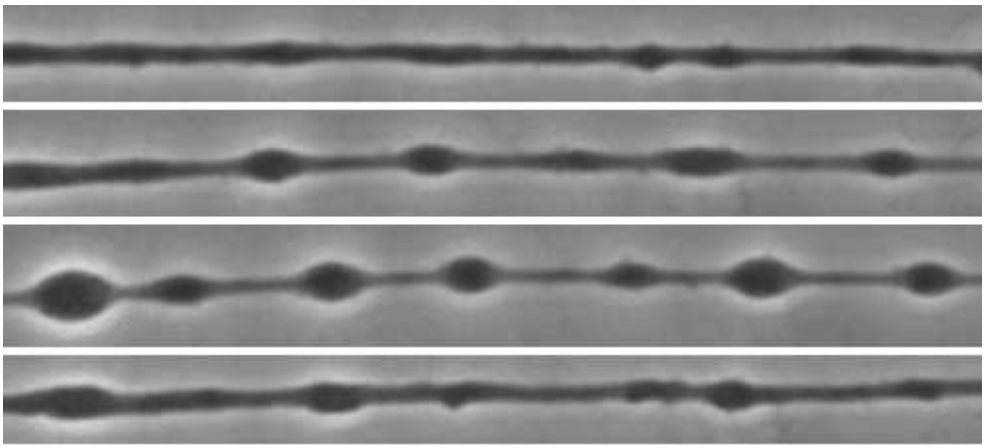

Figure 6.1: *Neurite response after a hypoosmotic shock, at times 0 s, 40 s, 60 s, 120 s. The neurite swells and the peristaltic modulation sets in. Both volume and modulation relax.*

6.1 Volume regulation : Results

The response of the neurite volume to hypoosmotic shocks is highly reproducible in its main features. After a dilution of the extracellular medium from an initial total solute concentration $\mathcal{C} \simeq 300$ mM to a lower value $D\mathcal{C}$, neurites swell. The volume V increases from its initial value until it reaches a maximum. If the shock is strong enough ($D < 0.8$), the volume relaxes back close to the initial value in a roughly exponential fashion. Once the volume has stabilized and the neurite has adapted to the new conditions, one may perform a hyperosmotic shock by switching the extracellular osmolarity back to its original value. The response is essentially the same, only "inverted": the neurite shrinks, the volume reaches a minimum and then increases back to the initial value. Both responses have timescales of similar magnitude. Fig.6.2 shows two typical experiments.

In order to describe the evolution in time of the volume we define the following variables. The main variables are the volume per unit length V (henceforth simply called "volume") and the area per unit length A (similarly called "area"). A neurite has an initial volume V_0. The initial rate of change of the volume, $\dot{V}_0$, is the magnitude from which we estimate the water permeability. Often an initial acceleration phase is seen in the volume evolution; only afterwards the rate $\dot{V}$ stabilises. This value is taken as initial slope (see Fig.6.3) After reaching a maximum volume V_M, the volume relaxes back to a final volume V_m close to its initial value V_0. This often, but not always, takes place in a roughly exponential fashion, defining the relaxation time τ_V. These variables are ill-defined, as often a slow, erratic "drift" of the volume is seen after relaxation, which complicates measuring τ_V. Once the neurite stabilizes at the lower external osmolarity $D\mathcal{C}$, a hyperosmotic shock is performed by switching back the original medium. The neurite then shrinks, the volume reaches a minimum which we will also call V_M, and then increases close to the initial volume. A shrinking rate and relaxation time are defined analogously to the swelling experiment.

Figure 6.2: *Volume V, area A, and pearling parameter $\sqrt{V}/A$ (relative to their initial values) as a function of time. The parameter $\sqrt{V}/A$ indicates any deviations from the cylindrical geometry.* **A:** *Experiment performed at temperature 36°C, dilution $D = 0.7$.* **A hypo:** *hypoosmotic shock. The external solute concentration is changed from $\mathcal{C}$ to $D\mathcal{C}$. The neurite swells and relaxes to a higher value. Since $\sqrt{V}/A$ does not change significantly, the shape remains cylindrical throughout.* **A hyper:** *hyperosmotic shock on the same neurite, induced by replacing the original medium; the external solute concentration changes from $D\mathcal{C}$ to $\mathcal{C}$.* **B:** *Experiment performed at temperature 15°C, dilution $D = 0.8$. Notice the different time scales.* **B hypo:** *hypoosmotic shock. The external solute concentration is changed from $\mathcal{C}$ to $D\mathcal{C}$. The neurite swells but does not relax. This behaviour is observed often at mild dilutions $D \leq 0.8$. As indicated by the change in $\sqrt{V}/A$, significant shape change ("pearling") was induced in spite of the dilution being mild. This is due to the low temperature. Notice that the cylindrical shape is recovered though the volume and area stay respectively 20% and 10% higher. These shape transformations are addressed in detail later in the chapter.* **B hyper:** *hyperosmotic shock on the same neurite, induced by replacing the original medium; the external solute concentration changes from $D\mathcal{C}$ to $\mathcal{C}$. No deviation from the cylindrical geometry is observed.*

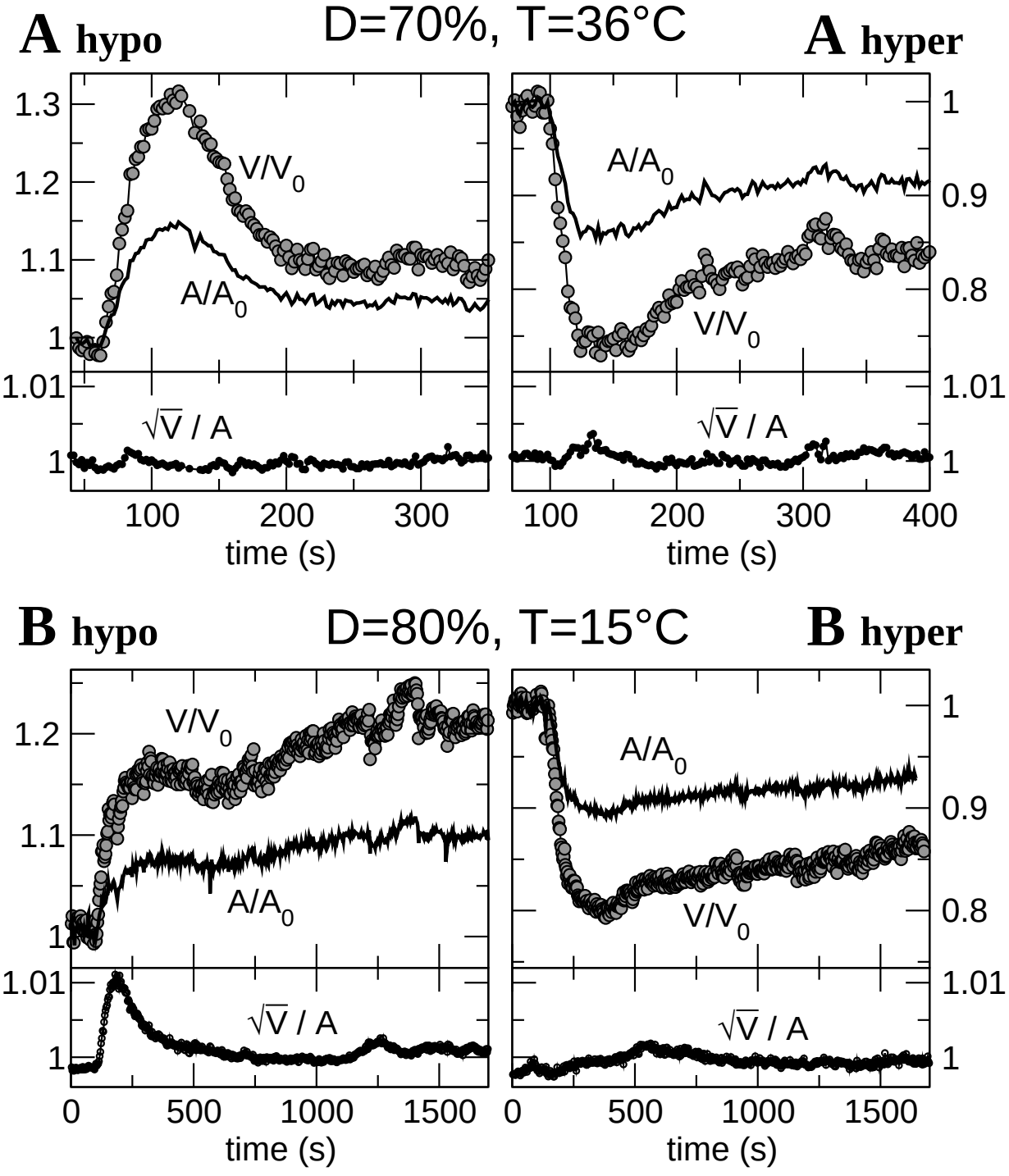

Figure 6.2: ⇐ **Caption on the left**

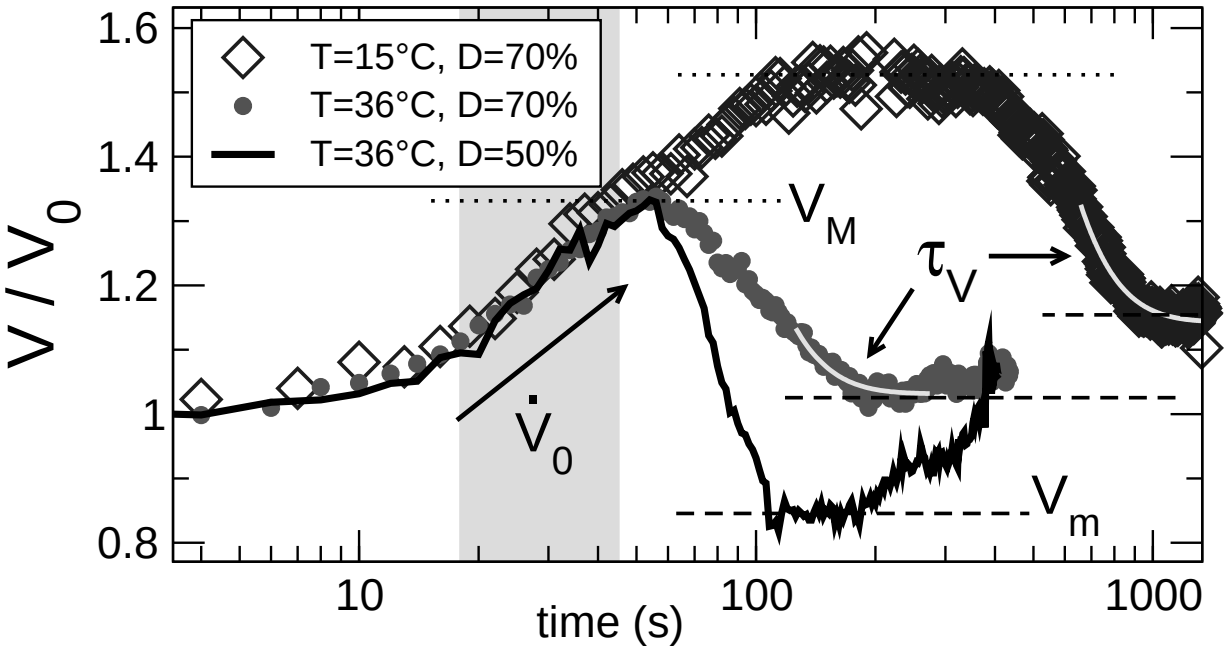

Figure 6.3: *Swelling and relaxation after a hypoosmotic shock performed at time $t = 0$. Normalised volume V/V_0 as a function of time for different conditions: $D = 50\%$, temp. 36°C (***black line***), $D = 70\%$, temp. 36°C (***shaded circles***), $D = 70\%$, temp. 15°C (***open diamonds***). Each curve is a different neurite. The shaded region is where the "initial" swelling rate $\dot{V}_0$ is measured, by fitting a linear function. The maximum volume attained is V_M, and the minimum is V_m. The bright curves are fits to exponential functions, giving the relaxation time τ_V. Notice the similar swelling rates for all curves, the strong undershoot of the volume at $D = 50\%$, and the much slower kinetics at the low temperature. These are all general trends of the volume response.*

The variables $V_0, \dot{V}_0, V_M, \tau_V, V_m$ characterising the evolution in time of the volume V are studied as a function of the extracellular concentration $D\mathcal{C}$ and temperature T.

Water permeability $\mathcal{L}_W$

The increase in volume following an hypoosmotic shock is due to the influx of water driven by the initial osmolarity difference across the membrane. As discussed in chapter 5, this flow should be given by $\dot{V} = A_0 \mathcal{L}_W (\Delta\Pi - \Delta p)$. At the beginning of the swelling phase one may expect (43) hydrostatic pressures to be negligible, and the osmotic pressure difference to be given by $\Delta\Pi = RT\mathcal{C}(1 - D)$. Estimation of the water permeability of the membrane is straightforward under these assumptions. We calculate $\dot{V}_0/A_0$ and look at it as a function of the initial osmotic pressure difference $\Pi_0(1 - D)$, as shown in Fig.6.4 for temperatures 33–36°C.

Under the aforementioned assumptions, one expects a straight line for the $\dot{V}_0/A_0(\,\Delta\Pi\,)$ dependence shown in Fig.6.4. This is not the case. Interestingly, at stronger shocks neurites do not swell much faster. Because of this nonlinearity, in order to estimate a water permeability we take the values at mild shocks ($D = 70\%$): $\mathcal{L}_W = \dot{V}_{D=70\%}/(A_0\, 0.3\, \Pi_0)$. This procedure is

only meant to give an order of magnitude estimate. In this way we calculate an effective water permeability $\mathcal{L}_W$ for different temperatures, as shown in the inset. The trend goes in the expected direction, $\mathcal{L}_W$ increasing with T. The change with temperature is feeble, about a factor of 2 within 20 K. Below we show that the relaxation time τ_W changes a factor of 10 in the same range of temperatures. Instead of $\mathcal{L}_W$, in the literature one often finds the permeability parameter $\mathcal{P} = RT\delta_W \mathcal{L}_W$, where δ_W is the molar density of water (1 mol/ 18 (cm)^3) and $RT\delta_W \sim 140$ MPa. Our results give $\mathcal{L}_W$ of the order of 10 nm/(MPa.s), which corresponds to $\mathcal{P} \simeq 1.4\,\mu$m/s. According to the literature, biological cells as well as lipidic membranes are as a rule 1–2 orders of magnitude more permeable (157, 168, 181, 182), even after blockage of water channels (183). Later in the chapter, it will be argued that the apparently lower permeability of neurites is due to significant hydrostatic pressures already present at the initial swelling phase.

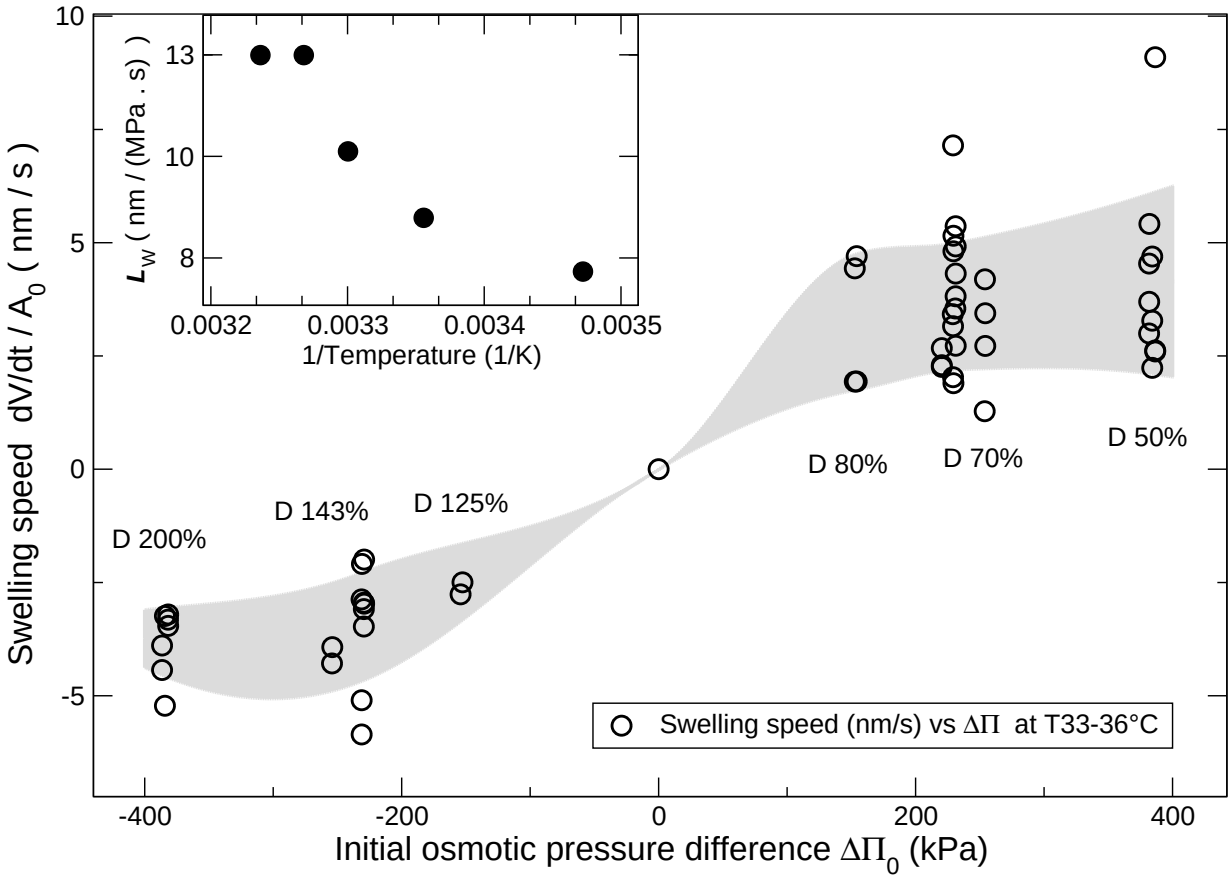

Figure 6.4: *Initial swelling speed (volume per unit time per unit area) as a function of the osmotic pressure difference, for temperatures* $33 - 36°C$*. The shaded region is a guide to the eye, an Akima spline going through the averages* $\pm$ *a standard deviation. Inset : water permeability* $\mathcal{L}_W$ *as a function of inverse temperature. The* $\mathcal{L}_W$ *values have been estimated from the value of* $\dot{V}/A_0$ *for* $D = 0.7$*.*

Maximum volume V_M

The maximum volume V_M is to a good approximation proportional to the inital volume V_0, as Fig.6.5 shows. This also holds for the minimum volume during shrinking. Thus we regard the relative maximum volume V_M/V_0, to do away with the dependence on the initial size. The relative maximum does not depend significantly on the temperature. Not surprisingly, it increases with the initial osmotic pressure difference $\Delta\Pi_0$, as seen in Fig.6.6.

The plot shows the data along with curves corresponding to perfect-osmometer behaviour. The latter corresponds to a membrane which neither allows ion leakage nor develops hydrostatic pressures. The volume must then increase until osmotic pressures are balanced, according to the equation $(V_0 - V_\infty)/(V - V_\infty) = D$. The dead volume V_∞ represents non-cytosolic internal volume, comprised mostly of proteins. Mammal cells have on the average a cytosolic protein concentration of $\sim 20\%$ (5). A reasonable value for PC12 neurites is $V_\infty \simeq 25\% V_0$, according to electron microscopy studies (153). The volume approaches V_∞ only at infinite external osmolarities $D = \infty$. The shaded regions correspond to $V > V_0/D$ for dilutions ($D < 1$) and to $V < V_0/D$ for reverse dilutions ($D > 1$). Were the volume to go into the shaded regions, one would wonder where the driving force comes from or what is wrong with the experiment;

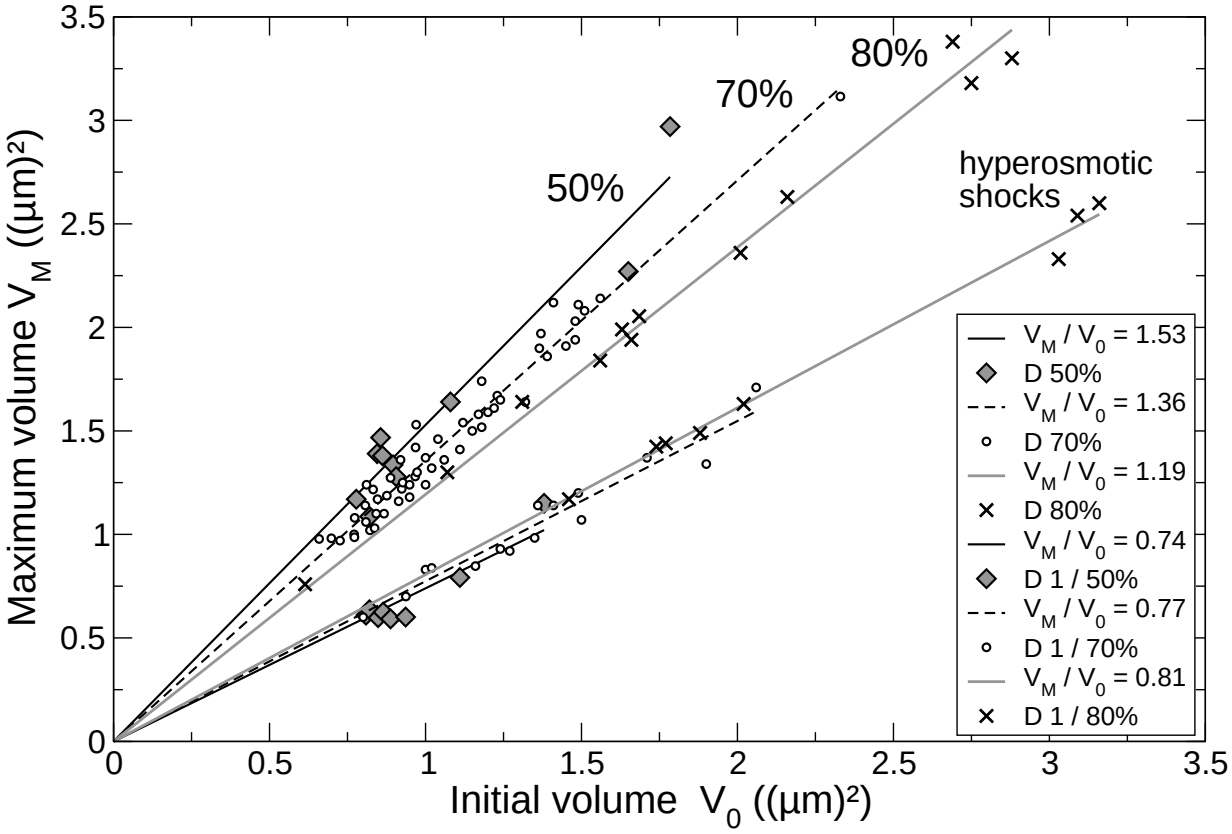

Figure 6.5: *Maximum volume V_M as a function of initial volume V_0. For reverse dilutions V_M is actually the minimum volume attained.*

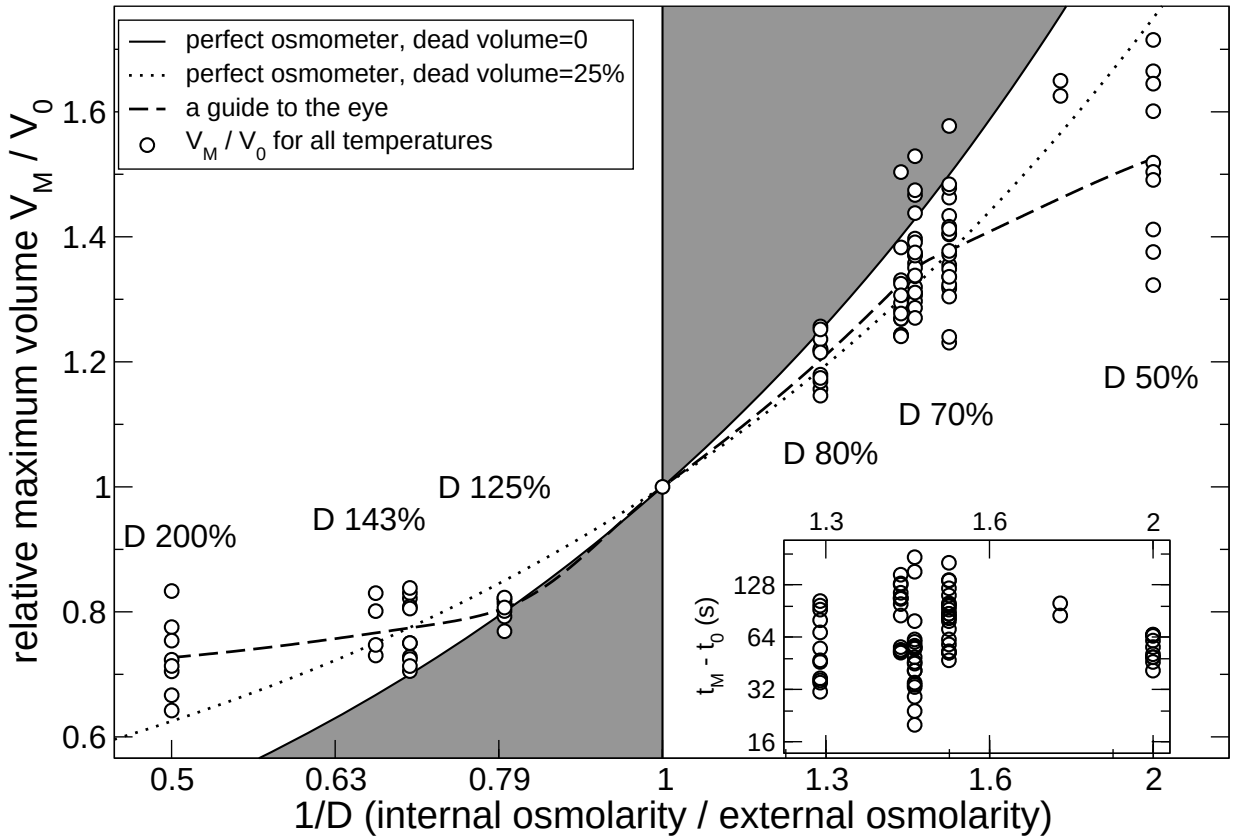

Figure 6.6: **Main plot** *: Maximum relative volume V_M/V_0 as a function of the osmotic pressure difference $\Delta\Pi$, for all temperatures. The broken line is a guide to the eye, corresponding to an Akima spline going through the average values. Curves corresponding to perfect osmometers with dead volumes of 0 (solid line) and 25% (dotted line) are shown. The shaded regions correspond to $V > V_0/D$ for $D < 1$, and to $V < V_0/D$ for $D > 1$.* **Inset** *: Time $t_M - t_0$ taken to reach the maximum volume V_M as a function of $1/D$.*

fortunately, this is not the case. Up to 70% shocks, neurites behave as osmometers with reasonable values for the dead volume, indicating that neither hydrostatic pressure has arisen nor significant ion flow has taken place during the swelling phase. At strong shocks (50%), however, neurites are no longer osmometers; they do not swell as much as they could. This indicates that either ion leakage takes place during the swelling phase, so that when the maximum is reached $\Delta\Pi < (1 - D)\,\Pi_0$, or that hydrostatic pressure arises, $\Delta p > 0$. That relaxation mechanisms show up at high shocks cannot be due to a time effect, since the time elapsed until V reaches its maximum V_M is essentially independent of the external osmolarity. This can be seen in the inset in Fig.6.6, which shows the time $t_M - t_0$ to reach the maximum volume.

Volume relaxation

The exponential relaxation time τ_V is not a well defined parameter, as departures from a simple exponential relaxation are quite common. At very mild shocks (80%), there is often no relaxation at all. At 50% shocks, often undershoot and recovery are observed. FIG Moreover, after the relaxation phase the volume only rarely stays constant; usually it displays a slow drift, which complicates measuring the characteristic time. All these complications may explain the large scatter in the data. However, since these departures from exponential relaxation are not systematic and cannot be addressed by fitting to something fancier, we stay with exponentials. The time τ_V so obtained is good enough to reveal a strong temperature dependence, shown in the Arrhenius-plot in Fig.6.7. The dashed line is an Arrhenius-like equation $\tau \propto 1/k \propto e^{\frac{\Delta G}{RT}}$, where k is the rate constant of a hypothetical thermally-activated process (1, 184). Though not perfect, the relaxation time does follow approximately an Arrhenius-trend, most likely indicating a major role for ion- or water-channels. From simple theoretical considerations, we do not expect exactly $\tau \propto 1/k$; even for the very simple elastic 1-ion model suggested in Ref.(43) the relaxation time

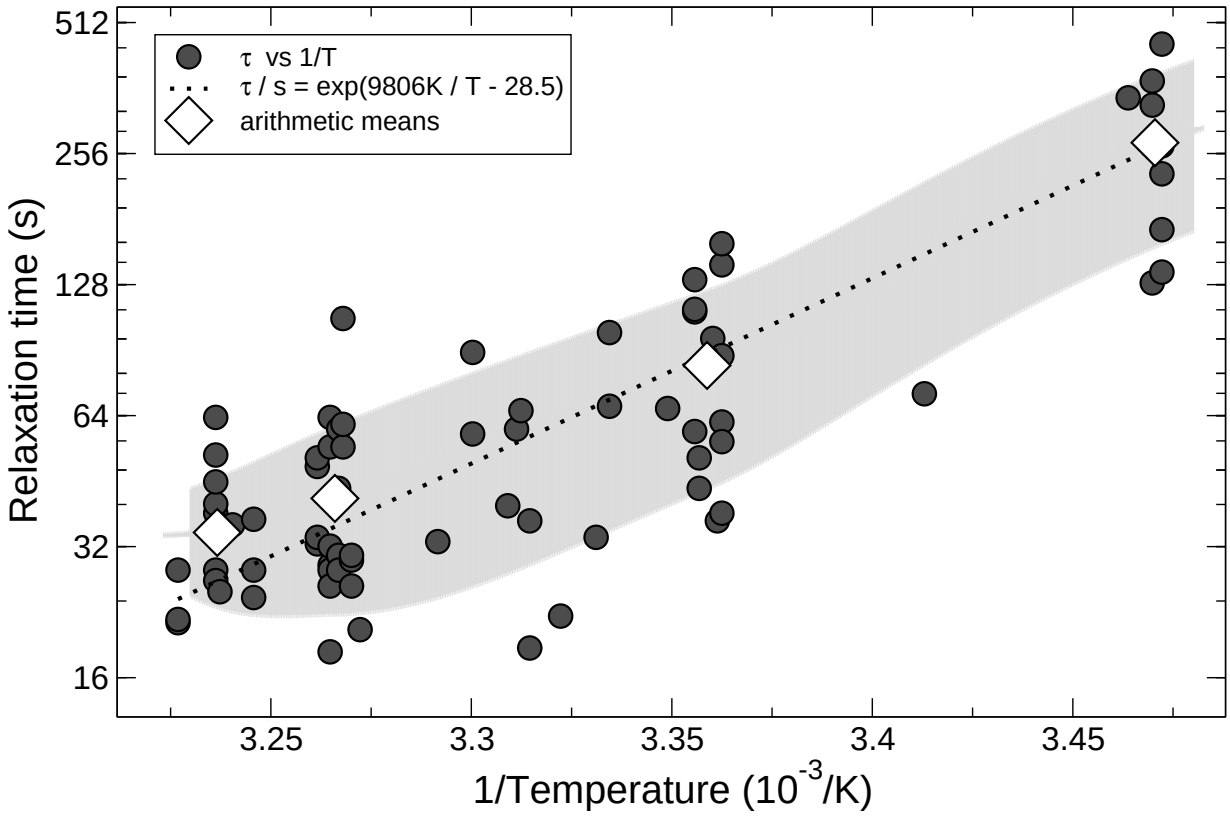

Figure 6.7: *Relaxation time as a function of inverse temperature 1/T. As a guide to the eye, the open diamonds show average values and the grey region gives the respective standard deviations. Dashed line : least squares fit to the form* $\tau \propto e^{\frac{\Delta G}{RT}}$.

is a more complicated function of the ion permeability, which only becomes $\tau \propto 1/k$ as a limit when $\mathcal{L}_W \to \infty$. The effective activation energy from the fit is $\Delta G \sim 33RT$, a typical order of magnitude in biological systems.

Final volume V_m

Neurites sometimes "undershoot" when they relax after a dilution, i.e. the minimum volume V_m is significantly lower than the initial volume V_0. At high temperatures this effect correlates with the osmotic pressure difference. At very weak shocks (80%), often no volume recovery is seen at all, so that $V_m > V_0$. At higher dilutions (50 %), the volume often goes beyond its original value. This can be seen in Fig.6.8.

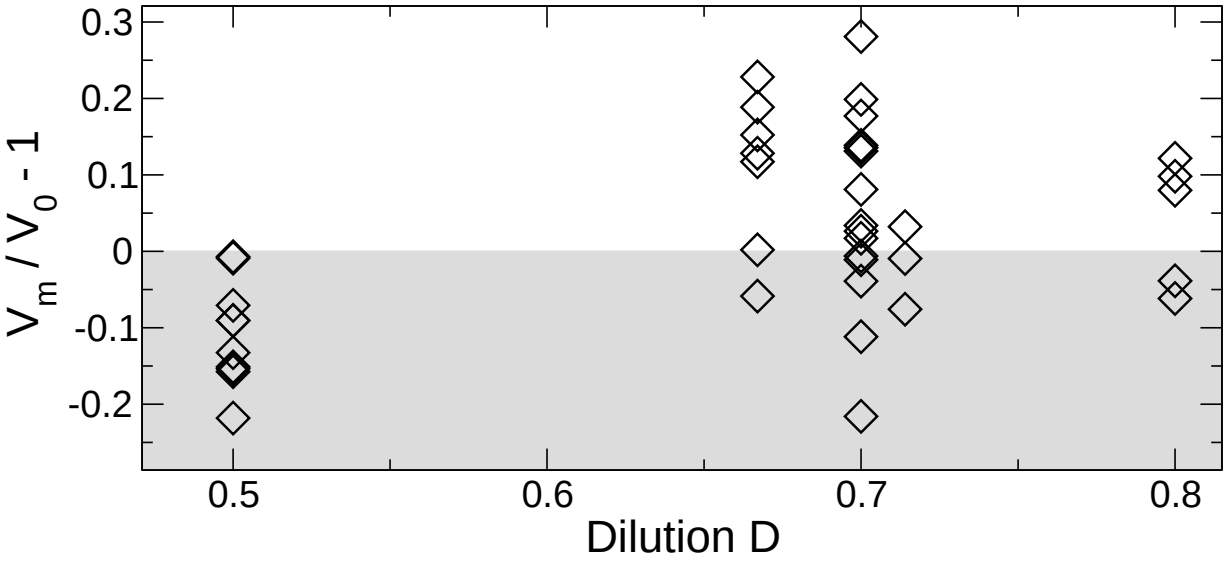

Figure 6.8: *Minimum volume V_m post-relaxation as function of the dilution D, for temperatures 30–36°C. The shaded region corresponds to "undershoots", where the volume relaxes after swelling beyond its initial value.*

Swelling versus shrinking

The water permeability $\mathcal{L}_W$ is independent of the flow direction. On the average, one obtains the same value from a swelling experiment as from a shrinking one. This is not the case for the relaxation time. Though it is particularly difficult to measure relaxation times from the hyperosmotic shocks, Fig.6.9 shows clearly that recovering from a reverse dilution takes 2–3 times longer. This suggests that the swelling rate is dominated by symmetric phenomena, such as permeation through the membrane or cytoskeleton-solvent friction, whereas the relaxation mechanisms change according to the type of shock.

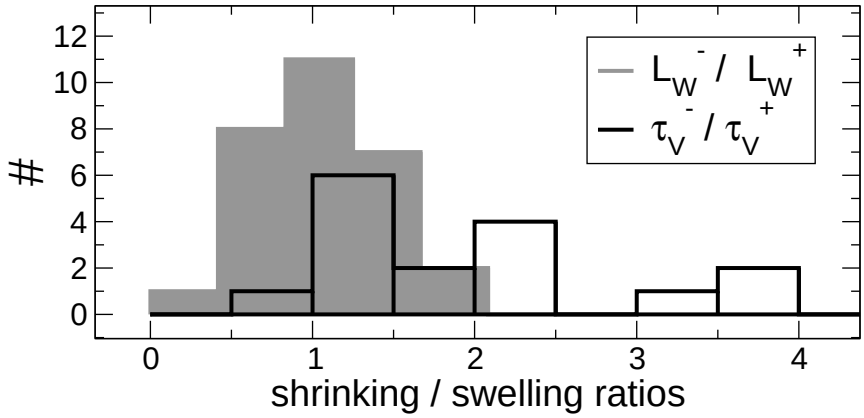

Figure 6.9: *Histograms of shrinking/swelling quotients. Shrinking/swelling ratio of relaxation times τ_V^-/τ_V^+ (***open boxes***). Shrinking/swelling ratio of permeabilities $\mathcal{L}_W^-/\mathcal{L}_W^+$ (***shaded boxes***). On the average, the permeabilities are independent of the flow direction, whereas relaxation times after a hyperosmotic shock are ~ 2 times longer than after hypoosmotic shocks.*

6.1.1 Volume regulation under cytoskeleton disruption

In order to assess the role of the cytoskeleton, we treat neurites with specific disrupting drugs and then apply a hypoosmotic shock. Except in the case of the myosin blocking drug Blebbistatin (BLE) (147), this is not a straightforward procedure, as cytoskeleton disruption itself leads to pearling. Both actin disruption by Latrunculin-A (LAT) (116) and microtubule disruption by Nocodazole (NOC) (119) induce in neurites strong, irreversible peristaltic modulations. At this stage, one knows for sure that cytoskeleton disruption has taken place, but experiments become difficult to perform due to increased neurite fragility. Strongly pearled neurites are moreover difficult to analyze. Therefore we chose to let the drug act for a few minutes until an effect could be observed, but before significant pearling developed. In the case of LAT treatment this usually meant "floppiness" of the axon, whereas for NOC we waited for the first varicosities to show up. In this way we could perform experiments on neurites still close to the cylindrical geometry. With Blebbistatin there is no difficulty, as it does not induce pearling. To ensure its effect we previously incubated neurites at 37° for about 1 hour at a very high concentration (50 μM, where its half-effect concentration C_{50} is $\sim 2\,\mu$M). All drugs were present both in the normal and in the diluted medium.

In order to dissolve the drugs in the culture medium, addition of dimethylsulfoxide (DMSO) is required. This is risky as DMSO itself has a myriad of effects on water and ion channels (183). Thus, as a control we also performed experiments in presence of DMSO 0.5%, equal to the highest DMSO concentration in any of the drug experiments.

In presence of LAT neurites lose all their connections to the substrate and become slack, shown by an increase in tortuosity and larger lateral fluctuations. In these conditions strong hypoosmotic shocks almost always make neurites detach, which limits these experiments to dilutions up to $D = 70\%$.

Faster swelling under drugs

The strongest effect of drugs in the time-evolution of the volume concerns the swelling rate. This effect is seen most clearly at 50% dilutions. The initial swelling speed $\dot{V}_0/A_0$ increases markedly after blebbistatin and nocodazol treatment. As shown in Fig.6.4, $\dot{V}_0/\Delta\Pi_0$ is not independent of $\Delta\Pi_0$, contradicting our idea that $\dot{V}_0 = A_0\,\mathcal{L}_W\Delta\Pi_0$ holds during the initial swelling phase. To that we can now add that microtubule or myosin disruption increases $\dot{V}_0/A_0$ noticeably.

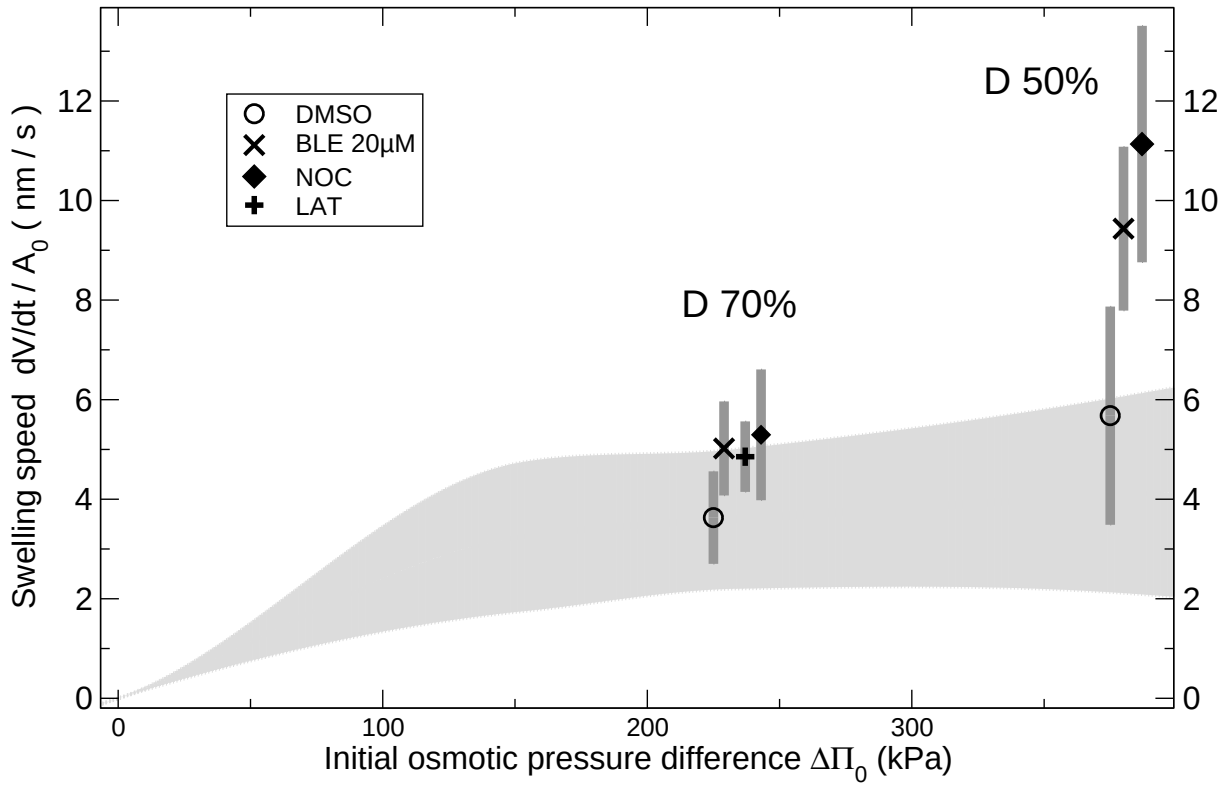

Figure 6.10: *Swelling speed $\dot{V}_0/A_0$ as a function of the initial osmotic pressure difference $\Delta\Pi_0$, for temperatures $33 - 36°C$. The grey region is a guide to the eye, corresponding to the experiments without drugs shown in Fig.6.4. Data for all drugs is shown as mean±2 S.E., according to the legend.*

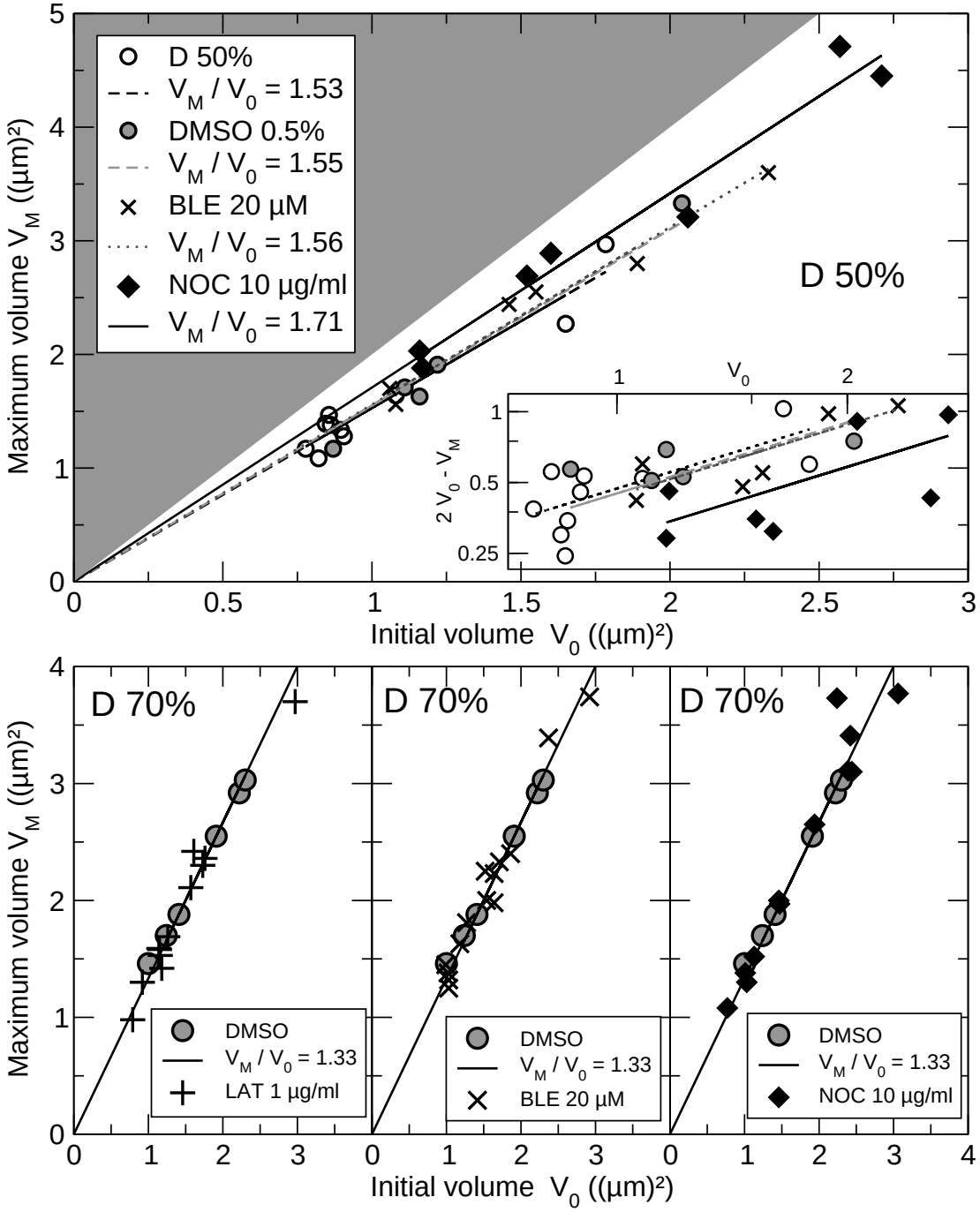

Figure 6.11: *Maximum volume V_M as a function of initial volume V_0 at temperatures 30-36°C.* **Top** *: 50% dilutions. Shown are : experiments without drugs (***open circles** *), DMSO 0.5 % (***shaded circles***), BLE 20 μM (***crosses***), and NOC 10 μg/ml (***black diamonds***). The dark region corresponds to $V_M/V_0 > 2$, the theoretical maximum for a 50% dilution.* **Inset** *: log-log plot showing the distance to the theoretical maximum, $2V_0 - V_M$, as a function of V_0. All lines are least-squares fits to $y \propto x$.* **Bottom** *: 70% dilutions.* **From left to right** *: treatment with LAT 1 μg/ml, BLE 20 μM, NOC 10 μg/ml. The data for DMSO 0.5% is shown for comparison. The lines are the fit to the DMSO data.*

Nocodazol increases swelling

A slight increase in the degree of swelling after a 50% shock is induced by nocodazol treatment, as shown in Fig.6.11. The lines are fits forced to go through the origin. Neither BLE-treatment nor DMSO alone have a significant effect on the maximum volume, whereas microtubule disruption increases the average swelling from 53% to 71%. This is not a small amount, as it has to be compared to its upper bound 100% corresponding to the osmometer value. The "forbbiden region" $V_M/V_0 > 2$ is shaded gray in the plot. As shown in the lower half of Fig.6.11, nocodazol does not affect V_M/V_0 at milder shocks (70%). Fig.6.12 shows that the perfect osmometer behavior which normally holds until $D = 70\%$ is extended by nocodazol up to 50% dilutions. This indicates that microtubule integrity is essential for the regulatory processes taking place during swelling.

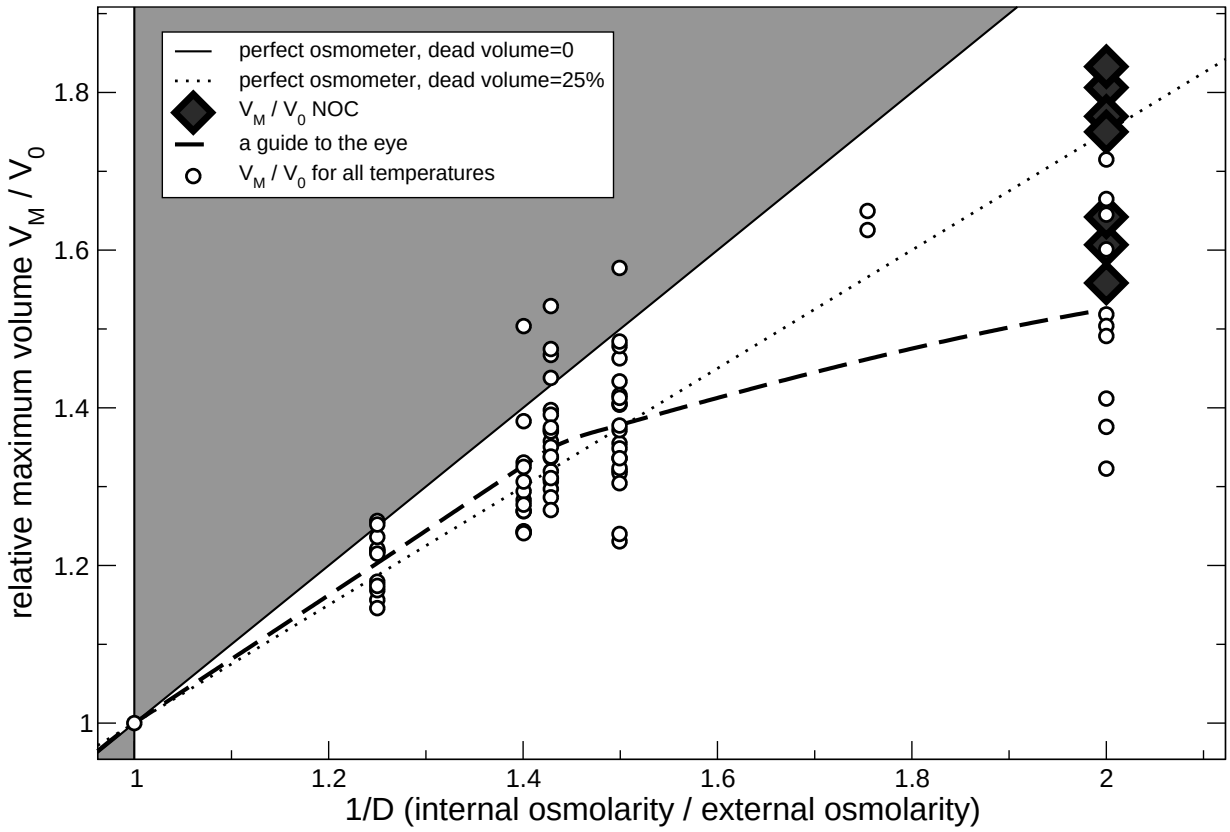

Figure 6.12: *Maximum relative volume V_M/V_0 as a function of the osmotic pressure difference $\Delta\Pi$, for all temperatures. The broken line is a guide to the eye, corresponding to an Akima spline going through the average values. Curves corresponding to perfect osmometers with dead volumes of 0 (solid line) and 25% (dotted line) are shown. The shaded region correspond to $V > V_0/D$. This is the same data as in Fig.6.6, but only for $D < 1$ and with the addition of the NOC experiments.*

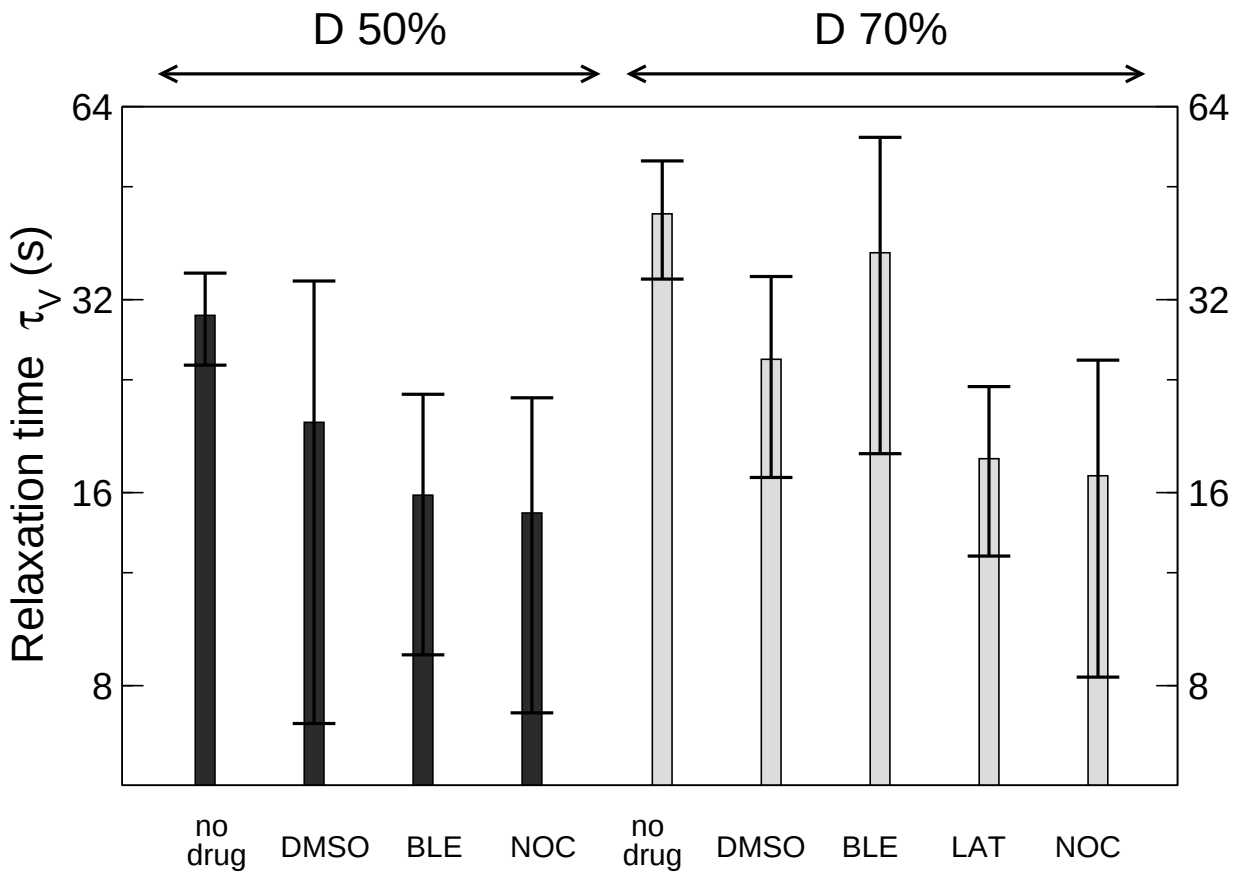

Figure 6.13: *Relaxation time τ_V for different drug treatments, at temperatures 30–36°C. Dark bars : 50% dilutions. Light bars : 70% dilutions. Data is shown as mean $\pm$2 S.E.*

Volume relaxation is still there

The most important result gained with drug-experiments is that cytoskeleton disruption does not abolish the relaxation phase. The relaxation time τ_V does not become longer under cytoskeleton disruption. In fact, a small but significant decrease is observed, as Fig.6.13 shows.

Moreover, neither myosin-II blocking nor actin or microtubule disruption prevents the volume from fully relaxing back to its initial value. Fig.6.14 shows the minimum volume V_m minus the initial one V_0 for all drugs and dilutions 50%–70%. The tendency to undershoot after a strong shock is seen to remain after all drug treatments. This, along with the absence of an increase in τ_V, is strongly against our previous ideas of the cytoskeleton providing the driving force for relaxation (43).

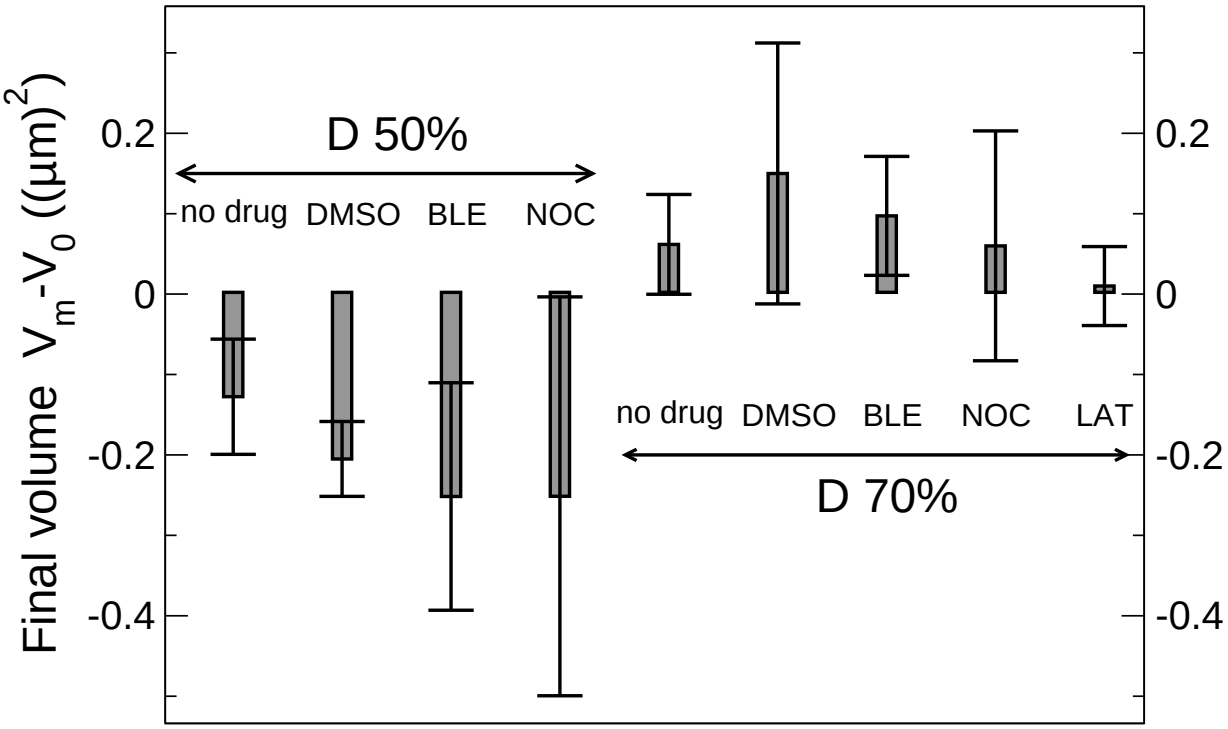

Figure 6.14: *Minimum volume post-relaxation V_m minus the initial volume V_0, at temperatures 33–$36°C$. On the left are 50% dilutions, on the right 70% dilutions. Negative values correspond to undershoots : after relaxation the neurite volume goes below its intial value. Concentrations: DMSO : 0.5%, BLE : 20 μM, NOC : 10 μg/ml, LAT : 1 μg/ml. Data is shown as mean $\pm$2 S.E.*

6.2 Pearling instability

When the hypoosmotic shock is strong enough, typically for $D \geq 70\%$ at temperatures in the range 30–36°C, a periodic peristaltic modulation sets in, grows without major changes in wavelength and eventually dies out. The following important features always hold:

- The modulation sets in only when the neurite *swells*, in a hypoosmotic shock experiment. Performing a hyperosmotic shock always induces shrinking, but never a cylindrical-peristaltic transition.
- The modulation sets in only at strong shocks. When done in small steps, the extracellular medium can be diluted to pure water without shape alterations (43).
- The modulation is never observed in a hyperosmotic shock, when *increasing* the extracellular osmolarity.
- During swelling, initially floppy and slack neurites become straight and tense. The modulation sets in precisely as the neurite straightens up. As the modulation vanishes, the neurite recovers its floppyness.
- The modulation is very periodic. The wavelength depends on the radius, in a roughly linear fashion. Typical wavenumbers $2\pi r_0/\lambda$ are in the range 0.3–0.5. Modes beyond the range 0.2–0.7 are never seen for the observed range of radii 0.4–1.1 μm.
- Where a change in the dominant mode is observed, it is always a coarsening evolution: longer wavelengths overtake shorter ones.

Cylinder-peristaltic shape transformations have been observed in membrane tubes, triggered by application of laser tweezers (44, 174). They have been successfully explained as shape instabilities triggered by membrane tension, the dominant wavenumber corresponding to the fastest growing mode in the linear regime (176). The results presented here support a similar explanation in axons. The fact that only fast, strong swelling triggers the modulation, as well as the straightening and decrease in floppynes, are evidences for mechanical tension as the driving force. The observation of coarsening confirms that the initially dominant mode is not more stable than others with longer wavelengths – it just grew faster. Finally, similar values for the dominant wavenumbers are observed. Fig.6.15 intends to convey a feeling for the situation in neurites.

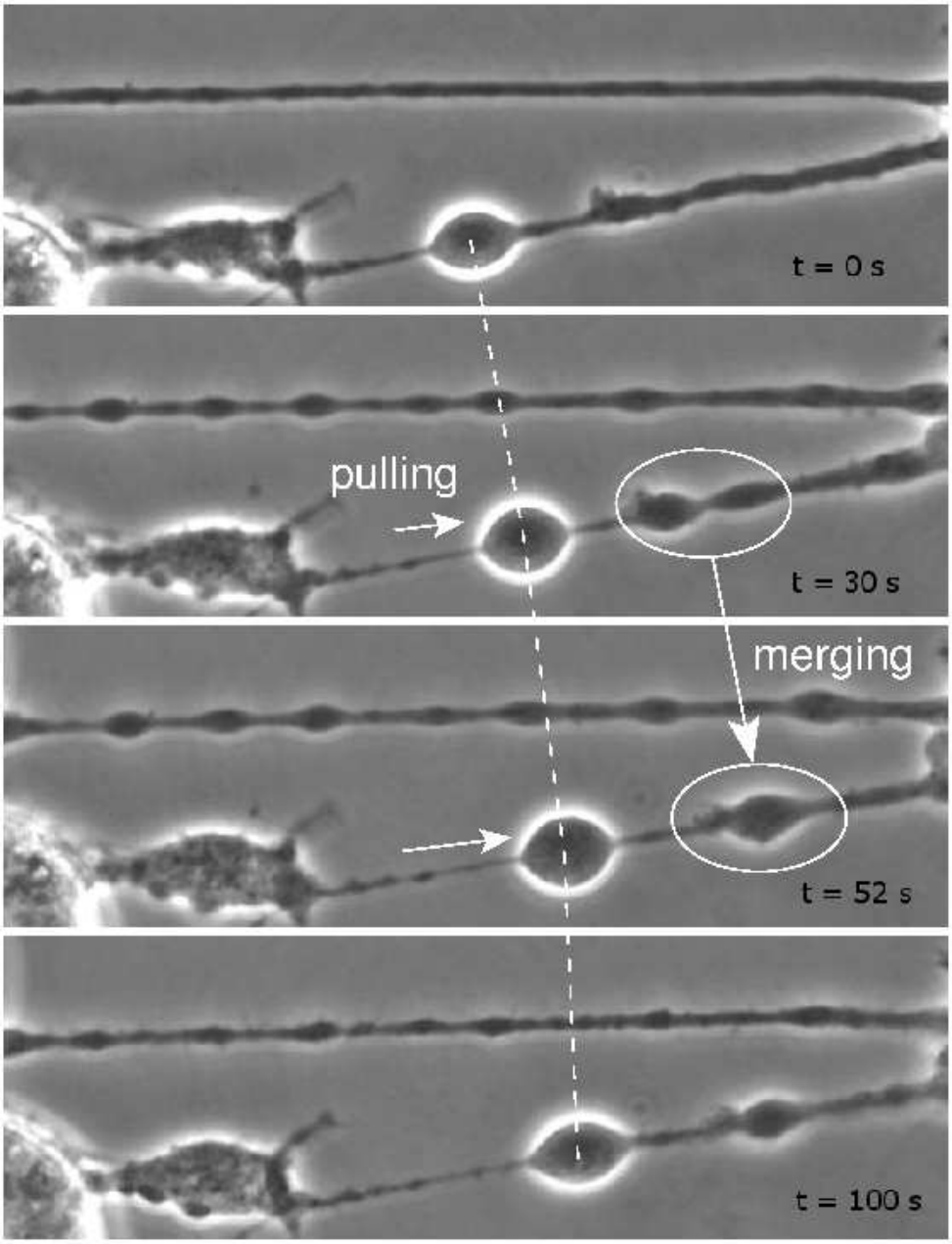

Figure 6.15: *Neurite response after a strong hypoosmotic shock at time $t = 0$ s. The neurite on the top shows strong pearling and relaxation. Once the relaxation is over, the neurite becomes tortuous and thin hair-like protusions grow out. The neurite volume "undershoots" below its initial value. The neurite on the bottom is already irregular to begin with. The biggest varicosity can be seen to swell, round up, and simultaneously move towards the right. An example of merging of two varicosities into one can also be seen. This illustrates the presence of tension in the membrane.*

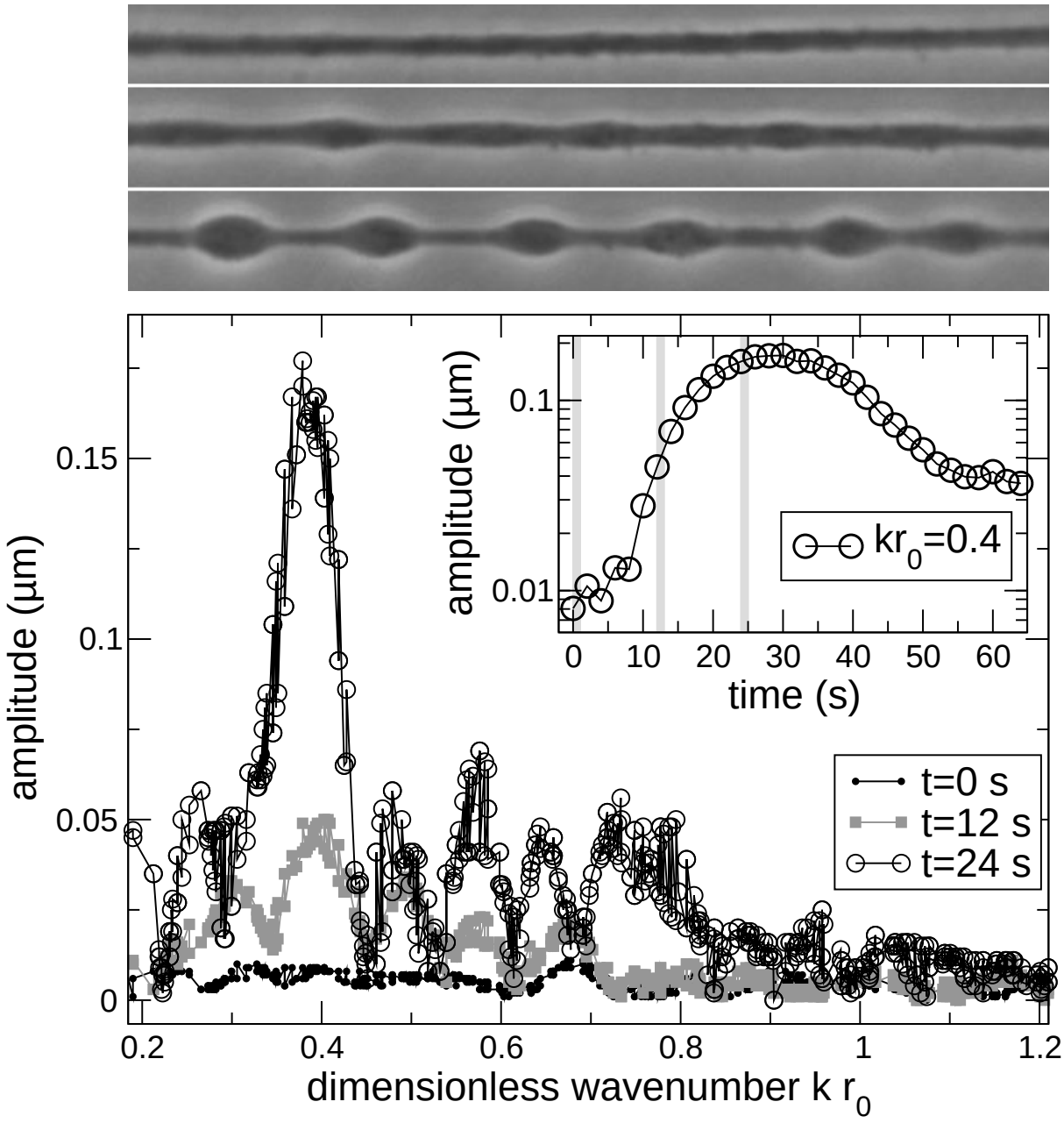

Figure 6.16: *Fourier spectrum of a neurite shape for different times.* **Images:** *Images of the neurite at times 0 s, 12 s, 24 s. The neurite diameter is* $\simeq 1\,\mu m$. **Plot:** *Spectra of the neurites shown in the images.* **Inset:** *Amplitude of the dominant mode as a function of time.*

In order to characterise the dominant modes at the onset of the instability, we took discrete Fourier transforms of the radius of the neurite. With the procedure discussed in chapter 5, the dominant wavenumber can be found with an accuracy of $\sim 10\%$. In most cases, the spectrum shows a well-defined fastest mode. Fig.6.16 shows an example. Sometimes coarsening is seen; the dominant mode in the spectrum slows down and is overtaken by an initially slower mode with a longer wavelength. An example is given in Fig.6.17. Coarsening does not takes place in a "continuous" fashion, by a smooth translation of the spectrum; rather, an already-present mode with a smaller wavenumber increases in amplitude until it dominates. Sometimes coarsening occures in a spatially local fashion as two varicosities abruptly merge into one, as shown before in Fig.6.15.

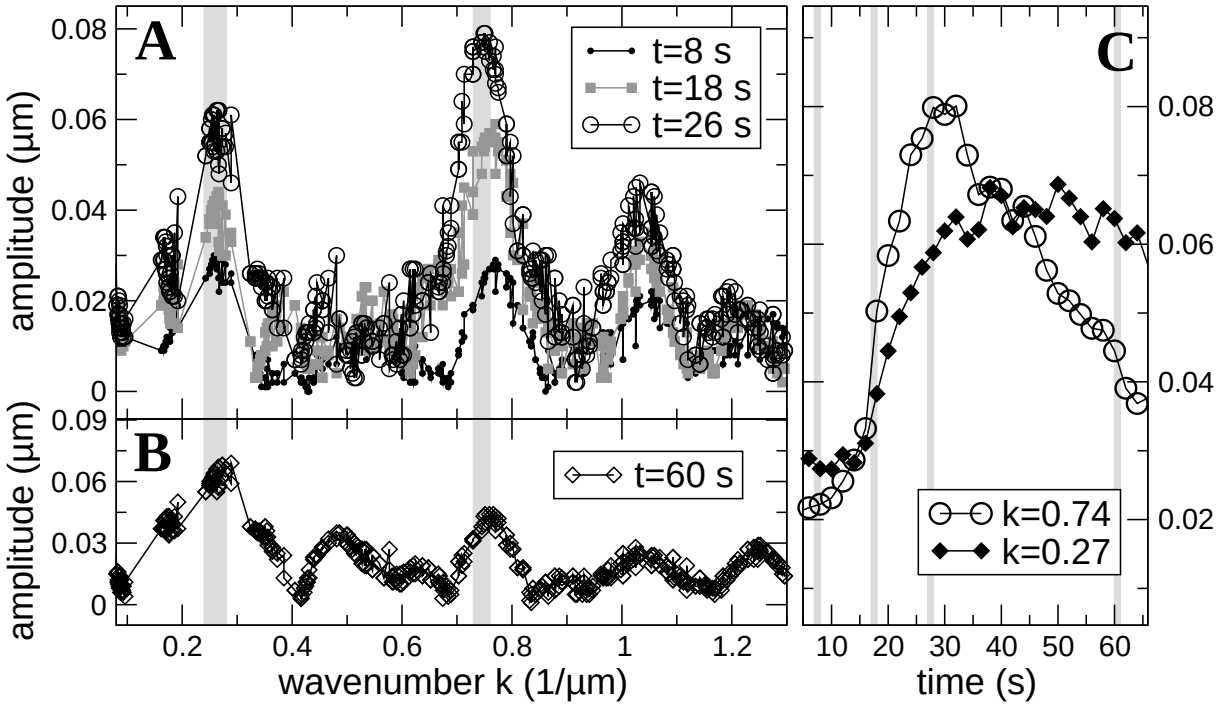

Figure 6.17: *Example of coarsening.* **A:** *Fourier spectra of neurite shape at times 8 s, 18 s, 28 s. The medium is diluted at* $t = 14$ *s.* **B:** *Fourier spectrum at* $t = 60$ *s. At this late stage, the initially dominant mode at* $k = 0.74\,\mu\mathrm{m}^{-1}$ *relaxes and a lower mode at* $k = 0.27\,\mu\mathrm{m}^{-1}$ *takes over.* **C:** *Evolution of the two main modes* $k = 0.74/\mu$*m,* $k = 0.27/\mu$*m: amplitude (*μ*m) as a function of time. The shaded areas indicate the times 8, 18, 28, 60 s, corresponding to the spectra shown in* **A, B**.

6.2.1 Effect of drugs

The dominant wavelength depends on the initial size of the neurite. As with most size dependences, the small range and large scatter complicate finding a functional form. Based on previous data indicating that the wavelength depends linearly on the initial radius r_0 (43), we take the adimensional wavenumber kr_0 to characterise the peristaltic modulation. The adimensional wavenumber kr_0 does not depend significantly on the dilution. Fig.6.18 shows kr_0 for different drug treatments. Though the effect is in general feeble, one may say that cytoskeleton perturbation increases the wavenumber.

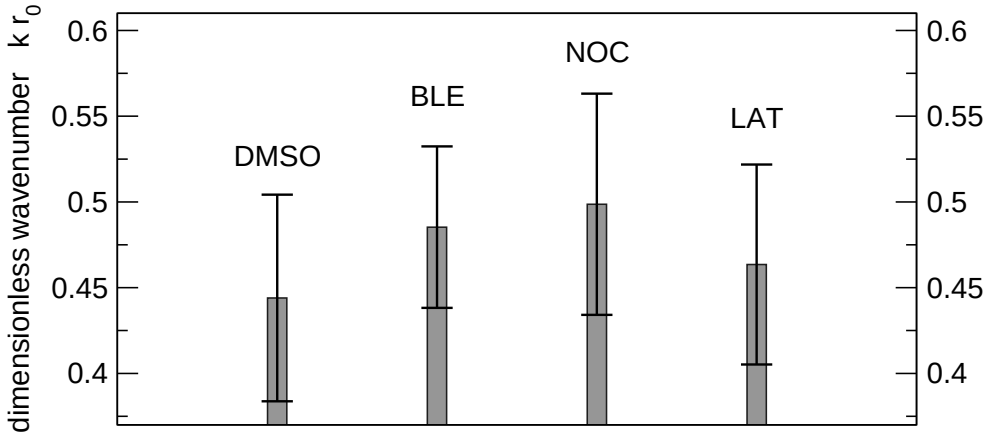

Figure 6.18: *Dimensionless wavenumber kr_0 for different drug treatments. Both 50% and 70% dilutions are averaged together. Data is shown as mean $\pm$2 S.E.*

The total extent of pearling is best quantified by the maximum value of the pearling parameter $\sqrt{V}/A$, which takes into account all modes present. Fig.6.19 shows it for different drug treatments. Here, the effect of the drugs is clear. Microtubule disruption in particular is seen to cause very strong pearling.

6.2.2 Area-pearling decoupling

The instability is seemingly triggered by a tension of elastic nature, due to the membrane stretch induced by the swelling. Unexpectedly, on the average the instability relaxes well before the volume and the area do. This can be seen in the experiment shown in Fig.6.20, where several reproducible features are present. The modulation sets in only after the volume and area change by a finite amount. On the average, this occurs at a relative change in area of 10%. The area reaches a maximum value $A_M/A_0 \sim 25\%$, a high value compared to the tensile strength of lipid bilayers, which rupture beyond 4–5% area change. Finally, the modulation vanishes well before the area and volume do; typically, when $A = A_0 + 0.8(A_M - A_0)$, i.e. the area has barely relaxed.

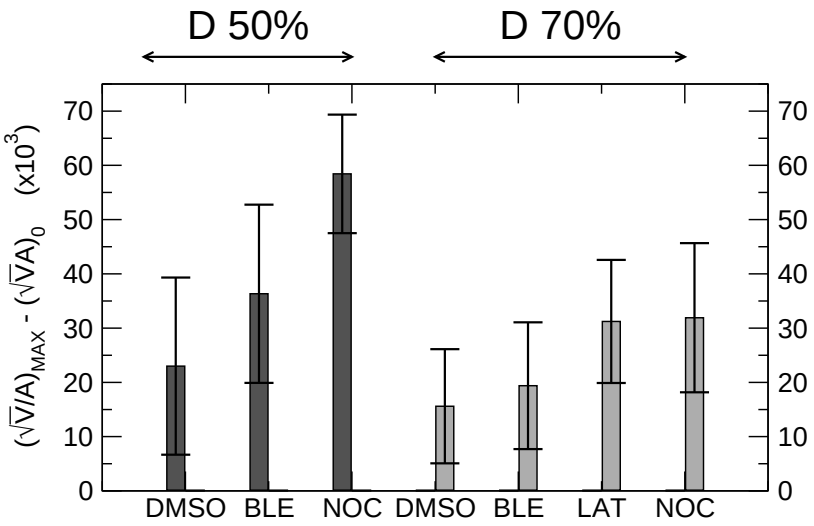

Figure 6.19: *Maximum value of the pearling parameter* $(\sqrt{V}/A)_{\mathrm{MAX}}$ *minus its initial value* $\sqrt{V_0}/A_0$*, for different drug treatments. Microtubule disruption is seen to have a strong effect on the extent of pearling.*

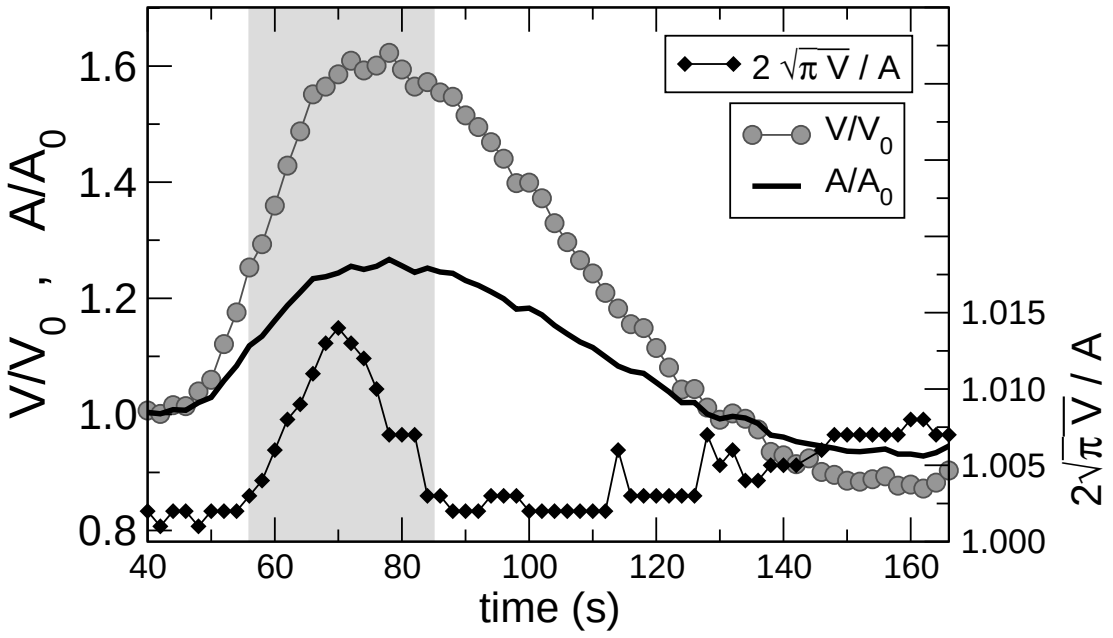

Figure 6.20: *Relative volume* V/V_0*, area* A/A_0*, and normalized degree of pearling* $2\sqrt{\pi V}/A$ *as a function of time. Control experiment performed in presence of DMSO, at 30°, dilution D = 50%. The shaded region corresponds to the peristaltic-modulation geometry, where the pearling parameter* $2\sqrt{\pi V}/A$ *deviates from 1. It can be seen that the cylindrical shape is recovered well before* V *and* A *have relaxed. Notice also the strong undershoot after relaxation both of* V *and* A*.*

6.3 Discussion

6.3.1 Pearling instability

Shape instabilities driven by surface tension have been known for a long time, beginning with the Rayleigh-Plateau instability in liquid jets (177, 185). In membrane tubes the situation is slightly different. Interfacial tension is not significant here; rather, one has an elastic tension arising out of membrane stretching, with enthalpic as well as entropic components (44, 174). Most important is the bending modulus of the membrane, which stabilises the cylindrical shape. Thus, the instability sets in only above a threshold tension (44). In biological systems, one may expect a much stronger stabilising effect due to the cytoskeletal gel connected to the membrane. This was demonstrated in Ref.(45), where pearling could be induced by actin disruption with Latrunculin-A.

Given this framework, the peristaltic modulation triggered by the hypoosmotic shock most likely obeys a similar mechanism. In this case the tension clearly arises out of membrane stretching due to neurite swelling. According to the detailed analysis of pearling in presence of the cytoskeletal gel undertaken in Ref.(43), the growth rate of the fastest mode increases steeply near the critical tension. Using realistic values for cytoskeletal elasticity, the critical tension is $\gamma \sim 3\,\mathrm{x}\,10^{-3}$ N/m, and the critical wavenumber $k\,r_0 \simeq 0.2$. One can estimate how much the membrane should be stretched to reach this tension. Lipidic bilayers as well as cell membranes (166, 186) have area stretch moduli of the order of 0.4 N/m, so that a relative area change of 1% would be necessary to trigger pearling. The observed value is $\sim 10\%$. Given the uncertainty in the measurement as well as in the precise values of cytoskeletal stiffness, the agreement is reasonable. In any case, as discussed below we believe addition of material to the membrane to take place, so the real stretch should be lower than its apparent value. At very high tensions, the theoretical wavenumber approaches a maximum, $k\,r_0 \to 0.65$, corresponding to an incompressible tube with vanishing elasticity (43, 176). The observed wavenumbers $k\,r_0$ lie in the range 0.3–0.5, well within the theoretical range 0.2– 0.65, showing cytoskeletal elasticity to be important in stabilising the neurite.

If the instability is indeed driven by a stretching-induced increase in membrane tension, it comes as a surprise that the pearling amplitude fully relaxes when the apparent area is still 10–20% larger than its initial value, as shown in Fig.6.20. The natural explanation is that material is added to the membrane as a response to the increased tension. This also explains the fact that relative changes in apparent area typically reach 20%, whereas membranes are known to break beyond 4–5% (see Ref.(186) and references therein). This extra material may come from intracellular stores via vesicle fusion. This is a reasonable hypothesis, since membrane addition in response to increased tension is a general feature of animal and plant cells (186). An alternative explanation is a change in apparent area via unfolding of membrane ruffles. This mechanism allows cells such as blood granulocytes to increase their apparent surface area by $\sim 100\%$ (187). We find this however unlikely, since electron microscopy shows PC12 neurites to have a rather smooth membrane, without invaginations (188). Finally, we cannot rule out the possibility of membrane flowing in from the ends of the neurite.

Based on the theoretical analysis in Ref.(43) and again taking a stretch modulus of 0.4 N/m, a

fastest wavenumber $k\,r_0 = 0.6$ corresponds to an area stretch of $\sim 3\%$. Therefore, our picture is consistent; the tension γ corresponding to the highest wavenumbers observed is not yet enough to break the membrane, but almost.

If a hydrostatic pressure difference is present, and the cytoskeletal gel is firmly connected to the membrane, adding area to the membrane will not lower its tension unless the gel also expands. Therefore a plastic flow process must also be taking place in the cytoskeletal gel, analogous to the uncoupling between apparent area and tension in the membrane. Unlike in the latter case where we expect addition of material to be the underlying mechanism, the decoupling between gel volume and tension most likely involves sliding of connections between cytoskeletal filaments.

6.3.2 A pearling mechanism which does not work

If one neglects lateral flow in the continuity equation 5.3 and only regards permeation through the membrane, the following dispersion relation can be found:

$$1 - (k\,r_0)^2 = \omega \frac{r_0^2}{\gamma\,\mathcal{L}_W}$$

This is a very unlikely explanation for the pearling instability. Taking 10 nm/(MPa.s) for $\mathcal{L}_W$ as estimated from the initial swelling, a radius $r_0 = 0.5\,\mu$m and an almost-lytic membrane tension $10^{-3}\,\mathrm{N/m}$ (186), the timescale for the instability growth is 10^5 s, 4 orders of magnitude slower than observed. Moreover, the dispersion relation gives a fastest mode with infinite wavelength, in disagreement with the measured values.

6.3.3 Volume Regulation

It was the interpretation of the peristaltic modulation as a membrane-tension triggered instability what motivated our study of the volume regulation process. The occurence of the pearling instability indicates that significant hydrostatic pressures can be sustained by the membrane for long times; roughly simultaneously, the neurite volume relaxes back to its initial value. The question arises immediately: do these pressures play a role in volume regulation? As discussed in Chapter 5, the idea has been around for some time, but up to date there is no clear experimental evidence.

A remarkable observation is that the swelling rate does not change significantly between 70% and 50% dilutions (see Fig.6.4). Moreover, microtubule disruption dramatically increases the swelling rate at 50%, yet barely at 70%. These results indicate that the initial swelling phase does not obey $\dot{V}_0 = A_0 \mathcal{L}_w\,\Delta\Pi_0$. It seems likely that significant hydrostatic pressures are present already at this early stage, in agreement with the pearling amplitude being stronger at $D = 50\%$. Thus, at stronger shocks the tension in the membrane must be significantly higher, though the swelling rate does not change much. But then, if this tension is of purely elastic nature, i.e. given solely by the extent of deformation of the cytoskeletal gel, why should it be higher? Though we do not have direct evidence, it is tempting to regard this as reflecting rate-independent plasticity. As discussed above, the fact that pearling relaxes well before the volume indicates that

plastic flow takes place. One may speculate that the plastic strain rate of the neurite cytoskeleton depends only weakly on stress, and that this plastic flow process determines the swelling rate $\dot{V}_0$. This would explain the observed facts: at $D = 50\%$ tensions are higher, resulting in stronger pearling, but the swelling rate does not change significantly.

Since at $D = 50\%$ the neurite does not reach maximum swelling in a significantly shorter time than at $D = 70\%$, it is surprising to see deviations from the osmometer behaviour only at $D = 50\%$, as shown in Fig.6.6. If the response mechanisms do not have more time to act, what stops the swelling? That the neurite senses the extracellular osmolarity seems unlikely. Based on the previous discussion, we suggest that hydrostatic pressure builds up at strong shocks and balances the osmotic pressure difference. Accordingly, after microtubule disruption neurites swell as much as perfect osmometers at $D = 50\%$. Similar results have been reported in red blood cells: cell swelling increases after disruption of the spectrin-actin network, approaching perfect osmometer behaviour (172).

At strong shocks, a clear difference is seen between the responses to hypo- and hyperosmotic shocks. After hypoosmotic swelling, volume relaxation is fast and often "undershoot" of the volume is observed, whereas after hyperosmotic shrinking the volume relaxation time τ_V is 2–3 times larger and "overshoot" is infrequent. It may be speculated that the high membrane tensions at $D = 50\%$ open up mechanosensitive channels, triggering more extensive regulatory mechanisms (148, 149).

Thus, hydrostatic pressures do seem to play a role in the volume evolution during the initial swelling phase. During the subsequent relaxation, however, they are irrelevant. This can already be suspected from the fact that pearling amplitude often relaxes well before volume regulation is over. More conclusive are the results from the cytoskeleton perturbation experiments. Neither the volume relaxation time τ_V becomes longer nor the final volume $V_m - V_0$ increases under the influence of drugs. The trend is in fact in the opposite direction, τ_V shortening slightly. The drugs undoubtedly have an effect on the neurites, as they increase markedly the swelling speed $\dot{V}_0/A_0$; moreover, as described above, the degree of pearling as well as the wavenumber increase. The effect on the pearling instability is particularly relevant, as they strongly indicate a reduction in the elasticity of the cytoskeletal gel.

As a function of the precise drug treatment, good agreement is seen between the volume and the pearling response. Microtubule disruption always has the largest effect. According to Cornet *et al*, volume regulation in round PC12 cells is not affected by microtubule disruption (161). This agrees with our hypothesis of a mechanical role for microtubuli, since these are organised very differently in round cells and neurites. In the latter, their bundle structure may provide a rigid scaffold opposing swelling. Moreover, electron microscopy observations of the ultrastructure of stretch-beaded nerves (189) show microtubules to be splayed out in the beads, suggesting that they are firmly connected to the membrane. The biochemical nature of this connection is at present not known. According to our results, treatment with Latrunculin-A or blebbistatin does not have such a strong effect on swelling or pearling as nocodazol treatment, suggesting that the actin cortex is not the link between microtubuli and membrane.

6.4 Outlook

The strong effects of microtubule disruption both in the swelling and in the pearling response beg for thorough study. Our results suggest that the effect of nocodazol on swelling is due to hydrostatic pressures balanced by plastic flow of the microtubule array. An easy way of studying this is to observe the effect of nocodazol on hyperosmotic shocks, since no significant membrane tension arises when the neurite shrinks. If the effect of nocodazol is symmetric, affecting the shrinking- as much as the swelling rate, then the idea is probably wrong. Also interesting would be to study swelling of neurites fixed at a low concentration of glutaraldehyde. If fixation precludes plastic behaviour, the swelling phase should change significantly. A complementary experiment would be to study volume regulation on round PC12 cells, e.g. by holding them with a laser tweezer as in Ref.(168).

These results suggest that tension in the membrane triggers a fast, strong ion efflux responsible for RVD. It is tempting to speculate on stretch-activated Ca^{2+} channels behind this response. It would be therefore interesting to do strong hypoosmotic shock in absence of extracellular Ca^{2+}, and see whether fast volume undershoot still takes place. Alternatively, one may block calcium channels with Gadolinium (150, 151).

A so far unexplored parameter is the dilution rate. Systematic experiments varying the dilution rate may shed light both on pearling and on volume regulation. In particular, it may help distinguish stretch-sensors from concentration-sensors. If the strong volume relaxation responses seen at $D = 0.5$ are indeed triggered by stretch-activated channels, then they should be absent when the external osmolarity is slowly taken to zero, without inducing pearling. Setting up a mixing chamber to perform such an experiment should be technically straightforward.

Appendix A

Visualising the confined cytoskeleton

Fibroblasts often respond to the presence of two fibronectin coated walls by spreading symmetrically between them. Under these conditions strong forces develop and highly reproducible mechanical behaviour can be observed. A typical concave shape typically sets in. These we will call “good cells” throughout. A major problem arises when trying to visualise the cytoskeleton of good cells. The bulky, three-dimensional cell-pulling geometry difficults the microscopic visualisation of the cytoskeleton. The plethora of details seen in typical fluorescence pictures, such as those shown in chapter 2, requires a flat, essentially two dimensional cell. Fig.A.1 shows the kind of image obtained in the cell-pulling geometry. Deconvolution analysis of the images could not reveal any significant structure. In living GFP-actin cells the situation is worsened by the GFP-actin monomers, which contribute to the fluorescent background. Because of these complications, alternative strategies had to be developed.

Figure A.1: *GFP-actin fibroblast between fibronectin coated microplates.*

A.1 Watching from below

If one wants to come close to the 2-dimensional cells where so much detail can be seen, yet hold them between two coated walls, how to proceed? A simple solution is to squash a monolayer of cells between two coated glass slides and observe them from below. By pressing on the cells, one can lead them into a flat "pancake" geometry. We know from the single-cell experiments that their mechanical behaviour does not change significantly in such conditions. By having many cells between the slides, the measurement becomes much more efficient in comparison to studying single cells between microplates. The difficulty is keeping the two slides parallel to each other, a problem which also arises in the rheology experiments described in Appendix B. Here, where no mechanical measurement is performed, simpler solutions are available. Cells were compressed between a slide and a lens with a large focal length of 40 cm. Since the curvature of the lens is small, on a length scale of $\sim 100\,\mu\mathrm{m}$ the cells meet an essentially flat surface. This has the advantage of not requiring any adjustment to obtained the desired parallelity between the faces. The lense was mounted on a commercial micromanipulator. The lense and slide are coated with fibronectin by 1 hour exposure to a 10 μg/ml solution in PBS. The cells are introduced in the chamber, pressed with the lense and then left under compression for 1 hour.

A.1.1 Fixation and staining procedure

We follow the protocol recommended by Small and coworkers (190, 191), increasing slightly the incubation times because of the confined geometry. All steps are done at room temperature. The general washing medium is cytoskeleton buffer (CB), with composition: glucose 5 mM, HEPES 10 mM, EDTA 5 mM, 150 mM NaCl, 5 mM $MgCl_2$, pH 6.1. Cells are rinsed with CB, then fixed with a mixture of 0.25 % glutaraldehyde, 0.5 % Triton X-100 in CB for 2 minutes, rinsed with CB, fixed during 20 minutes in a 2.5 % glutaraldehyde in CB solution, washed once again with CB and finally left in CB. Cells were stained with Phalloidin-Rhodamine (Sigma-Aldrich, St.Louis, MO, USA), following the procedures outlined in Ref. (190). After fixation, in order to reduce free aldehyde groups cells were left for 10 min in a freshly prepared solution of sodium borohydride 0.5 g/l in phosphate buffer (PBS). Afterwards the fixed and reduced cells were washed with CB and stained for 20 min with a phalloidin-rhodamine solution.

A.1.2 Results and Outlook

This geometry allows a better resolution. Phalloidin staining reveals "clumps" of fluorescence uniformly distributed over the substrate. Fig.A.2 shows an example. An advantage of the setup is that adhesion strength can be corroborated by shearing the cells. Only those cells adhering on both surfaces are deformed.

Lack of time precluded a thorough study of cytoskeletal structure in this geometry. A number of important experiments remain to be done. Among them, the observation on living cells of the development of focal contacts, or whether actin restructuring can be induced by stretching or shearing the cells. The images should be improved by using for the top surface a flat glass window instead of a lens. This can easily be done following the procedure outlined in Appendix

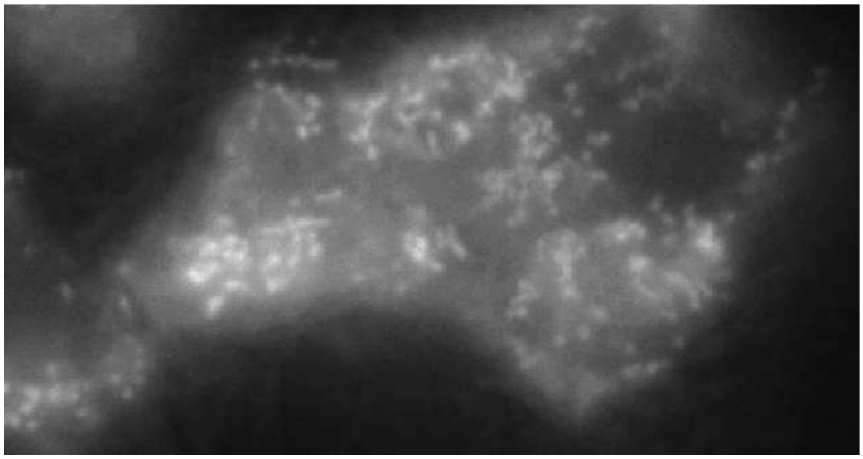

Figure A.2: *Fibroblasts adhering between two fibronectin-coated glass slides, observed from below, stained for F-actin with rhodamine-phalloidin. Notice the "clumpy" distribution of fluorescence.*

B. An interesting possibility would be to combine this geometry with total internal reflection fluorescence microscopy, which may be done on the bottom as well as on the top surface.

A.2 A pattern of walls

If the cytoskeleton is to be visualised at a high resolution, to gain information on the mesh size, distance between crosslinks, bending of individual filaments, degree of affinity, etc., one must do electron microscopy. This requires fixing and mounting the cells in the desired configuration. Once the cells are mounted and cut in thin slices, the rest is in principle straightforward. The crucial step is preparing the cells. For this, patterned substrates were made where the cells could adhere in the cell-pulling geometry. Particularly good turned out to be long, tall walls, $\sim 25\,\mu$m tall, $10\,\mu$m wide, separated by $10\,\mu$m. When cells are placed on the pattern, most of them crawl within a few minutes into the grooves, adopting shapes remarkably similar to those typically observed in the cell-pulling experiment. Since the grooves are $\sim 25\,\mu$m deep, the cells never reach the bottom and the topology is equivalent to that of the experiment.

Procedure

The pattern is made following a standard lithographic procedure, by shining UV light through a mask on a photoresist. To achieve high aspect ratios, the negative photoresist SU-8 50 (Microchem, Newton, MA, USA) was used. Coverslips were left in a Hellmanex II 1% solution overnight, rinsed with millipore water, cleaned with a "piranha" solution (50% H_2O_2, 50% H_2SO_4) for 10 minutes, rinsed with millipore water, left in millipore water for 10 minutes in a sonicator, placed on a heating plate and left for 1 hour at 200° to remove water completely.

Immediately afterwards they were introduced in methanol and sonicated for 10 minutes, transfered to acetone and again sonicated for 10 minutes. Finally they were left in a clean hood to dry. The clean coverslips were spin-coated with SU-8 photoresistor in 2 steps: 10 s at 500 rpm, 30 s at 3000 rpm. Immediately afterwards they were baked in 2 steps: 5 min at 65°C, 15 min at 95°C. Care was taken to minimise exposure to light during the bake. The coated coverslips were processed in an EVG620 mask aligner (EV Group). Best results were achieved by working in the hard contact mode, where the coverslip is pressed against the mask by a stream of air. The coverslips were exposed to UV light with an intensity of 40 mW/(cm)^2 for 6 s, and immediately afterwards baked in 2 steps: 1 min at 65°C, 4 min at 95°C. Exposed coverslips were developed with the developer XP SU-8 (Micro Resist Technology GmbH). The development time had to be fine-tuned for each set of coverslips, and was usually about 8 min. Immediately after development coverslips were rinsed with isopropanol and dried with a gush of nitrogen or argon. To fully harden the photoresistor the coverslips were baked for 10 min at 200°C.

Once hardened the substrate is indeed hard, so one can check the quality of the pattern by cutting it and observing it from the side. We cut the coverslips by running a diamond tip over the non-coated side; as the coverslip breaks, the pattern breaks along. Fig.A.3 shows the quality of the pattern.

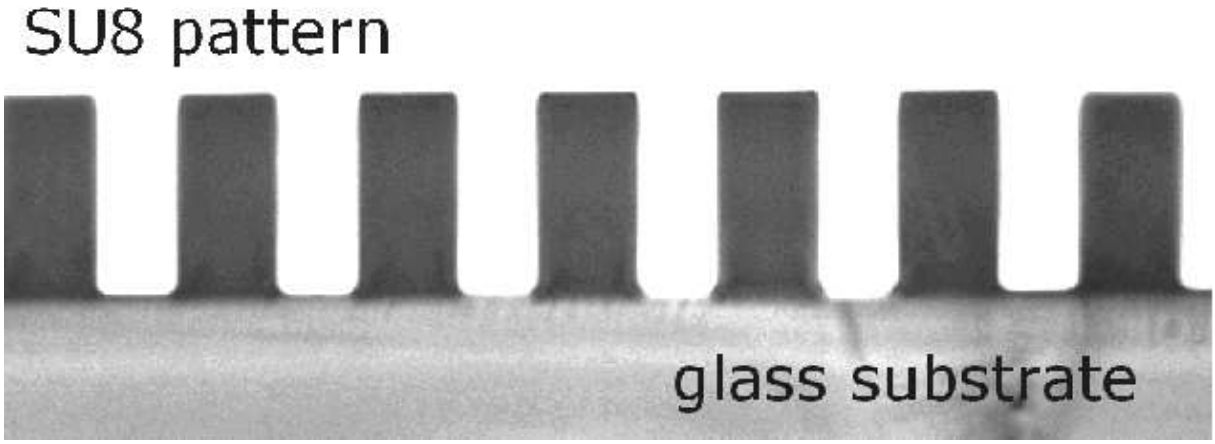

Figure A.3: *Side view of the SU8 pattern: light microscopy image. The walls are 10 μm thick, separated by 10 μm. The glass coverslip is on the lower side. The grooves are seen to be straight all the way down to the coverslip.*

A.2.1 Results

The pattern is coated with fibronectin by exposure to a 10 μg/ml fibronectin in PBS solution for 1 hour at room temperature, then rinsed with PBS. Fibroblasts are prepared following the procedures explained in chapter 3, and then simply dumped on the patterned substrate. After 10 minutes incubation, most cells have crawled into the grooves and spread evenly between two walls, as can be seen in Fig.A.4.

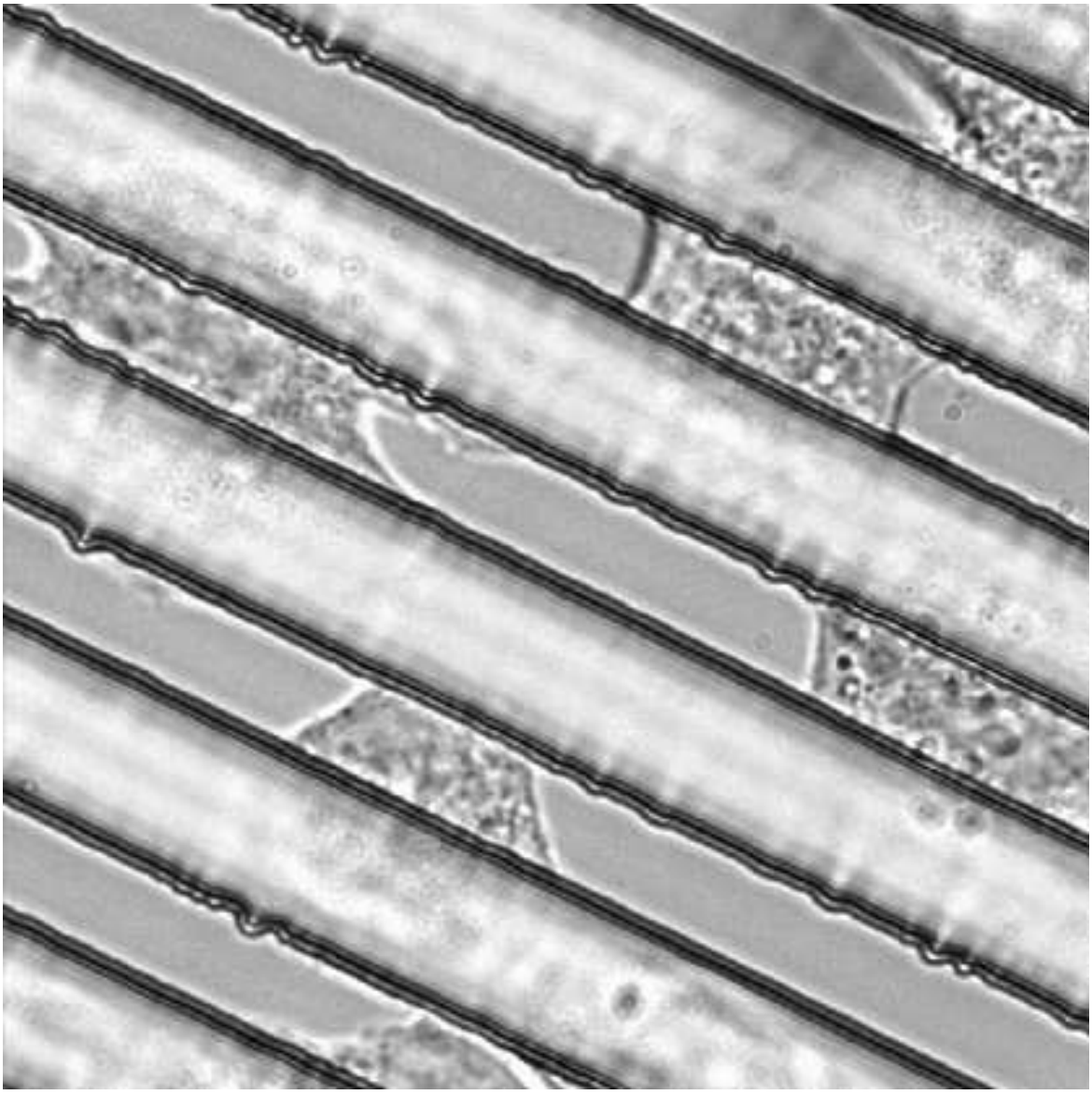

Figure A.4: *3T3 fibroblasts adhering between fibronectin coated walls.*

Fig.A.5 shows fibroblasts in the patterned substrate fixed and stained with phalloidin-rhodamine. Again, though some structure inside can clearly be seen, not much can be understood.

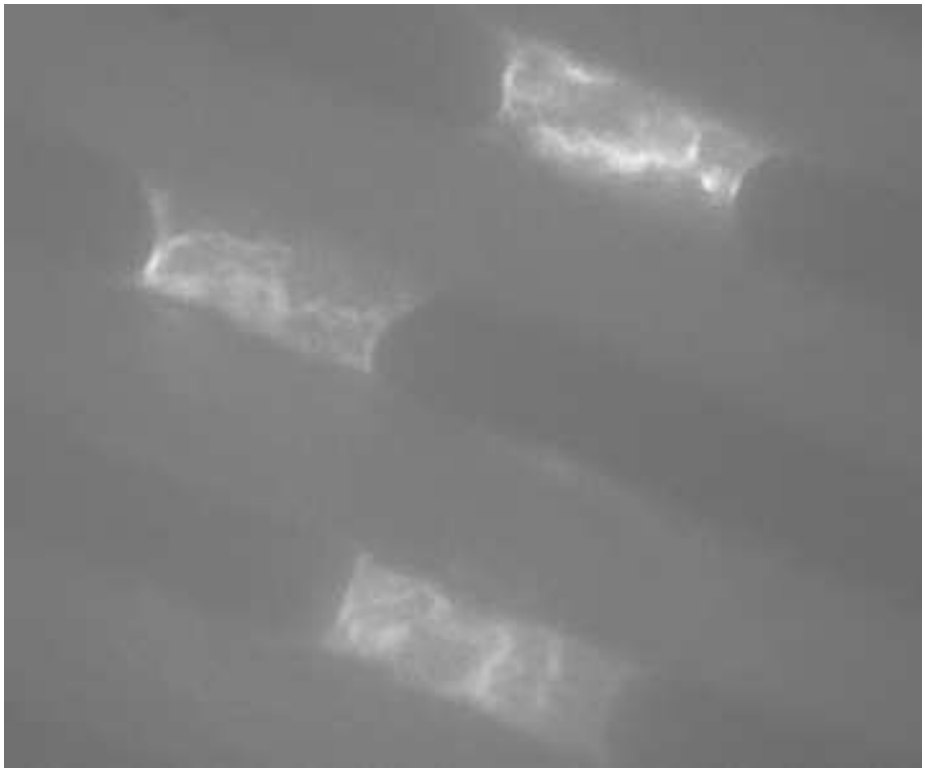

Figure A.5: *Fibroblasts in the patterned substrate stained with phalloidin-rhodamine to visualise F-actin.*

A.3 Outlook

The developed procedure works remarkably well. The shapes taken by the cells resemble closely those of good cells in the cell-pulling experiment. Some even spread in a tilted fashion, also seen in the experiment. In principle, the fibroblasts placed on the pattern can choose between adhering over the walls or crawling into the grooves. Most cells do the latter, which indicates that the cell-pulling shapes are a robust consequence of the geometry. Thus, one may expect cells inside the pattern to generate similar cytoskeletal structures as those in the cell-pulling rheometer.

The next step is doing electron microscopy on the cells in the pattern. The cells should be fixed and mounted; then slices can be cut and studied. Here the pattern geometry will be very helpful. One may for example cut along the grooves, to observe the cross-section perpendicular to the pulling direction. One may also cut parallel to the substrate and look for structure along the pulling direction. Can stress fibres be seen? Ideally, one would want to study the shape of actin filaments, and compare cross-sections perpendicular to the walls to the ones parallel to them. If the load is taken by filament bending, it may be resolvable by electron microscopy; to leave the linear regime a cantilever must be bent by $\gtrsim 30\%$.

Appendix B

Rheology of a fibroblast monolayer

As a complement to the single-fibroblast experiments, a collaboration with Prof. Nuri Aksel (Lehrstuhl für technische Mechanik und Strömungsmechanik, Universität Bayreuth) was initiated. The goal was to measure mechanical properties of living cells using commercial shear-rheometers, to provide an independent check of the single-cell results. For this, appropriate procedures must be developed. Large numbers of cells are necessary, and the cell-pulling geometry and boundary conditions must be mimicked.

B.1 Setup

The rheometer used is a Physica MCR-500 (Anton-Paar GmbH) in a plate-plate geometry. The bottom metal plate is fixed. The top metal plate rotates and is used to measure both torque and normal force.

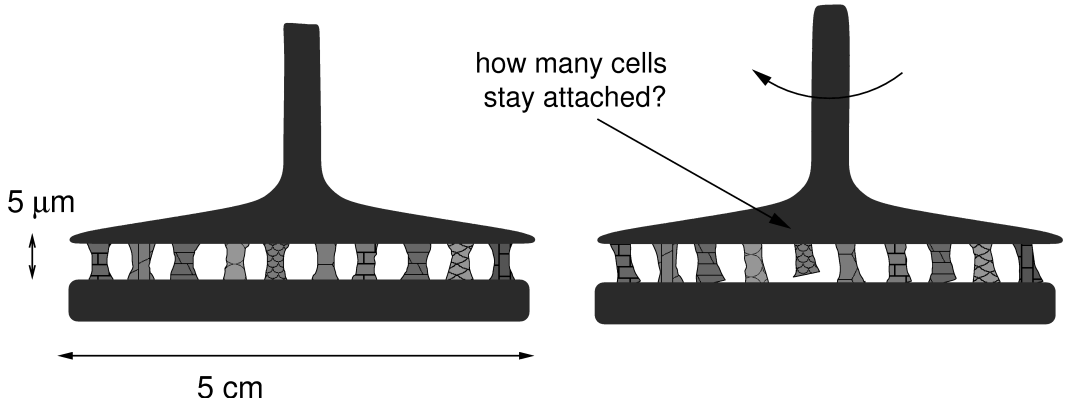

Figure B.1: *Cartoon illustrating the intended fibroblast-monolayer experiment. How does one prepare the system? How does one introduce between the plates a cell monolayer 5 μm thick and 5 cm wide? How many cells actually contribute to the force measurement?*

A major problem in measuring the mechanical properties of a monolayer of cells is achieving the required parallelity between the two faces on which the cells stick. Since cells are so soft, the total area must be of the order of 20 (cm)^2 for the rheometer to resolve forces. Cells being about 20μm in diameter, the opposing faces must be parallel to each other within $1\,\mu\mathrm{m}/10\,\mathrm{cm} = 10^{-5}\,\mathrm{rad}$. Such a precision is close to the rheometer specifications, but a preparation step is absolutely essential in order to ensure it. A further complication is the need to coat the plates with a fibronectin layer, for the cells to stick and develop positive pulling tensions. To tackle both problems, the following procedure was developed.

Glass plates with a surface flatness of $\sim$500 nm are fixed on the metal plates of the rheometer. To ensure perfect parallelity between the two faces of the glass plates, these are in close contact with each other throughout the fixation. This is accomplished by glueing them with an adhesive which cures in a few minutes under UV-exposure. The glass plates can then be coated with fibronectin and the cells introduced. Fig.B.2 illustrates the procedure.

1. The top glass plate is carefully put in contact with the bottom glass plate. By looking at the interference fringes generated in the spacing between the plates, the quality of the alignment can be checked. If the plates are optically flat, then achieving the desired parallelity only implies cleaning them properly. In particular, dust particles can be a problem.

2. Once the glass plates are satisfactorily in contact with each other, they are placed on the rheometer. The bottom glass plate is fixed to the bottom metal plate with wax, which can be easily removed by heating the metal plate to 60°C.

3. The top metal plate is brought down until contact with the top glass plate. This is automatically done by the rheometer as a normal zero-point setting.

4. The top metal and glass plates are glued together using the UV-curable adhesive Vitralit 6129 (Panacol-Elosol GmbH). This is a thick adhesive with a very low thermal expansion coefficient of 36 ppm/K, which later can be easily removed by leaving overnight in acetone. Being fairly viscous, the glue does not flow into the gap between the plates, which would complicate later disassembly. Application of a thin layer of glue on a few strategic places is enough. The glue is cured by exposure for a few minutes to UV light with a wavelength of 365 nm and an intensity of $\sim$100 mW/(cm)^2.

5. Once the glass plates are positioned, they must be coated, rinsed, and the cells must be introduced between them. This must be done without losing the parallelity gained in the previous steps. As a precaution, the top plate is not lifted by more than 2 mm at any time. Also, a mark is made on it to remember its angular position at the time of the fixation. Introducing the fibronectin solution is straightforward. Since the plates are clean and dry, at a spacing of $\sim\ 200\mu$m surface tension readily sucks the solution into the gap. The fibronectin solution is left between the plates for one hour. Then the top plate is brought down to a nominal gap of 1 μm, which pushes the solution out. To remove it completely from the plates, the fibronectin solution is sucked with a pipette or blown away. Aspiring it by capillary effect with a piece of cloth tissue is not a good idea, as paper fibers may get between the plates.

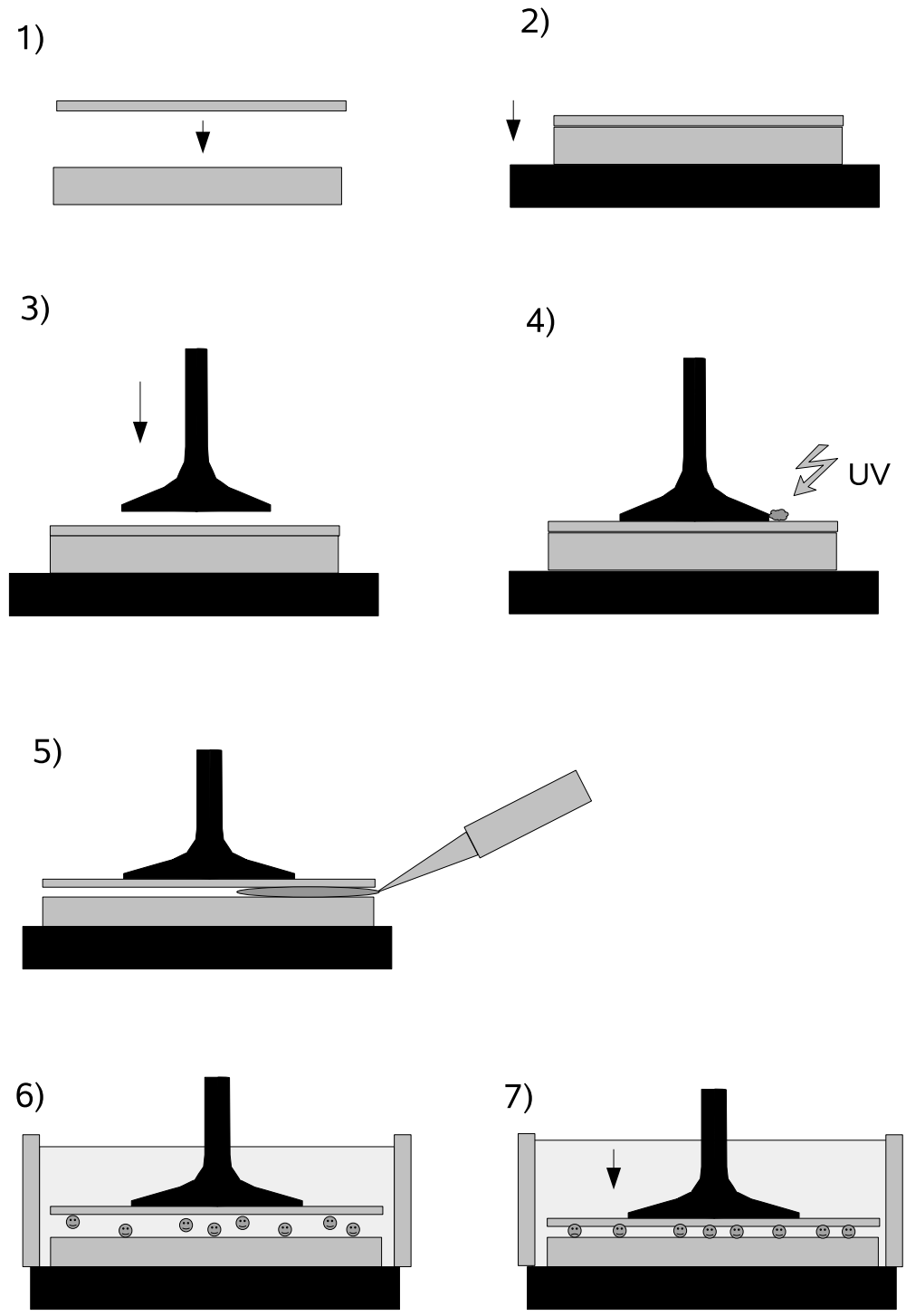

Figure B.2: *Experimental procedure.* **1:** *the glass plates are put in parallel contact with each other.* **2:** *the bottom plate is fixed on the rheometer.* **3:** *the top rheometer plate is brought down.* **4:** *the top glass plate is glued to the rheometer plate with UV-curable glue.* **5:** *the fibronectin solution is introduced and left for 1 hour, in order to coat the plates.* **6:** *the cell suspension is introduced. The top plate is immersed in medium with buffer.* **7:** *The top plate is brought down and the cells are compressed for about 1 hour, so that they stick well on both plates.*

6. The cell suspension is introduced in a similar fashion. Before lowering the top plate, it is mandatory to wait for about 10 minutes. The reason is that the cells must be allowed to sink down and stick on the bottom plate; otherwise, the outward movement of the liquid induced by bringing the plate down removes the cells. This must be avoided, as we need a very high cell density. Waiting for too long before bringing the plate down is also undesirable, since then the problem described in chapter 3 arises: the cells stick more onto the first plate, an unstable situation which leads to fast detachment.

7. After a prudential time, the top plate is brought down ensuring that its angular position is the same as during the fixation. The cells are compressed for about 1 hour, mimicking the procedure used for the single cell experiments.

B.2 Results

B.2.1 Frequency sweeps at different gaps

Fig.B.3 shows a series of frequency sweeps. A weak increasing trend of both moduli with the frequency is seen. The loss angle is $\simeq 10^\circ$. Our single-cell results show δ to be distributed over a range 10–30°. As discussed in Chapter2, power-law frequency dependences are equivalent to a broad, flat spectrum of relaxation times. The broader the spectrum, the lower the loss angle. In principle each fibroblast in the plate-plate rheometer should contribute independently to the force measurement, so the superposition argument can be extended to these experimental results. Thus, since the relaxation spectra of individual cells are broadly distributed, we expect indeed the frequency sweep measured by the rheometer to be even more "power-law-like", flatter and with a lower δ when compared to the response of single cells.

The crucial test in the experiment is lifting the plate to 200 μm and then repeating a frequency sweep. At such a separation between plates, no fibroblast is able to stay attached; either they will break or detach. This we know from single-cell experiments. When the top plate is brought down to 20 μm and a frequency sweep performed, the moduli have become about two orders of magnitude lower and forces are too low for the rheometer to measure, as shown in Fig.B.3. Lowering the top plate further, to 5 μm, restores the measurement: an approximate normal frequency sweep is obtained. Presumably, at this small gap we are compressing the cells again. Taken together, these results strongly indicate that we were indeed measuring on cells.

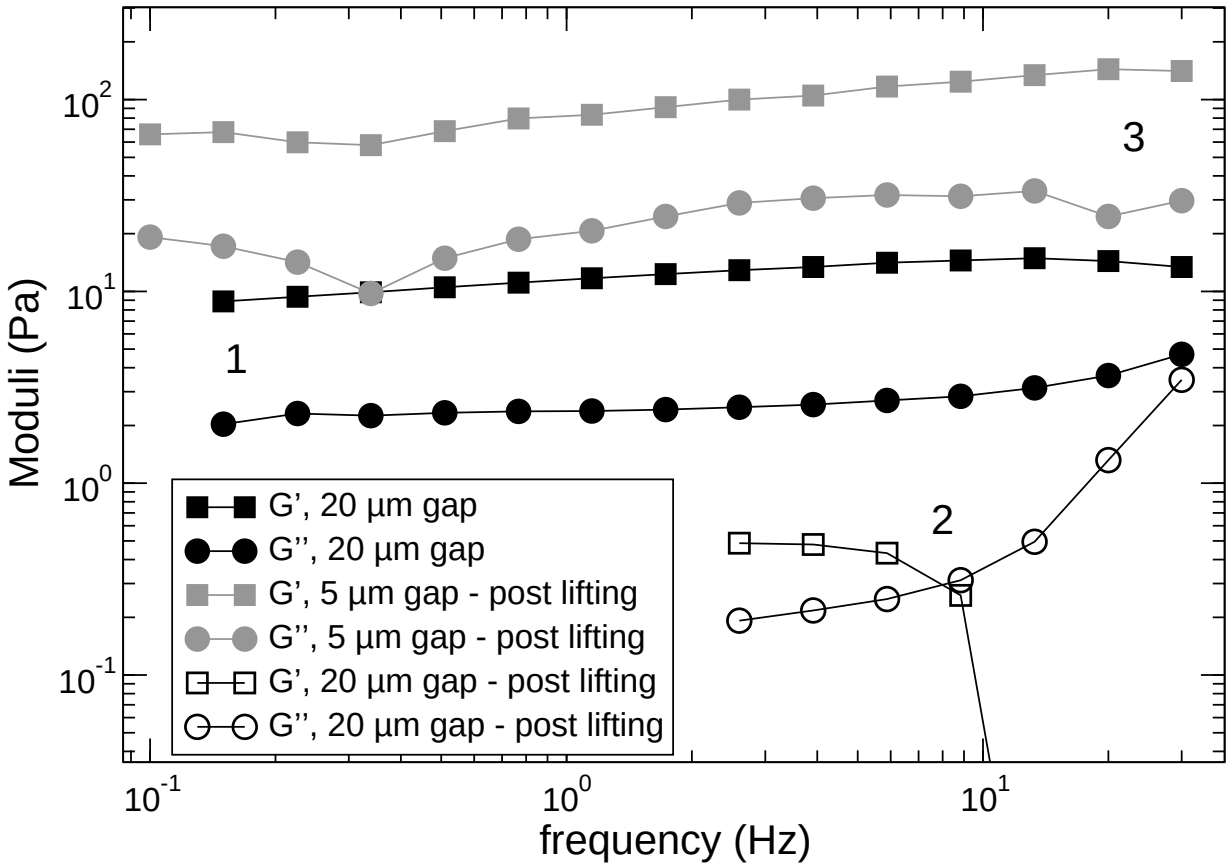

Figure B.3: *Frequency sweep at different distances between the plates.*
1 (black symbols): *Initial curve, at a* $20\,\mu m$ *gap.*
2 (open symbols): *Curve measured after increasing the gap to* $200\,\mu m$ *and bringing it immediately back to* $20\,\mu m$ *gap. The moduli have become too low for the rheometer to measure; presumably all cells detached during the very large stretch.*
3 (grey symbols): *Final measurement at* $5\,\mu m$ *gap. The moduli are again high; presumably we were compressing the cells.*

B.2.2 Step-strain

Fig.B.4 shows results from a second experiment performed in similar conditions, also with a 5 cm diameter glass plate. Here, a sequence of step strains was applied, measuring the shear stress relaxation curve each time. These can be well described as stretched exponentials, in agreement with the results on single cells. After each step strain the force relaxes to a nonzero value. As sucessive steps accumulate, the force increases steadily. This corresponds to a solid behaviour, as expected for cells. Again, to confirm that cells are being measured, the experiment is ended by applying a large deformation (200%) which cells cannot endure without breaking or detaching. The shear stress goes indeed to zero as expected.

B.3 Outlook

The results shown in Figs.B.3, B.4 are promising and demand further work in the procedure. In principle, the goal is to study the nonlinear properties of the cell monolayer as in the single-cell experiments, by superimposing small shear oscillations on a large deformation. Originally the idea was to impose a *longitudinal* large deformation, and relate the shear moduli to the normal force. However, the resolution of the normal force measurement is too low for our purposes. Two alternative approaches are: 1) to impose a large *shear* deformation, and 2) to improve the normal force measurement by using a scale.

1) If one is applying a large *shear* deformation the plate-plate geometry is not optimal, as the amount of shear increases radially. The cells near the edge of the plates will leave the linear regime, but the ones near the middle won't. The shear modulus measured by the superimposed oscillations will be an average over cells within and beyond the linear regime, and stiffening will be difficult to observe. Conceivably, at strains where the cells near the middle stiffen, those near the edge will break or detach. Thus stiffening might be not observed at all. Ideally one would want to have cells only at a given radius. To be able to measure, however, a large number of cells is necessary. As a compromise we suggest to have cells only on the outer edge, over a ~ 1 cm wide ring. This may be achieved by etching the bottom glass plate with fluorhydric acid, removing $\sim 20\,\mu\mathrm{m}$ of glass everywhere except on the desired outer ring.

2) A simple way of improving the resolution of the normal force measurement is to install a digital scale over the bottom plate of the rheometer. Inexpensive scales with heights of ~ 3 cm and resolutions of 1 mg are commercially available. Since the total shear amplitude is very low, an exact alignment of the scale is not necessary.

An essential improvement is visualising the cells between the plates during the experiment. This would provide an independent confirmation that the cells are actually there. Moreover, by taking a few images one could estimate the total amount of cells. It should even be possible to discern whether the cells are under shear, telling us how many cells are really sticking. For this, glass plates bigger than the top metal plate of the rheometer are necessary. Recently a sapphire plate with a diameter of 75 mm and a thickness of 2 mm was acquired.

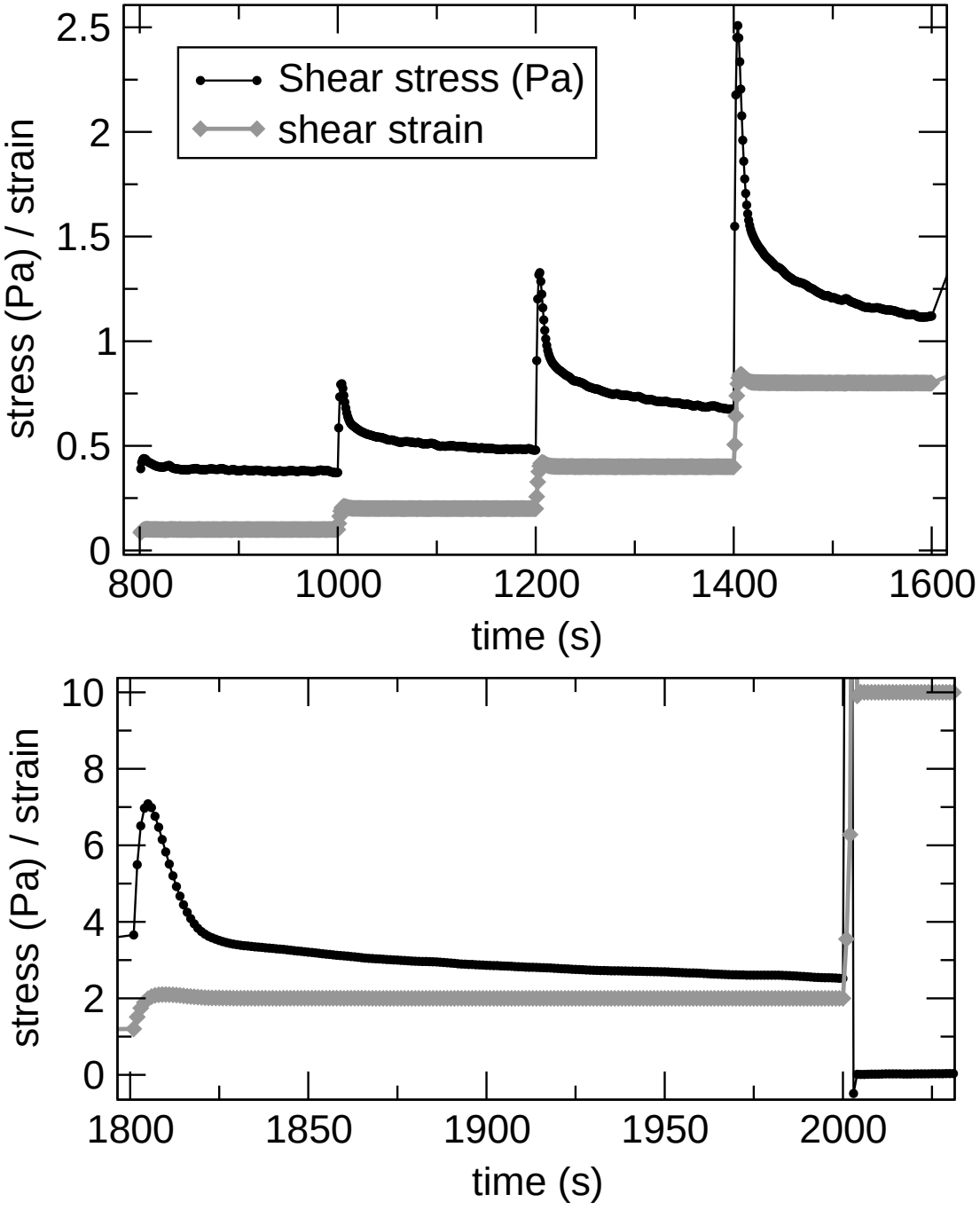

Figure B.4: *Step-strain experiment. The top plate is stepwise rotated, held at a constant angle and the stress relaxation curve measured. The procedure is repeated. The shear stress increases steadily without relaxing fully to zero. At* $t = 2000$ *s, a very large stretch amounting to* 200% *is applied. The shear stress is seen to relax to zero; presumably, all cells detached.*

Once these obstacles are overcome, what next? Providing an independent check of the single-cell results is still a goal, but direct comparison will be difficult due to the average over many cells. This can already be seen in the frequency sweeps, which are significantly flatter and more elastic than those on single cells. Rather, the technique could be exploited for screening purposes, as with it 10^6 cells can be measured within a few hours. Here it must be kept in mind that only good, well-sticking cells contribute to the measurement. This might be seen as disadvantageous, as not all cells can be analysed; we regard it rather as a positive feature – the experiment focuses on good cells. If combined with microscopic observation, the total amount of adhering cells may be measured and also be used to characterise the cell population. With this technique, one may also study the effect on mechanical behaviour of different biochemical coatings.

Summary

Biomechanics is a field of major biological relevance. In spite of the vast complexity of biological matter, a number of generic features are found to hold in the mechanics of soft tissues throughout all of its length scales. These include power-law frequency dependences typical of glasses, as well as rather unique exponential stress-strain relations. A major goal in biomechanics is to reduce its general features to those of the cytoskeleton, the filamentous scaffold which provides cells with mechanical integrity, architecture and contractility.

The first part of this report describes single-cell uniaxial stretching experiments performed on fibroblasts. Fibroblasts are found in connective tissue, close relatives of muscle particularly appropriate for mechanical measurements. By focusing on strong fibroblasts, which sustain high forces and can be deformed by large amounts, highly reproducible mechanical behaviour is observed. All major features of cell and tissue mechanics can be found: active contraction, stress stiffening, and plasticity.

When placed between fibronectin coated microplates, fibroblasts adopt a regular, symmetrical shape and generate forces, which highlights the convenience of the geometry for mechanical measurements. When a constant cell length ℓ is imposed, an increase with time of the pulling force F can be observed. This active behaviour can be probed in more detail by superimposing oscillations at frequencies in the range 0.1–1 Hz. In order to stay within the linear response regime, the deformation amplitude is kept below 5%. The response to the superimposed oscillations is then characterised by viscoelastic parameters, the modulus $|\Theta|$ and the loss angle δ. These are seen to be a function of the average force $\langle F \rangle$ acting on the cell. This master-relation holds for all cells. The modulus $|\Theta|$ is constant at low forces, equal to Θ_0; above a force F_C a crossover to power-law stress stiffening is observed, where $|\Theta|$ as a function of $\langle F \rangle$ goes as a power-law with exponents in the range 1-1.8. The loss angle δ depends only weakly on the average force. The parameters F_C and Θ_0 are strongly correlated, so that F_C/Θ_0 is similar for all cells.

Remarkably, the moduli are a function of the average force but are independent of the cell length. Therefore this mechanical behaviour is not strain stiffening; rather, it is an example of active, intrinsic *stress* stiffening. The precise way of sweeping force-space is irrelevant. Force-space can be explored in an "active" fashion by the cell itself, as in the experiment described above; or in a "passive" way as the experimentator stretches the cell. The master-relation is the same in both cases. A distinction between active and passive stress is thus artificial. The only significant limit to this stiffening relation is given by the deformation rate: it breaks down at stretching rates beyond ~ 200 nm/s.

The master-relation is the same when an unspecific coating such as aminosilane-glutaraldehyde is used, indicating that the response is due to essential properties of the force-bearing structures inside the cell. Accordingly, drug perturbation experiments indicate that the actomyosin system plays an essential role in the cell pulling geometry. Disruption of actin, or blocking myosin, has dramatic negative effects in stiffness, force generation and adhesion.

The stiffening relation shows a striking similarity to rheological measurements performed on purified actin gels. The exponents as well as the ratio F_C/Θ_0 are similar, in an unprecedented example of quantitative agreement between living and dead matter. In physiological conditions, actin networks have lengths and mesh sizes of the order of 100 nm, whereas the persistence length of actin filaments is about 10 μm. The general mechanical response of biopolymer gels clearly originates in this semiflexible behaviour of filaments. The precise mechanism is however at present not fully understood. Here, a simple explanation is proposed. It is shown that stress stiffening in fibroblasts bears a strong resemblance to the nonlinear mechanics of Euler-Bernoulli beams, which show a linear regime at low forces, and beyond 30% strain a crossover to power-law stiffening with an exponent 1.75.

Regardless of microscopic interpretations, our results can be compared with similar stiffening responses previously observed in biological materials. In whole tissues as well as at the micrometer scale, power-law stress stiffening with exponents close to 1 is a ubiquitous feature. However, a linear regime at low forces has not been reported in these experiments. Our experiments on single cells, with higher resolution and control, provide a connection between biomechanics and *in vitro* experiments on actin gels.

If a ramp experiment is performed, where the cell length ℓ is increased at a constant rate, an approximately linear relation between F and ℓ is observed beyond $\sim$10% stretch, over up to 100% deformations. Thus, stiffening can only be observed in a "differential" fashion, by superimposing small oscillations and relating the average force to the response parameters $|\Theta|$, δ. To reconcile this fact with the interpretation of stress stiffening as an elastic response, it is argued that plastic deformation sets in at deformations beyond $\sim 10\%$. In fact, the response of fibroblasts to large amplitude deformations strikingly resembles the well-known plasticity of metals. Fibroblasts can be described as showing kinematic (or directional) hardening, a hallmark of composite materials. These consist of a plastic matrix with embedded elastic solutes. Reproducible features of fibroblast mechanics, such as softening in loading-unloading cycles, can be well described in these terms. Though a thorough characterisation remains for the future, a promising phenomenological framework has been found.

Given the well defined mechanical features of fibroblasts in the cell-pulling geometry, it is desirable to extend the experiment to many-cell experiments, which would allow for fast screening of genetically modified cells. With this goal, a procedure was devised to measure mechanical properties of about 10^5 fibroblasts simultaneously using a commercial rheometer. Fibroblasts are held between two optically flat glass plates attached to a rheometer, in a plate-plate geometry. Key to the success of the experiment is a very precise alignment of the glass plates, which is given by the assembly procedure. Using the experience gained from single-cell experiments, encouraging preliminary measurements were obtained.

Also desirable to complement the cell-pulling measurements is microscopic visualisation of the cytoskeletal structure in these conditions. However, the bulky 3-dimensional geometry precludes resolving fine details. As an alternative approach, a patterned substrate was developed, consisting of $10\,\mu$m wide, $30\,\mu$m deep grooves. When coated with fibronectin, fibroblasts crawl into the grooves and adopt shapes remarkably similar to that of the cell-pulling geometry. The advantage of the pattern is that with it a large number of cells in the cell-pulling geometry can be fixed, stained, and mounted. In the future, this should allow for large-scale observation via electron or confocal microscopy.

The second part of this report addresses experiments performed on neurites. These comprise axons –the processes extended by neurons– as well as PC12 neurites, a model system for axons. These are long, cylindrical membrane tubes filled with an array of longitudinally arranged microtubules. Throughout, neurites are perturbed by means of changes in osmotic pressure. By means of image analysis, the evolution in time of neurite volume and area after a hypo- or hyperosmotic shock can be accurately measured.

After a sudden increase in the external osmotic pressure, axons swell and a cylindrical-peristaltic shape transformation sets in. We interprete this transition as a Rayleigh-Plateau-like instability triggered by elastic membrane tension, similar to the pearling instability known in membrane tubes. To determine the contribution of the cytoskeleton to neurite stability, hypoosmotic shock experiments are performed in presence of specific drugs and the spectrum of the neurite shape is measured. In this way the contribution of microtubuli is shown to be especially important. Microtubuli disruption by nocodazol strongly increases the maximum amplitude of the instability, as well as slightly increases the wavenumber of the fastest mode.

Following the evolution in time of neurite volume and instability amplitude shows that the volume relaxes back to its initial value, and the peristaltic modulation vanishes as the cylindrical shape is recovered. However, the shape relaxes well before the volume and area do. This indicates that membrane tension decouples from the apparent area and volume during the relaxation phase. We hypothesise that material is added to the membrane by means of vesicle fusion.

The evolution in time after hypoosmotic shock of the neurite volume can be approximately described by an initial swelling rate, a maximum volume, and a relaxation time. These parameters were measured at different temperatures and initial osmotic pressure differences $\Delta\Pi_0$. The swelling rate depends nonlinearly on the initial osmotic pressure difference: it saturates beyond $\Delta\Pi_0 = 0.3\,\mathrm{RT}\,300\,\mathrm{mM}$. The maximum volume V_M scales linearly with the initial volume V_0. Studying V_M/V_0 as a function of $\Delta\Pi_0$ reveals that at mild shocks, $\Delta\Pi_0 \leq 0.3\,\mathrm{RT}\,300\,\mathrm{mM}$, neurites swell as much as perfect osmometers before the relaxation phase begins. At stronger shocks, $\Delta\Pi_0 = 0.5\,\mathrm{RT}\,300\,\mathrm{mM}$, neurites swell significantly less than perfect osmometers. Therefore, during the swelling phase either the internal osmolarity has already changed, or hydrostatic pressures develop. The relaxation time as a function of the temperature closely follows an Arrhenius dependence, suggesting the rate-limiting factor of the relaxation to be the movement of ions through channels.

Similar experiments were also performed under drug-induced perturbation of actin, myosin and microtubuli. Cytoskeleton perturbation does not have any significant effect on volume relaxation, indicating that it takes place solely by changes in osmolarity, without a significant role for hydrostatic pressures. A clear effect of drugs is seen in the initial swelling phase, especially after

microtubuli disruption by nocodazol. The rate and extent of swelling are significantly higher. Taking the effect of drugs on the evolution of neurite volume together with that on the pearling instability, we suggest that hydrostatic pressure is present in the initial swelling phase and determines the swelling rate.

In conclusion, reproducible, quantitative experiments at the single-cell level have been developed which address biologically relevant phenomena. Following a time-honoured tradition in physics, both the cell-pulling experiments and the shape transformations in axons address highly symmetric systems, where the geometry does not preclude the understanding. First interpretations of the observed phenomena have been found, in terms of generic behaviours common to all objects under tension.

Bibliography

1. Glaser, R. 1996. Biophysik. Gustav Fischer, Jena, 4th edition.

2. Volkenshtein, M. V. 1981. Biophysics. Mir, Moscow, 1st edition.

3. Schrödinger, E. 1967. What is life? Cambridge University Press, Cambridge.

4. James Press, S. and Tanur, J. M. 2001. The subjectivity of scientists and the bayesian approach. John Wiley and Sons,Inc., New York.

5. Bray, D. 2001. Cell Movements : from molecules to motility. Garland Publishing, Inc., New York, 2nd edition.

6. Love, A. E. H. 1944. A treatise on the mathematical theory of elasticity. Dover, New York.

7. Lubliner, J. 1990. Plasticity theory. Macmillan Publishing Company, New York, 1st edition.

8. Fung, Y. C. 1993. Biomechanics: Mechanical properties of living tissues. Springer Verlag, New York.

9. Howard, J. 2001. Mechanics of Motor Proteins and the Cytoskeleton. Sinauer Associates, Inc., Sunderland, Massachusetts.

10. Bischofs, I. B. and Schwarz, U. S. 2003. Cell organization in soft media due to active mechanosensing. Proc. Natl. Acad. Sci. USA 100:9274–9279.

11. Choquet, D., Felsenfeld, D. P., and Sheetz, M. P. 1997. Extracellular matrix rigidity causes strengthening of integrin-cytoskeleton linkages. Cell 88:39–48.

12. Janmey, P. A. 1998. The cytoskeleton and cell signaling: component localization and mechanical coupling. Physiol. Rev. 78:763–781.

13. Alberts, B., Bray, D., Lewis, J., Raff, M., Roberts, K., and Watson, J. D. 1994. Molecular Biology of the Cell. Garland Publishing, Inc., New York, 3rd edition.

14. Gerbal, F., Noireaux, V., Sykes, C., Jülicher, F., Chaikin, P., Ott, A., Prost, J., Golsteyn, R. M., Friederich, E., Louvard, D., Laurent, V., and Carlier, M. F. 1999. On the ”listeria” propulsion mechanism. Pramana - J. Phys. 53:155–170.

15. Betz, T., Lim, D., and Käs, J. A. 2006. Neuronal growth: a bistable stochastic process. Phys.Rev.Lett 96:098103.

16. Hatwalne, Y., Ramaswamy, S., Rao, M., and Adithi Simha, R. 2004. Rheology of active-particle suspensions. Phys.Rev.Lett. 92:118101.

17. Kruse, K., Joanny, J. F., Jülicher, F., Prost, J., and Sekimoto, K. 2004. Asters, vortices, and rotating spirals in active gels of polar filaments. Phys.Rev.Lett. 92:078101.

18. Kruse, K. and Jülicher, F. 2000. Actively contracting bundles of polar filaments. Phys.Rev.Lett. 85:1778–1781.

19. Sawada, Y. and Sheetz, M. P. 2002. Force transduction by triton cytoskeletons. J. Cell Biol. 156:609–615.

20. Lansing Taylor, D. and Fechheimer, M. 1982. Cytoplasmic structure and contractility: the solation–contraction coupling hypothesis. Phil.Trans.R.Soc.Lond. B299:185–197.

21. Taylor, D. L., Condeelis, J. S., Moore, P. L., and Allen, R. D. 1973. The contractile basis of amoeboid movement. I. The chemical control of motility in isolated cytoplasm. J.Cell.Biol. 59:378–394.

22. Oster, G. F. and Odell, G. M. 1984. The mechanochemistry of cytogels. Physica 12D:333–350.

23. Nédélec, F. J., Surrey, T., and Maggs, A. C. 2001. Dynamic concentration of motors in microtubule arrays. Phys.Rev.Lett. 86:3192–3195.

24. Nédélec, F. J., Surrey, T., Maggs, A. C., and Leibler, S. 1997. Self-organization of microtubules and motors. Nature 389:305–308.

25. Bausch, A. R. and Kroy, K. 2006. A bottom-up approach to cell mechanics. Nature Physics 2:231–238.

26. Janmey, P. A., Hvidt, S., Käs, J., Lerche, D., Maggs, A., Sackmann, E., Schliwa, M., and Stossel, T. P. 1994. The mechanical properties of actin gels. Elastic modulus and filament motions. J. Biol. Chem. 269:32503–32513.

27. Janmey, P. A., Hvidt, S., Lamb, J., and Stossel, T. P. 1990. Resemblance of actin-binding protein/actin gels to covalently crosslinked networks. Nature 345:89–92.

28. Nakamura, F., Osborn, E., Janmey, P. A., and Stossel, T. P. 2002. Comparison of filamin a-induced cross-linking and arp2/3 complex-mediated branching on the mechanics of actin filaments. J. Biol. Chem. 277:9148.

29. Xu, J., Tseng, Y., and Wirtz, D. 2000. Strain Hardening of Actin Filament Networks. Regulation by the dynamic cross-linking protein α-actinin. J. Biol. Chem. 275:35886–35892.

30. Gardel, M. L., Shin, J. H., MacKintosh, F. C., Mahadevan, L., Matsudaira, P., and Weitz, D. A. 2004. Elastic behavior of cross-linked and bundled actin networks. Science 304:1301–1305.

31. Storm, C., Pastore, J. J., MacKintosh, F. C., Lubensky, T. C., and Janmey, P. A. 2005. Nonlinear elasticity in biological gels. Nature 435:191–194.

32. Bausch, A. R., Möller, W., and Sackmann, E. 1999. Measurement of local viscoelasticity and forces in living cells by magnetic tweezers. Biophys.J. 76:573–579.

33. Fabry, B., Maksym, G. N., Butler, J. P., Glogauer, M., Navajas, D., and Fredberg, J. J. 2001. Scaling the microrheology of living cells. Phys. Rev. Lett. 87:148102.

34. Fabry, B., Maksym, G. N., Butler, J. P., Glogauer, M., Navajas, D., Taback, N. A., Millet, E. J., and Fredberg, J. J. 2003. Time scale and other invariants of integrative mechanical behavior in living cells. Phys. Rev. E 68:041914.

35. Fernández, P., Pullarkat, P. A., and Ott, A. 2006. A master relation defines the nonlinear viscoelasticity of single fibroblasts. Biophys. J. 90:3796–3805.

36. Rotsch, C. and Radmacher, M. 2000. Drug-induced changes of cytoskeletal structure and mechanics in fibroblasts: an atomic force microscopy study. Biophys. J. 78:520–535.

37. Stamenović, D. and Coughlin, M. F. 1999. The role of prestress and architecture of the cytoskeleton and deformability of cytoskeletal filaments in mechanics of adherent cells: a quantitative analysis. J. Theor. Biol. 201:63–74.

38. Thoumine, O. and Ott, A. 1997. Time scale dependent viscoelastic and contractile regimes in fibroblasts probed by microplate manipulation. J. Cell. Science 110:2109–2116.

39. Verdier, C. 2003. Rheological properties of living materials. from cells to tissues. J. Theo. Med. 5:67–91.

40. Guck, J., Ananthakrishnan, R., Mahmood, H., Moon, T. J., Casey Cunningham, C., and Käs, J. 2001. The optical stretcher: a novel laser tool to micromanipulate cells. Biophys.J. 81:767–784.

41. Heidemann, S. R. and Wirtz, D. 2004. Towards a regional approach to cell mechanics. Trends Cell Biol. 14:160–166.

42. Schwarz, U. S. and Safran, S. A. 2002. Elastic interactions of cells. Phys.Rev.Lett 88:048102.

43. Pullarkat, P., Dommersnes, P., Fernández, P., Joanny, J.-F., and Ott, A. 2006. Osmotically induced shape transformations in axons. Phys. Rev. Lett. 96:048104.

44. Bar-Ziv, R. and Moses, E. 1994. Instability and “pearling” states produced in tubular membranes by competition of curvature and tension. Phys. Rev. Lett. 73:1392–1395.

45. Bar-Ziv, R. and Moses, E. 1999. Pearling in cells: a clue to understanding cell shape. Proc. Natl. Acad. Sci. USA 96:10140–10145.

46. Pike, C., Cummings, B., and Cotman, C. 1992. β-Amyloid induces neuritic dystrophy in vitro: similarities with Alzheimer pathology. Neuroreport 3:769–772.

47. Shannon, P., Smith, C., Deck, J., Ang, L., M., H., and Becker, L. 1998. Axonal injury and the neuropathology of shaken baby syndrome. Acta Neuropathol. 95:625–631.

48. Ochs, S., Pourmand, R., Jersild, R., Jr., and Friedman, R. 1997. The origin and nature of beading: A reversible transformation of the shape of nerve fibers. Prog. Neurobiol. 52:391–426.

49. Al-Noori, S. and Swann, J. 2000. A role for sodium and chloride in kainic acid - induced beading of inhibitory interneuron dendrites. Neuroscience 101:337–348.

50. Tanelian, D. and Markin, V. 1997. Biophysical and functional consequences of receptor-mediated nerve fiber transformation. Biophys.J. 72:1092–1108.

51. Lang, F., Busch, G., Ritter, M., Völkl, H., Waldegger, S., Gulbins, E., and Häussinger, D. 1998. Functional significance of cell volume regulatory mechanisms. Physiol. Reviews 78:247.

52. MacKnight, A. D. C. 1987. Volume maintenance in isosmotic conditions. In R. Gilles, A. Kleinzeller, and L. Bolis, editors, Cell Volume Control: Fundamental and comparative aspects in animal cells., pages 3–43. Academic Press, San Diego.

53. Sarkadi, B. and Parker, J. 1991. Activation of ion transport pathways by changes in cell volume. Biochim. Biophys. Acta 407:1071.

54. Hernandez, J. and Cristina, E. 1998. Modelling cell volume regulation in nonexcitable cells: the roles of the Na^+ pump and of cotransport systems. Am. Physiol. Soc. page C1067.

55. Strieter, J., Stephenson, J., Palmer, L., and Weinstein, A. 1990. Volume-activated chloride permeability can mediate cell volume regulation in a mathematical model of a tight epithelium. J. Gen. Physiol. 96:319–344.

56. Colclasure, G. and Parker, J. 1992. Cytosolic Protein Concentration is the Primary volume signal for Swelling-induced [K-Cl] Cotransport in dog red cells. J. Gen. Physiol. 100:1.

57. Morris, C. 1990. Mechanosensitive ion channels. J. Membr. Biol. 113:93–107.

58. Strange, K. 2004. Cellular volume homeostasis. Adv.Physiol.Educ. 28:155–159.

59. Tomasek, J. J., Gabbiani, G., Hinz, B., Chaponnier, C., and Brown, R. A. 2002. Myofibroblasts and mechanoregulation of connective tissue remodelling. Nature Rev. 3:349–363.

60. Liu, X. and Pollack, G. H. 2002. Mechanics of f-actin characterized with microfabricated cantilevers. Biophys. J. 83:2705–2715.

61. Bear, J. E., Krause, M., and Gertler, F. B. 2001. Regulating cellular actin assembly. Curr. Opin. Cell Biol. 13:158–166.

62. Machesky, L. M. and Gould, K. L. 1999. The Arp2/3 complex: a multifunctional actin organizer. Curr. Opin. Cell Biol. 11:117–121.

63. Loisel, T. P., Boujemaa, R., Pantaloni, D., and Carlier, M. F. 1999. Reconstitution of actin-base motility of Listeria and Shigella using pure proteins. Nature 401:613–616.

64. Matsudaira, P. 1994. Actin crosslinking proteins at the leading edge. Semin. Cell. Biol. 5:165–174.

65. Reisler, E., Smith, C., and Seegan, G. 1980. Myosin minifilaments. J. Mol. Biol. 143:129.

66. Fenn, W. O. 1923. A quantitative comparison between the energy liberated and the work performed by the isolated sartorius muscle of the frog. J. Physiol. (Lond) 58:175–203.

67. Veigel, C., Molloy, J. E., Schmitz, S., and Kendrick-Jones, J. 2003. Load-dependent kinetics of force production by smooth muscle myosin measured with optical tweezers. Nature Cell Biol. 5:980–986.

68. Riveline, D., Ott, A., Jülicher, F., Winkelmann, D. A., Cardoso, O., Lacapère, J. J., Magnúsdóttir, S., Viovy, J. L., Gorre-Talini, L., and Prost, J. 1998. Acting on actin: the electric motility assay. Eur. Biophys. J. 27:403–408.

69. Jülicher, F. and Prost, J. 1995. Cooperative molecular motors. Phys.Rev.Lett. 75:2618–2621.

70. Zhu, C., Bao, G., and Wang, N. 2000. Cell mechanics: mechanical response, cell adhesion, and molecular deformation. Annu. Rev. Biomed. Eng. 02:189–226.

71. Rivero, F., Köppel, B., Peracino, B., Bozzaro, S., Siegert, F., Weijer, C. J., Schleicher, M., Albrecht, R., and Noegel, A. A. 1996. The role of the cortical cytoskeleton: F-actin crosslinking proteins protect against osmotic stress, ensure cell size, cell shape and motility, and contribute to phagocytosis and development. J. Cell Sci. 109:2679–2691.

72. Pasternak, C., Spudich, J. A., and Elson, E. L. 1989. Capping of surface receptors and concomitant cortical tension are generated by conventional myosin. Nature 341:549–551. When probed by cell-poking, resting *Dictyostelium* mutants lacking myosin are about 30% softer than normal cells. ATP depletion increases the stiffness of normal cells by a factor of 5, whereas no effect is seen in mutants.

73. Burridge, K., Chrzanowska-Wodnicka, M., and Zhong, C. 1997. Focal adhesion assembly. Trends Cell Biol. 7:342–347.

74. Wehrle-Haller, B. and Imhof, B. A. 2002. The inner lives of focal adhesions. Trends Cell Biol. 12:382–389.

75. Calderwood, D. A., Shattil, S. J., and Ginsberg, M. H. 2000. Integrins and actin filaments: reciprocal regulation of cell adhesion and signaling. J. Biol. Chem. 275:22607–22610.

76. Yamada, K. M. and Miyamoto, S. 1995. Integrin transmembrane signaling and cytoskeletal control. Curr. Opin. Cell Biol. 7:681–689.

77. Lotz, M. M., Burdsal, C. A., Erickson, H. P., and McClay, D. R. 1989. Cell adhesion to fibronectin and tenascin: quantitative measurements of initial binding and subsequent strengthening response. J. Cell Biol. 109:1795–1805.

78. Riveline, D., Zamir, E., Balaban, N. Q., Schwarz, U. S., Ishizaki, T., Narumiya, S., Kam, Z., Geiger, B., and Bershadsky, A. D. 2001. Focal contacts as mechanosensors: externally applied local mechanical force induces growth of focal contacts by an mDia1-dependent and ROCK-independent mechanism. J. Cell Biol. 153:1175–1185.

79. Katoh, K., Kano, Y., Masuda, M., Onishi, H., and Fujiwara, K. 1998. Isolation and contraction of the stress fiber. Mol. Biol. Cell 9:1919–1938.

80. Katoh, K., Kano, Y., Amano, M., Onishi, H., Kaibuchi, K., and Fujiwara, K. 2001. Rho-kinase-mediated contraction of isolated stress fibers. J. Cell Biol. 153:569–583.

81. Grinell, F. 1994. Fibroblasts, myofibroblasts, and wound contraction. J. Cell Biol. 124:401–404.

82. Hinz, B., Mastrangelo, D., Iselin, C. E., Chaponnier, C., and Gabbiani, G. 2001. Mechanical tension controls granulation tissue contractile activity and myofibroblast differentiation. Am. J. Pathology 159:1009–1020.

83. Brenig, W. 1989. Statistical theory of heat. Nonequilibrium phenomena. Springer, Berlin.

84. Götze, W. and Sjögren, L. 1992. Relaxation processes in supercooled liquids. Rep. Prog. Phys. 55:241–376.

85. Healy, W. P. 1976. Primitive causality and optically active molecules. J.Phys.B: Atom.Molec.Phys. 9:2499–2510.

86. Wagner, K. W. 1913. zur theorie der unvollkommenen dielektrika. Ann. Physik .

87. Neubert, H. K. P. 1963. A simple model representing internal damping in solid materials. Aeronaut. Q. 14:187–197.

88. Fung, Y. C. 1972. Stress–strain-history relations of soft tissues in simple elongation. In Y. Fung, N. Perrone, and M. Anliker, editors, Biomechanics: Its Foundations and Objectives. Prentice-Hall, Englewood Cliffs, NJ.

89. Jaynes, E. T. 2001. Probability theory: the science of logic. Cambridge University Press, Cambridge.

90. Fung, Y. C. B. 1967. Elasticity of soft tissues in simple elongation. Am. J. Physiol. 213:1532–1544.

91. Aubert, X. 1955. Intervention d'un elément élastiane pur dans la contraction du muscle strié. Arch. Intern. Physiol. Biochim. 63:197–202.

92. Obara, K., Nobe, K., Nobe, H., Kolodney, M. S., de Lanerolle, P., and Paul, R. J. 2000. Effects of microtubules and microfilaments on $[\mathrm{Ca}^{2+}]_i$ and contractility in a reconstituted fibroblast fiber. Am. J. Physiol. Cell Physiol. 279:C785–C796.

93. Wakatsuki, T., Kolodney, M. S., Zahalak, G. I., and Elson, E. L. 2000. Cell mechanics studied by a reconstituted model tissue. Biophys. J. 79:2353–2368.

94. Lenormand, G., Millet, E., Fabry, B., Butler, J. P., and Fredberg, J. J. 2004. Linearity and time-scale invariance of the creep function in living cells. J.R.Soc.Lond.Interface .

95. Smith, B. A., Tolloczko, B., Martin, J. G., and Grütter, P. 2005. Probing the viscoelastic behavior of cultured airway smooth muscle cells with atomic force microscopy: stiffening induced by contractile agonist. Biophys. J. doi:10.1529/biophysj.104.046649.

96. Sollich, P. 1998. Rheological constitutive equation for a model of soft glassy materials. Phys. Rev. E 58:738–759.

97. Sollich, P., Lequeux, F., Hébraud, P., and Cates, M. E. 1997. Rheology of soft glassy materials. Phys. Rev. Lett. 78:2020–2023.

98. Kühne, M., Dumitras, M., and Friedrich, C. 2006. Morphologische und rheomechanische eigenschaften von fasernetzwerken aus tektonen. DPG Tagung.

99. Hyun, K., Kim, S. H., Ahn, K. H., and Lee, S. J. 2002. Large amplitude oscillatory shear as a way to classify the complex fluids. J. Non-Newtonian Fluid Mech. 107:51–65.

100. Wang, N., Tolic-Nørrelykke, I. M., Chen, J., Mijailovich, S. M., Butler, J. P., Fredberg, J. J., and Stamenović, D. 2002. Cell prestress. I. Stiffness and prestress are closely associated in adherent contractile cells. Am. J. Physiol. Cell Physiol. 282:C606–C616.

101. Trepat, X., Grabulosa, M., Puig, F., Maksym, G. N., Navajas, D., and Farré, R. 2004. Viscoelasticity of human alveolar epithelial cells subjected to stretch. Am. J. Physiol. Lung. Cell. Mol. Physiol. 287:L1025–L1034.

102. Kole, T. P., Tseng, Y., Huang, L., Katz, J. L., and Wirtz, D. 2004. Rho kinase regulates the intracellular micromechanical response of adherent cells to Rho activation. Mol. Biol. Cell 15:3475–3484.

103. Frey, E., Kroy, K., and Wilhelm, J. 1998. Viscoelasticity of biopolymer networks and statistical mechanics of semiflexible polymers. In S. Mathotra and J. Tuszynski, editors, Advances in Structural Biology, volume 5. Jai Press, London.

104. Keller, M., Tharmann, R., Dichtl, M. A., Bausch, A. R., and Sackmann, E. 2003. Slow filament dynamics and viscoelasticity in entangled and active actin networks. Phil. Trans. R. Soc. Lond. A 361:699.

105. Sato, M., Schwarz, W. H., and Pollard, T. D. 1987. Dependence of the mechanical properties of actin/α-actinin gels on deformation rate. Nature 325:828–830.

106. Tempel, M., Isenberg, G., and Sackmann, E. 1996. Temperature-induced sol-gel transition and microgel formation in α-actinin cross-linked actin networks: A rheological study. Phys. Rev. E 54:1802.

107. Tseng, Y., An, K. M., Esue, O., and Wirtz, D. 2004. The bimodal role of filamin in controlling the architecture and mechanics of f-actin networks. J. Biol. Chem. 279:1819.

108. Humphrey, D., Duggan, D., Saha, D., Smith, D., and Käs, J. 2002. Active fluidization of polymer networks through molecular motors. Nature 416:413.

109. Todaro, G. J. and Green, H. 1963. Quantitative studies of the growth of mouse embryo cells in culture and their development into established lines. J. Cell. Biol. 17:299–313.

110. Todaro, G. J., Habel, K., and Green, H. 1965. Antigenic and cultural properties of cells doubly transformed by polyoma virus and sv40. Virology 27:179–185.

111. Drexler, H. G., Dirks, W., MacLeod, W. R. A. F., Quentmeier, H., Steube, K. G., and Uphoff, C. C. 2001. DSMZ Catalogue of Human and Animal Cell Lines. Braunschweig.

112. Pullarkat, P. A. 2006. Shape oscillations of freely suspended fibroblasts. Submitted.

113. Katsumi, A., Wayne Orr, A., Tzima, E., and Schwartz, M. A. 2004. Integrins in mechanotransduction. J. Biol. Chem. 279:12001–12004.

114. Findley, W. N., Lai, J. S., and Onaran, K. 1976. Creep and relaxation of nonlinear viscoelastic materials: with an introduction to linear viscoelasticity. North-Holland Publishing Company, Toronto.

115. Miller, A. K., editor. 1987. Unified constitutive equations for creep and plasticity. Elsevier applied science, Essex, 2nd edition.

116. Spector, I., Shochet, N. R., Kashman, Y., and Groweiss, A. 1983. Latrunculins: novel marine toxins that disrupt microfilament organization in cultured cells. Science 219:493–495.

117. Herrmann, C., Wray, J., Travers, F., and Barman, T. 1992. Effect of 2,3-butanedione monoxime on myosin and myofibrillar ATPases. An example of an uncompetitive inhibitor. Biochemistry 31:12227–12232.

118. Saitoh, M., Ishikawa, T., Matsushima, S., Naka, M., and Hidaka, H. 1987. Selective inhibition of catalytic activity of smooth muscle myosin light chain kinase. J. Biol. Chem. 262:7796–7801.

119. De Brabander, M., Van de Veire, R., Aerts, R., Borgers, M., and Janssen, P. 1976. The effects of methyl[5-(2-thienylcarbonyl)-1H-benzimidazol-2-yl]carbamate (R 17 934, NSC 238159), a new synthetic antitumoral drug interfering with microtubules, on mammalian cells cultured in vitro. Cancer Res. 36:905–916.

120. Ott, A., Magnasco, M., Simon, A., and Libchaber, A. 1993. Measurement of the persistence length of polymerized actin using fluorescence microscopy. Phys. Rev. E. 48:R1642–R1645.

121. Groot, R. D., Bot, A., and Agterof, W. G. M. 1996. Molecular theory of strain hardening of a polymer gel: Application to gelatin. J. Chem. Phys. 104:9202–9219.

122. Ford, L. E., Huxley, A. F., and Simmons, R. M. 1981. The relation between stiffness and filament overlap in stimulated frog muscle fibres. J. Physiol. 311:219–249.

123. Dembo, M. and Wang, Y. L. 1999. Stresses at the cell-to-substrate interface during locomotion of fibroblasts. Biophys. J. 76:2307–2316.

124. Wrobel, L. K., Fray, T. R., Molloy, J. E., Adams, J. J., Armitage, M. P., and Sparrow, J. C. 2002. Contractility of single human dermal myofibroblasts and fibroblasts. Cell Motil. Cytoskel. 52:82–90.

125. Bray, D. and Thomas, C. 1975. The actin content of fibroblasts. Biochem. J. 147:221–228.

126. Head, D. A., Levine, A. J., and MacKintosh, F. C. 2003. Deformation of cross-linked semiflexible polymer networks. Phys. Rev. Lett. 91:108102.

127. Heussinger, C. and Frey, E. 2006. Stiff polymers, foams, and fiber networks. Phys. Rev. Lett. 96:017802.

128. MacKintosh, F. C., Käs, J., and Janmey, P. A. 1995. Elasticity of semiflexible biopolymer networks. Phys. Rev. Lett. 75:244425.

129. Heussinger, C. and Frey, E. 2006. Floppy modes and non-affine deformations in random fiber networks. Phys. Rev. Lett. .

130. Heussinger, C. and Frey, E. 2006. The role of architecture in the elastic response of semiflexible polymer and fiber networks. Phys. Rev. E .

131. Wilhelm, J. and Frey, E. 2003. Elasticity of stiff polymer networks. Phys. Rev. Lett. 91:108103.

132. Levine, A. J., Head, D. A., and MacKintosh, F. C. 2004. The deformation field in semiflexible networks. J. Phys.: Cond. Matter 16:S2079–S2088.

133. Onck, P. R., Koeman, T., van Dillen, T., and van der Giessen, E. 2005. Alternative explanation of stiffening in cross-linked semiflexible networks. Phys.Rev.Lett. 95:178102.

134. Bronstein, I. N. and Semendjajew, K. A. 1984. Taschenbuch der Mathematik. Harri Deutsch, Frankfurt am Main, 21th edition.

135. Dwight, H. B. 1972. Table of integrals and other mathematical data. MacMillan, New York, 10th edition.

136. Kroy, K. and Frey, E. 1996. Force-extension relation and plateau modulus for wormlike chains. Phys. Rev. Lett. 77:306–309.

137. Medalia, O., Weber, I., Frangakis, A. S., Nicastro, D., Gerisch, G., and Baumeister, W. 2002. Macromolecular architecture in eucaryotic cells visualized by cryoelectron tomography. Science 298:1209–1213.

138. Satcher, R. L. and Dewey, C. F., Jr. 1996. Theoretical estimates of mechanical properties of the endothelial cell cytoskeleton. Biophys. J. 71:109–118.

139. Stouffer, D. C. and Thomas Dame, L. 1996. Inelastic deformation of metals. Models, mechanical properties, and metallurgy. John Wiley, Inc., New York, 1st edition.

140. Moan, G. D. and Embury, J. D. 1979. A study of the bauschinger effect in al–cu alloys. Acta Metall. 27:903–914.

141. Melan, E. 1938. zur plastizität des räumlichen kontinuums. Ing.Archiv 9:116–126.

142. Prager, W. 1955. The theory of plasticity: a survey of recent achievements. Proc.Inst.Mech.Engrs. 169:41–57.

143. Prager, W. and Geiringer, H. 1934. Mechanik isotroper körper im plastischen zustand. Ergebnisse der exakten Naturwissenschaften 13.

144. Krempl, E. 1987. Models of viscoplasticity. some comments on equilibrium (back) stress and drag stress. Acta Mech. 69:25–42.

145. Miller, A. K. 1987. The MATMOD equations. In A. Miller, editor, Unified constitutive equations for creep and plasticity, pages 139–219. Elsevier applied sciences, Essex.

146. Kocks, U. F. 1987. Constitutive behavior based on crystal plasticity. In A. Miller, editor, Unified constitutive equations for creep and plasticity, pages 1–88. Elsevier applied sciences, Essex.

147. Straight, A. F., Cheung, A., Limouze, J., Chen, I., Westwood, N. J., Sellers, J. R., and Mitchison, T. J. 2003. Dissecting temporal and spatial control of cytokinesis with a Myosin II inhibitor. Science 299:1743–1747.

148. Arora, P., Bibby, K., and McCulloch, C. 1994. Slow oscillations of free intracellular calcium ion concentration in human fibroblasts responding to mechanical stretch. J.Cell.Physiol. 161:187–200.

149. Light, D., Attwood, A., Siegel, C., and Baumann, N. 2003. Cell swelling increases intracellular calcium in *necturus* erythrocytes. J.Cell Sci. 116:101–109.

150. Clemo, H. and Baumgarten, C. 1997. Swelling-activated gd^{3+}-sensitive cation current and cell volume regulation in rabbit ventricular myocytes. J.Gen.Physiol. 110:297–312.

151. Guilak, F., Zell, R., Erickson, G., Grande, D., Rubin, C., McLeod, K., and Donahue, H. 1999. Mechanically induced calcium waves in articular chondrocytes are inhibited by gadolinium and amiloride. J.Orthop.Res. 17:421–429.

152. Greene, L. and Tischler, A. 1976. Establishment of a noradrenergic clonal line of rat adrenal pheochromocytoma cells which respond to nerve growth factor. Proc.Natl.Acad.Sci.USA 73:2424–2428.

153. Roger Jacobs, J. and Stevens, J. 1986. Changes in the organization of the neuritic cytoskeleton during nerve growth factor-activated differentiation of pc12 cells: a serial electron microscopic study of the development and control of neurite shape. J.Cell Biol. 103:895–906.

154. Bray, D. 1984. Axonal growth in response to experimentally applied mechanical tension. Dev.Biol. 102:379–389.

155. Dennerll, T. J., Lamoureux, P., Buxbaum, R. E., and Heidemann, S. R. 1989. The cytomechanics of axonal elongation and retraction. J. Cell Biol. 109:3073–3083.

156. van't Hoff, J. 1887. Die rolle des osmotischen druckes in der analogie zwischen lösungen und gasen. Z.Phys.Chem. 1:481–508.

157. Weiss, T. 1996. Cellular Biophysics. MIT Press.

158. Kiil, F. 1989. Molecular mechanisms of osmosis. Am.J.Physiol. 256:R801–R808.

159. Garrahan, P. and Rega, A. 1977. Transporte a través de la membrana celular. OEA, Washington,D.C.

160. Henson, J. 1999. Relationships between the actin cytoskeleton and cell volume regulation. Microscopy research and technique 47:155–162.

161. Cornet, M., Delpire, E., and Gilles, R. 1988. Relations between cell volume control, microfilaments and microtubules networks in t2 and pc12 cultured cells. J. Physiol. Paris 83:43–49.

162. D'Alessandro, M., Russell, D., Morley, S., Davies, A., and Birgitte Lane, E. 2002. Keratin mutations of epidermolysis bullosa simplex alter the kinetics of stress response to osmotic shock. J. Cell Sci. 115:4341–4351.

163. Suchyna, T., Besch, S., and Sachs, F. 2004. Dynamic regulation of mechanosensitive channels: capacitance used to monitor patch tension in real time. Phys Biol 1:1.

164. Downey, G., Grinstein, S., Sue-A-Quan, A., Czaban, B., and Chan, C. 1995. Volume regulation in leukocytes: requirement for an intact cytoskeleton. J. Cell Physiol. 163:96–104.

165. Wan, X., Harris, J., and Morris, C. 1995. Responses of neurons to extreme osmomechanical stress. J. Memb. Biol. 145:21–31.

166. Craelius, W., Huang, C.-J., Guber, H., and Palant, C. 1997. Rheological behavior of rat mesangial cells during swelling in vitro. Biorheology 34:387–403.

167. Weinstein, A. 1997. Dynamics of cellular homeostasis: recovery time for a perturbation from equilibrium. Bull. Math. Biol. 59:451.

168. Lucio, A., Santos, R., and Mesquita, O. 2003. Measurements and modeling of water transport and osmoregulation in a single kidney cell using optical tweezers and videomicroscopy. Phys. Rev. E 68:041906.

169. Kleinzeller, A. 1965. The volume regulation in some animal cells. Arch. Biol. 76:217–232.

170. Cantielo, H. 1997. Role of actin filament organization in cell volume and ion channel regulation. J. Exp. Zoology 279:425.

171. Mills, J. 1987. The cell cytoskeleton: Possible role in volume control. In R. Gilles, A. Kleinzeller, and L. Bolis, editors, Cell volume control: fundamental and comparative aspects in animal cells, pages 75–101. Academic Press,Inc., San Diego.

172. Heubusch, P., Jung, C., and Green, F. 1985. The osmotic response of human erythrocytes and the membrane cytoskeleton. J.Cell.Physiol 122:266–272.

173. Cornet, M., Ubl, J., and Kolb, H.-A. 1993. Cytoskeleton and ion movements during volume regulation in cultured pc12 cells. J. Membrane Biol. 133:161–170.

174. Bar-Ziv, R., Moses, E., and Nelson, P. 1998. Dynamic excitations in membranes induced by optical tweezers. Biophys.J. 75:294–320.

175. Li, J. and Fontelos, M. 2003. Drop dynamics on the beads-on-string structure for viscoelastic jets: a numerical study. Phys.Fluids 15:922–937.

176. Nelson, P., Powers, T., and Seifert, U. 1995. Dynamic theory of pearling instability in cylindrical vesicles. Phys. Rev. Lett. 74:3384.

177. Chandrasekhar, S. 1970. Hydrodynamic and hydromagnetic stability. Dover, New York, 3 edition.

178. Rayleigh, L. 1899. On the instability of jets. Scientific papers 1:361–371.

179. Bray, D. 1991. Isolated chick neurons for the study of axonal growth. In G. Banker and K. Goslin, editors, Culturing Nerve Cells, pages 119–136. MIT Press, Cambridge.

180. Greene, L., Sobeih, M., and Teng, K. 1991. Methodologiesfor the culture and experimental use of the pc12 rat pheochromocytoma cell line. In G. Banker and K. Goslin, editors, Culturing Nerve Cells, pages 207–226. MIT Press, Cambridge.

181. Huster, D., Jin, A., Arnold, K., and Gawrisch, K. 1997. Water permeability of polyunsaturated lipid membranes measured by ^{17}O NMR. Biophys.J. 73:855–864.

182. Maric, K., Wiesner, B., Lorenz, D., Klussmann, E., Betz, T., and Rosenthal, W. 2001. Cell volume kinetics of adherent epithelial cells measured by laser scanning reflection microscopy: determination of water permeability changes of renal principal cells. Biophys.J. 80:1783–1790.

183. van Hoek, A. N., de Jong, M. D., and van Os, C. H. 1990. Effects of dimethylsulfoxide and mercurial sulfhydryl reagents on water and solute permeability of rat kidney brush border membranes. Biochim.Biophys.Acta 1030:203–210.

184. Blumenfeld, L. A. and Tikhonov, A. N. 1994. Biophysical thermodynamics of intracellular processes: molecular machines of the living cell. Springer, Berlin.

185. Rayleigh, L. 1892. On the instability of a cylinder of viscous liquid under capillary force. Philos.Mag. 34:195.

186. Morris, C. and Homann, U. 2001. Cell surface area regulation and membrane tension. J. Membr. Biol. 179:79–102.

187. Evans, E. and Yeung, A. 1989. Apparent viscosity and cortical tension of blood granulocytes determined by micropipette aspiration. Biophys.J. 56:151–160.

188. Pullarkat, P., Ott, A., and Acker, G. 2002. Unpublished results.

189. Ochs, S., Jersild, R., Jr., Pourmand, R., and Potter, C. 1994. The beaded form of myelinated nerve fibers. Neuroscience 61:361–372.

190. Mies, B., Rottner, K., and Small, J. V. 1998. Multiple immunofluorescence microscopy of the cytoskeleton. In J. Celis, editor, Cell biology: a laboratory handbook, volume 2, pages 469–476. Academic press, San Diego.

191. Small, J. V., Rottner, K., Hahne, P., and Anderson, K. I. 1999. Visualising the actin cytoskeleton. Microsc.Res.Tech. 47:3–17.

Danksagung

Für Hilfe, Ratschläge, und vor allem Freundlichkeit danke ich meinen Kollegen am EPI: Wolfgang Michel, Timo Mai, Jordi Soriano-Fradera, Paul Hurych, Cyrille Vezy, Judith Fischer, Philipp Baaske, Thomas Naiser, Andrea Hanold, Ralf Pihan, Uwe Schmelzer, Prof. H. Pascher, Andreas Winter, Wolfgang Kellner, Jens Fürst.

Einen besonderen Dank an Margot Lenich, die herausragende Sekretärin von EPI, die eine gute Freundin von mir geworden ist, und stets hilfsbereit viele meiner Probleme gelöst hat – nicht nur die mit der Arbeit verbunden.

Thanks Prof. Dr. Albrecht Ott for giving me this opportunity, for the freedom in developing the project and the interesting discussions. At your side I have learnt much about authority and good leadership.

I am extremely grateful to Pramod A. Pullarkat for leading me out of the darkness. Thanks for teaching me. Thanks for your friendship and for your company while holding the tail of the tiger. Thanks Sageena Chandran Pullarkat and Pooja for many nice moments.

Danke Karsten Kruse, meinem zweiten Gutachter, dass er sich als Theoretiker auf meine experimentelle Arbeit eingelassen hat. Zusammentreffen zwischen Theoretikern und Experimentatoren sind immer fruchtbar.

Vielen Dank Klaus Kroy, für deine großzügige Unterstützung in vertragslosen Zeiten. Die Zusammenarbeit mit dir hat mir in kurzer Zeit viel gebracht.

Danke den Leuten am Lehrstuhl für technische Mechanik und Strömungsmechanik (Fakultät für Angewandte Naturwissenschaften, Universität Bayreuth): Lutz Heymann, Prof. Nuri Aksel, und Gabi Jena, für eine sehr angenehme Zusammenarbeit in gutem Arbeitsklima.

Danke Heinz Krejtschi und Mitarbeitern an der mechanischen Werkstatt im NWI, für die meisterhaften Leistungen.

Danke Frank Jülicher und Ralf Everaers für die hilfreichen Diskussionen, und vor allem für die kritischen Anmerkungen.

Fussball, Grillabende, Whiskyabende, haben viel Spaß gemacht dank Silke Oellerich, Albert Voit, Richard Hildner, Robert Kühn, Gerhard Wittko, Michael Häckel, Laura Torre Lorente, Erwin Lang, Alberto de Lózar Muñoz, Alejandro Luque Estepa, und vielen mehr.

Gracias a Carmen Pérez León por la buena onda, por ser tan piola y salirte del molde.

Gracias maru por tantas cosas. Gracias Antonio y Leticia Cristodero por el cariño, la hospitalidad y las recetas.

Der Familie Hartung habe ich viel zu verdanken. Nur die Korrekturen an meiner Arbeit und die Einführung in die Oper seien hier erwähnt.

Gracias a mi familia por bancarme.